Design of hybrid nanomaterials made of organophosphorus transition metal complexes covalently bonded to metal naoparticles

Elena Martín Morales

THÈSE

En vue de l'obtention du

DOCTORAT DE L'UNIVERSITÉ DE TOULOUSE

Délivré par l'Université Toulouse 3 - Paul Sabatier

Présentée et soutenue par

Elena MARTIN MORALES

Le 6 juillet 2020

Elaboration de nanomatériaux hybrides constitués par des complexes organophosphorés de métal de transition directement coordonnés à des nanoparticules métalliques.

Ecole doctorale : **SDM - SCIENCES DE LA MATIERE - Toulouse**

Spécialité : **Chimie Organométallique et de Coordination**

Unité de recherche :
LCC - Laboratoire de Chimie de Coordination

Thèse dirigée par
Alain IGAU et Karine PHILIPPOT

Jury

M. SYLVAIN NLATE, Rapporteur
Mme AUDREY DENICOURT-NOWICKI, Rapporteure
M. NICOLAS MEZAILLES, Examinateur
M. JEAN-CYRILLE HIERSO, Examinateur
M. ALAIN IGAU, Co-directeur de thèse
Mme KARINE PHILIPPOT, Co-directrice de thèse
M. PIERRE SUTRA, Invité

Acknowledgements

First of all, I would like to thank Dr. Audrey Denicourt-Nowicki, Dr. Sylvain Nlate, Dr. Nicolas Mézailles and Dr. Jean-Cyrille Hierso for accepting to be the jury members of my thesis.

My deepest gratitude to my supervisors Dr. Karine Philippot and Dr. Alain Igau who have guided me through the doctoral research. I would like to thank you for giving me the opportunity to work in this project, and for being so supportive until the end. I would also like to thank Dr. Pierre Sutra, for his involvement and for being so encouraging.

I really want to thank Yannick Coppel, Christian Bijani, Vincent Collière, Alix Saquet, Alain Moreau, and the rest of the technical service of the LCC. I feel very lucky for all the things I learned working with them, it has been one of the best parts of this PhD.

I would like to extend my gratitude to Dr. Pierre Lecante for X-ray analyses and to Jerome Esvan for the XPS measurements. Also, to Iker del Rosal and Romuald Poteau, for sharing their quantized knowledge with me and for the enriching discussions.

I would like to warmly thank Dr. Xavier Sala, Dr. Jordi García-Antón and Dr. Núria Romero for welcoming me in their team at the Universitat Autònoma de Barcelona, and for their support during these years. I would also like to thank Pr. Nin Yang for having me in his group at the National University of Singapore and to the Université Fédérale de Toulouse for the mobility grant that made it possible.

I would like to thank all the members of the team L for being always so supportive and generous, Alexia, Catherine, Emmanuel, François, Lassané, Laura, Laurent, Léa, Lorraine, Miquel, Quyen, Roberto, Rosa, Thomas and of course Paul, the best partner during this adventure. It has been a pleasure to work with all of you.

Also, I would like to thank our neighbours from team O, Maxime, Ségolène , Guillaume, Kévin, Aurélien, Clémence, Marco and all the people I met in the LCC throughout my stay.

Thanks Kasia, Angelica and Roberto for making it better and Paul and Charline for being the 🏠 of these years.

Finally, grazie mille Piero por haber sido el motivo de estos años; and to my family and friends from home, muchas gracias, gràcies! ♥

ABSTRACT

The unique properties of metal nanoparticles (MNPs), commonly considered at the borderline between those displayed by molecular compounds and those typical of bulk metals, account for their extended application in diverse fields like electronics, optics, medicine or catalysis. The stabilization of MNPs can be performed in solution by the use of various stabilizers such as polyols, polymers, surfactants, ionic liquids or ligands that are deliberately added in the synthesis medium. The adequate choice of the stabilizer is also a way to functionalize the MNPs and confer them specific properties like solubility in a given media, enantioselective catalytic properties or optical properties, as non-exhaustive examples. Because of their large panel of applications, transition metal complexes (TMCs) have been associated to MNPs to form hybrid nanomaterials mainly through the use of pendant ligands. This fundamental PhD work lies in this domain of research, with the aim to achieve novel hybrid nanomaterials *via* a direct coordination of TMCs at the surface of MNPs. This type of hybrid nanomaterials may give rise to additional properties, different from their two respective original entities. On the basis of coordination chemistry and nanochemistry tools, unprecedented hybrid nanomaterials made of mononuclear organophosphorus Ru(II)-polypyridyl complexes covalently bonded onto the surface of ruthenium nanoparticles (RuNPs) were successfully synthesized following a one-pot organometallic procedure. A complete characterization of the prepared hybrid nanomaterials, by the combination of physical and chemical analytic techniques, is reported.

Besides state-of-the-art techniques for nanoparticle characterization (TEM, WAXS, XPS), liquid and solid-state NMR techniques were applied in order to determine the surface environment of the RuNPs. DFT theoretical calculations, based on a Ru_{55} cluster model, strongly supported the experimental results and showed that the most stable nanohybrid conformer involves a covalent interaction between the chlorine atom of the organophosphorus Ru(II)-polypyridyl complex and the RuNP surface, thus forming a direct bridge between the complex and the NPs. An additional aromatic π-type chelating interaction between one of the bipyridine ligands and the RuNP metal surface was also evidenced. NMR spectroscopy data evidenced that in addition to the inner stabilizing layer resulting from the direct coordination of the complex onto the NP surface, other organophosphorus Ru(II)-polypyridyl complexes surround the hybrids, thus forming an outer stabilizing layer. Electrostatic interaction is believed to occur between the complex counterparts from the inner and outer layers.

The electronic properties of the nanohybrid were studied by voltammetric techniques and DFT calculations (projected Density of States). The behavior experimentally observed evidenced the unique

hybrid character of the nanomaterial, which displays an electrochemical gap (E_{ox}-E_{red}) typical of a "molecule-like" redox character and very different from that observed for RuNPs stabilized by classical ligands. Preliminary catalytic studies on the photoinduced hydrogen evolution reaction, as a part of the water-splitting process, and the transformation of CO_2 into formic acid have also been performed.

As perspectives, the synthesis of other Ru-based nanohybrids was evaluated by using Ru(II)-polypyridyl complexes bearing organophosphorus ligands of different nature. Also, first results in the synthesis of nanohybrids made of NPs of other metals (Co, Pt) have been obtained.

This work reports an effective way to potentially access a large variety of unprecedented hybrid nanomaterials made of mononuclear transition metal complexes covalently bonded to well-defined metal nanoparticles. Given its versatility, our procedure should allow developing hybrid nanomaterials with tunable properties towards a large domain of applications.

RÉSUMÉ

Les propriétés uniques des nanoparticules métalliques (MNPs), à la frontière de celles des composés moléculaires et des matériaux massifs, permettent leur utilisation dans des domaines aussi large que l'électronique, l'optique, la médecine ou la catalyse. La stabilisation des MNPs est effectuée en solution en utilisant divers stabilisants tels que des polyols, des polymères, des tensioactifs, des liquides ioniques ou des ligands ajoutés dans le milieu de synthèse. Le choix judicieux du stabilisant est un moyen de fonctionnaliser les MNPs et de leur conférer des propriétés spécifiques comme la solubilité dans différents media ou bien des propriétés optiques par exemple. En raison de leur large éventail de propriétés, des complexes de métaux de transition (TMCs) ont été associés aux MNPs pour obtenir des nanomatériaux hybrides, principalement grâce à l'utilisation de « connecteurs organiques ». Les travaux fondamentaux décrits dans cette thèse se situent dans ce domaine de recherche, avec comme objectif la synthèse de nouveaux nanomatériaux hybrides *via* une coordination directe entre le TMC et la surface de la MNP. Il est raisonnable de penser que ces nanomatériaux hybrides pourraient conduire à de nouvelles propriétés, différentes de celles de leurs deux composantes.

En utilisant les outils de la chimie de coordination et de la nanochimie, des nanomatériaux hybrides constitués de complexes organophosphorés Ru(II)-polypyridines liés de manière covalente à la surface de nanoparticules de ruthénium (RuNPs) ont été synthétisés *via* une procédure de synthèse en une seule étape. La caractérisation complète des nanomatériaux hybrides par la combinaison des techniques analytiques physiques et chimiques a permis de définir la structure de ces nouveaux systèmes.

Les caractérisations physiques (TEM, WAXS, XPS) et chimiques (RMN à l'état liquide et solide) ont été menées pour déterminer la structure et l'environnement de surface des RuNPs. Des calculs DFT, basés sur un modèle de cluster Ru_{55}, ont conforté les résultats expérimentaux et ont montré que la structure du nanohybride la plus stable implique une interaction covalente entre l'atome de chlore du complexe organophosphoré Ru(II)-polypyridines et la surface RuNP, formant ainsi un lien direct entre le complexe et les MNPs. Une interaction chélatante de type π aromatique entre l'un des ligands bipyridines et la surface métallique RuNP, a également été mise en évidence. Les données de spectroscopie RMN ont démontré qu'en plus de la couche de stabilisation interne, d'autres molécules de complexes organophosphorés Ru(II)-polypyridyne entourent les hybrides, formant ainsi une couche de stabilisation externe.

Les propriétés électroniques du nanohybride ont été étudiées par électrochimie. Le comportement observé expérimentalement a mis en évidence le caractère hybride unique du nanomatériau, qui

présente un saut électrochimique (E_{ox}-E_{red}) typique d'une MNP à comportement moléculaire et très différent de celui observé pour les RuNPs stabilisés par des ligands classiques.

Des études catalytiques préliminaires sur la réaction d'évolution de l'hydrogène photo-induite, dans le cadre de la réaction de décomposition de l'eau, et la transformation du CO_2 en acide formique ont été réalisées.

Comme perspectives, la synthèse d'autres nanohybrides à base de Ru a été évaluée en utilisant des complexes Ru(II)-polypyridynes incorporant des ligands organophosphorés de nature différente. Des premiers résultats sur la synthèse de nanohybrides impliquantd'autres NPs (Co, Pt) ont aussi été obtenus.

Ces travaux devraient permettre l'accès à une grande variété de nanomatériaux hybrides, constitués de complexes de métaux de transition mononucléaires liés de manière covalente à des nanoparticules métalliques bien définies, aux propriétés diverses pour un large domaine d'applications.

TABLE OF CONTENTS

GENERAL INTRODUCTION 1

CHAPTER 1 5

1. INTRODUCTION 5
2. GENERALITIES ON METAL NANOPARTICLES 6
   - 2.1. General properties 6
   - 2.2. Synthesis methods 8
   - 2.3. Stabilization modes 9
   - 2.4. Conclusions 11
3. TRANSITION METAL COMPLEXES ASSEMBLED TO METAL NANOPARTICLES: STATE OF THE ART 11
   - 3.1. TMCs assembled to AuNPs 13
     - *3.1.1. Functionalized TMCs for the grafting on AuNPs 15*
       - *3.1.1.1 Grafting through thiol pendant ligands 15*
       - *3.1.1.2 Grafting through non-thiol pendant ligands 25*
     - *3.1.2. Surface-functionalized AuNPs for the complexation of TMCs 27*
     - *3.1.3. Electrostatic binding of TMCs to AuNPs 32*
     - *3.1.4. Miscellaneous TMC-AuNPs hybrid systems 34*
   - 3.2. TMCs assembled to MNPs with M = Ag, Rh, Pd, Cu, Co and Ft-Pt 38
     - *3.2.1. Functionalized TMCs for the grafting on MNPs 38*
     - *3.2.2. Surface-functionalized MNPs for the complexation of TMCs 40*
     - *3.2.3. Electrostatic binding of TMCs to MNPs 42*
     - *3.2.4. Miscellaneous TMC-MNPs hybrid systems 44*
4. CONCLUSIONS 45
5. REFERENCES 47

CHAPTER 2 57

1. INTRODUCTION 57
2. GENERAL FEATURES OF RUTHENIUM NANOPARTICLES 59
3. SYNTHESIS OF THE HYBRID NANOMATERIAL $([RuPMe]_N\text{-}RuNPs)^+(PF_6^-)_N$ 62
4. CHARACTERIZATION OF THE HYBRID NANOMATERIAL $([RuPMe]_N\text{-}RuNPs)^+(PF_6^-)_N$ 67
   - 4.1. Physical characterization recorded by HRTEM, WAXS and ICP 67
   - 4.2. Characterization by liquid and solid-state NMR spectroscopy 70
     - *4.2.1. Liquid NMR spectroscopy 70*
     - *4.2.2. Solid-state NMR spectroscopy 79*

4.3. Quantification of hydrides and CO adsorption modes: a surface study on the ([RuPMe]$_n$-RuNPs)$^+$(PF_6^-)$_n$ hybrid 82
4.3.1. Titration of hydrides at the surface of the hybrid nanomaterial 82
4.3.2. Adsorption of CO at the surface of the hybrid nanomaterial 84
5. THEORETICAL CALCULATIONS ON THE HYBRID NANOMATERIAL 86
5.1. Coordination of the [RuPMe]$^+$ complex at the RuNP surface 86
5.2. On the role of the PF_6^- anion in the hybrid structure 90
6. X-RAY PHOTOELECTRON SPECTROSCOPY ON ([RUPME]$_N$-RUNPS)$^+$(PF_6^-)$_N$ 93
7. CONCLUSIONS 99
8. REFERENCES 103

CHAPTER 3 109

1. INTRODUCTION 109
2. ELECTROCHEMICAL PROPERTIES OF ([RUPME]$_N$-RUNPS)$^+$(PF_6^-)$_N$ AND OTHER RUNPS STABILIZED BY CLASSICAL LIGANDS 111
2.1. Overview of the electrochemistry of organophosphorus Ru(II)-polypyridyl complexes 111
2.2. Overview of the electrochemistry of metal nanoparticles 113
2.3. Electrochemical studies on ([RuPMe]$_n$-RuNPs)$^+$(PF_6^-)$_n$ and RuNPs stabilized by classical ligands 119
2.3.1. Experimental set-up and procedure 119
2.3.2. Electrochemistry of the ([RuPMe]$_n$-RuNPs)$^+$(PF_6^-)$_n$ hybrid 121
2.3.3. Electrochemistry of RuNPs stabilized by classical ligands 124
2.3.4. Comparative analysis: ([RuPMe]$_n$-RuNPs)$^+$(PF_6^-)$_n$ vs. RuNPs stabilized by classical ligands 128
2.3.5. Theoretical calculations: pDOS, pCOHP and pMPA charges 130
2.4. Conclusions on the electrochemical studies 132
3. PRELIMINARY CATALYTIC STUDIES WITH ([RUPME]$_N$-RUNPS)$^+$(PF_6^-)$_N$ 134
3.1. Photochemical reduction of H^+ for water splitting 134
3.1.1. Photochemical HER with ruthenium-based nanocatalysts 134
3.1.2. Preliminary results with ([RuPMe]$_n$-RuNPs)$^+$(PF_6^-)$_n$ hybrid 136
3.1.3. Conclusions on the activity of ([RuPMe]$_n$-RuNPs)$^+$(PF_6^-)$_n$ towards the photocatalytic HER 139
3.2. Chemical reduction of CO_2 into formic acid 139
3.2.1. CO_2 transformation into formic acid ruthenium-based nanocatalysts 140
3.2.2. Experimental results 141
3.2.3. Conclusions on the activity of ([RuPMe]$_n$-RuNPs)$^+$(PF_6^-)$_n$ and RuNPs stabilized by simple ligands on the catalytic formation of HCOOH 143
4. CONCLUSIONS 145
5. REFERENCES 147

CHAPTER 4 153

1. INTRODUCTION 153
2. STABILIZATION OF RUNPS WITH SELECTED FUNCTIONALIZED ORGANOPHOSPHORUS RU(II)-POLYPYRIDYL COMPLEXES 154
   2.1. Synthesis and characterization of the $([RuPH]_n\text{-}RuNPs)^+(PF_6^-)_n$ hybrid nanomaterial 154
      2.1.1. Synthesis of the $[RuPH]^+PF_6^-$ complex 155
      2.1.2. Synthesis of the $([RuPH]_n\text{-}RuNPs)^+(PF_6^-)_n$ hybrid nanomaterial 156
      2.1.3. Characterization of the $([RuPH]_n\text{-}RuNPs)^+(PF_6^-)_n$ hybrid nanomaterial 159
   2.2. Synthesis and characterization of $([RuPO]_n\text{-}RuNPs)^+(PF_6^-)_n$ hybrid nanomaterial 163
      2.2.1. Synthesis of the $[RuPO]^+PF_6^-$ complex 164
      2.2.2. Synthesis of the $([RuPO]_n\text{-}RuNPs)^+(PF_6^-)_n$ hybrid nanomaterial 166
      2.2.3. Characterization of the $([RuPO]_n\text{-}RuNPs)^+(PF_6^-)_n$ hybrid nanomaterial 167
   2.3. Conclusions on the stabilization of RuNPs with $[RuPH]^+PF_6^-$ and $[RuPO]^+PF_6^-$ complexes 171
3. FIRST RESULTS ON THE STABILIZATION OF CONPS AND PTNPS WITH ORGANOPHOSPHORUS RU(II)-POLYPYRIDYL COMPLEXES 172
   3.1. Synthesis and preliminary characterization of $([RuPH]_n\text{-}CoNPs)^+(PF_6^-)_n$ 172
   3.2. Synthesis of $([RuPMe]_n\text{-}PtNPs)^+(PF_6^-)_n$ 175
   3.3. Conclusions on the Co and Pt-based hybrid systems 177
4. CONCLUSIONS 177
5. REFERENCES 179

EXPERIMENTAL SECTION 181

1. GENERALITIES 181
   1.1. Operation conditions 181
   1.2. Reactants 181
      1.2.1. Solvents and gases 181
      1.2.2. Metal complexes, ligands and inorganic salts 182
      1.2.3. Organometallic precursors 183
2. SYNTHESES 183
   2.1. Synthesis of organophosphorus ruthenium(II) polypyridyl complexes 183
      2.1.1. Synthesis of $[(bpy)_2Ru(Ph_2PMe)Cl]PF_6$, $[RuPMe]^+PF_6^-$ 183
      2.1.2. Synthesis of $[(bpy)_2Ru(Ph_2PH)Cl]PF_6$, $[RuPH]^+PF_6^-$ 184
      2.1.3. Synthesis of $[(bpy)_2Ru(P(O)Ph_2)CH_3CN]PF_6$, $[RuPO]^+PF_6^-$ 184
   2.2. Synthesis of metal nanoparticles 185
      2.2.1. Synthesis of hybrid nanoparticles 185
      2.2.2. Synthesis of RuNPs stabilized by ligands 185
3. CHARACTERIZATION TECHNIQUES 186

3.1. Electron microscopy 186
3.2. ICP-OES 186
3.3. Wide-Angle X-Ray Scattering 186
3.4. Nuclear Magnetic Resonance (NMR) Spectroscopy 187
3.5. X-Ray Photoelectron Spectroscopy 187
4. SURFACE REACTIVITY STUDIES 188
4.1. Hydride quantification 188
4.1.1. Reaction with norbornene and GC-MS detection 188
4.1.2. Calculation of R_{surf}/Ru ratio and of reacted hydrides 188
4.2. ^{13}CO adsorption 190
5. ELECTROCHEMICAL STUDIES 190
6. CATALYTIC REACTIONS 190
6.1. HER 190
6.2. CO_2 hydrogenation 191
7. COMPUTATIONAL DETAILS 192
8. REFERENCES 195

GENERAL CONCLUSION 197

RESUME EN FRANÇAIS 201

Abbreviations

(alphabetical order)

0D – zero-dimensional

2MPy – 2-mercaptopyridine

4MPy – 4-mercaptopyridine

ANTA – amino-nitrilotriacetic acid

ATP^{2-} – adenosine-5'-triphosphate

BINOL – 1,1'-bi-2-naphthol

BNP – bis-*p*-nitrophenyl phosphate

bpy – bipyridine

C_{CLU} – double layer capacitance of a nanoparticle

cod – 1,5-cyclooctadiene

coe – cyclooctadienyl

cot – 1,3,5-cyclooctatriene

CPMG – Carr-Purcell-Meiboom-Gill

CV – Cyclic Voltammetry

Cy – cyclohexyl

DFT – Density Functional Theory

DLS – Dynamic Light Scattering

DMAP – 4-dimethylaminopyridine

DMF – *N,N*-dimethylformamide

DMSO – dimethyl sulfoxide

DOSY – Diffusion Ordered SpectroscopY

dppb – bisdiphenylphosphinobutane

dppd – 1,10-bis(diphenylphosphino) decane

dppf – 1,1'-bis(diphenylphosphino) ferrocene

dppm – diphenylphospinomethane

EDTA – ethylenediaminetetraacetic acid

EDX – Energy-Dispersive X-ray Spectroscopy

Fc – ferrocene

FFT – Fast Fourier Transform

FRET – Förster Resonance Energy Transfer

FT-IR – Fourier-Transform Infrared

GC – Glassy Carbon

GC-MS – Gas Chromatography-Mass Spectroscopy

H_2salten – bis(3-salicylideneaminopropyl) amine

H_2dodecanesalten – bis(3-salicylidene-aminopropyl)dodecanamine

H_2tolylthiosalten – bis(3-salicylideneaminopropyl)-*p*-tolylthiolamine)

hcp – hexagonal close-packed

HDA – hexadecylamine

HER – Hydrogen Evolution Reaction

HOMO – highest occupied molecular orbital

HPLC – high-performance liquid chromatography

HRTEM – High Resolution Transmission Electron Microscopy

ICP-OES – Inductively coupled plasma – optical emission spectrometry

ITO – indium tin oxide

MAS – Magic Angle Spinning

Me – methyl

MLCT – metal-to-ligand charge-transfer

MNPs – metal nanoparticles (M=Ru, Co, Pt, Au, Ag, Rh, Cu, etc.)

MPA – 3-mercaptopropionic acid

MRI – Magnetic Resonance Imaging

MS – mass spectroscopy

MTY – metal time yield

MV^{2+} – methyl viologen

NADH – reduced nicotinamide adenine dinucleotide

nbe – norbornene

NHC – N-heterocyclic carbene

NMR – Nuclear Magnetic Resonance

NTA – nitrilotriacetic acid

PBE – Perdew, Burke and Ernzerhof functional

pCOHP – projected crystal orbital Hamilton population

pDOS – projected Density of States

pMPA – projected Mulliken population analysis

Ph – phenyl

PP – 4-phenylpyridine

PTA – 1,3,5-triaza-7-phosphaadamantane

PVP – Polyvinylpyrrolidone

PZT – 2-pyrazin-2-ylethanethiol

RDF – Radial Distribution Function

ROESY – Rotating Overhauser Effect Spectroscopy

RR – Resonance Raman

SCE – Saturated Calomel Electrode

SERS – Surface-Enhanced Raman Scattering

SPR – Surface plasmon resonance

SPB – Surface plasmon band

SSB – Spinning Side Bands

SWV – Square Wave Voltammetry

TEM – Transmission Electron Microscopy

TEOA – triethanolamine

TGA – Thermogravimetric analysis

THF – tetrahydrofuran

TMCs – transition metal complexes

TOAB – tretraoctylammonium bromide

ToF-SIMS – Time-of-flight second ion mass spectroscopy

TOF – Turnover frequency

TON – Turnover number

tpphz – tetrapyridophenazine

TPA – triphenylamine

tpy – terpyridine

UV-vis – ultraviolet-visible

VASP – Vienna *ab initio* simulation package

WAXS – Wide-Angle X-Ray Scattering

XPS – X-Ray Photoelectron Spectroscopy

XRD – X-Ray Diffraction

General Introduction

Nanosciences form a vast and interdisciplinary domain where the principles of physics, chemistry, material science and engineering meet and overlap, thus allowing the development of new concepts and materials whose properties are unique. The strong interest devoted to this domain of research, and most particularly to metal-based nanospecies, derives from their intrinsic properties, commonly considered at the borderline between those of molecular species and those of their bulk counterparts (quantum size and electronic effects, high surface/volume ratio, etc.). Because of their remarkable properties, metal nanospecies can find applications in diverse fields such as biology, medicine, microelectronics, optics or catalysis.

During the past decades, important advances have been made in nanochemistry regarding the design of size, shape and composition-controlled metal nanoparticles (MNPs). The synthesis of well-controlled MNPs allows getting better insights on the parameters that can affect their physico-chemical properties. One of these parameters with strong effect on the characteristics of MNPs, is the stabilizing agent (polymers, surfactants or ligands, among others). When ligands are used for the stabilization of MNPs, the interactions that take place between these ligands and the metal surface atoms can be compared to the ligand interaction with the metal centers in homogeneous complexes. Indeed, we can also speak of ligand coordination at the surface metal sites of the MNPs, alike the coordinated ligands to metal centers in molecular complexes. Being at the interface between the metal cores and the media and forming a stabilizing shell, coordinated ligands can tune the surface properties of MNPs through electronic or steric effects, which is of paramount importance for their solubility, stability and reactivity.

The appropriate association between a metal core, chosen for its intrinsic properties (optical, magnetic catalytic, etc.), and a stabilizing shell of specific nature (polymers, chiral ligands, enzymes, or metal complexes, etc.), is an efficient way to access hybrid nanomaterials with multiple functionalities. This PhD work lies in this context of multifunctionality, by proposing the development of novel hybrid nanomaterials consisting in the assembly of a metal transition complex (TMC) with metal nanoparticles (MNPs), from which properties, different from those observed for each of the individual entities, can be expected.

As it will be seen in the bibliographic review presented in the first Chapter of this manuscript, the development of TMC-NPs nanohybrids is a recent domain of research, with the main studies published in the last two decades. The majority of the examples reported in the literature concern gold or silver nanoparticles, mainly for applications in sensing or catalysis. Only a few examples involve

nanoparticles of other metals like Co, Pd, Rh, Cu, or bimetallic FePt. To reach the target TMC-MNPs nanohybrids, several synthetical approaches have been developed, such as the grafting of TMCs to the surface of MNPs, for instance, through organic spacers or by electrostatic interactions between TMCs and the stabilizing shell of MNPs. However, the methods described can display some drawbacks. One can cite, for instance, the use of metal precursors for the preparation of the nanoparticles that contain halogens, which can then be present at the MNP surface; or the use of multi-step methods, usually based on ligand exchange procedures, for the anchoring of the metal complex at the MNP surface. Also, in most of the cases, the characterization of the nature of the interaction between the TMCs and the MNPs is poorly explored, while this can be of utmost importance if one wants to establish structure-properties relationships.

A recognized method to obtain well-defined metal nanoparticles is the organometallic approach. This approach has been demonstrated to provide controlled metal NPs with reproducible physico-chemical properties. The choice of the metal source is of high importance regarding the resulting metal surface purity. Olefinic metal precursors are privileged as their treatment under hydrogen liberates alkanes as the only byproducts that are inert towards the metal surface. Our group has been strongly interested in varying the nature of the stabilizer in order to study the effect on the properties of the obtained nanoparticles, including their surface properties related to the surface composition. The ligands are either simple or sophisticated (mainly containing amines, thiols, carbenes or phosphines as coordinating functions) and were shown to influence the surface and the catalytic properties of the obtained particles either in colloidal or supported conditions.

Motivated by the interest of varying the stabilizers and the vast range of properties that can be expected by the assembly of MNPs and TMCs (novel electronic properties, chemical reactivity, etc.), we decided to study the ability of transition metal complexes to act as direct stabilizers of metal nanoparticles, by following a one-pot synthesis protocol. More precisely, the target objective of this PhD work was to design novel nanohybrids by the direct coordination of organophosphorus polypyridyl Ru(II) complexes at the surface of metal nanoparticles. To the best of our knowledge, this has not been yet reported in the literature.

For this purpose, the toolboxes of phosphorous chemistry, transition metal chemistry, coordination chemistry and nanochemistry as developed in our group have been applied, which allowed to carry out fine fundamental studies in the domain of TMC-MNPs nanohybrids.

The results obtained in the frame of this PhD work are presented in the next parts of this manuscript as following:

After a brief report on the general properties of metal nanoparticles, Chapter 1 focuses on the state-of-the-art of the synthesis of hybrid nanomaterials composed of TMCs and MNPs. The general trends reported in the literature for the synthesis of such hybrid nanomaterials are disclosed, providing an overview of the nature of the interactions between TMCs and MNPs explored to date.

The synthesis and fine characterization of a novel hybrid nanomaterial, made of ruthenium nanoparticles (RuNPs) stabilized by a mononuclear organophosphorus Ru(II)-polypyridyl complex, $[Ru(bpy)_2(PPh_2Me)Cl]PF_6$, are reported in Chapter 2. The precise structure of the novel hybrid nanomaterial has been determined by the combination of experimental analyses and theoretical studies.

Chapter 3 is devoted to the study of the electrochemical and preliminary catalytic properties of the nanohybrid described in Chapter 2. In the first part, the electrochemical properties of the nanohybrid have been deeply discussed and compared to those of metal nanoparticles stabilized by classical ligands. In the second part, preliminary results on the catalytic properties of the material in the photocatalytic hydrogen evolution reaction and the transformation of CO_2 into formic acid are presented.

Chapter 4 is a perspective of our research line. First results on the synthesis of nanohybrid systems of different compositions are presented. They are based on the use of (i) different organophosphorus Ru(II) polypyridyl complexes as stabilizers, $[Ru(bpy)_2(PPh_2H)Cl]PF_6$ and $[Ru(bpy)_2(P(O)Ph_2P)CH_3CN]PF_6$, or (ii) other metals than ruthenium (Pt, Co) as NP cores, for the composition of the hybrids.

CHAPTER 1

1. Introduction

The fast development of nanoscience and nanotechnology urged the scientific community to establish a common and recognized definition; the materials with at least one dimension ranging in the nanometer scale (from 1 to 100 nm) are considered to belong to the "nanomaterials" category. Finding a unanimous definition for the term "nanomaterial" has always been a matter of controversy and the strictly dimensional requirement appeared to be not sufficiently narrow. Thus, it is nowadays accepted that the term nanomaterial, in addition to the nanoscale dimension, relates to the appearance of a novel physical or chemical property, unusual for the bulk counterpart [1]. In this sense, metal nanoparticles may fulfil both conditions. Their unique properties account for their growing interest for applications in fields like electronics, optics, biology, medicine or catalysis.

The first part of this chapter will describe the general properties of metal nanoparticles, as well as the main methods and stabilization modes applied for their synthesis. The second part is an illustration of how the intrinsic properties of metal nanoparticles can be enhanced and fine-tuned by their combination with metal complexes that can be incorporated *via* different interaction modes with their respective surface. Indeed, the association of a metal complexes with metal nanoparticles leading to the formation of a particular class of nanomaterials, often called "nanohybrids", has become a novel subject of interest in recent years. As it has been reported in numerous studies, in these nanohybrids specific physicochemical properties, sometimes different from those of complexes and nanoparticles separately, can be expected. The state-of-the-art of this interdisciplinary research field has been explored in the frame of this PhD work. It is worth to mention that we limited our study to nanohybrid systems that imply a chemical method for the formation of the metal nanoparticles as well as only to complexes of transition metals. Inorganic structures of transition metal elements, such as oxometallates [2,3], or inorganic salts of transition metals of the type $RuCl_3$ [4] are out of the scope of this study. Thus, publications, describing the synthesis, characterization and applications of hybrid nanomaterials made of metal nanoparticles (MNPs) associated to transition metal complexes (TMCs) and of interest with regard to our PhD objectives, will be hereafter presented. The abbreviation TMC-MNPs will be often used to refer to this type of nanohybrids.

2. Generalities on metal nanoparticles

Metal nanoparticles are considered zero-dimensional (0D) nanomaterials, having all their three dimensions comprised between 1 and 100 nm (Fig. 1) [5]. This "nano" condition has a high impact on the fundamental properties of this kind of materials.

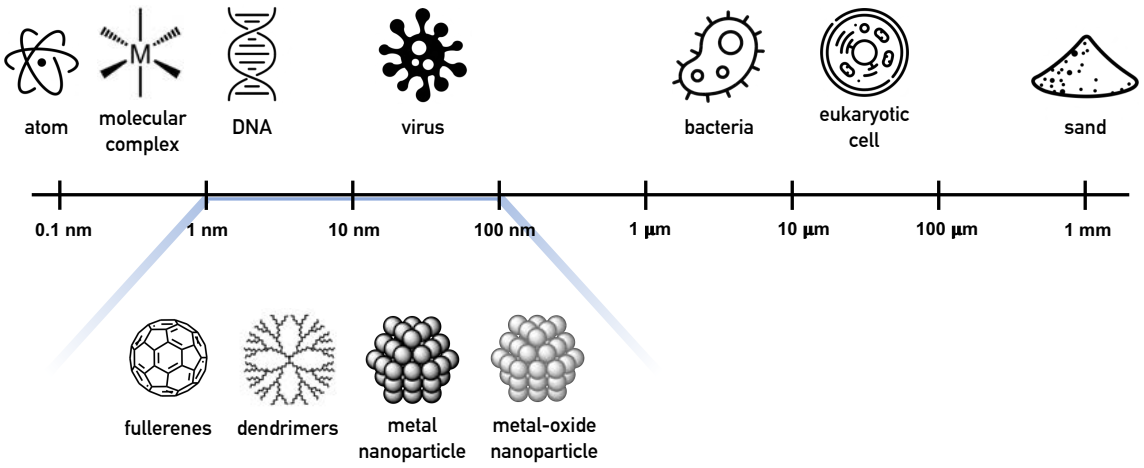

Figure 1. Size of nanoscale materials relative to atomic, micrometric and millimetric objects.

Physical properties of metal nanoparticles (MNPs) are different from those of their bulk counterparts, and a well-known example is the decrease in the melting point of a finely divided metal when a critical particle size is reached [6,7]. The continuous electronic properties of bulk materials fade when scaling down their size, the way in which electrons are arranged becomes closer to that of atomic species, and new surface features appear.

2.1. General properties

A first consequence of reaching the nanoscale size range is the phenomenon known as quantum confinement. Bulk metals are considered to have an indefinitely extended molecular orbital where electrons are delocalized. At the nano-size, the electronic band structure is lost, electrons are confined and discrete energy levels, closer to those of molecular species, become predominant (Fig. 2). Consequently, the physical properties of metal nanoparticles are neither those of bulk metals nor those of molecular compounds, and they strongly depend on the particle size [8].

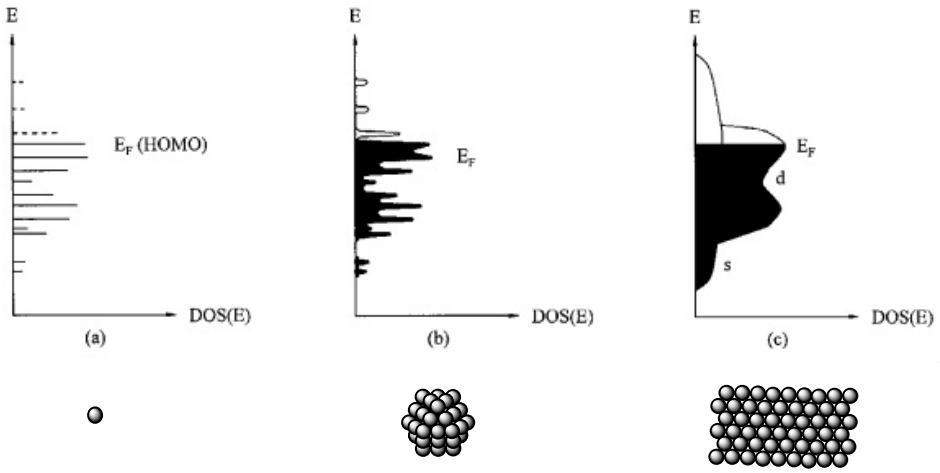

Figure 2. Transition of electronic states from atomic metal species (a), to metal nanoparticles (b) and bulk metals (c). E_f stands for Fermi energy, reproduced from [8].

As seen in Figure 2, in bulk metals, the Fermi energy (E_f) of the free electron is comparable to the highest occupied molecular orbital (HOMO) of a finite molecular system.

Another size effect at the nano-regime is the drastic increase of the ratio of the number of surface atoms compared to that in the metal core when decreasing particle sizes down (Fig. 3). With respect to the inner lattice, surface atoms are coordinatively unsaturated, especially those in the edges and corners, and are thus higher in energy [9]. Accordingly, the number and nature of species present at the surface of metal nanoparticles strongly influence their reactivity, a factor of special concern in catalysis [10].

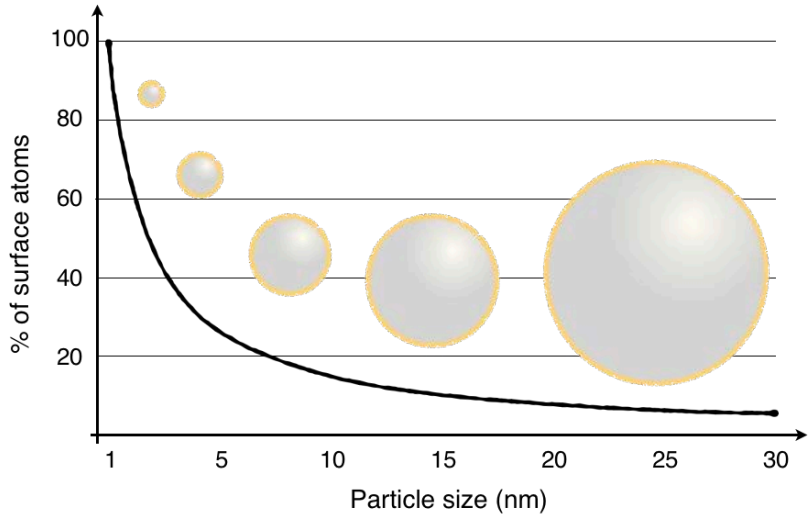

Figure 3. Surface/bulk atomic ratios as a function of particle size.

At small sizes, metallic surface contributions have high influence. The properties provided by defects and distortions, typically undercoordinated-surface atoms, are predominant to those conferred by the bulk-like core atoms. As a consequence, synthetical methods providing good control in size and morphology of metal nanoparticles are necessary to obtain reproducible nanomaterials with reproducible properties. Also, the type of surface stabilization (nature and adsorption strength of the stabilizer, ratio of surface coverage, etc.) will have a great impact on the nanoparticle final properties. These aspects are discussed hereafter.

2.2. Synthesis methods

The methods for the synthesis of metal nanoparticles are usually classified into two categories: top-down and bottom-up approaches. The top-down approaches (such as high-energy ball milling [11] or nanolithography [12]), considered physical methods, consist in the fragmentation of bulk materials into smaller species. Even if large amounts of particles can be produced, downscaling routes generally lead to populations of nanoparticles with wide size distributions and poor control on their final composition [13]. Upscaling or bottom-up approaches are based on the construction of nanostructures by the chemical assembly of smaller building blocks. Fundamentally, they are solution-phase chemistry methods [14]; nanoparticles or colloids are formed in solution or suspension (the different stabilizing modes of the generated nanoparticles are presented thereafter). Colloidal syntheses of nanoparticles allow for a higher control of particle size, shape and composition than physical methods. Examples of bottom-up synthetical approaches are (i) thermal decomposition, (ii) electrochemical reduction, (iii) atomic metal vapor condensation, (iv) photochemical or ultrasonic reduction, (v) chemical reduction of metal salts and (vi) ligand displacement or reduction from organometallic or metal-organic precursors [15,16].

Of special concern for this PhD project is the synthesis of metal nanoparticles by the decomposition of organometallic precursors under mild reaction conditions, a method commonly known as the organometallic approach [17,18]. By ligand displacement or reduction of zero/low-valent organometallic or metal organic precursors, usually by applying mild temperature and/or H_2 or CO pressure, metal atoms are released in solution and the nucleation process starts (see Fig. 4). The nucleation and growth of the nanoparticles are controlled by addition of a stabilizing agent from the beginning of the synthesis process, which can coordinate to the growing surface of the metal nanoparticle and stop the growth (ligand) or sterically limit it (polymer) both preventing aggregation. Organic ligands or polymers, small molecules like CO or CH_3OH, ionic liquids or heterogeneous supports (silica, alumina, carbon nanotubes, etc.) can be used to stabilize MNPs synthetized by this method (*vide infra*).

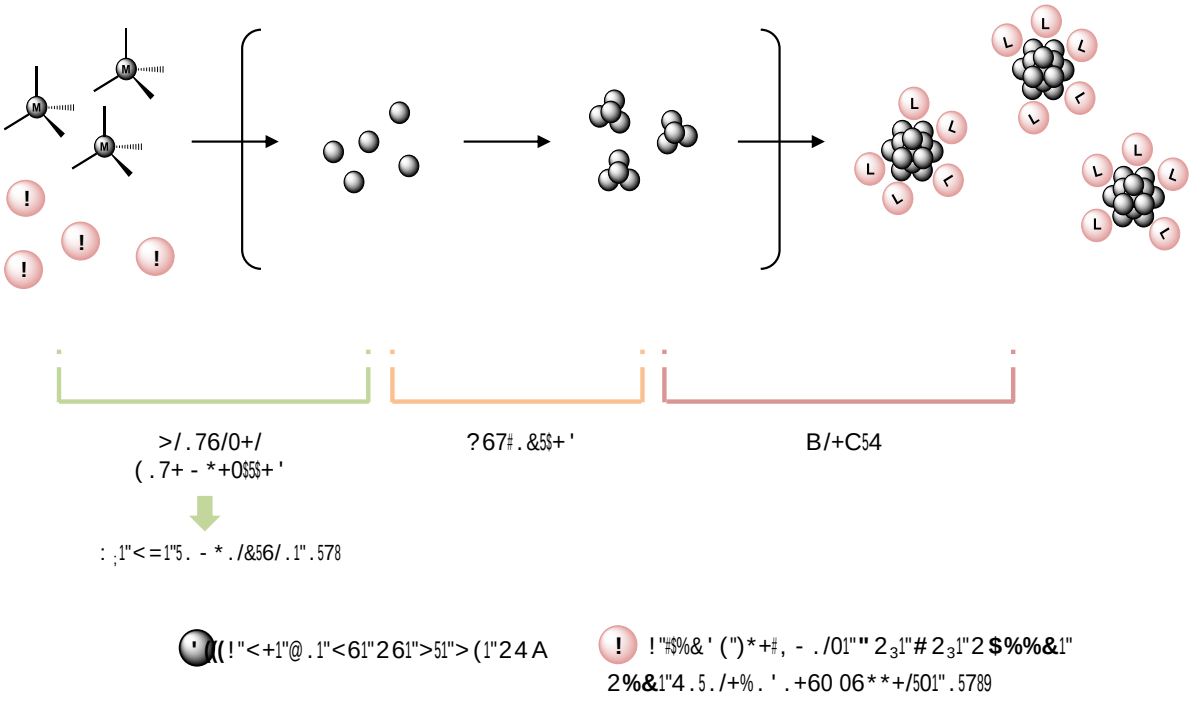

Figure 4. Schematic representation of the organometallic approach for the synthesis of metal nanoparticles.

By the accurate choice of the metallic precursor, the reaction conditions (solvent, temperature, and/or pressure) and the nature of the stabilizer, a vast variety of nano-objects can be synthetized, with good control of size, shape and surface environment. Besides, this synthetic method avoids the use of strong reducing salts or metal halides which are sometimes considered a source of pollution.

2.3. Stabilization modes

Stabilizing agents are necessary to decrease the contribution of the surface atoms to the total free energy of nanoparticles, preventing their coalescence and spontaneous agglomeration into metal bulk. The stabilizing layer creates an interface between the nanoparticle surface and the media; therefore, the nature of the stabilizer will determine the final properties of the nanomaterial (e.g. optical, magnetic or catalytic properties). For instance, a given stabilizer can favor the growth of a nanocrystal in a certain direction or ensure its stability in different solvents [19]. Moreover, since the stabilizers hinder surface active sites they will have a key role on the catalytic activity of the nanoparticles [10].

Four different modes of stabilization are commonly recognized, namely steric, electrostatic, electrosteric stabilizations and ligand coordination (see Figure 5) [15]:

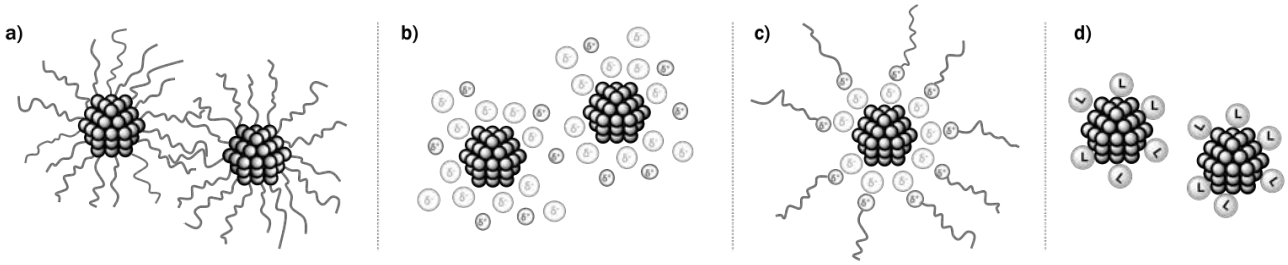

Figure 5. Main stabilization modes of metal nanoparticles: (a) steric, (b) electrostatic, (c) electrosteric stabilization and (d) stabilization by ligand.

i) Steric stabilization

In the stabilization of metal nanoparticles with bulky species like polymers, oligomers, dendrimers or surfactants (see ref. [20] for examples), the steric barrier generated by the stabilizer around the particles prevents their aggregation (Fig. 5a). For instance, stabilization of metal nanoparticles with poly(N-vinyl-2-pyrrolidone) (PVP) is very common in catalytic studies, including those with nanoparticles prepared by the organometallic approach [21]. It is often considered that PVP does not have or has only weak interaction with the metal surface. Such a weak and dynamic interaction of PVP with the metal surface leaves accessible active sites for adsorption of other species. Besides, it offers good solubility in both water and organic solvents (like THF or toluene).

ii) Electrostatic stabilization

Ionic species, such as citrate ions [22], can readily adsorb on electrophilic metal surfaces. The presence of ionic pairs surrounding the nanoparticles generates an electrical double layer that will stabilize and prevent aggregation by interparticle repulsive forces (Fig. 5b).

iii) Electrosteric stabilization

A combination of electrostatic and steric stabilization is obtained when using ionic surfactants, such as quaternary ammonium salts (NR_4X) [23,24]. Ionic liquids [25,26] are also electrosteric stabilizers that can be tuned to achieve the desired size and solubility of the nanoparticles (Fig. 5c).

iv) Stabilization by a ligand

Amines, phosphines, thiols, carbenes, and other traditional ligands [27] used in molecular coordination chemistry can coordinate to the surface of metallic nanoparticles and stabilize them. Stabilization can also be achieved by solvent molecules like alcohols (methanol, isopropanol, heptanol, etc.) [28] (Fig. 5d).

2.4. Conclusions

Physical and chemical properties of metal nanoparticles are strongly influenced by their size, morphology and the nature of the surface species. These surface species, including voluntary added stabilizing agents and byproducts that can result from the synthesis, not only can govern the properties of the nanoparticles but also can directly influence the interaction of the nanoparticle with the media and with other chemical compounds. Specific characteristics can be achieved, for instance, by the coordination of sophisticated ligands able to provide properties like enantioselective catalytic properties [29,30] or better solubility [31] of nanoparticles in a given media. The incorporation of metal complexes at the metal surface of nanoparticles has also been considered as a means to obtain nanomaterials with innovative chemical and physical properties. Ferrocenyl, polypyridyl or chiral transition metal complexes are some examples.

In the next part of this chapter, reports from the literature dedicated to hybrid nanomaterials, namely MNPs incorporating molecular TMCs in the close environment of their surface, will be described.

3. Transition metal complexes assembled to metal nanoparticles: state of the art

As previously mentioned, physicochemical properties of metal nanoparticles are strongly influenced by the species present at their surface. Following this premise and envisaging the production of novel materials with original properties, transition metal complexes bearing new functionalities have been associated to metal nanoparticles. In such assemblies, a rational choice of the TMC fragment can provide the nanoparticles with redox groups, additional photophysical properties or just enrich their catalytic reactivity by the presence of different metal centers. These hybrid nanomaterials find applications in fields like sensing, catalysis, biomedical imaging or electronics.

Besides being a means to afford new functionalities on MNPs, the assembly of nanospecies and TMCs might give rise to new, synergistic properties, different from those of the two respective original entities. The first publications on the combination of metal complexes and metal nanoparticles have been reported in the late nineties. An early example of the synergistic properties arising from such nanohybrids is the assembly of allyl ruthenium dimers on pre-functionalized gold colloids [32]. The resulting hybrid material exhibited unusual activity towards the ring-opening metathesis polymerization reaction, in comparison with that of the unbound homogeneous complex (see section 3.1.2. for a more detailed description).

During the two last decades, synthesis of other nanohybrids incorporating metal NPs and TMCs with diverse characteristics and applications have been described. As mentioned above, our bibliographic study is centered on nanohybrids containing MNPs connected to metal TMCs, exclusively. In the next parts, terms like incorporation, anchoring, grafting, association or assembly will be used to describe hybrid systems where connections between the NPs and the TMCs result from the use of a pendant ligands (either from the TMCs or the NPs or both). In these cases, the connections do not imply a ligand from the first coordination sphere of the TMC. The term coordination will be reserved to the few cases in which the interaction TMC-MNP occurs through a ligand of the TMC lying in its first sphere of coordination. In this case, the connector takes part in the stabilization of the two entities (NP and TMC) and can thus be considered as a bridging ligand between them.

In order to classify the different studies described hereafter, we chose to organize them as a function of the nature of the "connection" between the MNPs and the TMCs. Four different types of connection are distinguished (see Figure 6): (a) covalent grafting *via* pendant groups on the transition metal complexes, (b) complexation of the transition metal complexes to the nanoparticle stabilizing layer, (c) association through electrostatic interaction and (d) miscellaneous systems (e.g. π-stacking, host-guest interactions).

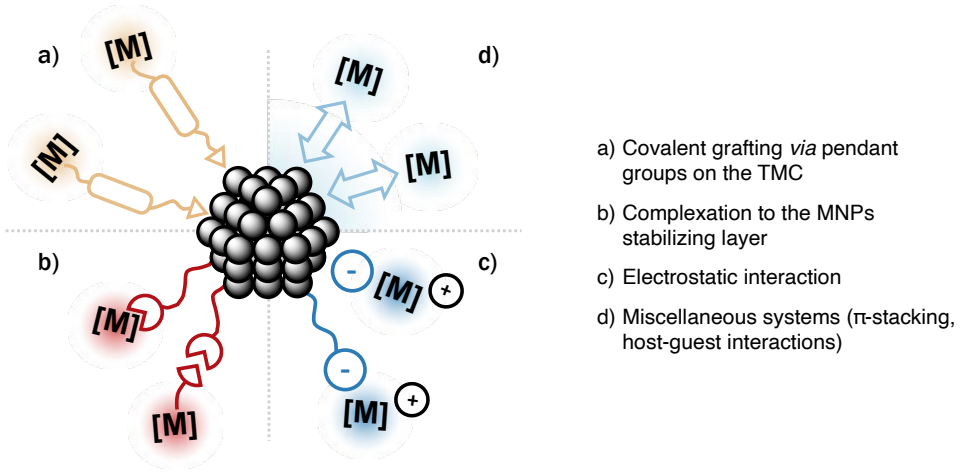

Figure 6. Schematic representation of the four connection modes between metal nanoparticles and transition metal complexes.

Section 3.1. describes the state-of-the-art of TMCs associated to gold nanoparticles (AuNPs). Due to their easy synthetical preparation and unique optical properties, principally plasmon absorption, hybrid systems based on gold nanoparticles have been the most explored. There are, however, a few examples in which metal nanoparticles of other metals are reported for the construction of TMC-MNPs nanohybrids, which are detailed in section 3.2.

3.1. TMCs assembled to AuNPs

Given their remarkable chemical stability, good biocompatibility and notably, singular optoelectronic properties, gold colloids have historically received a lot of attention [33]. The surface electrons of gold nanoparticles (electron density formed by the partially filled 6s orbitals), collectively oscillate when irradiated at a certain wavelength, giving rise to the phenomenon known as surface plasmon resonance (SPR) (see Figure 7a). An absorption band between 500 and 550 nm, known as surface plasmon band (SPB), arises from this phenomenon [34]. The position and intensity of the SPB is strongly influenced by the particle size and shape; no absorption band is detected for gold nanoparticles smaller than 2 nm, for instance. Changes on the media, solvent or the agglomeration of nanoparticles can also cause peak shifts. Nanoparticles of silver and copper (AgNPs and CuNPs) are also known for their plasmonic properties, but given their resistance to oxidation, gold nanoparticles provide access to stable systems with easy handling and have been thus more developed.

Another characteristic of plasmonic nanoparticles is that, besides the characterization techniques usually applied for metal nanoparticles (electron microscopy, elemental analyses, Fourier-Transform Infrared (FT-IR) spectroscopy, X-Ray photoelectron spectroscopy (XPS), nuclear magnetic resonance (NMR) spectroscopy, etc.) their surface state can be easily followed by ultraviolet-visible (UV-vis) spectroscopy. This distinguishing feature becomes of valuable interest when AuNPs and TMCs are assembled. For example, addition of a $[Fe(CN)_5(2MPy)]^{3-}$ (2Mpy = 2-mercaptopyridine) complex to a dispersion of citrate-capped gold nanoparticles induced a shift of the initial plasmon band from 520 nm to 640 nm (see Figure 7b) [35]. This shift, resulting from the aggregation of the AuNPs, had already been observed when adding the 2MPy ligand alone to citrate-capped gold nanoparticle dispersion. Thus, the UV-vis technique allowed the authors to conclude on the decoordination of the 2MPy ligand from the Fe-metal center after addition of the $[Fe(CN)_5(2MPy)]^{3-}$ complex to the colloidal solution, and subsequent nanoparticle aggregation.

Studying the optical properties of TMC-MNPs nanohybrids is of special interest when the plasmonic NPs are combined with light-emitting complexes. Plasmonic nanoparticles can quench the fluorescence of emitting complexes when the plasmon absorption band and the emission band of the complex spectrally overlap, as illustrated in Figure 7c. The survey of this phenomenon becomes an additional way to monitor the connection of an emitting complex to a gold nanoparticle [36].

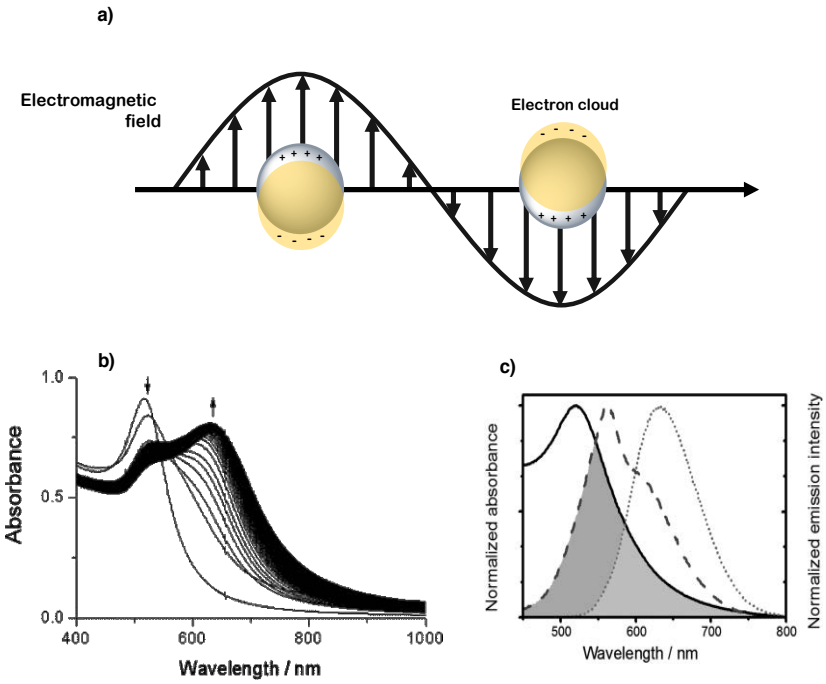

Figure 7. (a) Schematic representation of the plasmon collective oscillation of the NPs electron cloud. (b) Spectra of citrate-stabilized gold colloids upon successive addition of $[Fe(CN)_5(2MPy)]^{3-}$, reproduced from ref. [35]. (c) Spectral overlap of the absorption spectrum of β −cyclodextryn-capped gold colloids (solid), and the emission spectra of a Ru(II) (dashed) and Re(I) (dotted) complexes, reproduced from ref. [36].

Concerning the colloidal synthesis of gold nanoparticles, two main approaches are described in the literature. The first one, reported in the early fifties by Turkevich *et al.* [22], consists on the reduction of $HAuCl_4$ with citrate anions in a boiling aqueous solution. As a result of the citrate oxidation, the dicarboxy acetone derivative becomes the real stabilizing specie (see Figure 8a). Citrate-capped gold nanoparticles of around 20 nm are obtained by this method. Size ranges from 15 to 150 nm can be observed by adjusting the trisodium citrate to $HAuCl_4$ ratio [37]. Smaller particles (1.5 to 5 nm) are obtained following the second route, published in 1994 by Brust and Schiffrin [38], and considered a milestone in the colloidal synthesis of gold particles [39]. The gold precursor $HAuCl_4$ is dissolved in water and by means of a phase-transfer agent, typically tetraoctylammonium bromide (TOAB), is transferred to a toluene phase. The gold precursor is then reduced by the addition of an aqueous solution of $NaBH_4$ in the presence of thiols as stabilizers (see Figure 8b). The resulting organothiol-protected gold nanoparticles are soluble in organic solvents; they are also thermally and air-stable. For the synthesis of gold nanoparticles decorated with transition metal complexes these two procedures are frequently applied, often with slight modifications.

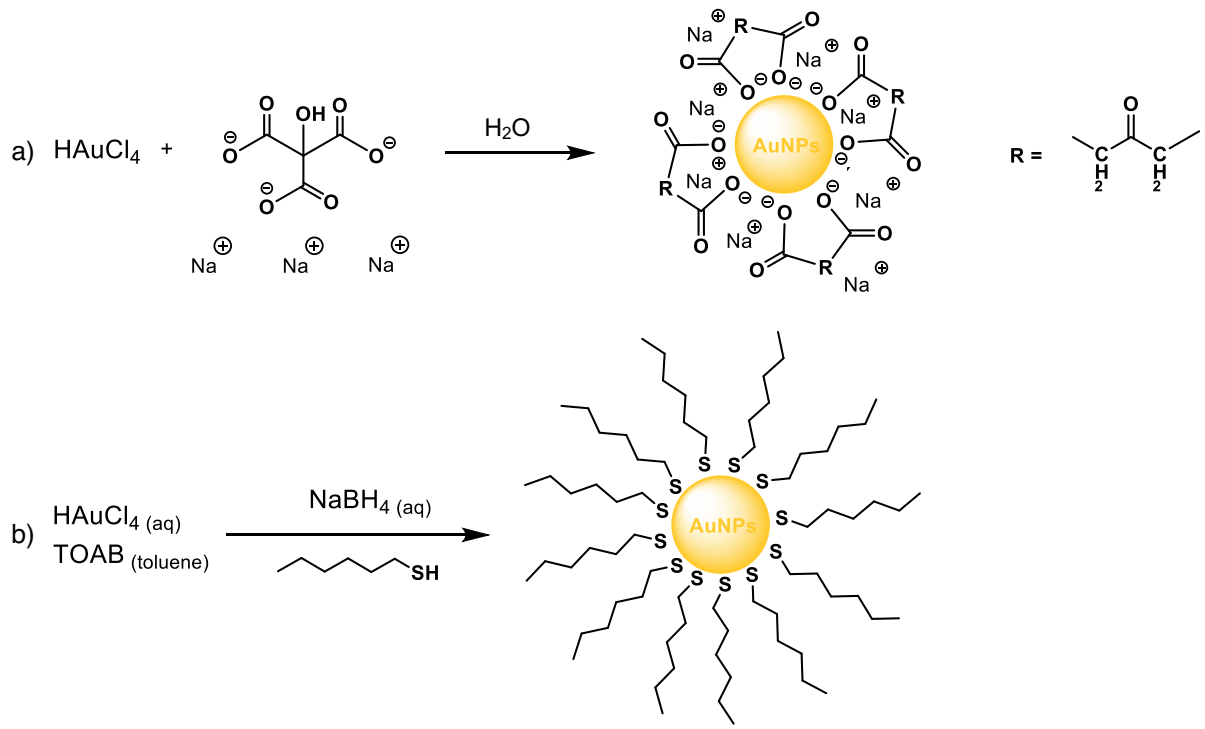

Figure 8. Scheme of gold nanoparticles formation by (a) the Turkevich method, as described in ref. [37] and (b) the two-phase Brust-Schiffrin method.

3.1.1. Functionalized TMCs for the grafting on AuNPs

The use of ligands with coordinating end-groups as tethers to anchor transition metal complexes to the surface of gold NPs is a frequent practice. By this way the transition metal fragment is connected to the gold nanoparticles through a spacer unit, for example, a long alkyl chain. The use of thiol groups has been largely exploited due to the affinity of sulfur with gold surfaces, but other pendant functional groups such as amines or pyridine derivatives have also been explored.

Following this approach, colloidal solutions of gold nanoparticles capped with transition metal complexes are generally achieved by two different routes: 1) either by direct synthesis, using a functionalized complex as stabilizing agent, or 2) by a two-step procedure based on the replacement of the original stabilizers (usually citrate, alkylthiols or the weakly stabilizing TOAB) at the surface of pre-stabilized nanoparticles by an appropriate functionalized complex.

3.1.1.1 Grafting through thiol pendant ligands

Thiols are known to coordinate on gold surfaces forming ordered layers. Gold-sulfur covalent interactions usually take place through the deprotonation of the corresponding thiol and subsequent formation of a thiyl radical ($RS^{\cdot}$) and a thiolate-gold bond (RS-Au). The strength of the thiolate-gold interaction is similar to covalent Au-Au bonds leading thus to very stable interactions. Interactions

with gold atoms through the lone-pair of the sulfhydride (RSH) can also take place, but, in that case, weaker bonds are formed [40]. For the functionalization of gold colloids with TMCs bearing thiol pendant groups, the strong affinity of the Au and S elements allows to (a) displace other ligands or (b) *in-situ* stabilize gold NPs following a Brust-like synthesis. In a general way, and also in the study of TMC-MNPs nanohybrids involving Au-S interactions, it is difficult to ascertain whether the Au-S interaction takes place through the deprotonated thiol or through the sulfhydride group. Besides monothiols, other sulfur-containing groups such as dithiols, disulfides, protected thiolates or dithiocarbamate derivatives have been used to anchor TMCs to AuNPs [41]. Some examples are presented in the following paragraphs.

Ru(II) polypyridyl complexes with monothiol grafting groups

Ru(II) polypyridyl complexes have interesting redox properties and display luminescence that can be quenched by gold nanoparticles. Ru(II)-polypyridyl derivatives have been grafted onto citrate-capped gold colloids pre-immobilized on a gold electrode, by precipitation of the colloidal suspension onto the surface of the electrode. As a reference, the same complex was grafted on a bare gold electrode. The photocurrent induced by photoexcitation of the tris(bipyridine)Ru(II) units was found to be 15 times larger for the system containing the gold nanoparticles [42]. The light-induced formation of redox species has been studied for a another tris(bipyridine)Ru(II)-AuNPs system [43]. In that case the grafting was performed *via* a ligand-exchange reaction between the monothiol appended Ru(II)-polypyridyl complex on preformed AuNPs capped with a monothiol derivative of triethyleneglycol (see Fig. 9a). In the ^{1}H NMR of the nanohybrid, the absence of the -SH proton, the change in multiplicity of the α-CH_2 signal and a general broadening of the peaks, were indicative of the binding of the ruthenium(II) dye to the AuNP surface. Electron transfer between different $Ru(bpy)_3^{2+}$ groups due to their close proximity when grafted to AuNPs surface was observed.

Gunnlaugsson *et al*. studied the changes in the absorption and emission spectra of a group of Ru(II)-polypyridyl-capped AuNPs upon DNA binding (see Fig. 9b, for an example) [44,45]. In this study, the nanohybrids were synthesized by a ligand exchange approach on TOAB-stabilized AuNPs. The grafting was evidenced by the quenching of the emission of the Ru(II) complexes observed after their reaction with the AuNPs surface. Similarly, other authors attached a tris(bipyridine)ruthenium(II) complex bearing two thiol pendant ligands to the surface of AuNPs by partial displacement of the non-ionic fluorinated surfactant (Zonyl 7950) used as initial stabilizer [46]. The resulting nanohybrids were shown of interest in the detection of biomolecules and in cellular imaging.

Two different Ru(II)-polypyridyl complexes with an aminobenzene group as spacer between the metal center and the thiol tether have been used for the direct stabilization of gold nanoparticles [47]. For

the NO derivative (see Fig. 9c), absorption bands in the range of 388-391 nm corresponding to the Ru(II)→NO^+ metal-to-ligand charge-transfer (MLCT) bands were observed. These nanohybrids were able to release NO when irradiated with visible light.

Ru(II)-polypyridyl complexes with two 4-aminotiophenol substituents were added to a solution of citrate-capped gold nanoparticles and the reaction was followed by UV-vis absorption spectroscopy [48]. The initial SPB at ca. 522 nm observed for the citrate-AuNPs was shifted leading to a new band at wavelengths higher than 600 nm. This result indicated the surface functionalization of the AuNPs by the complex and subsequent formation of a chain-like nanoparticle assembly, where the complexes acted as interparticle bridge.

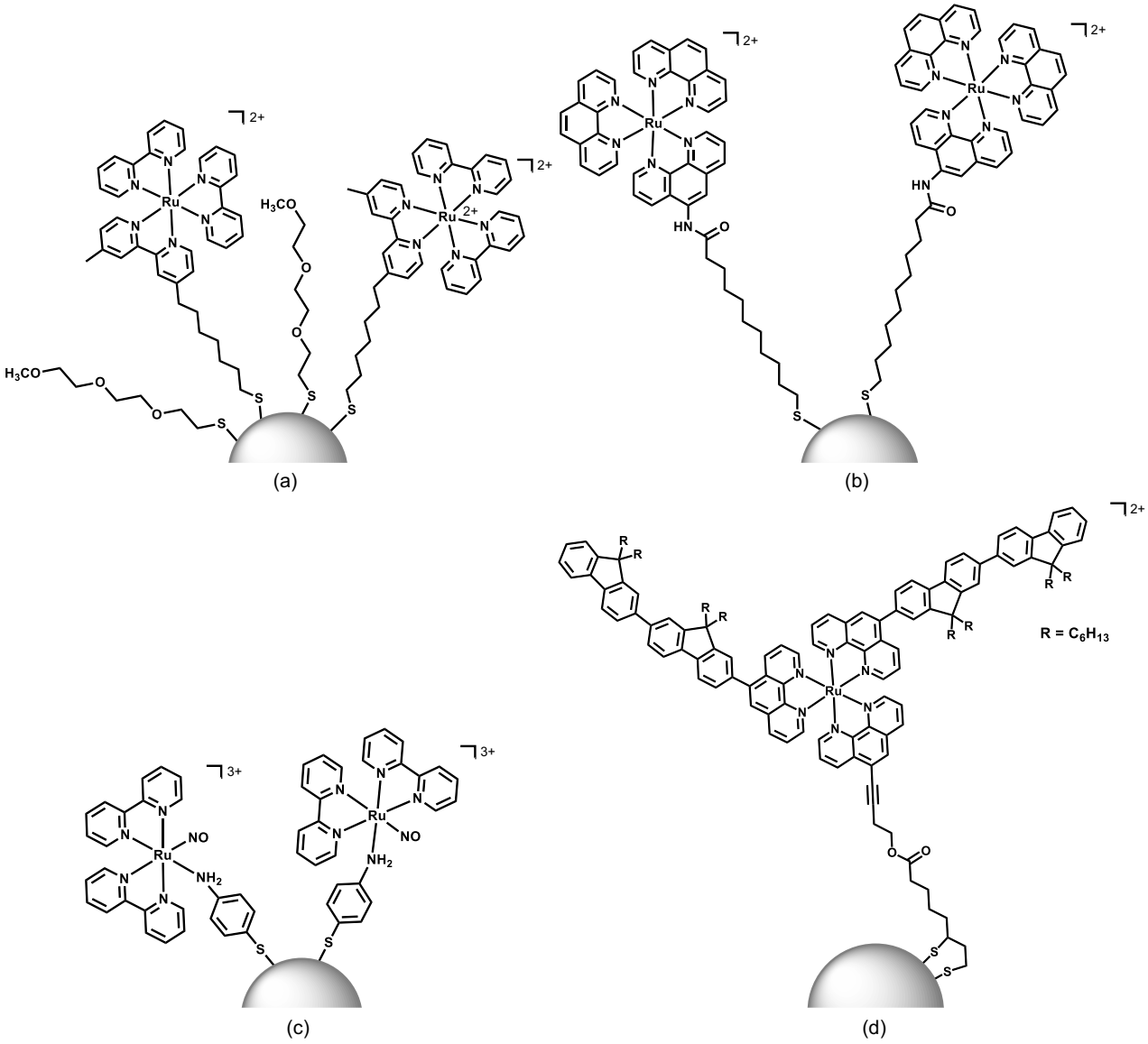

Figure 9. Ru(II)-polypyridyl complexes grafted to the surface of AuNPs through thiol-based groups described in references (a) [43], (b) [45], (c) [47] and (d) [49].

Ru(II) polypyridyl complexes with endocyclic disulfide grafting groups

Endocyclic disulfide bonds can provide bidentate coordination to AuNPs surfaces, compared to the monodentate coordination mode of thiol ligands. Disulfide functions have been used, for instance, to anchor Ru(II)-polypyridyl complexes featuring non-linear optical properties [49] *via* a Brust-type synthesis. In that case, the disulfide pendant groups of the Ru(II)-polypyridyl complexes acted as stabilizers during the synthesis of the AuNPs (see Fig. 9d). The hydrodynamic diameter of the resulting nanohybrids (8.6 nm) determined by dynamic light scattering (DLS) was compared with the metallic diameter of the nano-objects measured by transmission electron microscopy (TEM) (2-3 nm). The difference observed between these two values is indicative of the thickness of the layer of stabilizing complexes coating the AuNPs. A similar complex was grafted to the surface of preformed AuNPs stabilized with DMAP (DMAP = 4-dimethylaminopyridine) *via* a ligand exchange process [50]. Note that Re(I) carbonyl complexes were also used in this study, it will be detailed later on.

Homobimetallic Ru(II)-diphosphine complexes with disulfides as grafting groups

The dissociation of the disulfide bond of an homobimetallic Ru(II) complex allowed for the coordination of the separated Ru(II) units to the surface of gold nanoparticles, as the result of the favorable formation of Au-S bonds. (see Fig. 10a) This could be achieved by an exchange reaction at the surface of preformed citrate-stabilized gold colloids (11.9 ± 0.9 nm) and also by direct reduction of the $HAuCl_4$ gold precursor with $NaBH_4$ in the presence of the bimetallic disulfide complex (2.9 ± 0.2 nm) [51]. By ^{1}H NMR spectroscopy it was observed how some characteristic protons of the Ru(II) complex moved upfield once attached to the AuNPs. Shifts in ^{31}P NMR signals were also observed; the initial resonances at -12.7 and 9.3 ppm of the dppm (dppm = diphenylphosphinomethane) ligands moved to the substantially shielded -18.6 and 3.2 ppm chemical shifts, respectively. This behavior was attributed to a change of local environment of the complex when grafted on the surface of gold nanoparticles.

Ru(II)-polypyridyl, Ru(II)-diphosphine and Ni(II)-diphosphine complexes with dithiocarbamate grafting groups

Complexes holding dithiocarbamate tethers have also been explored as stabilizers of AuNPs given their strong interaction with gold surfaces. The dithiocarbamate group of a Ru(II) tris-bipyridyl complex allowed the direct stabilization of AuNPs (2.9 nm) upon reduction of $NaAuCl_4$ in a mixture of acetonitrile and methanol [52]. Quenching of the complex emission by the nanoparticles was considered as positive proof of the complex grafting. The fact that simple alkane thiols were not able to replace a tris(bipyridine)ruthenium(II) derivative coordinated through a dithiocarbamate group (see Fig. 10b) evidences the strength of this type of interaction. Wilton-Ely *et al.* studied the anchoring

of ruthenium(II) [53] and nickel(II) [54] dithiocarbamate complexes onto gold nanoparticles through this functional group. However, poor information on the characterization of the nanohybrids was given by the authors.

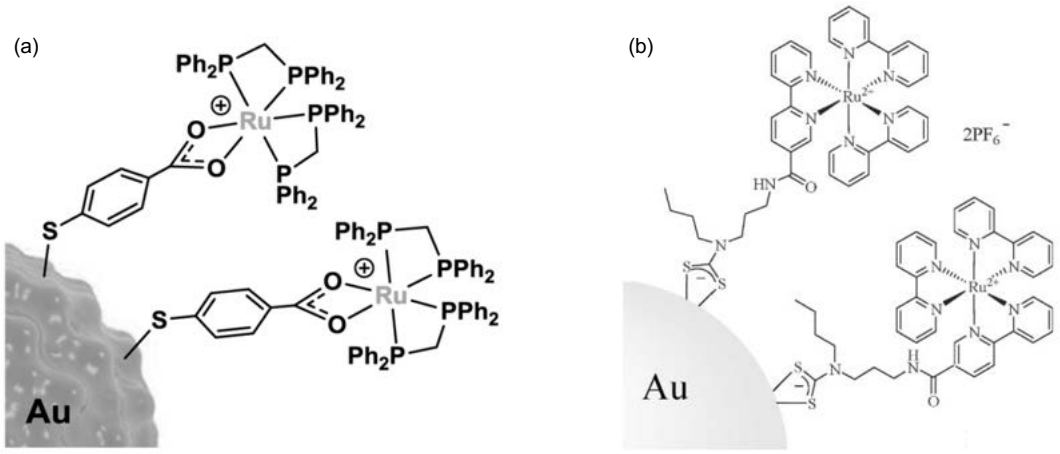

Figure 10. AuNPs with (a) ruthenium surface units grafted after dissociation of disulfide bond, reproduced from ref. [51] and (b) ruthenium(II)-trisbipyridine grafted through dithiocarbamate groups, reproduced from ref. [52].

Ir(III)-polypyridyl complex with dithiolate as grafting group

An unusual example, reported by Mayer and coworkers [55], is the use of a dithiolate-appended Ir complex as both reductant of $HAuCl_4$ used as gold precursor and stabilizer of the resulting gold nanoparticles (see Fig. 11). The reducing character of the Ir(III) complex was compared to that of the uncomplexated 4,5-diazafluorenedithiolate proligand, and it was observed that the presence of the cationic Ir(III) metal center accelerates the reduction step. The NMR and emission data of the complex after its grafting at the AuNP surface were compared with initial data. The broad resonances and quenching of the complex luminescence observed evidenced the complex proximity with the nanoparticles.

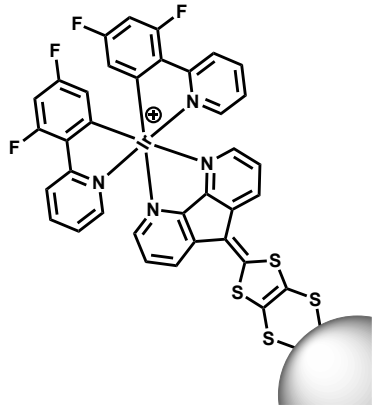

Figure 11. Dithiolate-appended Ir(III) complex, reducing and capping agent of AuNPs, described in ref. [55].

Re(I)-tricarbonyl complexes with protected thiols and endocyclic disulfides as grafting groups

The grafting of visible-light-emitting rhenium(I) tricarbonyl complexes on the surface of gold nanoparticles led to nanohybrids with luminescent properties. Re(I) tricarbonyl complexes having a protected thiol group, in the form of thioacetate, were attached to the surface of PEG-SH-stabilized gold nanoparticles [56]. Energy-dispersive X-ray spectroscopy (EDX) confirmed the presence of both Au and Re in the nanohybrids. Interestingly, although being connected to the surface of the nanoparticles, the Re(I) complex retained exploitable ^{3}MLCT emission. The authors attributed this result to the poor spectral overlap between the emission profile of the Re(I) complex, at 549 nm, and the absorption of the gold nanoparticle, at ca. 475 nm.

As previously observed for Ru(II) complexes, endocyclic disulfide groups were also used by Yam and coworkers to associate Re(I) tricarbonyl complexes to gold nanoparticles [50,57]. The anchoring of the dithiolate group of the positively charged Re(I) complexes on citrate-capped gold nanoparticles resulted in nanoparticle aggregation [57]. For comparison purpose, similar Re(I) complexes without dithiolate groups were added to the citrate-stabilized gold colloids. In that case, more severe aggregation occurred as consequence of the adsorption of these Re(I) cationic complexes on the AuNPs surface and interaction with the citrate-capping groups.

In marked contrast, when the ligand exchange was performed on gold nanoparticles stabilized by 4-dimethylaminopyridine (DMAP), the addition of the Re(I) complex (see Fig. 12) didn't result in any aggregation [50]. By FT-IR, the carbonyl ligand and ester group υ(C=O) stretches of the complex were identified on the nanohybrid. Additionally, the hydrodynamic diameter measured by DLS was ca. 15 nm larger than the metallic diameter observed by TEM. Förster Resonance Energy Transfer (FRET) studies were performed, and the energy transfer quenching mechanism between the Re(I) center and the gold nanoparticles was found to be dependent on the spacer length. When the ester bond between the metal centers and the gold nanoparticles was cleaved by the enzymatic activity of esterase, the complex was released, quenching no longer occurred and reactivation of the emission properties was observed. The described nonhybrids might find application in esterase recognition.

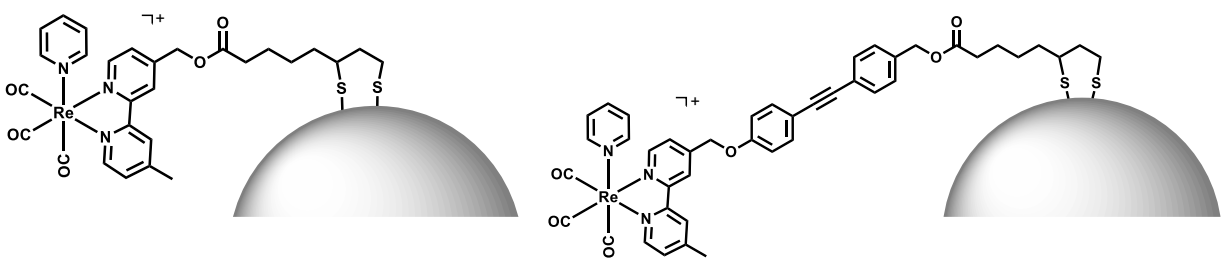

Figure 12. Examples of Re(I)-tricarbonyl complexes described in ref. [50].

Rh(I) complexes with monothiol grafting groups

Chiral rhodium(I)-diphosphine complexes with an alkylthiol pendant group were grafted on the surface of gold colloids and the resulting nanohybrids (see Fig. 13) were tested as catalysts for the hydrogenation of methyl α-acetamidocinnamate [58]. The nanohybrids were synthetized *via* a ligand exchange reaction on gold colloids stabilized by alkanethiols of different lengths and different end groups (polar, NH_2 and OH, and non-polar, CH_3 and adamantyl). Enantioselectivities and conversions similar to those observed with the corresponding unbound complex were obtained, for the non-polar colloids, and the catalysts could be recycled and restored after the hydrogenation reaction.

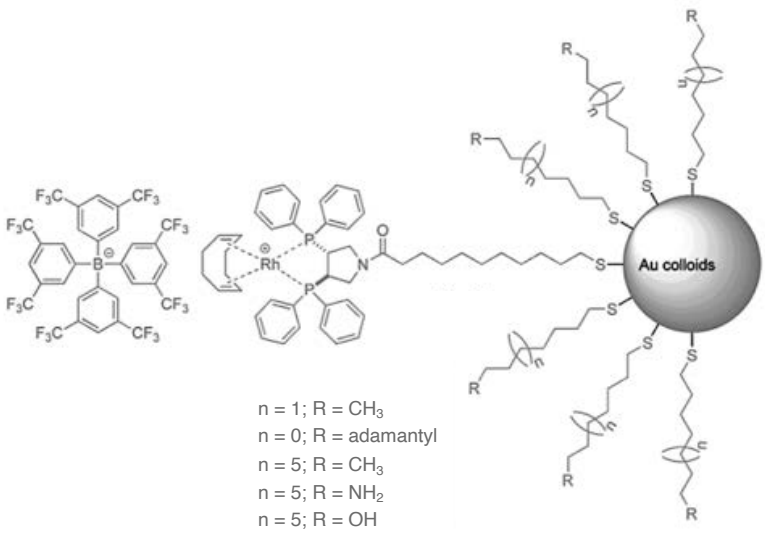

Figure 13. Rh(I) complexes incorporated on the surface of Au colloids by ligand-exchange strategy, reproduced from ref. [58].

Eu(III) complexes with monothiol grafting groups

Luminescent Eu(III)-coated gold nanoparticles were synthesized by displacement of the initial stabilizing citrate shell by the thiol groups of the added europium complex [59]. Upon addition of the complex a red-shift of 7 nm on the SPB was observed (527 nm against initial 520 nm), attributed by the authors to a change in the dielectric constant of the nanoparticles and characteristic of the adsorption of thiols on pre-stabilized citrate gold colloids. The Eu(III)-modified nanoparticles displayed red luminescence. In contrast, when a monothiol-appended Eu(III) complex was attached to pre-formed DMAP-capped gold nanoparticles, the SPB blue-shifted (520 nm to 510 nm) [60].

Gd(III) complex with dithiocarbamate grafting groups

Recently, a Gd(III) dithiocarbamate complex was grafted on the surface of gold nanoparticles to provide a nanohybrid with application as magnetic resonance imaging (MRI) contrast agent [61]. The

$HAuCl_4$ precursor was reduced with $NaBH_4$ in the presence of the Gd(III) complex and other surface units, such as thioglucose or thiol-terminated folic acid, in order to synthesize a multifunctional hybrid nanomaterial. Inductively coupled plasma – optical emission spectrometry (ICP-OES) and thermogravimetric analysis (TGA) techniques allowed the authors to estimate a number of 120 Gd chelates per Au nanoparticle (size = 4.4 nm).

Zn(II)-porphyrin and Zn(II)-phthalocyanine complexes with disulfide and monothiol grafting groups, respectively.

The ligand-exchange strategy was also employed to graft a zinc(II)-porphyrin disulfide derivative onto dodecanethiol-capped gold nanoparticles for application in anion sensing. The gold nanoparticles functionalized by the zinc(II)-porphyrin were found to display higher binding affinities towards Cl^-, $H_2PO_4^-$, Br^-, I^- and NO_3^- than the metalloporphyrin alone [62] (see Fig. 14a). The free metalloporphyrin is conformationally flexible, and its association with anions is entropically less favorable than the grafted analogue. The authors claim that the "pre-organization" of such receptors on the gold surface reduces the energetic cost of binding. Also, a thiolated zinc(II)-phthalocyanine complex was used to directly stabilize gold nanoparticles following the Brust method with the aim to obtain a nanomaterial of potential interest as photosensitizer agent for photodynamic therapy [63]. The TOAB used for the phase-transfer of the gold precursor appeared to remain in interaction with the nanohybrid, assumedly through van der Waals interaction between the alkyl substituents of the phthalocyanine macrocycle and the tetraoctylammonium cation. The presence of the phase-transfer agent on the final nanomaterial makes it soluble in polar solvents (see Fig. 14b).

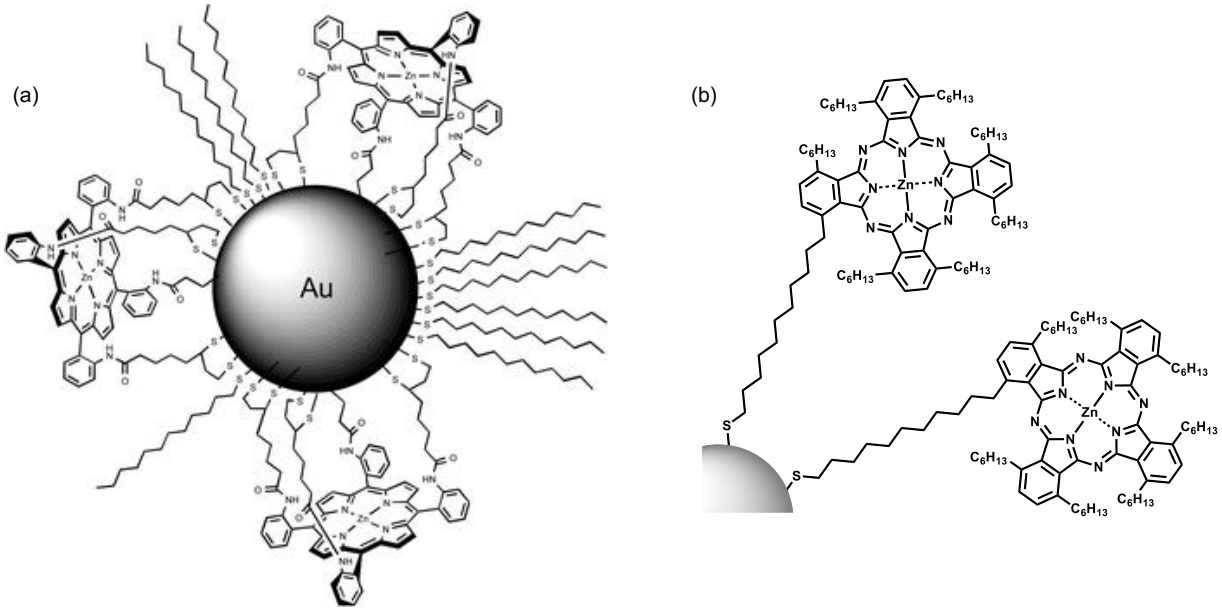

Figure 14. (a) Zn(II)-porphyrin derivative assembled to dodecanethiol-capped AuNPs, reproduced from ref. [62]. (b) Zn(II)-phthalocyanine complexes assembled to AuNPs described in ref. [63].

Pentacyanidoferrate(II) complexes with thiol grafting groups

Toma *et al.* studied the interaction of different pentacyanidoferrate(II) complexes having pendant thiol groups with gold nanoparticles. In a first study, they compared the addition of two different complexes over citrate-stabilized gold colloids. By addition of the $[Fe(CN)_5(2MPy)]^{3-}$ complex, in which the sulfur atom of the 2MPy ligand is coordinated to the iron center, leaching of the labile 2MPy took placed and induced aggregation of the colloids. In contrast, strong stabilization was observed for the $[Fe(CN)_5(4MPy]^{3-}$ (4MPy = 4-mercaptopyridne), which has a free thiol group to coordinate to the AuNP surface [35]. In a similar way [64], the anchoring of a $[Fe(CN)_5(PZT)]^{3-}$ complex (PZT = 2-pyrazin-2-ylethanethiol) at the surface of citrate-capped gold nanoparticles through its thiol pendant group offered repulsive electrostatic interactions that allowed to maintain a stable colloidal solution. The characteristic MLCT absorption band of the iron complex (460 nm) was observed as a shoulder of the SPB of the AuNPs at 520 nm. Interestingly, by addition of dimethyl sulfoxide (DMSO) to the gold colloidal solution, the PZT ligand of the complex was substituted and the so-formed complex $[Fe(CN)_5dmso]^{3-}$ was dissociated from the gold nanoparticle surface. The resulting PZT-stabilized gold nanoparticles aggregated, as confirmed by the appearance of a SPB above 600 nm.

Ferrocene groups with monothiols as grafting groups

Ferrocenyl-functionalized gold nanoparticles constitute another class of hybrid nanomaterials which has been intensively explored. Indeed, ferrocene-capped gold nanoparticles are of special interest in electrochemical applications [65]. Ferrocene groups are known to be chemically inert, thermally stable and redox active. Also, the cyclopentadienyl ligands can be chemically modified to provide different functionalities, including pendant groups. Regardless of strategies recently explored (see section 3.1.3.), the incorporation of ferrocene moieties onto the surface of gold nanoparticles is mainly performed using ferrocenyl-modified alkanethiol ligands.

The research on gold nanoparticle functionalization with ferrocenyl groups started with the seminal works of Murray and coworkers [66,67]. They attained the poly-functionalization of alkanethiolate-gold colloids by exchange reactions with various ω-substituted alkanethiols. By this way, different poly-hetero-ω-functionalized gold colloids having ferrocene terminal groups, together with phenyl, bromo, vinyl or methyl ester groups, among others, were obtained. ^{1}H NMR spectroscopy allowed to identify the different end-groups in the colloid. Typically, the resonances were broader for the groups connected to the gold NP surface through shorter alkyl chains.

A biferrocene-terminated alkanethiol has been used by Nishihara and coworkers [68] for the functionalization of octanethiol-stabilized AuNPs (see Fig 15a). Cyclic voltammetry (CV) studies indicated the presence of two reversible oxidation peaks, $E_{1/2}$ = 0.105 and $E_{1/2}$ = 0.517 V (*vs.* Ag/Ag^+),

at similar positions to those observed for the biferrocene complex free in solution. At oxidative potentials higher than 0.9 V (*vs*. Ag/Ag^+) a film of AuNPs on glassy carbon (GC) and indium tin oxide (ITO) electrodes was formed by electrodeposition. This phenomenon, not observed for the monoferrocene analogue, can be exploited for the construction of controlled nanoparticle layers [69,70]. As they are nanomaterials with high concentration of redox active ferrocene species on the surface, other authors synthesized ferrocenylalkanethiol-capped AuNPs for applications in electrochemical detection of DNA [71], and with potential use in energy-storage devices [72].

Bifunctional systems containing both ferrocenyl and Ru(II)-polypyridyl groups together with a thiol grafting group (see Fig 15b) have been also considered for the design of molecular electronic gold wires with different redox subunits [73]. In the obtained hybrid nanomaterial, the carbon resonances of the ferrocenyl (60-80 ppm) and terpyridyl moieties (110-170 ppm) could be identified by solution ^{13}C NMR.

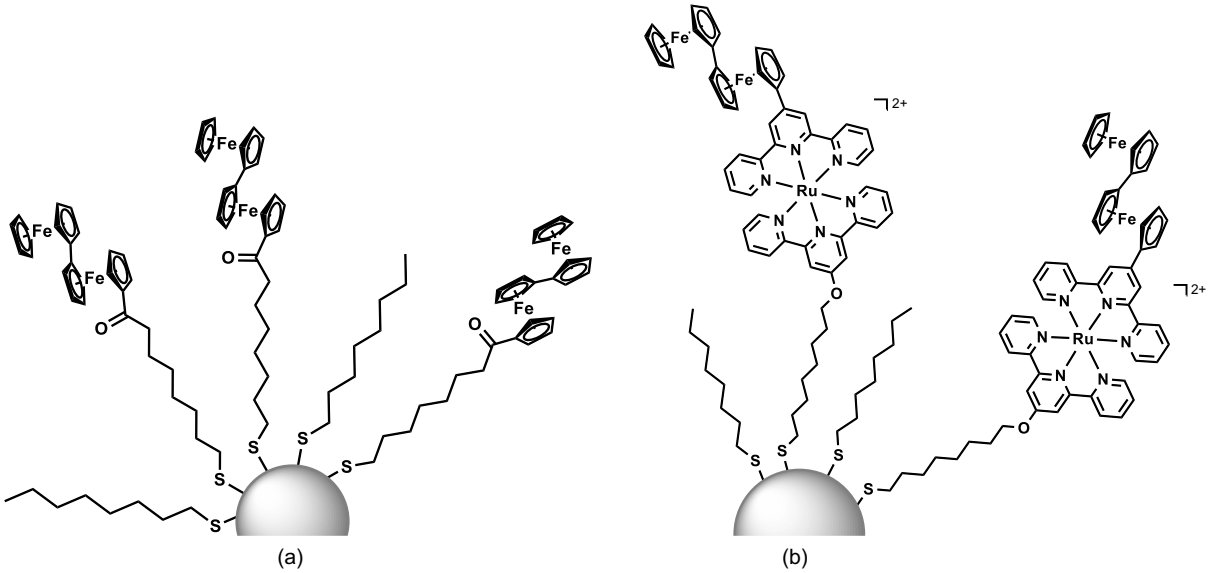

Figure 15. (a) Biferrocene-modified AuNPs and (b) biferrocenyl-functionalized Ru(II)terpyridine AuNPs, described in references [68] and [73], respectively.

With application in electrochemical titration of oxoanions, Astruc and coworkers used amidoferrocenyl-terminated alkanethiols (see Fig 16a) to functionalize organothiol-capped gold nanoparticles by a ligand exchange reaction. A single reversible wave at $E_{1/2}$=0.220 V (vs $FeCp_2^{0/+}$) was observed by CV, which indicates that all the ferrocene groups appear identical in the electrochemical time scale. Cathodically shifted waves appeared upon interaction with $H_2PO_4^-$ (ΔE=220 mV) and HSO_4^- (ΔE=45 mV) [74]. The sensing properties of these hybrid nanomaterials were compared to those of amidoferrocene dendrimers, that require, incidentally, more demanding synthetic procedures. Hydrogen-bonding between the oxoanions and the amidoferrocenium group was observed. Note that

the incorporation of an electron withdrawing group on the cyclopentadienyl ligand, such as an acetyl group, was found to improve the recognition of the oxoanions [75]. Also for the detection of $H_2PO_4^-$ and HSO_4^-, and in addition, adenosine-5'-triphosphate (ATP^{2-}), silylferrocenyl and amidoferrocenyl dendrons with a thiol pendant group were adsorbed on the surface of gold nanoparticles, either by ligand-exchange with dodecanethiol-stabilized AuNPs or by following a direct Brust-type synthesis (see Fig. 16b, as example) [76,77]. The resulting hybrid nanomaterials resembled nanoparticle-cored dendrimers and displayed tunable responses in the oxoanion sensing: the larger the generation of the dendrimer, the larger the shift of the redox potential upon interaction with the oxoanions [78].

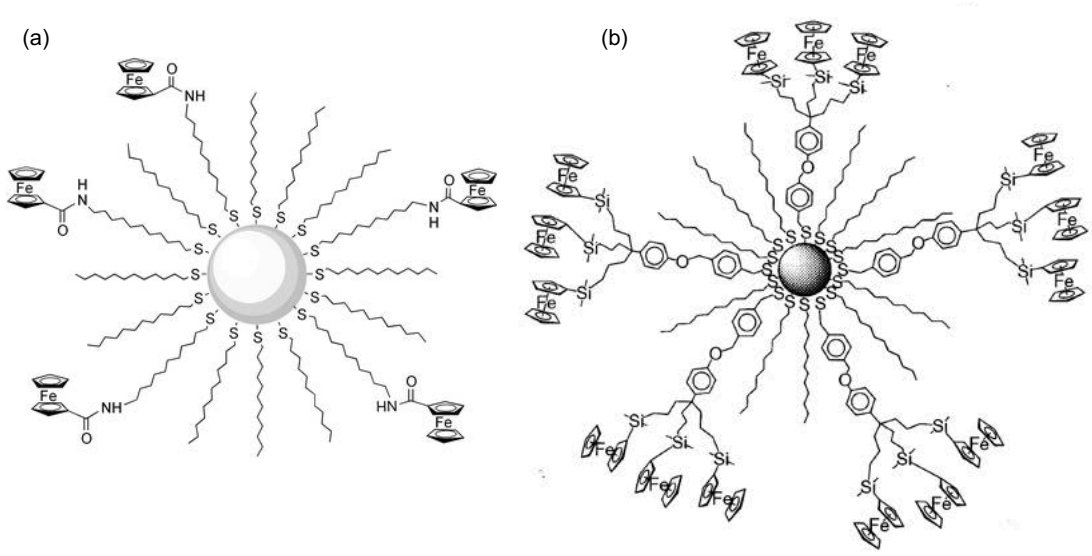

Figure 16. (a) Amidoferrocenyl-functionalized AuNPs, reproduced from ref. [74]. (b) Dendronized AuNPs incorporating silylferrocenyl dendrons, reproduced from ref. [78].

3.1.1.2 Grafting through non-thiol pendant ligands

Besides thiol-grafting, the anchoring of metal complexes at the surface of gold nanoparticles has been explored using a few other functional groups able to interact with gold surfaces, such as amine, pyridine, phenanthroline or ketone groups.

The grafting of fully conjugated metal-polypyridyl complexes was studied by Mayer, Sécheresse and coworkers. Having a fully conjugated spacer group instead of a long alkyl chain was expected to favor the electronic transfer between the nanoparticle surface and the metallic center of the complex. For example, Ru(II)-polypyridyl complexes with pendant conjugated pyridine and phenanthroline groups were used to synthesize gold nanoparticles in water and acetonitrile, by reduction of $HAuCl_4$ with $NaBH_4$ in presence of the corresponding complexes [79]. For the aqueous systems, the chloride salts of the Ru(II) complexes were employed, while the hexafluorophosphate salts were used for the

syntheses in acetonitrile. Interaction of the bidentate phenanthroline group with the surface of AuNPs (Fig 17a) led to regularly coated nanoparticles. It was observed that when $HAuCl_4$/Ru(II) ratios were high, meaning high Cl^- concentrations, flocculation in acetonitrile occurred. This pointed to a spontaneous anionic exchange between the highly concentrated Cl^- coming from the gold precursor and the PF_6^- counteranion of the Ru(II) complex. XPS data of the hybrid synthesized in acetonitrile indicated a matching Ru/Cl ratio, reinforcing the theory of anion exchange, as well as the integrity of the complex once grafted at the surface of AuNPs. Electrochemical studies on the nanohybrid composed by a Ru(II)-polypyridyl complex connected to the gold surface by monodentate pyridine coordinating group (Fig 17b) were performed. A reversible oxidation wave was observed in acetonitrile, assigned to the Ru^{2+}/Ru^{3+} redox couple. The gold nanoparticle is believed to stabilize the HOMO level of the bound complex; therefore, its oxidation potential is slightly lower than the unbound one. In the same study, stabilization of AuNPs by a Ru(II)-polypyridyl having a monodentate thiophene group was compared to the pyridine and phenanthroline systems previously described. The authors observed weaker interaction between the thiophene group and the AuNPs. The phenantroline-terminated Ru(II) complex was also coordinated to the surface of pre-formed gold nanoparticles by displacement of the weakly stabilizing TOAB [80]. Substitution of Cl^- by PF_6^- counteranion allowed to transfer the nanohybrids from water to acetonitrile.

A luminescent Ir(III) complex was grafted to the surface of AuNPs through a pyridine end-group, by addition to a solution of dodecylamine-stabilized gold colloids. The hydrodynamic diameter measured by DLS (9.8 nm) was found to be ca. two times larger than that observed by TEM (5 nm). The photophysical properties of the grafted complex were studied and compared to those of a similar Ir(III) complex with no apparent anchoring group, simply adsorbed on the AuNPs. Luminescence lifetimes of the Ir(III) complex were affected by its grafting to the AuNP surface [81].

To pursue photophysical studies, a Ru(II)-polypyridyl complex having a tpphz anchoring group was grafted to gold nanoparticles (tpphz = tetrapyridophenazine) [82]. $NaBH_4$ was added to a two-phase mixture of $HAuCl_4$ and TOAB (water/toluene). Addition of the Ru(II) complex to the solution yielded stable nanoparticles. A combination of Raman techniques (namely resonance Raman (RR), and surface-enhanced Raman scattering (SERS), see section below) gave evidence on the attachment of the complex to the AuNP surface through the tpphz bidentate ligand. Besides, the authors indicated that the electronic structure of the Ru(II) complex might be modified upon grafting to the gold nanoparticle. In another study involving characterization by SERS spectroscopy [83], a Ru(II) complex with dicarboxybipyridine ligands and triphenylamine (TPA) pendant groups was grafted to the surface of citrate-capped AuNPs. In acetonitrile, the grafting takes place through the TPA groups (see Fig. 17c), while in water and ethanol grafting can also occur through the carboxylate groups.

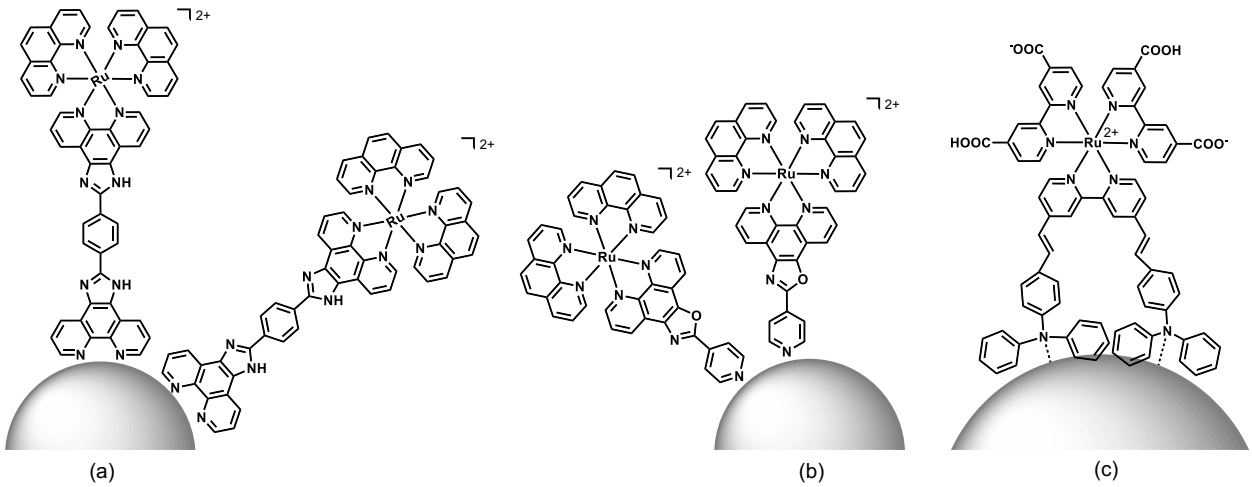

Figure 17. Ru(II)-polypyridyl complexes in interaction with AuNPs surfaces through (a) phenanthroline and (b) pyridine groups, described in ref. [79], and (c) TPA pendant groups (in acetonitrile) described in ref. [83].

Gold nanoparticles could be directly synthesized by using as stabilizer a Ru(II)-polypyridyl complex having a pendant amino group. Amino groups are generally considered to be weakly coordinating species. The interaction between the AuNPs and the amino pendant group of the Ru(II)-polypyridyl complex was confirmed by XPS analysis which showed a negative shift of -NH_2-related binding energy. The resulting hybrid nanomaterial exhibited electro-chemiluminescence properties under cyclic voltammetry [84].

Grafting of a Ru(II)-polypyrdiyl with an amino group to gold surfaces has also been performed by the addition of the complex to a solution of citrate-capped gold colloids [48]. A mild bathochromic shift (522 nm to 529 nm) and appearance of an additional band at 609 nm were observed. In the same study, the grafting of a similar complex, with a ketone group instead of an amine, was explored. Interestingly, besides a red shift on the SPB (522 nm to 531 nm), the shape of the AuNPs changed from spherical to cubic and also some aggregates were observed. This was attributed by the authors to the ability of the ketone to stabilize the Au-Ru(II) surface crystal planes.

3.1.2. Surface-functionalized AuNPs for the complexation of TMCs

Another approach to connect transition metal complexes with metal nanoparticles is to couple them at the outer side of the stabilizing shell that surrounds the NPs. This concept reminds to the "click chemistry" method which is a well-known and straightforward pathway to couple different entities in organic synthesis [85]. Herein, the stabilizers of the NPs are carefully chosen in order to act as bridges between NP and the transition metal complex entities. In one side the stabilizer binds to the surface of the AuNPs (usually *via* sulfur interactions), while a terminal coordinating group at its other side is available to interact with the transition metal complex.

An example of this approach comes from the aforementioned work of Bartz *et al.* [32] where gold colloids functionalized with thiols bearing terminal hexadiene groups were reported. The reaction between these functionalized AuNPs and $RuCl_3$ led to the coordination of ruthenium species to the terminal diene yielding Cl-bridged allyl-type ruthenium dimers anchored at the gold surface. This nanomaterial was found to be catalytically active in the ring-opening metathesis polymerization reaction, achieving higher rates than the homogeneous analogue. Presumably, when grafted to the AuNP surface, the Ru dimers are arranged in a way that favors the interaction of the active Ru sites with the monomer and the growing polymer chain.

Other nanohybrids were prepared following the same approach. For example, envisaging enantioselective catalysis gold nanoparticles were stabilized with (*R*)-BINOL-terminated disulfides ((*R*)-BINOL = (*R*)-1,1'-bi-2-naphthol). According to the authors, addition of $Ti(O\text{-}i\text{-}Pr)_4$ to these functionalized AuNPs led to the formation of the corresponding Ti-BINOLate complexes, active in the catalytic asymmetric alkylation of benzaldehyde [86].

Similarly, hexanethiol-capped gold nanoparticles were functionalized with thiol-tethered bisoxazoline ligands that further reacted with $Cu(OTf)_2$. The heterogenized chiral copper(II) complex catalyzed the *ene* reaction between 2-phenylpropene and ethyl glyoxylate with an efficiency similar to that of the corresponding homogeneous complex but with easier separation procedures [87]. Also, chiral tetradentate salen ligands were integrated at the surface of octanethiol-protected gold nanoparticles *via* a ligand exchange procedure. The complexation reaction of the chelating salen ligands with $Co(OAc)_2$, followed by oxidation of the cobalt centers by trifluoromethanesulfonic acid, was an effective way to build salen-Co(III) species on the AuNP surface (see Fig. 18a) [88]. The resulting hybrid nanomaterial was evaluated as catalyst in the hydrolytic kinetic resolution of hexene-1-oxide, with similar results than the homogeneous analogue and easy catalyst recovery and recycling.

The valence tautomeric behavior of a cobalt(II/III) semiquinone complex immobilized on the surface of AuNPs was studied by Shultz *et al*. [89]. For that, gold nanoparticles stabilized by 1-mercapto-6-(4'-methyl)bipyridine ligands were reacted with $Co_4(3,5\text{-}(t\text{-}Bu)_2C_6H_2O_2)_8$. The formation of the Co complex was verified by IR, by comparing the vibrational modes of the analogue free complex with those observed in the hybrid nanomaterial. Due to the presence of paramagnetic species, no characteristic signals were observed in the ^1H NMR spectra of the final nanohybrid. Due to a lower accessibility of the solvent at the surface of the nanoparticle, the thermodynamic parameters for the valence tautomerism ($\Delta H°$ and $\Delta S°$) of the bound Co semiquinone complex were attenuated, in comparison to its homogeneous analogue.

With the aim of studying of the hydrolysis of DNA phosphodiester bonds, $Zn(NO_3)_2$ was added to a mixture of pre-functionalized gold nanoparticles and the catalysis model substrate, bis-*p*-nitrophenyl phosphate (BNP). The authors report a full binding of the Zn(II) to the bis(6-amino-2-pyridylmethyl) surface units (see Fig 18b), explained by a stabilization of the activity after 1 equivalent of Zn(II) salt is added. The superior reactivity observed when using the nanohybrid compared to that of the homogenous Zn(II) counterpart is attributed to confinement of the Zn(II) species onto the gold surface [90].

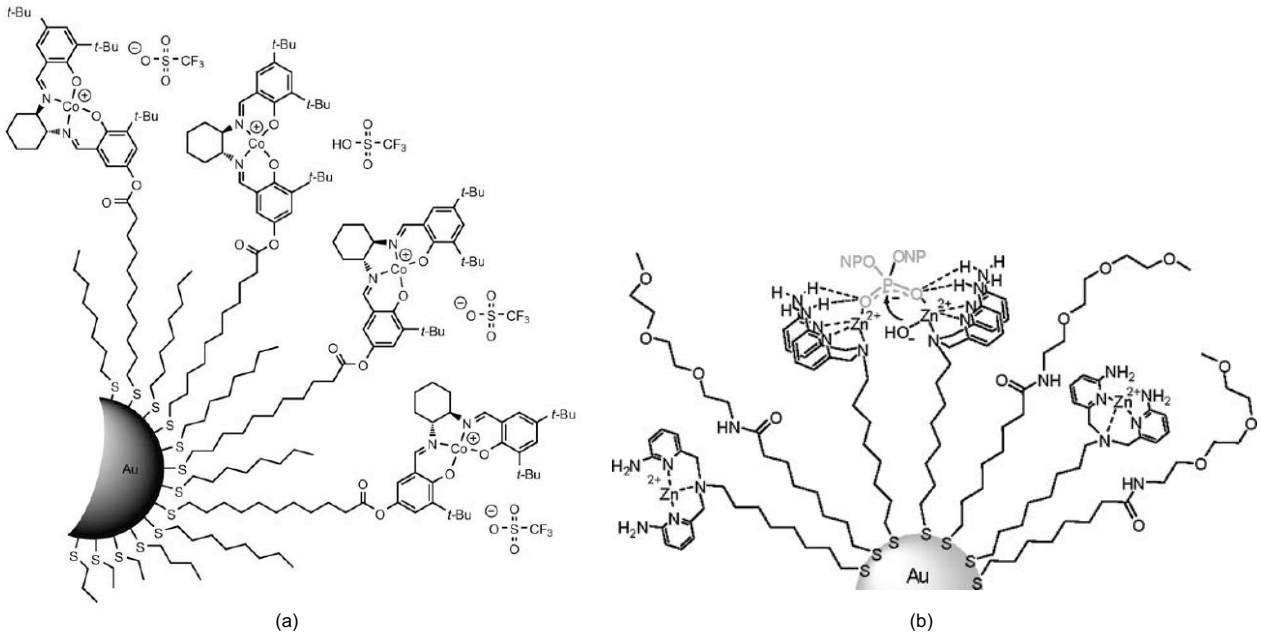

Figure 18. (a) Salen-Co(III) complexes built on the surface of AuNPs, reproduced from ref. [88] and (b) Zn(II) surface units immobilized on AuNPs, in interaction with BNP model substrate, reproduced from ref. [90].

The studies mentioned in the last paragraphs report good activities of catalysts anchored at the surface of gold nanoparticles, but the characterization of the resulting nanohybrids is barely detailed. It is thus difficult to estimate their real structure. $[RuCl_2(p\text{-cymene})]_2$ and $[RhCl(cod)]_2$ transition metal complexes were coupled to the terminal pyridine groups of thiol ligands coordinated at the surface of AuNPs. The resonances of the *p*-cymene and the cod ligands were detected in the ^1H NMR spectra of the respective hybrids. Preliminary catalytic tests showed poor activity of the hybrid nanomaterials in the isomerization of geraniol and the hydrogenation of 1-octene [91]. More effective was the immobilization of a Fe(II)-benzoylformate complex [92] at the surface of AuNPs through thiol-terminated amino-pyridine ligands (see Fig. 19), which entailed an improved reactivity towards oxidative decarboxylation of benzoylformic acid in comparison to its homogeneous analogue. Proofs of the complexation of the Fe(II) center were given by the appearance of a shoulder (between

365-382 nm) in the absorption spectra of the nanohybrid, additional to the SPB of the AuNPs, and a paramagnetically shifted ^{1}H-NMR spectrum.

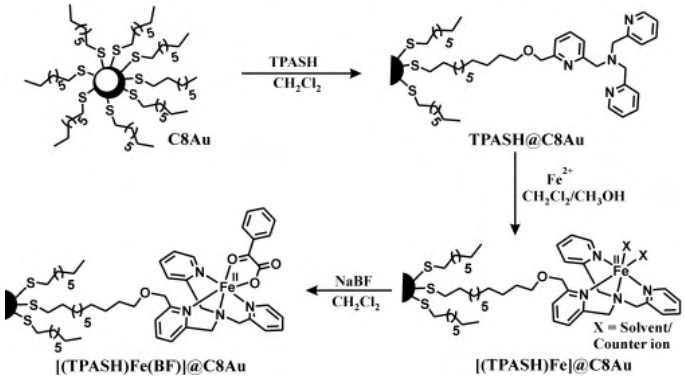

Figure 19. Scheme of the stepwise immobilization of Fe(II)-benzoylformate complexes on AuNPs pre-functionalized with tripodal N_4 ligands (TPASH), reproduced from ref. [92].

Fritz *et al*. [93] dedicated a study to the understanding of the organization of a silver(I) complex on the surface of gold nanoparticles (see Fig. 20a). For the synthesis of the nanohybrid, $AgNO_3$ was reacted with previously functionalized bioxazoline-gold nanoparticles. Techniques like DLS, UV-vis measurements and Density Functional Theory (DFT) calculations proved the proximity of the silver atom of the complex and the surface of the nanoparticle. Of particular interest were XPS analysis results, which allowed to (i) confirm the binding of Ag(I) to the nitrogen atoms of the bioxazoline ligand and (ii) note a shift to lower binding energies for the Au4f signal. This latter observation indicates an increase in electron density at the gold surface atoms, consequence of the close distance between the positively charged Ag(I) metal center and the surface of the nanoparticles.

The carboxyl terminations of 3-mercaptopropionic acid (MPA)-capped AuNPs have been used to coordinate Re(I) [94] and Ru(II) complexes [95] (see Fig 20b), forming a quasi-core-shell organometallic structure around the gold cores. Also, Schiffrin *et al.* [96] built amino-nitrilotriacetic cobalt(II) complexes on the surface of AuNPs by the stepwise modification of carboxylate surface units, which yielded nanomaterials for histidine-tagged protein immobilization. The FT-IR spectrum of the nanohybrid revealed the characteristic vibrational modes of the amide and the carboxylate groups of the complex.

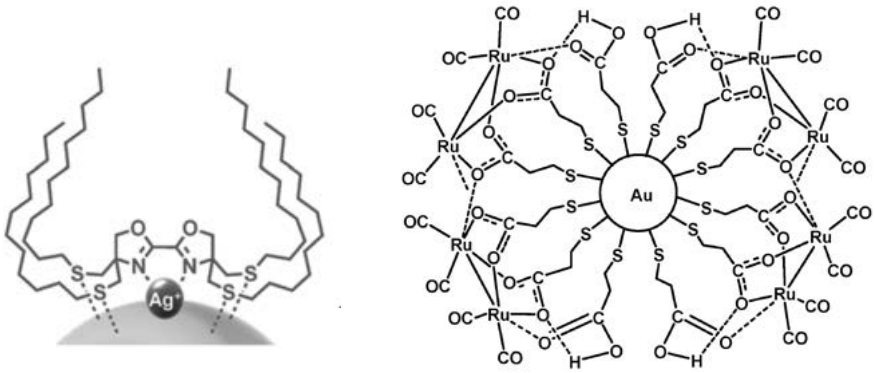

Figure 20. (a) Ag(I) ions immobilized on bioxazoline-capped AuNPs, reproduced from ref. [93]. (b) Ru(II) dicarbonyl carboxylate species on the surface of AuNPs, reproduced from ref. [95].

Designed for MRI, gold colloids were modified with a dithiocarbamate derived polydentate heterocycle for the chelation of Gd(III) ions. The broad signals of the water molecules bound to the Gd(III) centers and the detection of paramagnetic species in the hybrid nanomaterial by ^{1}H NMR spectroscopy confirmed the incorporation of the lanthanide at the AuNP surface [97].

Iron(III) complexes derived from Schiff base ligands, studied for their specific magnetic properties, were built on the surface of gold nanoparticles (see section 3.1.4. for other examples) by the reaction of Fe^{3+} ions and gold colloids capped by a tolylthiosalten^{2-} ligand (H_2tolylthiosalten = bis(3-salicylideneaminopropyl)-*p*-tolylthiolamine) [98]. The functionalized gold nanoparticles were synthesized by reduction of $HAuCl_4$ with $NaBH_4$ in the presence of the tolylthiosalten^{2-} ligand, in *N,N*-dimethylformamide (DMF). After purification and redispersion in DMF (stable colloidal solution) and ethanol/water mixture (partial agglomeration), a $FeCl_3$ salt was added and the corresponding [(tolylthiosalten)Fe(solvent)]$^{+}$ was formed. After addition of Fe^{3+} ions, agglomerates in ethanol/water were disassembled due to electrostatic repulsion between the cationic complexes formed on the NP surface. To evaluate the role of the repulsions, ammonium thiocyanate was added. Ligand substitution between the solvent molecule coordinated to the iron(III) center and the thiocyanate generated neutral complexes, [(tolylthiosalten)Fe(NCS)]; aggregation was then again observed.

Gold nanoparticles bearing free terpyridine surface groups as available donor groups allowed the complexation of transition metal fragments, such as Ru(II)-terpyridine units, at their surface. An example is the reaction of terpyridine-functionalized gold nanoparticles with Ru(tpy)Cl_3. UV-vis analysis of the obtained nanohybrid displayed a SPB band at around 510 nm and the MLCT band at 483 nm, characteristic of the bis(terpyridine)Ru(II) complex [99]. In the presence of an alkyl spacer between the Ru center and the gold surface, the main electrochemical characteristics of the resulting

Ru(II)-terpyridine complex, namely the half-wave potentials of the redox process related to $Ru^{2+/3+}$ at $E_{1/2}$=0.93 V (vs. Ag/Ag^+) and the terpyridine ligand at $E_{1/2}$=-1.52 V and $E_{1/2}$=-1.71 V (vs. Ag/Ag^+), were preserved. An entirely conjugated Ru(II)-terpyridine system [100] was also achieved by the reaction of a $Ru(tpy)Cl_3$ derivative with the 4'-(2-mercaptopyridyl)-2,2':6',2"-terpyridine used for the AuNPs stabilization. In this case, the influence of the AuNPs on the final photophysical and electrochemical properties of the Ru(II) complexes has not yet been studied. There are also some examples where the use of terpyridine-functionalized gold nanoparticles has been extended to the formation of 3D assemblies by complexation of Co^{2+} [101], or Fe^{2+} [102] ions.

The complexation of metal ions with the end groups of the stabilizing ligand shell can drastically modify some properties of the metal NPs such as polarity, dispersion in a given solvent or optical features. For example, the addition of Zn^{2+} to a solution of terpyridine-functionalized gold nanoparticles limits interparticle interactions and thus, prevents their aggregation [103]. In another study, aggregated nanomaterials were obtained by coordinating Zn^{2+}, Fe^{2+}, Cu^+ or Ag^+ ions to the terpyridine terminal groups of functionalized gold nanoparticles, therefore acting as interparticle bridges. In the case of iron, for instance, upon addition of Fe^{2+} ion, the formation of the corresponding $Fe(tpy)_2$ complex was confirmed by the appearance of its characteristic absorption band (450-600 nm) [104].

The studies described in the last paragraph illustrate how changes on the physical properties of metal nanoparticles can happen upon coordination of metal cationic species on free ligands of the stabilizing layer of nanoparticles. Such changes can be easily monitored which makes these systems interesting for applications in metal cation recognition or sensing. There are several examples in which AuNPs functionalized with crown ethers [105], carboxylic acids [106] or bipyridines [107] have been used for the detection of cations [108].

3.1.3. Electrostatic binding of TMCs to AuNPs

A third approach for the connection of transition metal cationic complexes, either to the ligand layer surrounding the nanoparticles or by direct adsorption on the NP surface, is based on electrostatic interactions.

For instance, the reversible interaction between $[Ru(bpy)_3]^{2+}$ and tiopronin-capped AuNPs was followed by fluorescence studies by Murray and coworkers [109]. Quenching of fluorescence was observed to increase with pH, when the electrostatic binding of the cationic Ru(II) complex is favored by the deprotonation of tiopronin. In the contrary, it decreased upon addition of a competing cation that caused release of $[Ru(bpy)_3]^{2+}$. In a following work [110], the influence of the core size of the tiopronin-capped gold nanoparticles on the quenching of the $[Ru(bpy)_3]^{2+}$ luminescence was studied.

Core sizes from 1.3 nm to 3.9 nm were considered. Larger gold cores displayed higher quenching constants.

Adsorption of $[Ru(bpy)_3]^{2+}$ complexes on the surface of gold colloids was studied by steady-state and time-resolved emission measurements [111]. On citrate-capped gold nanoparticles, association of the $[Ru(bpy)_3]^{2+}$ to the nanoparticles was observed by displacement of citrate, while on gold nanoparticles capped with marcaptooctanoic acid, there seemed to be an equilibrium between $[Ru(bpy)_3]^{2+}$ physisorbed on the NP surface and free in solution (three $[Ru(bpy)_3]^{2+}$ species were identified: free $[Ru(bpy)_3]^{2+}$, $[Ru(bpy)_3]^{2+}$ electrostatically adsorbed on the ligand layer and $[Ru(bpy)_3]^{2+}$ closer to the surface, adsorbed after displacement of a fraction of the initial stabilizers).

Ferrocenyl-decorated gold nanoparticles have already proven to be systems of interest (see section 3.1.1.1.), notably for electrochemical applications. Astruc and coworkers [112] went a step further and used ferrocene (Fc) as single electron reductant to both reduce $HAuCl_4$ precursor and directly stabilize the resulting gold nanoparticles. The reaction is stoichiometric (3 equiv. of Fc for 1 eq. of Au^{III}) and exergonic; the difference in redox potentials between aqueous $AuCl_4^-$ and Fc in organic solvents is considered the driving force of the electron transfer. The results are gold nanoparticles electrostatically stabilized by chlorine and ferricenium ions (as confirmed by a UV-vis band at 600 nm) (Fig. 21a). Additionally, a change in the pH of the reaction mixture and the presence of Au(I) species observed by XPS are indicative of the active role of hydronium ions on the stabilization of the nanoparticle surface. This role was actually confirmed when in the reaction of Fc with $AuCl_3$ only aggregates were obtained. Even though the electron transfer takes place within a few seconds, the size of the nanoparticles (ca. 18 nm) is bigger than those obtained when more conventional reducing agents, for instance $NaBH_4$, were used. The activity of this nanohybrid system towards the reduction of 4-nitrophenol, a model reaction that allows evaluation of the catalyst surface, was observed to be lower than that of smaller AuNPs. The use of ferrocene bearing substituents of different bulkiness in the cyclopentadienyl ring was also explored (for example, see Fig. 21b), including a ferrocene-terminated dendrimer [113]. Both steric and electronic features of the substituents grafted on the ferrocenyl fragments were found to affect the electron-transfer rate, and the size of the gold nanoparticles formed (13 to 35 nm). In this study, the ferrocenyl termini of the dendrimer-derived entities served as both reductant and stabilizer of the nanoparticles, in contrast to the dendronized nanohybrid described in the previous section, where the gold nanoparticle was the core of the hybrid structure. Due to the marked steric hinderance of the ferrocenyl-dendrimer entity, the reaction was found to be slower than using other ferrocene derivatives.

The reduction of $HAuCl_4$ by electron-reservoir metallocenes ($19e^-$ sandwich complexes) was also explored for the formation of Au-based nanohybrids in the presence of PVP, where the metallocenes

acted as both reducing and stabilizing agents. The resulting nanohybrids were compared to those obtained using as reductants hydride-donors or hydride reservoir (hydride-rich neutral sandwich complexes) with analogous structure. The metallocene complexes used in this study have higher reductant power than ferrocenes and yielded comparably smaller gold nanoparticles (4.2-6.8 nm against 13-35 nm) [114]. After the reaction, UV-vis analysis confirmed the presence of the oxidized form of the introduced metallocene species for all the systems studied. Even if the synthesis of the so-obtained AuNPs was performed in the presence of PVP, the metallocenes form an electrostatic layer around the NPs which avoids the contact of the polymer with the surface and therefore leaves some surface sites for interaction with substrates. Generally, the hybrid nanomaterials built with hydride-reservoir metallocenes, and in particular those capped with the hydride cobaltocene, gave better results than the hybrids prepared with electron-reservoir metallocenes in the catalytic reduction of 4-nitrophenol by $NaBH_4$. It is important to note that the metallocenes do not exhibit any catalytic activity in their oxidized form. Other nanocatalysts have been successfully synthetized following this approach (see section 3.2.3).

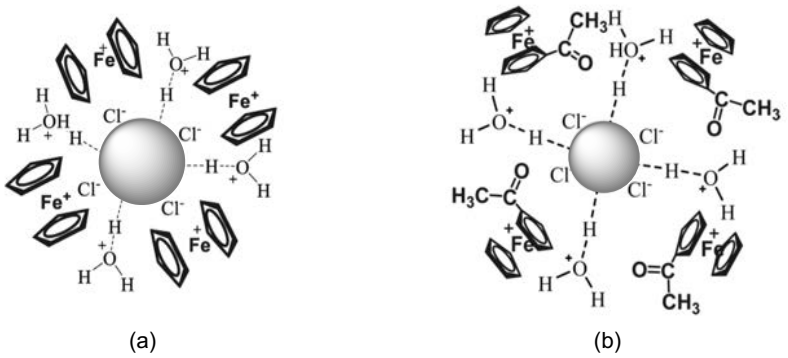

Figure 21. (a) Ferricinium chloride-stabilized AuNPs, reproduced from ref. [112] and (b) acetylferricinium chloride-stabilized AuNPs, reproduced from ref. [113].

3.1.4. Miscellaneous TMC-AuNPs hybrid systems

Even though there are not many examples in the literature, the incorporation of complexes on the surface of gold nanoparticles can also occur *via* interactions that are not a covalent grafting of a spacer *via* a pendant group neither electrostatic.

For instance, functionalization of AuNPs by cyclodextrins, cage molecules which are well-known to form inclusion complexes, was reported for the first time by Kaifer *et al*. In their work, thiolated cyclodextrins were adsorbed on the surface of gold colloids, either by ligand-exchange [115] or by one-step stabilization [116] methods. The resulting nanohybrids effectively acted as host units for ferrocene-containing molecules. The inclusion of ferrocene entities inside the β-cyclodextrin cavities

on the surface of AuNPs was evidenced by electrochemical methods and by competition reactions with 1-adamantanol. By the use of sufficiently amphiphilic ferrocenylammonium derivatives as guest molecules, the water-soluble gold nanoparticles could be transferred to chloroform. The reversible host-guest interaction with ferrocenylammonium molecules was also studied by ^{1}H-NMR [117]. Other authors assembled cyclodextrin-modified AuNPs to ferrocene coated electrodes to enhance their activity in the voltammetric analysis of ascorbic acid [118].

Ru(II) and Re(I) TMCs bearing a pendant adamantane group have also been assembled to cyclodextrin units at the surface of AuNPs [36]. Solid proof of the host-guest interaction was given by (i) the broadening of the proton signals of the adamantane groups in NMR studies as a result of their proximity to the gold surface and (ii) a correlation with the cyclodextrin protons observed by Rotating frame Overhauser Effect Spectroscopy (ROESY) experiments. Quenching of luminescence occurred in a greater extent for the Re(I) complex, probably since its spectral overlap with the SPB is larger than for Ru(II). The Förster Resonance Energy Transfer (FRET) properties of the nanohybrids could be thus modified by the nature of the chromophore and the length of the alkyl spacer.

An original example is the use of neutral phthalocyanine-lanthanide complexes (terbium and lutetium) to stabilize gold colloids through van der Waals interactions (Figure 22). The $HAuCl_4$ precursor was reduced by $NaBH_4$ in a water/toluene solution in the presence of these Tb(III) and Lu(III) bis(phthalocyanate) complexes, that stabilize the gold surface by π-stacking *via* the phthalocyanine conjugated system [119]. XPS measurements demonstrated that the phthalocyanine complexes maintained their neutral electronic state when capping the AuNPs. The weak interaction between the two entities is most likely the reason of the weak interparticle electronic coupling observed during electron transport studies. Single-electron tunneling behavior has been observed for the Lu(III)–AuNPs nanomaterial, a property of interest for the fabrication of electronic devices.

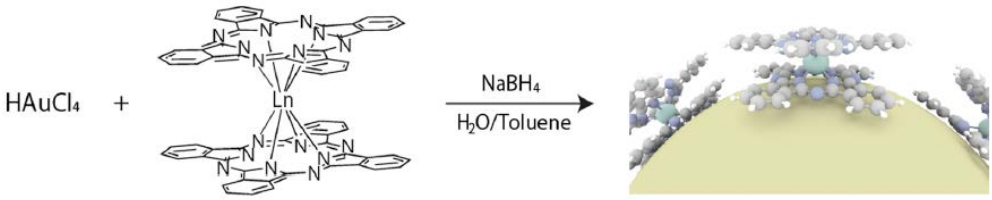

Figure 22. Synthesis scheme of bis(phthalocyaninato)lanthanide(III) protected AuNPs (Ln = Lu, Tb), reproduced from ref. [119].

In a recent study [120], a family of ruthenium alkynyl complexes displaying a “star” structure have been associated to gold nanoparticles following a Brust-like methodology. This approach yielded nanohybrids with non-linear optical properties. The complexes used consisted on tris(1,2,3-triazolyl)-, tri(2-thienyl)- or triphenyl-benzene cores, connected through phenylethynyl π-bridges to terminal

trans-Ru(II) TMCs. For the synthesis of the nanohybrids, $HAuCl_4$ was reduced with $NaBH_4$ in a two-phase system (water/toluene), in presence of TOAB and the complexes, used as stabilizers. When, as a control experiment, the individual "branches" of the "star complexes" were used as stabilizing agents, no nanoparticles were obtained, which evidenced the importance of the branched configuration for the stabilization. By ^{31}P NMR spectroscopy and cyclic voltammetry experiments, characteristics similar to those of the free ruthenium alkynyl complexes were identified in the data recorded for the nanohybrids. The ^{31}P NMR spectra displayed a singlet corresponding to the phosphorous atoms of the 1,2-bis(diphenylphosphino)ethane ligand coordinated to the Ru(II) center, at chemical shifts similar to those observed for the complexes alone in solution. Likewise, for the three systems, reversible metal-centered redox processes were observed at similar potentials to those obtained for the unbound complexes. UV-vis spectroscopy allowed to identify SPB corresponding to the gold NPs and the $\pi - \pi^*$ and MLCT transitions of the complexes. To evaluate the strength of the interaction between the "star" complexes and the AuNP surface, solvatochromic studies based on modifying the polarity of the solvent were performed. It was considered that the weaker the interaction with the TMC, the stronger the interaction with the media (more responsive to environmental changes) and therefore, the stronger solvatochromic shift. By this experiment, the ruthenium alkynyl complex having the triphenyl-benzene core was found to exhibit the weaker interaction. Considering the complex with the 2-thienyl groups (see Fig. 23 right), molecular modeling indicated that the AuNPs may be covered by four/five complex entities, these latter stabilizing the NPs *via* strong Au-S and weaker π-type Au-aryl interactions. The coverage of the AuNP surface by the ruthenium alkynyl "star" complexes is considered not complete, and solvent molecules are presumed to interact with the naked surface regions too. The results obtained in the non-linear optical studies performed highlighted the interest of the nanohybrids developed for such applications.

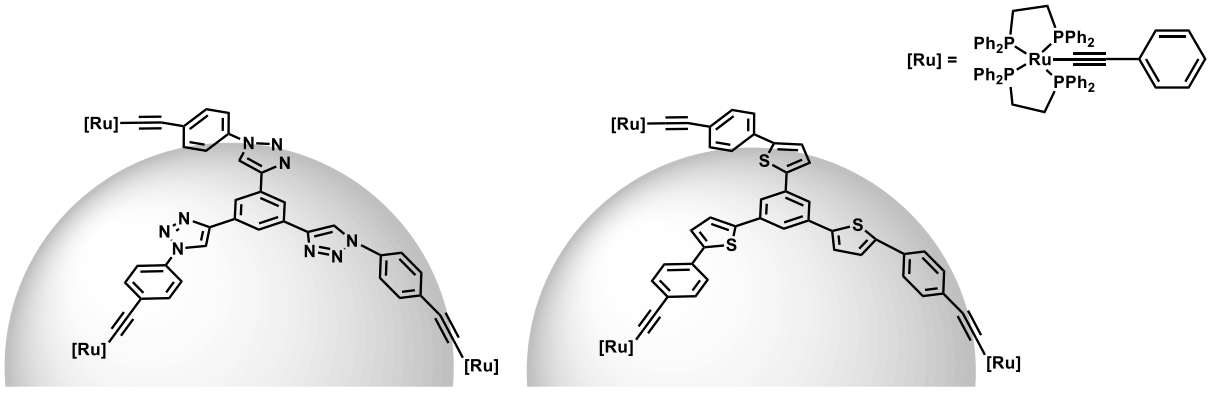

Figure 23. Ruthenium alkynyl "star" compounds with 1,4-(1,2,3-triazolyl) (left) or 2,5-thienyl (right) moieties stabilizing AuNPs described in ref. [120].

The coordination of TMCs to the surface of AuNPs *via* the use of ambidentate NCS ligand will be also here described. Being located in the first coordination sphere of the TMC, the NCS ligand is not considered as a pendant ligand. The grafting takes place through the free sulfur atom of the isothiocyanate group thus forming a three-atom bridge between the AuNP surface and the TMC.

Commercially available ruthenium dyes (N719, N749 and Z907) widely used in solar cell sensitization, bearing isocyanate and carboxyl groups known for their affinity towards semiconductor surfaces, were associated to AuNPs [82]. Solutions of the dyes were added to colloidal aqueous solutions of citrate-capped AuNPs. A redshift of 7 nm on the initial SPB (535 nm) indicated modification of the surface state of the citrate-stabilized AuNPs. Resonance Raman (RR) and surface-enhanced Raman Scattering (SERS) spectroscopies allowed to evaluate the binding of the dyes to the AuNPs surface. Enhancement of molecular bond resonances is commonly observed in SERS spectra for molecules or groups directly bound to a gold surface. In comparison to the RR spectra of the dyes in water, the SERS spectra of the gold nanohybrids displayed an enhanced CN-stretching vibration. This observation indicated that the ruthenium dyes are coordinated to the surface of the AuNPs through the free sulfur atoms of the isothiocyanate ligands (see Fig. 24a). As no spectral changes were observed between the dyes in solution and those coordinated to the AuNP surface by comparison of RR and SERS data, the authors concluded that the dyes maintained their electronic structure and photochemical properties. In a previous study [83], the different binding modes of a ruthenium dye (N719) to a gold surface, studied by SERS spectroscopy, were found to be solvent dependent (see Fig. 24b and 24c): in acetonitrile, the coordination took place *via* the isothiocyanate ligands, while in water and ethanol, they can also bind through their carboxylate groups.

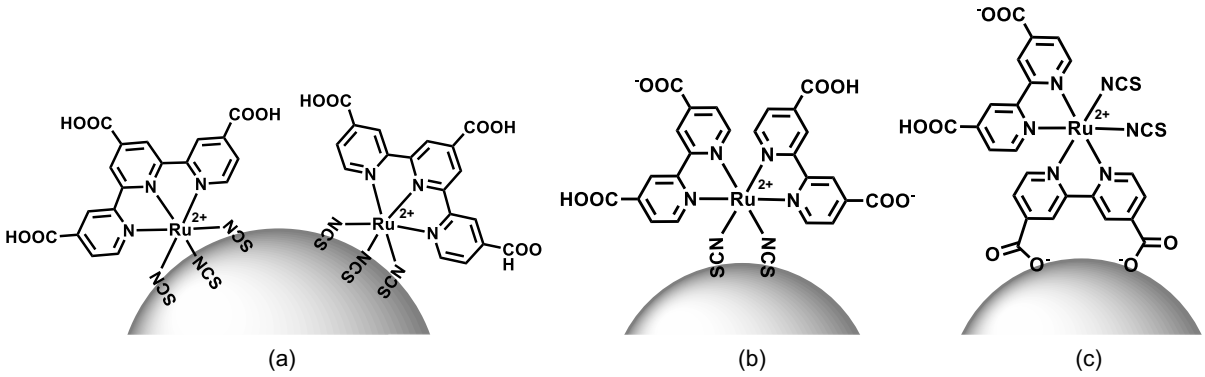

Figure 24. (a) Interaction of the ruthenium dye N749 with the surface of AuNPs in aqueous media, described in ref. [82]. Interaction of the ruthenium dye N719 with AuNPs surface in (b) acetonitrile and (c) water or ethanol media, described in ref. [83].

Also iron(III) salten derivatives were grafted on the surface of AuNPs *via* the coordination of ambidentate thiocyanate ligands, following a direct stabilization method [98]. In DMF, $HAuCl_4$ was

reduced with $NaBH_4$ (aqueous solution) in the presence of [(salten)Fe(NCS)] and [(dodecanesalten)Fe(NCS)] complexes (H_2salten = bis(3-salicylideneaminopropyl)amine, H_2dodecanesalten = bis(3-salicylideneaminopropyl)dodecanamine). When using the [(salten)Fe(NCS)] complex, gold aggregates were obtained. The inability of this neutral complex to stabilize AuNPs was attributed to the lack of steric or electrostatic repulsions that would prevent aggregation. Steric repulsion could be induced by the incorporation of a long alkyl substituent to the amine group of the salten ligand, as in the [(dodecanesalten)Fe(NCS)] complex, which allowed getting stable AuNPs colloidal solutions.

3.2. TMCs assembled to MNPs with M = Ag, Rh, Pd, Cu, Co and Ft-Pt

At a lower extent, similar synthetical approaches as those reported for the development of TMC-AuNPs nanohybrids have been applied for the synthesis of TMC-MNPs nanohybrids of other metals. In this context, silver-based nanohybrids have also attracted some interest as, like gold, silver nanoparticles, AgNPs, also display plasmonic properties (SPB band at ca. 420 nm) [121]. Their photophysical properties add to their interest in optical applications and comparative studies between TMC-AgNPs and TMC-AuNPs are recurring.

The combination of TMCs with MNPs, other than gold and silver, is generally more focused on catalytic applications. TMC-MNPs hybrid systems based on Pd, Rh and Cu NPs, and magnetic Co and FePt NPs, are some of the examples found in the literature. Confinement of TMC active sites at the MNP surface, good organization favoring interaction with substrates and easier catalyst recoveries, for instance, by magnetic decantation, are some of the interests of TMC catalyst immobilization on the surface of MNPs.

3.2.1. Functionalized TMCs for the grafting on MNPs

Biferrocene units have been incorporated to octylthiolate-capped palladium nanoparticles (3.8 ± 0.8 nm) by a ligand exchange process [122]. The number of octylthiolate ligands susbtituted by biferrocene-terminated thiolates was estimated by ^{1}H NMR measurements, considering the ratio of integrals of the biferrocene protons (3.8-4.6 ppm, broadened signal) and the methyl protons of octylthiolate (0.8 ppm). The ligand exchange was also followed by FT-IR spectroscopy where the disappearance of the ν(SH) absorption peak at 2568 cm^{-1} confirmed the elimination of free biferrocene thiol derivative during the purification process, while the appearance of an additional ν(C=O) absorption peak at 1654 cm^{-1}, slightly lower than that of the free biferrocene thiol derivative, was observed. Cyclic voltammetry of the nanohybrid showed two one-step oxidations, at $E_{1/2}$ = 0.175 and 0.577 V (*vs.* Ag/Ag$^+$), and as previously observed for gold-based analogous systems, electro-oxidative deposition of PdNPs layers on the electrode took place. The phenomenon of electrodeposition is

attributed by the authors to an aggregation process caused by the accumulation of charges around the NP surface. This phenomenon can be exploited for the controlled building of metal nanoparticle networks [69].

Palladium-cored ferrocenyl-terminated dendrimers were prepared and evaluated as catalysts for the Suzuki-Miyaura and styrene hydrogenation reactions [123]. The synthesis of this hybrid nanomaterial was performed in THF by reduction of the $[PdCl_2(CH_3CN)_2]$ complex, used as metal precursor, by lithium triethylborohydride, $Li(Et)_3BH$, in the presence of TOAB. The nonaferrocenyl thiol dendron was then added at different ratios. A 5:1 reactant ratio ($[PdCl_2(CH_3CN)_2]$/nonaferrocenyl thiol dendron) was found optimal for catalytic applications, and hydrogenation of styrene under mild conditions (room temperature; 1 bar of H_2) was achieved. It is assumed that at a 5:1 ratio, the organization of the thiolated dendrons around the PdNP cores (1.5 nm diameter) leaves active surface sites free for the interaction with substrates (higher dendron concentration inhibited surface sites, and with lower dendrons, coagulation occurred).

As it has been previously described, AuNPs functionalized by a diruthenium disulfide complex were synthesized and characterized [51]. The same disulfide complex was used to directly form PdNPs upon reduction of $[PdCl_2(CH_3CN)_2]$ with $Li(Et)_3BH$ in the presence of TOAB in THF (ca. 2 nm diameter). Although presence of Ru was confirmed by EDX, TGA analysis of the purified nanohybrid pointed to a low coverage of the Pd surface by the Ru(II) units. Unlike their gold analogues, the Pd nanohybrids were insoluble in common deuterated solvents which limited further characterization. Ru(II)-polypyridyl complexes with pendant pyridine and phenanthroline groups were used to prepare AgNPs in acetonitrile upon reduction of $AgNO_3$ with aqueous $NaBH_4$ [124]. The AgNPs size was controlled by the $AgNO_3$/Ru(II) complex ratio and the nature of the anchoring group, sizes from 1 to 20 nm could be obtained. Changes in the UV-vis absorption spectra of the TMCs were observed when bound to the silver surface: the intensity of the absorption bands assigned to π-π intraligand transitions decreased and it increased for the MLCT bands. The easy redispersion in water of the silver nanohybrids might be facilitated by an exchange between the PF_6^- counteranions, brought by the complex, and the NO_3^- brought by $AgNO_3$ [79]. Anion exchange between PF_6^- and Cl^- has already been observed in acetonitrile for AuNPs coated with the same Ru(II) complexes.

As it was made with AuNPs [81], a luminescent iridium(III) complex with a pyridine pendant group was grafted, by a ligand exchange procedure, to dodecylamine-stabilized AgNPs (9 ± 3 nm). When grafted to the silver surface, the luminescence of the complex is quenched, but in a less efficient way than for the gold analogue. A lower spectral overlap of the Ir(III) and AgNPs compared to the AuNPs counterparts explains this observation.

AgNPs (10-23 nm diameter) were prepared by reduction of $AgNO_3$ with $NaBH_4$ in the presence of Ru(II) complexes bearing pyridine pendant groups. The insolubility of the nanohybrids in common deuterated solvents made NMR characterization impossible. Even though, IR spectroscopy displayed the characteristic bands of Ru-phosphine complex on the surface, and EDX confirmed presence of ruthenium, phosphorous and silver in the nanohybrid [125].

Hybrid AgNPs were synthesized using heteroleptic dipyrrinato nickel(II) complexes, with pyridine anchoring groups, as stabilizing agents. Different ratios of $AgNO_3$/Ni(II) were employed, which led to different NP sizes (10 to 20 nm mean diameter) [126]. The complexation of Ag^+ cations to the pyridine groups was studied by ^1H NMR. While pyridyl protons moved downfield, due to the reduced electron density, and signals broadened, the resonances of the other protons appeared at the usual chemical shifts. By DFT calculations the electron density on the Ni(II) complex was found to be located on the pyridyl nitrogen, favoring the interaction with Ag atoms through this group, in agreement with NMR observations. The activity of the silver nanohybrids as catalysts for the reduction of 4-nitrophenol to 4-aminophenol with $NaBH_4$ was evaluated and compared to that of PVP-stabilized AgNPs and to the free Ni(II) complexes. Higher catalyst concentration and longer reaction times were required for PVP-AgNPs, whereas no conversion was observed for the unbound Ni(II) complexes, thus illustrating the interest to combine the two entities in the hybrid.

A family of ferrocenyl-based compounds, incorporating diphenyl phosphine ligands and substituents of different nature and bulkiness in the pentadienyl ring, were used to build rhodium based nanohybrids [127]. The organometallic precursor [Rh(η^3-C_3H_5)$_3$] was decomposed by applying hydrogen pressure (3 bar) in dichloromethane solution, in the presence of the ferrocenylphosphine ligands, obtaining nanoparticle sizes between 1.1 and 1.7 nm. The surface coverage of the resulting nanohybrids was evaluated by exposure to CO atmosphere, and subsequent analysis of the different CO coordination modes on the Rh surface by FT-IR. Bidentate ferrocenylphosphine ligands bring greater surface coverage than a monodentate one. Indeed, RhNPs stabilized with the monodentate ferrocenylphosphine ligand were more active in arene hydrogenation of ethylbenzene than those stabilized by bidentate ligands.

3.2.2. Surface-functionalized MNPs for the complexation of TMCs

Agents for protein binding, based on magnetic nanoparticles, were prepared by pre-functionalization of Fe-Pt NPs with nitrilotriacetic acid (NTA) terminated thiols, followed by reaction with $NiCl_2 \cdot 6H_2O$ [128]. The Fe $2p_{3/2}$ and Pt $4f_{7/2}$ regions of the XPS spectra displayed characteristic energies of Fe-S and Pt-S bonds generated at the Fe-Pt NP surface after reaction with the NTA terminated thiols. Time-of-flight second ion mass spectroscopy (ToF-SIMS) confirmed the chelation of Ni^{2+} ions with the NTA

groups. Efficient binding of the NTA-Ni(II) surface units to histidine-tagged proteins was observed. Interestingly, in the absence of coordinated Ni(II) species, NTA surface units show insignificant binding.

An amino-nitrilotriacetic Co(II) complex, ANTA-Co(II), was assembled to silver nanoparticles functionalized with thioctic acid (TA) by a stepwise procedure [129]. FT-IR spectroscopy showed the characteristic vibrational modes of the amido linkage between the carboxylate end-groups and the ANTA-Co(II) complex. The SPB of the thioctic acid silver nanoparticles, initially centered at ca. 400 nm, was broadened towards 512 nm, the typical absorption of the ANTA-Co(II). A number of 165 Co atoms per silver nanoparticle (5.2 ± 0.8 nm) was estimated by atomic emission spectroscopy AES-ICP analysis. The ANTA-Co(II) complex on the surface contains two labile H_2O ligands that can readily undergo substitution reactions. Based on this mechanism, AuNPs containing imidazole terminated ligands were observed to react with the ANTA-Co(II) silver hybrids through the lone pair of the imidazole group, thus generating larger nanoparticle assemblies (Figure 25).

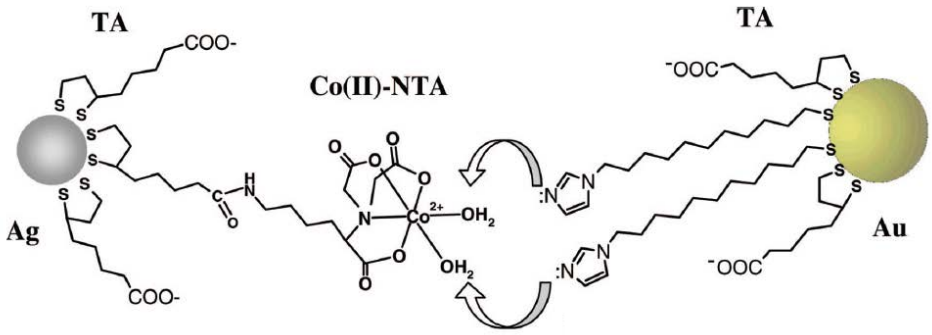

Figure 25. Reaction strategy for assembly of ANTA-Co(II) silver and imidazole modified gold nanoparticles, reproduced from ref. [129].

Hexanethiol-capped palladium nanoparticles (1.9 nm) were functionalized, by a ligand exchange reaction, with alkanethiolate derivatives having free phosphine end-groups [130]. The nanoparticles where then reacted with a series of organometallic complexes: $[PdCl(\eta^3\text{-}2\text{-}MeC_3H_4)]_2$, $[IrCl(cod)]_2$, $[RhCl(cod)]_2$, $[RuCl_2(p\text{-cymene})]_2$ (see Fig. 26). Characterization by ^1H NMR displayed the typical resonances of the allyl, cod and *p*-cymene groups, respectively. In ^{31}P NMR, sharp peaks between 22 and 25 ppm were observed for $PdCl(\eta^3\text{-}2\text{-}MeC_3H_4)$, IrCl(cod) and $RuCl_2$(*p*-cymene) metal fragments after coordination of the phosphine end-group, and a doublet appeared for the RhCl(cod) fragment at 31 ppm. Similarly, $[RhCl(CO)_2]_2$ and $[RhCl(cod)]_2$ with silver triflate, AgOTf, as halide abstractor, were coordinated to the free phosphine group. The ^{31}P NMR spectra of the RhCl(CO) and $RhCl(cod)^+$ (OTf^-) fragments were consistent with a cis disposition of the phosphine ligands coordinated to the Rh centers (see Fig. 26). The Pd nanohybrids were later evaluated as catalysts for C-C coupling,

hydrogenation and hydrovinylation reactions [131]. PdNPs with PdCl(η^3-2-MeC_3H_4) peripheral groups were also used to catalyze the sequential hydrovinylation of 4-bromostyrene followed by C-C Suzuki reaction with phenylboronic acid. The authors concluded that (i) the hydrovinylation is mediated by the PdCl(η^3-2-MeC_3H_4) units and (ii) the Pd core and Pd(0) species (generated by decomposition of Pd(η^3-2-MeC_3H_4) are responsible for the C-C coupling reaction.

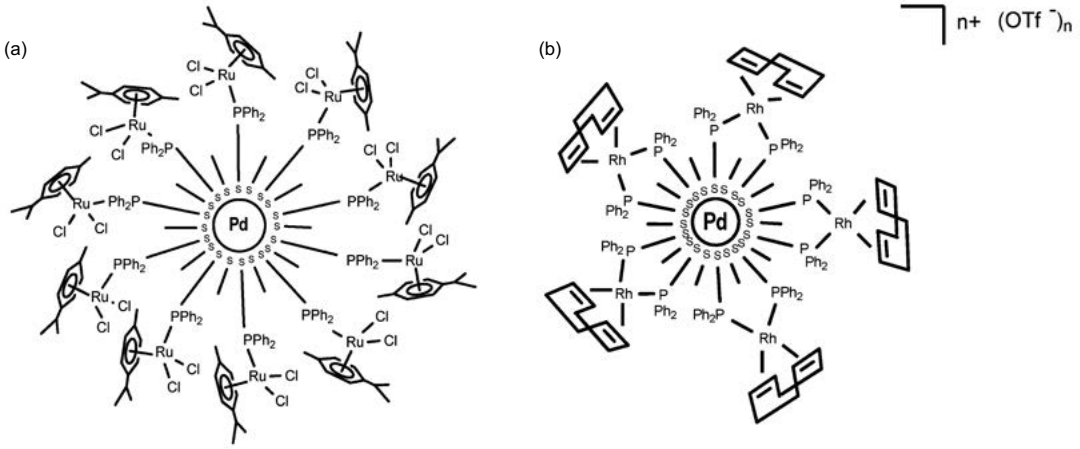

Figure 26. Pd nanoparticles incorporating (a) RuCl(*p*-cymene) and (b) RhCl(cod)$^+$ organometallic surface units, reproduced from ref. [130].

Cobalt nanoparticles (8-13 nm) were synthesized using a mixture of oleic acid and chiral amino alcohol ligands as capping agents, for their application as a magnetically recyclable platform for ruthenium-catalyzed asymmetric hydrogenation of ketones [132]. The hydrogenation transfer of acetophenone performed in the presence of the functionalized Co colloids and $[RuCl_2(p\text{-cymene})]_2$ showed better activities and selectivities than those obtained in the absence of the Co colloid platform in the same reaction conditions. The coordination modes of the Ru(II) centers to the Co colloids are, however, not detailed.

3.2.3. Electrostatic binding of TMCs to MNPs

The interaction between citrate-apped AgNPs (ca. 20 nm) and $[Ru(bpy)_3]^{2+}$ and $[Os(bpy)_3]^{2+}$ was studied by absorption and time-resolved emission measurements [111]. The characteristic absorption bands of each complexes could be observed. Minor shifts on the SPBs of the AgNPs were caused by a slight change in the dielectric function of the silver surface upon absorption of the $[Ru(bpy)_3]^{2+}$ and $[Os(bpy)_3]^{2+}$ complexes. The emission intensity of the $[Ru(bpy)_3]^{2+}$ by the AgNPs is quenched in a more effective way than that of $[Os(bpy)_3]^{2+}$ analogous system.

$[Ru(bpy)_3]^{2+}$ complexes were attached through electrostatic interactions to the carboxylate end groups of 3-mercaptopropionic acid-stabilized AgNPs [133]. The resulting nanohybrid displayed

absorbance peaks characteristic of $[Ru(bpy)_3]^{2+}$ and a moderate SPB of AgNPs at ca. 423 nm. Regarding the emission spectra, a maximum fluorescence is observed at 610 nm for unbound $[Ru(bpy)_3]^{2+}$. This emission is considerably decreased and slightly shifted when the complex is bound to the AgNPs. The nanohybrids were modified by a chitosan coating which could selectively bind salicylic acid molecules with high binding affinities.

As it has been previously described, Astruc and coworkers used ferrocene, and electron and hydride reservoir metallocene complexes, as reductants of $HAuCl_4$ salts and electrostatic stabilizers of the resulting AuNPs [112–114]. Following the same approach, metallocene-stabilized palladium nanoparticles were synthesized by the reduction of K_2PdCl_4 salt in presence of PVP [114] obtaining PdNPs sizes from 3.0 to 3.8 nm (4.7 and 9.1 nm for more bulky complexes). The system synthesized by using the cobaltocene hydride derivative was that displaying better results in the catalytic reduction of 4-nitrophenol by $NaBH_4$, as observed for the gold analogue, and the Suzuki-Miyaura coupling between bromobenzene and phenylboronic acid. Activation of the surface by the hydride reservoir metallocene complexes is believed to induce the better in activities of systems synthesized with hydride reservoir derivatives. Reduction of different silver salts ($AgNO_3$, AgF and $AgBF_4$) by cobaltocene in a water/THF media was also explored (Fig. 27) [134]. While the range of AgNP sizes obtained for the different Ag salts is narrow (3.0 to 3.2 nm), the SPB maxima had different positions, which is attributed to a perturbation of the surface electronic state produced by the interaction with each different anion. In comparison to the metallocene-stabilized Pd and Au nanohybrids earlier described [114], higher rate constants on the catalyzed reduction of 4-nitrophenol by $NaBH_4$ were obtained for the cobalticinium-stabilized AgNPs, especially those with F^- counteranions.

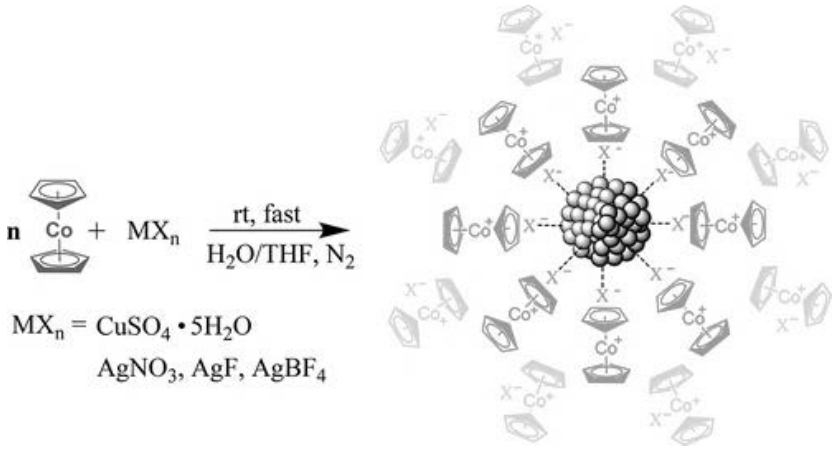

Figure 27. Synthesis of CuNPs and AgNPs by reaction of $CuSO_4 \cdot 5H_2O$ or Ag salt with cobaltocene, reproduced from ref. [134]. For CuNPs, n = 2; for AgNPs, n = 1 and MX_n = AgX (X = NO_3, F, BF_4).

Likewise, $CuSO_4 \cdot 5H_2O$ was reduced by cobaltocene (Fig. 26) [134]. By UV-vis spectroscopy, no SPB is observed for the resulting CuNPs (too small particle size, 1.7 nm) but a broad absorption band at 397 nm is attributed to cobalticinium species. Some SO_4^- anions are believed to establish weak L-type interactions with the Cu surface and the rest remain in electrostatic interaction with the cobalticinium cations, forming a stabilizing network. The hybrid CuNPs is an efficient catalyst for the Cu-catalyzed alkyne-azide cycloaddition reaction with water insoluble substrates. In a similar way, rhodium nanoparticles were prepared by reduction of $RhCl_3$ with cobaltocene [135]. The resulting cobalticinium chloride-stabilized RhNPs (1.3 nm) catalyzed the transfer hydrogenation of nitrobenzene with *i*-propanol, the hydrolysis of ammonia borane and the benzene hydrogenation to cyclohexane with good efficiencies.

3.2.4. Miscellaneous TMC-MNPs hybrid systems

In an uncommon example [136], a Pd-NHC complex (NHC = N-heterocyclic carbene) was reversibly immobilized on graphene-coated CoNPs (Fig. 28) for the hydroxycarbonylation of aryl halides. The Pd-NHC complex bears pendant pyrene groups that readily establish temperature dependent π-π interactions with the graphene layer, in water. At high temperatures (100 °C), desorption of the Pd-NHC catalyst from the surface occurs and they are easily re-adsorbed on the graphene-CoNPs after the catalytic reaction by cooling down, thus allowing facile catalyst separation.

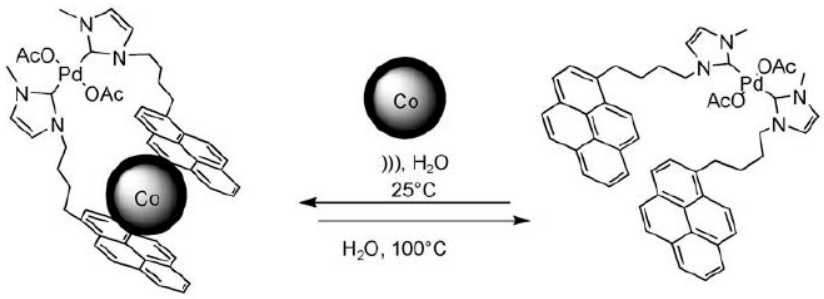

Figure 28. Scheme of the reversible immobilization of the pyrene-tagged Pd-NHC complex on carbon-coated CoNPs, reproduced from ref. [136].

Following a ligand-exchange strategy, the surface of magnetic Fe-Pt nanoparticles was modified with a Mn(II) tricarbonyl complex [137]. An hexane solution of Fe-Pt NPs stabilized by oleylamine and oleic acid was treated with a solution of [(η^6-hydroquinone)-$Mn(CO)_3$]BF_4 in DMSO. Deprotonation of the hydroquinone group by the oleylamine, followed by decoordination of the generated oleylammonium salt, liberates surface sites that are then free for the coordination of the resulting [(η^5-semiquinone)$Mn(CO)_3$] *via* a quinone oxygen atom. After the ligand-exchange reaction, oleylammonium molecules might remain in interaction with the alkyl chains of oleic acid, and the Fe-Pt

surface-modified assembly is soluble in DMSO. The coordination of the Mn(II) complex was followed by FT-IR spectroscopy. The tricarbonyl stretches of the [(η^5-semiquinone)$Mn(CO)_3$] (originally at 2066 and 1967 cm^{-1}) were observed at 2041 and 1966 cm^{-1} for the bound complex. Comparing these results with those obtained for the same complex coordinated to the surface of Fe_3O_4 NPs (2047 and 1977 cm^{-1}), it was assumed that the [(η^5-semiquinone)$Mn(CO)_3$] complex was interacting with the Pt surface atoms in the case of the FePt NPs.

As previously described for gold [83], ruthenium dyes were also coordinated to the surface of silver nanoparticles in different solvents. It was observed, by Raman techniques, that the nature of the solvent (hydrogen bond acceptor, hydrogen bond donor, or both) influenced the coordination through isocyanate or carboxylate groups of the dyes. In acetonitrile, a strong and shifted thiocyanate band indicates that the coordination of the dye to the silver surface takes place through this group. In water and in ethanol, the dye can also bind through the COO^- groups.

4. Conclusions

A literature survey dedicated to the building of nanohybrids by the association of transition metal complexes and metal nanoparticles, named as TMC-MNPs, has been reported in this Chapter, from the first reports published in the late 90s until now. As illustrated all along this chapter, up to now, this domain of research has been largely dominated by gold nanoparticles. The main reasons for this development are (i) the chemical stability of AuNPs and their straightforward preparation, but also (ii) their remarkable optical properties which can find applications in domains such as sensing and non-linear optics. For similar interests, but to a lesser extent, several reports also describe the assembly of transition metal complexes and silver nanoparticles. Only a few examples describe the preparation of nanohybrids which associate cobalt, palladium, rhodium, cupper and iron-platinum nanoparticles and transition metals complexes.

Among all the hybrid nanomaterials TMC-MNPs reported to date, we were able to distinguish four different strategies for the assembly of TMCs and MNPs, and to classify them accordingly:

(a) grafting of the TMCs at the MNPs surface *via* pendant anchoring groups on the TMCs

(b) complexation of the TMCs at the MNPs surface *via* pendant anchoring groups on the MNPs stabilizing layer

(c) association of the two components, MNPs and TMCs, through electrostatic interaction

(d) miscellaneous systems (e.g. π-pi-stacking, host-guest interactions)

Association of the two components by means of pendant ligands, from either the MNPs or the TMCs, is by far the strategy most widely reported in the literature. In such way, the transition metal centers in the respective complexes and the metal surface of MNPs are connected to each other *via* organic spacers of various lengths to form the corresponding hybrid nanomaterial TMCs-MNPs.

Interestingly, association of TMCs and MNPs has been achieved with the use of the ambidentate NCS ligands originally incorporated in the coordination sphere of the TMCs. Therefore, a three-atom linker bridges the surface of the AuNP and the TMC.

Hybrid nanomaterials resulting from the assembly of TMCs and MNPs bring together the chemical and/or physical properties of the TMCs and those of the MNPs. As mentioned in the references cited, these nanohybrid structures display innovative properties that can be exploited in the field of biomedicine, electronics, sensing and catalysis.

In the following chapter, the synthesis and characterization of an unprecedented hybrid nanomaterial, made by organophosphorus Ru(II)-polypyridyl complexes and RuNPs will be described. This work has been developed on the basis of expertise in the chemistry of main group elements, in transition metal chemistry and nanochemistry, present in our group.

5. References

1. *Nanotechnology*; Schmid, G., Ed.; Wiley-VCH: Weinheim, 2008; ISBN 978-3-527-31732-5.

2. De bruyn, M.; Neumann, R. Stabilization of Palladium Nanoparticles by Polyoxometalates Appended with Alkylthiol Tethers and their Use as Binary Catalysts for Liquid Phase Aerobic Oxydehydrogenation. *Adv. Synth. Catal.* **2007**, *349*, 1624–1628.

3. Martín, S.; Takashima, Y.; Lin, C.-G.; Song, Y.-F.; Miras, H.N.; Cronin, L. Integrated Synthesis of Gold Nanoparticles Coated with Polyoxometalate Clusters. *Inorg. Chem.* **2019**, *58*, 4110–4116.

4. Abo-Hamed, E.K.; Pennycook, T.; Vaynzof, Y.; Toprakcioglu, C.; Koutsioubas, A.; Scherman, O.A. Highly Active Metastable Ruthenium Nanoparticles for Hydrogen Production through the Catalytic Hydrolysis of Ammonia Borane. *Small* **2014**, *10*, 3145–3152.

5. Synthesis, Characterization, and Applications of Zero-Dimensional (0D) Nanostructures. In *Synthesis and Applications of Inorganic Nanostructures*; John Wiley & Sons, Ltd, 2017; pp. 21–146 ISBN 978-3-527-69815-8.

6. Buffat, Ph.; Borel, J.-P. Size effect on the melting temperature of gold particles. *Phys. Rev. A* **1976**, *13*, 2287–2298.

7. Lai, S.L.; Guo, J.Y.; Petrova, V.; Ramanath, G.; Allen, L.H. Size-Dependent Melting Properties of Small Tin Particles: Nanocalorimetric Measurements. *Phys. Rev. Lett.* **1996**, *77*, 99–102.

8. *Nanoscale materials in chemistry*; Klabunde, K.J., Richards, R., Eds.; 2nd ed.; Wiley: Hoboken, N.J, 2009; ISBN 978-0-470-22270-6.

9. *Nanomaterials: an introduction to synthesis, properties and application*; Vollath, D.; Wiley-VCH: Weinheim, 2008; ISBN 978-3-527-31531-4.

10. Philippot, K.; Serp, P. Concepts in Nanocatalysis. In *Nanomaterials in Catalysis*; John Wiley & Sons, Ltd, 2012; pp. 1–54 ISBN 978-3-527-65687-5.

11. Fecht, H.J.; Hellstern, E.; Fu, Z.; Johnson, W.L. Nanocrystalline metals prepared by high-energy ball milling. *Metall. Trans. A*. **1990**, *21*, 2333-2337.

12. Le-The, H.; Berenschot, E.; Tiggelaar, R.M.; Tas, N.R.; van den Berg, A.; Eijkel, J.C.T. Large-scale fabrication of highly ordered sub-20 nm noble metal nanoparticles on silica substrates without metallic adhesion layers. *Microsyst. Nanoeng.* **2018**, *4*:4.

13. Park, J.; Joo, J.; Kwon, S.G.; Jang, Y.; Hyeon, T. Synthesis of Monodisperse Spherical Nanocrystals. *Angew. Chem. Int. Ed.* **2007**, *46*, 4630–4660.

14. Cushing, B.L.; Kolesnichenko, V.L.; O'Connor, C.J. Recent Advances in the Liquid-Phase Syntheses of Inorganic Nanoparticles. *Chem. Rev.* **2004**, *104*, 3893–3946.

15. Roucoux, A.; Schulz, J.; Patin, H. Reduced Transition Metal Colloids: A Novel Family of Reusable Catalysts? *Chem. Rev.* **2002**, *102*, 3757–3778.

16. Aiken, J.D.; Finke, R.G. A review of modern transition-metal nanoclusters: their synthesis, characterization, and applications in catalysis. *J. Mol. Catal. Chem.* **1999**, *145*, 1–44.

17. Amiens, C.; Chaudret, B.; Ciuculescu-Pradines, D.; Collière, V.; Fajerwerg, K.; Fau, P.; Kahn, M.; Maisonnat, A.; Soulantica, K.; Philippot, K. Organometallic approach for the synthesis of nanostructures. *New J. Chem.* **2013**, *37*, 3374.

18. Philippot, K.; Chaudret, B. Organometallic approach to the synthesis and surface reactivity of noble metal nanoparticles. *Comptes Rendus Chim.* **2003**, *6*, 1019–1034.

19. Niu, Z.; Li, Y. Removal and Utilization of Capping Agents in Nanocatalysis. *Chem. Mater.* **2014**, *26*, 72–83.

20. Astruc, D.; Lu, F.; Aranzaes, J.R. Nanoparticles as Recyclable Catalysts: The Frontier between Homogeneous and Heterogeneous Catalysis. *Angew. Chem. Int. Ed.* **2005**, *44*, 7852–7872.

21. Ibrahim, M.; Garcia, M.A.S.; Vono, L.L.R.; Guerrero, M.; Lecante, P.; Rossi, L.M.; Philippot, K. Polymer versus phosphine stabilized Rh nanoparticles as components of supported catalysts: implication in the hydrogenation of cyclohexene model molecule. *Dalton Trans.* **2016**, *45*, 17782–17791.

22. Turkevich, J.; Stevenson, P.C.; Hillier, J. A study of the nucleation and growth processes in the synthesis of colloidal gold. *Discuss. Faraday Soc.* **1951**, *11*, 55–75.

23. Özkar, S.; Finke, R.G. Nanocluster Formation and Stabilization Fundamental Studies: Ranking Commonly Employed Anionic Stabilizers *via* the Development, Then Application, of Five Comparative Criteria. *J. Am. Chem. Soc.* **2002**, *124*, 5796–5810.

24. Denicourt-Nowicki, A.; Roucoux, A. Odyssey in Polyphasic Catalysis by Metal Nanoparticles. *The Chemical Record* **2016**, *16*, 2127–2141.

25. *Nanocatalysis in Ionic Liquids*; Prechtl, M.H.G., Ed.; Wiley-VCH Verlag GmbH & Co. KGaA: Weinheim, Germany, 2016; ISBN 978-3-527-69328-3.

26. Prechtl, M.H.G.; Campbell, P.S.; Scholten, J.D.; Fraser, G.B.; Machado, G.; Santini, C.C.; Dupont, J.; Chauvin, Y. Imidazolium ionic liquids as promoters and stabilising agents for the preparation of metal(0) nanoparticles by reduction and decomposition of organometallic complexes. *Nanoscale* **2010**, *2*, 2601-2606.

27. Lara, P.; Philippot, K.; Chaudret, B. Organometallic Ruthenium Nanoparticles: A Comparative Study of the Influence of the Stabilizer on their Characteristics and Reactivity. *ChemCatChem.* **2013**, *5*, 28–45.

28. Pelzer, K.; Vidoni, O.; Philippot, K.; Chaudret, B.; Collière, V. Organometallic Synthesis of Size-Controlled Polycrystalline Ruthenium Nanoparticles in the Presence of Alcohols. *Adv. Funct. Mater.* **2003**, *13*, 118–126.

29. Nasar, K.; Fache, F.; Lemaire, M.; Béziat, J.-C.; Besson, M.; Gallezot, P. Stereoselective reduction of disubstituted aromatics on colloidal rhodium. *J. Mol. Catal.* **1994**, *87*, 107–115.

30. Bönnemann, H.; Braun, G.A. Enantioselectivity Control with Metal Colloids as Catalysts. *Chem. – Eur. J.* **1997**, *3*, 1200–1202.

31. Debouttière, P.-J.; Martinez, V.; Philippot, K.; Chaudret, B. An organometallic approach for the synthesis of water-soluble ruthenium and platinum nanoparticles. *Dalton Trans.* **2009**, 10172-10174.

32. Bartz, M.; Küther, J.; Seshadri, R.; Tremel, W. Colloid-Bound Catalysts for Ring-Opening Metathesis Polymerization: A Combination of Homogenous and Heterogeneous Properties. *Angew. Chem. Int. Ed.* **1998**, *37*, 2466–2468.

33. Daniel, M.-C.; Astruc, D. Gold Nanoparticles: Assembly, Supramolecular Chemistry, Quantum-Size-Related Properties, and Applications toward Biology, Catalysis, and Nanotechnology. *Chem. Rev.* **2004**, *104*, 293–346.

34. Yeh, Y.-C.; Creran, B.; Rotello, V.M. Gold nanoparticles: preparation, properties, and applications in bionanotechnology. *Nanoscale* **2012**, *4*, 1871–1880.

35. Nunes, F.S.; Bonifácio, L.D.S.; Araki, K.; Toma, H.E. Interaction of 2- and 4-Mercaptopyridine with Pentacyanoferrates and Gold Nanoparticles. *Inorg. Chem.* **2006**, *45*, 94–101.

36. Leung, F.C.-M.; Au, V.K.-M.; Song, H.-O.; Yam, V.W.-W. Dual Esterase- and Steroid-Responsive Energy Transfer Modulation of Ruthenium(II) and Rhenium(I) Complex Functionalized Gold Nanoparticles. *Chem. - Eur. J.* **2015**, *21*, 16448–16454.

37. Zhao, P.; Li, N.; Astruc, D. State of the art in gold nanoparticle synthesis. *Coord. Chem. Rev.* **2013**, *257*, 638–665.

38. Brust, M.; Walker, M.; Bethell, D.; Schiffrin, D.J.; Whyman, R. Synthesis of thiol-derivatised gold nanoparticles in a two-phase Liquid–Liquid system. *J. Chem. Soc. Chem. Commun.* **1994**, *0*, 801–802.

39. Liz-Marzán, L.M. Gold nanoparticle research before and after the Brust–Schiffrin method. *Chem Commun* **2013**, *49*, 16–18.

40. Häkkinen, H. The gold–sulfur interface at the nanoscale. *Nat. Chem.* **2012**, *4*, 443–455.

41. Wilton-Ely, J.D.E.T. The surface functionalisation of gold nanoparticles with metal complexes. *Dalton Trans.* **2008**, 25–29.

42. Kuwahara, Y.; Akiyama, T.; Yamada, S. Facile Fabrication of Photoelectrochemical Assemblies Consisting of Gold Nanoparticles and a Tris(2,2‘-bipyridine)ruthenium(II)–Viologen Linked Thiol. *Langmuir* **2001**, *17*, 5714–5716.

43. Pramod, P.; Sudeep, P.K.; Thomas, K.G.; Kamat, P.V. Photochemistry of Ruthenium Trisbipyridine Functionalized on Gold Nanoparticles. *J. Phys. Chem. B* **2006**, *110*, 20737–20741.

44. Elmes, R.B.P.; Orange, K.N.; Cloonan, S.M.; Williams, D.C.; Gunnlaugsson, T. Luminescent Ruthenium(II) Polypyridyl Functionalized Gold Nanoparticles; Their DNA Binding Abilities and Application As Cellular Imaging Agents. *J. Am. Chem. Soc.* **2011**, *133*, 15862–15865.

45. Martínez-Calvo, M.; Orange, K.N.; Elmes, R.B.P.; Poulsen, B. la C.; Williams, D.C.; Gunnlaugsson, T. Ru(II)-polypyridyl surface functionalised gold nanoparticles as DNA targeting supramolecular structures and luminescent cellular imaging agents. *Nanoscale* **2015**, *8*, 563–574.

46. Rogers, N.J.; Claire, S.; Harris, R.M.; Farabi, S.; Zikeli, G.; Styles, I.B.; Hodges, N.J.; Pikramenou, Z. High coating of Ru(II) complexes on gold nanoparticles for single particle luminescence imaging in cells. *Chem Commun.* **2014**, *50*, 617–619.

47. M. Díaz-García, A.; Fernández-Oliva, M.; Ortiz, M.; Cao, R. Interaction of nitric oxide with gold nanoparticles capped with a ruthenium(II) complex. *Dalton Trans.* **2009**, *0*, 7870–7872.

48. Vilvamani, N.; Chhatwal, M.; Bhowmick, I.; Gupta, R.D.; Awasthi, S.K. Gold nanocomposite assemblies using functionalized Ru(II)-polypyridyl complexes. *RSC Adv.* **2016**, *6*, 55507–55513.

49. Moreau, J.; Lux, F.; Four, M.; Olesiak-Banska, J.; Matczyszyn, K.; Perriat, P.; Frochot, C.; Arnoux, P.; Tillement, O.; Samoc, M.; et al. A 5-(difluorenyl)-1,10-phenanthroline-based Ru(II) complex as a coating agent for potential multifunctional gold nanoparticles. *Phys. Chem. Chem. Phys.* **2014**, *16*, 14826–14833.

50. Leung, F.C.-M.; Tam, A.Y.-Y.; Au, V.K.-M.; Li, M.-J.; Yam, V.W.-W. Förster Resonance Energy Transfer Studies of Luminescent Gold Nanoparticles Functionalized with Ruthenium(II) and Rhenium(I) Complexes: Modulation *via* Esterase Hydrolysis. *ACS Appl. Mater. Interfaces* **2014**, *6*, 6644–6653.

51. Robson, J.A.; Gonzàlez de Rivera, F.; Jantan, K.A.; Wenzel, M.N.; White, A.J.P.; Rossell, O.; Wilton-Ely, J.D.E.T. Bifunctional Chalcogen Linkers for the Stepwise Generation of Multimetallic Assemblies and Functionalized Nanoparticles. *Inorg. Chem.* **2016**, *55*, 12982–12996.

52. Vickers, M.S.; Cookson, J.; Beer, P.D.; Bishop, P.T.; Thiebaut, B. Dithiocarbamate ligand stabilised gold nanoparticles. *J Mater. Chem.* **2006**, *16*, 209–215.

53. Knight, E.R.; Cowley, A.R.; Hogarth, G.; Wilton-Ely, J.D.E.T. Bifunctional dithiocarbamates: a bridge between coordination chemistry and nanoscale materials. *Dalton Trans.* **2009**, 607–609.

54. Knight, E.R.; Leung, N.H.; Lin, Y.H.; Cowley, A.R.; Watkin, D.J.; Thompson, A.L.; Hogarth, G.; Wilton-Ely, J.D.E.T. Multimetallic arrays: Symmetrical bi-, tri- and tetrametallic complexes based on the group 10 metals and the functionalisation of gold nanoparticles with nickel-phosphine surface units. *Dalton Trans.* **2009**, 3688-3697.

55. Nasr, G.; Guerlin, A.; Dumur, F.; Baudron, S.A.; Dumas, E.; Miomandre, F.; Clavier, G.; Sliwa, M.; Mayer, C.R. Dithiolate-Appended Iridium(III) Complex with Dual Functions of Reducing and Capping Agent for the Design of Small-Sized Gold Nanoparticles. *J. Am. Chem. Soc.* **2011**, *133*, 6501–6504.

56. Hallett, A.J.; Christian, P.; Jones, J.E.; Pope, S.J.A. Luminescent, water-soluble gold nanoparticles functionalised with ^{3}MLCT emitting rhenium complexes. *Chem. Commun.* **2009**, 4278–4280.

57. Li, M.-J.; Liu, X.; Nie, M.-J.; Wu, Z.-Z.; Yi, C.-Q.; Chen, G.-N.; Yam, V.W.-W. New Rhenium(I) Complexes: Synthesis, Photophysics, Cytotoxicity, and Functionalization of Gold Nanoparticles for Sensing of Esterase. *Organometallics* **2012**, *31*, 4459–4466.

58. Belser, T.; Stöhr, M.; Pfaltz, A. Immobilization of Rhodium Complexes at Thiolate Monolayers on Gold Surfaces: Catalytic and Structural Studies. *J. Am. Chem. Soc.* **2005**, *127*, 8720–8731.

59. Lewis, D.J.; Day, T.M.; MacPherson, J.V.; Pikramenou, Z. Luminescent nanobeads: attachment of surface reactive Eu(III) complexes to gold nanoparticles. *Chem. Commun.* **2006**, 1433.

60. Massue, J.; Quinn, S.J.; Gunnlaugsson, T. Lanthanide Luminescent Displacement Assays: The Sensing of Phosphate Anions Using Eu(III)−Cyclen-Conjugated Gold Nanoparticles in Aqueous Solution. *J. Am. Chem. Soc.* **2008**, *130*, 6900–6901.

61. Chabloz, N.G.; Wenzel, M.N.; Perry, H.L.; Yoon, I.; Molisso, S.; Stasiuk, G.J.; Elson, D.S.; Cass, A.E.G.; Wilton-Ely, J.D.E.T. Polyfunctionalised Nanoparticles Bearing Robust Gadolinium Surface Units for High Relaxivity Performance in MRI. *Chem. – Eur. J.* **2019**, *25*, 10895–10906.

62. Beer, P.D.; Cormode, D.P.; Davis, J.J. Zinc metalloporphyrin-functionalised nanoparticle anion sensors. *Chem. Commun.* **2004**, 414-415.

63. Hone, D.C.; Walker, P.I.; Evans-Gowing, R.; FitzGerald, S.; Beeby, A.; Chambrier, I.; Cook, M.J.; Russell, D.A. Generation of Cytotoxic Singlet Oxygen *via* Phthalocyanine-Stabilized Gold Nanoparticles: A Potential Delivery Vehicle for Photodynamic Therapy. *Langmuir* **2002**, *18*, 2985–2987.

64. Toma, S.H.; Bonacin, J.A.; Araki, K.; Toma, H.E. Controlled Stabilization and Flocculation of Gold Nanoparticles by Means of 2-Pyrazin-2-ylethanethiol and Pentacyanidoferrate(II) Complexes. *Eur. J. Inorg. Chem.* **2007**, *2007*, 3356–3364.

65. Astruc, D. Why is Ferrocene so Exceptional? *Eur. J. Inorg. Chem.* **2017**, *2017*, 6–29.

66. Hostetler, M.J.; Green, S.J.; Stokes, J.J.; Murray, R.W. Monolayers in Three Dimensions: Synthesis and Electrochemistry of ω-Functionalized Alkanethiolate-Stabilized Gold Cluster Compounds. *J. Am. Chem. Soc.* **1996**, *118*, 4212–4213.

67. Ingram, R.S.; Hostetler, M.J.; Murray, R.W. Poly-hetero-ω-functionalized Alkanethiolate-Stabilized Gold Cluster Compounds. *J. Am. Chem. Soc.* **1997**, *119*, 9175–9178.

68. Horikoshi, T.; Itoh, M.; Kurihara, M.; Kubo, K.; Nishihara, H. Synthesis, redox behavior and electrodeposition of biferrocene-modified gold clusters. *J. Electroanal. Chem.* **1999**, *473*, 113–116.

69. Yamada, M.; Nishihara, H. Electrochemical construction of an alternating multi-layered structure of palladium and gold nanoparticles attached with biferrocene moieties. *Chem. Commun.* **2002**, 2578–2579.

70. Yamada, M.; Nishihara, H. Electrodeposition of Biferrocene Derivative-Attached Gold Nanoparticles: Solvent Effects and Lithographic Assembly. *Langmuir* **2003**, *19*, 8050–8056.

71. Wang, J.; Li, J.; Baca, A.J.; Hu, J.; Zhou, F.; Yan, W.; Pang, D.-W. Amplified Voltammetric Detection of DNA Hybridization *via* Oxidation of Ferrocene Caps on Gold Nanoparticle/Streptavidin Conjugates. *Anal. Chem.* **2003**, *75*, 3941–3945.

72. Wolfe, R.L.; Balasubramanian, R.; Tracy, J.B.; Murray, R.W. Fully Ferrocenated Hexanethiolate Monolayer-Protected Gold Clusters. *Langmuir* **2007**, *23*, 2247–2254.

73. Dong, T.-Y.; Shih, H.-W.; Chang, L.-S. Synthesis and Redox Behavior of Biferrocenyl-Functionalized Ruthenium(II) Terpyridine Gold Clusters. *Langmuir* **2004**, *20*, 9340–9347.

74. Labande, A.; Astruc, D. Colloids as redox sensors: recognition of $H_2PO_4^-$ and HSO_4^- by amidoferrocenylalkylthiol–gold nanoparticles. *Chem. Commun.* **2000**, 1007–1008.

75. Labande, A.; Ruiz, J.; Astruc, D. Supramolecular Gold Nanoparticles for the Redox Recognition of Oxoanions: Syntheses, Titrations, Stereoelectronic Effects, and Selectivity. *J. Am. Chem. Soc.* **2002**, *124*, 1782–1789.

76. Daniel, M.-C.; Ruiz, J.; Nlate, S.; Palumbo, J.; Astruc, D.; Blais, J.-C. Gold nanoparticles containing redox-active supramolecular dendrons that recognize $H_2PO_4^-$. *Chem. Commun.* **2001**, 2000–2001.

77. Daniel, M.-C.; Ruiz, J.; Nlate, S.; Blais, J.-C.; Astruc, D. Nanoscopic Assemblies between Supramolecular Redox Active Metallodendrons and Gold Nanoparticles: Synthesis, Characterization, and Selective Recognition of $H_2PO_4^-$, HSO_4^-, and Adenosine-5'-Triphosphate (ATP^{2-}) Anions. *J. Am. Chem. Soc.* **2003**, *125*, 2617–2628.

78. Astruc, D.; Daniel, M.-C.; Ruiz, J. Dendrimers and gold nanoparticles as exo-receptors sensing biologically important anions. *Chem. Commun.* **2004**, 2637-2649.

79. Mayer, C.R.; Dumas, E.; Miomandre, F.; Méallet-Renault, R.; Warmont, F.; Vigneron, J.; Pansu, R.; Etcheberry, A.; Sécheresse, F. Polypyridyl ruthenium complexes as coating agent for the formation of gold and silver nanocomposites in different media. Preliminary luminescence and electrochemical studies. *New J. Chem.* **2006**, *30*, 1628–1637.

80. Mayer, C.R.; Dumas, E.; Sécheresse, F. 1,10-Phenanthroline and 1,10-phenanthroline-terminated ruthenium(II) complex as efficient capping agents to stabilize gold nanoparticles: Application for reversible aqueous–organic phase transfer processes. *J. Colloid Interface Sci.* **2008**, *328*, 452–457.

81. Miomandre, F.; Stancheva, S.; Audibert, J.-F.; Brosseau, A.; Pansu, R.B.; Lepeltier, M.; Mayer, C.R. Gold and Silver Nanoparticles Functionalized by Luminescent Iridium Complexes: Synthesis and Photophysical and Electrofluorochromic Properties. *J. Phys. Chem. C* **2013**, *117*, 12806–12814.

82. Zedler, L.; Theil, F.; Csáki, A.; Fritzsche, W.; Rau, S.; Schmitt, M.; Popp, J.; Dietzek, B. Ruthenium dye functionalized gold nanoparticles and their spectral responses. *RSC Adv.* **2012**, *2*, 4463-4471.

83. Pérez León, C.; Kador, L.; Peng, B.; Thelakkat, M. Influence of the Solvent on the Surface-Enhanced Raman Spectra of Ruthenium(II) Bipyridyl Complexes. *J. Phys. Chem. B* **2005**, *109*, 5783–5789.

84. Yu, Y.; Zhou, M.; Cui, H. Synthesis and electrochemiluminescence of bis(2,2′-bipyridine)(5-amino-1,10-phenanthroline) ruthenium(II)-functionalized gold nanoparticles. *J. Mater. Chem.* **2011**, *21*, 12622-12625.

85. Li, N.; Binder, W.H. Click-chemistry for nanoparticle-modification. *J. Mater. Chem.* **2011**, *21*, 16717-16734.

86. Marubayashi, K.; Takizawa, S.; Kawakusu, T.; Arai, T.; Sasai, H. Monolayer-Protected Au Cluster (MPC)-Supported Ti–BINOLate Complex. *Org. Lett.* **2003**, *5*, 4409–4412.

87. Ono, F.; Kanemasa, S.; Tanaka, J. Reusable nano-sized chiral bisoxazoline catalysts. *Tetrahedron Lett.* **2005**, *46*, 7623–7626.

88. Belser, T.; Jacobsen, E.N. Cooperative Catalysis in the Hydrolytic Kinetic Resolution of Epoxides by Chiral [(salen)Co(III)] Complexes Immobilized on Gold Colloids. *Adv. Synth. Catal.* **2008**, *350*, 967–971.

89. Bin-Salamon, S.; Brewer, S.; Franzen, S.; Feldheim, D.L.; Lappi, S.; Shultz, D.A. Supramolecular Control of Valence-Tautomeric Equilibrium on Nanometer-Scale Gold Clusters. *J. Am. Chem. Soc.* **2005**, *127*, 5328–5329.

90. Bonomi, R.; Selvestrel, F.; Lombardo, V.; Sissi, C.; Polizzi, S.; Mancin, F.; Tonellato, U.; Scrimin, P. Phosphate Diester and DNA Hydrolysis by a Multivalent, Nanoparticle-Based Catalyst. *J. Am. Chem. Soc.* **2008**, *130*, 15744–15745.

91. Gonzàlez de Rivera, F.; Angurell, I.; Rossell, O.; Seco, M.; Llorca, J. Organometallic surface functionalization of gold nanoparticles. *J. Organomet. Chem.* **2012**, *715*, 13–18.

92. Sheet, D.; Halder, P.; Paine, T.K. Enhanced Reactivity of a Biomimetic Iron(II) α-Keto Acid Complex through Immobilization on Functionalized Gold Nanoparticles. *Angew. Chem. Int. Ed.* **2013**, *52*, 13314–13318.

93. Fritz, E.-C.; Nimphius, C.; Goez, A.; Würtz, S.; Peterlechner, M.; Neugebauer, J.; Glorius, F.; Ravoo, B.J. Sequential Surface Modification of Au Nanoparticles: From Surface-Bound Ag^{I} Complexes to Ag^{0} Doping. *Chem. - Eur. J.* **2015**, *21*, 4541–4545.

94. Pérez-Mirabet, L.; Surinyach, S.; Ros, J.; Suades, J.; Yáñez, R. Gold and silver nanoparticles surface functionalized with rhenium carbonyl complexes. *Mater. Chem. Phys.* **2012**, *137*, 439–447.

95. Wang, S.; Sim, W.-S. Au Nanoparticles Encapsulated in Ru Carbonyl Carboxylate Shells. *Langmuir* **2006**, *22*, 7861–7866.

96. Abad, J.M.; Mertens, S.F.L.; Pita, M.; Fernández, V.M.; Schiffrin, D.J. Functionalization of Thioctic Acid-Capped Gold Nanoparticles for Specific Immobilization of Histidine-Tagged Proteins. *J. Am. Chem. Soc.* **2005**, *127*, 5689–5694.

97. Sung, S.; Holmes, H.; Wainwright, L.; Toscani, A.; Stasiuk, G.J.; White, A.J.P.; Bell, J.D.; Wilton-Ely, J.D.E.T. Multimetallic Complexes and Functionalized Gold Nanoparticles Based on a Combination of d- and f-Elements. *Inorg. Chem.* **2014**, *53*, 1989–2005.

98. Mayer, C.R.; Cucchiaro, G.; Jullien, J.; Dumur, F.; Marrot, J.; Dumas, E.; Sécheresse, F. Functionalization of Gold Nanoparticles by Iron(III) Complexes Derived from Schiff Base Ligands. *Eur. J. Inorg. Chem.* **2008**, *2008*, 3614–3623.

99. Ito, M.; Tsukatani, T.; Fujihara, H. Preparation and characterization of gold nanoparticles with a ruthenium-terpyridyl complex, and electropolymerization of their pyrrole-modified metal nanocomposites. *J. Mater. Chem.* **2005**, *15*, 960-964.

100. Mayer, C.R.; Dumas, E.; Michel, A.; Sécheresse, F. Gold nanocomposites with rigid fully conjugated heteroditopic ligands shell as nanobuilding blocks for coordination chemistry. *Chem. Commun.* **2006**, 4183–4185.

101. Zhang, X.; Li, D.; Zhou, X.-P. From large 3D assembly to highly dispersed spherical assembly: weak and strong coordination mediated self-aggregation of Au colloids. *New J. Chem.* **2006**, *30*, 706.

102. Selvakannan, P.R.; Dumas, E.; Dumur, F.; Péchoux, C.; Beaunier, P.; Etcheberry, A.; Sécheresse, F.; Remita, H.; Mayer, C.R. Coordination chemistry approach for the end-to-end assembly of gold nanorods. *J. Colloid. Interface Sci.* **2010**, *349*, 93–97.

103. Montalti, M.; Prodi, L.; Zaccheroni, N.; Beltrame, M.; Morotti, T.; Quici, S. Stabilization of terpyridine covered gold nanoparticles by metal ions complexation. *New J. Chem.* **2007**, *31*, 102–108.

104. Norsten, T.B.; Frankamp, B.L.; Rotello, V.M. Metal Directed Assembly of Terpyridine-Functionalized Gold Nanoparticles. *Nano Lett.* **2002**, *2*, 1345–1348.

105. Lin, S.-Y.; Liu, S.-W.; Lin, C.-M.; Chen, C. Recognition of Potassium Ion in Water by 15-Crown-5 Functionalized Gold Nanoparticles. *Anal. Chem.* **2002**, *74*, 330–335.

106. Kim, Y.; Johnson, R.C.; Hupp, J.T. Gold Nanoparticle-Based Sensing of "Spectroscopically Silent" Heavy Metal Ions. *Nano Lett.* **2001**, *1*, 165–167.

107. Ipe, B.I.; Yoosaf, K.; Thomas, K.G. Functionalized Gold Nanoparticles as Phosphorescent Nanomaterials and Sensors. *J. Am. Chem. Soc.* **2006**, *128*, 1907–1913.

108. Beloglazkina, E.K.; Majouga, A.G.; Romashkina, R.B.; Zyk, N.V.; Zefirov, N.S. Gold nanoparticles modified with coordination compounds of metals: synthesis and application. *Russ. Chem. Rev.* **2012**, *81*, 65–90.

109. Huang, T.; Murray, R.W. Quenching of $[Ru(bpy)_3]^{2+}$ Fluorescence by Binding to Au Nanoparticles. *Langmuir* **2002**, *18*, 7077–7081.

110. Cheng, P.P.H.; Silvester, D.; Wang, G.; Kalyuzhny, G.; Douglas, A.; Murray, R.W. Dynamic and Static Quenching of Fluorescence by 1–4 nm Diameter Gold Monolayer-Protected Clusters. *J. Phys. Chem. B* **2006**, *110*, 4637–4644.

111. Glomm, W.R.; Moses, S.J.; Brennaman, M.K.; Papanikolas, J.M.; Franzen, S. Detection of Adsorption of Ru(II) and Os(II) Polypyridyl Complexes on Gold and Silver Nanoparticles by Single-Photon Counting Emission Measurements. *J. Phys. Chem. B* **2005**, *109*, 804–810.

112. Ciganda, R.; Irigoyen, J.; Gregurec, D.; Hernández, R.; Moya, S.; Wang, C.; Ruiz, J.; Astruc, D. Liquid–Liquid Interfacial Electron Transfer from Ferrocene to Gold(III): An Ultrasimple and Ultrafast Gold Nanoparticle Synthesis in Water under Ambient Conditions. *Inorg. Chem.* **2016**, *55*, 6361–6363.

113. Ciganda, R.; Gu, H.; Hernandez, R.; Escobar, A.; Martínez, A.; Yates, L.; Moya, S.; Ruiz, J.; Astruc, D. Electrostatic Assembly of Functional and Macromolecular Ferricinium Chloride-Stabilized Gold Nanoparticles. *Inorg. Chem.* **2017**, *56*, 2784–2791.

114. Fu, F.; Wang, Q.; Ciganda, R.; Martinez-Villacorta, A.M.; Escobar, A.; Moya, S.; Fouquet, E.; Ruiz, J.; Astruc, D. Electron- and Hydride-Reservoir Organometallics as Precursors of Catalytically Efficient Transition Metal Nanoparticles in Water. *Chem. – Eur. J.* **2018**, *24*, 6645–6653.

115. Liu, J.; Mendoza, S.; Román, E.; Lynn, M.J.; Xu, R.; Kaifer, A.E. Cyclodextrin-Modified Gold Nanospheres. Host−Guest Interactions at Work to Control Colloidal Properties. *J. Am. Chem. Soc.* **1999**, *121*, 4304–4305.

116. Liu, J.; Ong, W.; Román, E.; Lynn, M.J.; Kaifer, A.E. Cyclodextrin-Modified Gold Nanospheres. *Langmuir* **2000**, *16*, 3000–3002.

117. Liu, J.; Alvarez, J.; Ong, W.; Román, E.; Kaifer, A.E. Phase Transfer of Hydrophilic, Cyclodextrin-Modified Gold Nanoparticles to Chloroform Solutions. *J. Am. Chem. Soc.* **2001**, *123*, 11148–11154.

118. Zuo, F.; Luo, C.; Zheng, Z.; Ding, X.; Peng, Y. Supramolecular Assembly of β-Cyclodextrin-Capped Gold Nanoparticles on Ferrocene-Functionalized ITO Surface for Enhanced Voltammetric Analysis of Ascorbic Acid. *Electroanalysis* **2008**, *20*, 894–899.

119. Noda, Y.; Noro, S.; Akutagawa, T.; Nakamura, T. Gold nanoparticle assemblies stabilized by bis(phthalocyaninato)lanthanide(III) complexes through van der Waals interactions. *Sci. Rep.* **2014**, *4*, 3758.

120. Quintana, C.; Morshedi, M.; Wang, H.; Du, J.; Cifuentes, M.P.; Humphrey, M.G. Exceptional Two-Photon Absorption in Alkynylruthenium–Gold Nanoparticle Hybrids. *Nano Lett.* **2019**, *19*, 756–760.

121. Mahmudin, L.; Suharyadi, E.; Utomo, A.B.S.; Abraha, K. Optical Properties of Silver Nanoparticles for Surface Plasmon Resonance (SPR)-Based Biosensor Applications. *J. Mod. Phys.* **2015**, *06*, 1071–1076.

122. Yamada, M.; Quiros, I.; Mizutani, J.; Kubo, K.; Nishihara, H. Preparation of palladium nanoparticles functionalized with biferrocene thiol derivatives and their electro-oxidative deposition. *Phys. Chem. Chem. Phys.* **2001**, *3*, 3377–3381.

123. Lu, F.; Didier, A. Catalytically Active Palladium Nanoparticle-Cored Ferrocenyl-Terminated Dendrimers: Palladium Nanoparticle-Cored Ferrocenyl-Terminated Dendrimers. *Eur. J. Inorg. Chem.* **2015**, *2015*, 5595–5600.

124. Mayer, C.R.; Dumas, E.; Sécheresse, F. Size controlled formation of silver nanoparticles by direct bonding of ruthenium complexes bearing a terminal mono- or bi-pyridyl group. *Chem. Commun.* **2005**, 345–347.

125. Naeem, S.; Ribes, A.; White, A.J.P.; Haque, M.N.; Holt, K.B.; Wilton-Ely, J.D.E.T. Multimetallic Complexes and Functionalized Nanoparticles Based on Oxygen- and Nitrogen-Donor Combinations. *Inorg. Chem.* **2013**, *52*, 4700–4713.

126. Gupta, R.K.; Dubey, M.; Li, P.Z.; Xu, Q.; Pandey, D.S. Size-Controlled Synthesis of Ag Nanoparticles Functionalized by Heteroleptic Dipyrrinato Complexes Having meso-Pyridyl Substituents and Their Catalytic Applications. *Inorg. Chem.* **2015**, *54*, 2500–2511.

127. Ibrahim, M.; Wei, M.M.; Deydier, E.; Manoury, E.; Poli, R.; Lecante, P.; Philippot, K. Rhodium nanoparticles stabilized by ferrocenyl-phosphine ligands: synthesis and catalytic styrene hydrogenation. *Dalton Trans.* **2019**, *48*, 6777–6786.

128. Xu, C.; Xu, K.; Gu, H.; Zhong, X.; Guo, Z.; Zheng, R.; Zhang, X.; Xu, B. Nitrilotriacetic Acid-Modified Magnetic Nanoparticles as a General Agent to Bind Histidine-Tagged Proteins. *J. Am. Chem. Soc.* **2004**, *126*, 3392–3393.

129. Sendroiu, I.E.; Schiffrin, D.J.; Abad, J.M. Nanoparticle Organization by a Co(II) Coordination Chemistry Directed Recognition Reaction. *J. Phys. Chem. C* **2008**, *112*, 10100–10107.

130. Friederici, M.; Angurell, I.; Rossell, O.; Seco, M.; Divins, N.J.; Llorca, J. Facile Synthesis of Palladium Nanoparticles Protected with Alkanethiolates Functionalized with Organometallic Fragments. *Organometallics* **2012**, *31*, 722–728.

131. Friederici, M.; Angurell, I.; Rossell, O.; Seco, M.; Muller, G. Exploring palladium nanoparticles protected with alkanethiolates functionalized with organometallic units as potential catalysts for sequential reactions. *J. Mol. Catal. Chem.* **2013**, *376*, 7–12.

132. Michalek, F.; Lagunas, A.; Jimeno, C.; Pericàs, M.A. Synthesis of functional cobalt nanoparticles for catalytic applications. Use in asymmetric transfer hydrogenation of ketones. *J. Mater. Chem.* **2008**, *18*, 4692-4697.

133. Veerapandian, M.; Zhu, X.X.; Giasson, S. Chitosan-modified silver@ruthenium hybrid nanoparticles: evaluation of physico-chemical properties and bio-affinity with sialic acid. *J. Mater. Chem. B* **2015**, *3*, 665–672.

134. Fu, F.; Ciganda, R.; Wang, Q.; Tabey, A.; Wang, C.; Escobar, A.; Martinez-Villacorta, A.M.; Hernández, R.; Moya, S.; Fouquet, E.; et al. Cobaltocene Reduction of Cu and Ag Salts and Catalytic Behavior of the Nanoparticles Formed. *ACS Catal.* **2018**, *8*, 8100–8106.

135. Wang, W.; Ciganda, R.; Wang, C.; Escobar, A.; Martinez-Villacorta, A.M.; Ramirez, M. de los A.; Hernández, R.; Moya, S.E.; Ruiz, J.; Hamon, J.-R.; et al. High catalytic activity of Rh nanoparticles generated from cobaltocene and $RhCl_3$ in aqueous solution. *Inorg. Chem. Front.* **2019**.

136. Wittmann, S.; Schätz, A.; Grass, R.N.; Stark, W.J.; Reiser, O. A Recyclable Nanoparticle-Supported Palladium Catalyst for the Hydroxycarbonylation of Aryl Halides in Water. *Angew. Chem. Int. Ed.* **2010**, *49*, 1867–1870.

137. Kim, S.B.; Cai, C.; Kim, J.; Sun, S.; Sweigart, D.A. Surface Modification of Fe_3O_4 and FePt Magnetic Nanoparticles with Organometallic Complexes. *Organometallics* **2009**, *28*, 5341–5348.

CHAPTER 2

1. Introduction

As mentioned in the general introduction, the aim of this PhD work consists on the preparation of novel hybrid nanomaterials, made of mononuclear organophosphorus Ru(II)-polypyridyl complexes covalently linked to the metallic surface of ruthenium nanoparticles and their fine characterization. In order to perform the synthesis and the characterization of the transition metal complexes, the metal nanoparticles and the hybrid nanomaterial, both the properties of the coordination, organometallic and organophosphorus chemistry have been employed.

At the first step, molecular Ru(II)-polypyridyl complexes incorporating an organophosphorus ligand in their coordination sphere have been synthesized. The preparation of these complexes followed previous works in the group. Ru(II)-polypyridyl complexes are thermally and chemically robust and display rich electrochemical and photophysical properties, characteristics that account for their application in fields like photovoltaics or photocatalysis. Coordination of organophosphorus ligands to the Ru(II)-polypyridyl fragment has proven to be a very powerful approach to modify the electronic properties of such complexes, as demonstrated by UV-vis absorption spectroscopy, luminescence and electrochemical studies [1]. By changing the donor and acceptor abilities of the organophosphorus ligands, a wide range of redox and spectroscopic properties have been achieved. For instance, the $Ru^{II/III}$ oxidation potential of a Ru(II) terpyridine bipyridine complex incorporating a tricyclohexylphosphine ligand, PCy_3, is 1.32 V, compared to that of the corresponding complex with a triphenylphosphite ligand, $P(OPh)_3$, which is 1.61 V (vs. SCE, at r.t. and in CH_3CN). It is important to note that such an exceptional 290 mV range is attained using ligands from a same family which are coordinated through the same P-heteroatom with the same oxidation state [2]. Coordination of phosphoryl ligands also entails changes in the photophysical properties of such Ru(II)-polypyridine complexes [3] and the proton acceptor ability of the P=O unit offers new opportunities to explore intermolecular interactions like hydrogen bonding [4]. In summary, Ru(II)-polypyridine complexes bearing organophosphorus ligands coordinated to their metal center present tunable reactivity and electronic properties, which makes them of high interest to combine with metal nanoparticles.

In the other hand, the preparation of the metal nanoparticles was based on the organometallic approach developed in the group. This synthesis method has proven to be very efficient to provide small and well-controlled nanoparticles of various metals [5,6]. Compared to other nanoparticle systems studied in our group before, the novelty of this work is the use of organophosphorus Ru(II)-

polypyridyl entities as stabilizing agent. Ruthenium nanoparticles (RuNPs) have been chosen for these innovative fundamental studies due to (i) the possibility to use a ruthenium organometallic complex as the metal source that releases only inert byproducts when decomposed, (ii) the skills accumulated in the group for the synthesis of RuNPs, thus allowing us to compare the new hybrid nanomaterial with other systems, and (iii) the possibility that ruthenium offers to perform liquid and solid NMR experiments, in contrast to other metals such as palladium or platinum [7] that exhibit pronounced Knight Shift effects.

The work described in this chapter is thus centered on the use of a mononuclear cationic organophosphorus polypyridyl ruthenium complex, $[(bpy)_2Ru(PPh_2Me)Cl]PF_6$, referred in the following parts of this manuscript as $[RuPMe]^+PF_6^-$, as stabilizing agent of RuNPs. From a first view, this objective was ambitious since a bonding interaction between $[RuPMe]^+PF_6^-$ complex and the surface of the nanoparticles was, *a priori*, uncertain. Indeed, the chosen complex doesn't have any "obvious" pendant group susceptible to directly bond to a metal surface. For their part, phosphines are known to stabilize ruthenium NPs [8–10] but in the present case, the phosphorous atom of the methyldiphenylphosphine ligand, PPh_2Me, is already involved in a P-Ru(II) bond inside the complex and then is not available to coordinate to the metal surface. However, this phosphine ligand is a precious probe for ^{31}P and ^{1}H-NMR studies in order to detect any effect of the coordination of $[RuPMe]^+$ to the surface of metal nanoparticles. A π −type interaction through the bipyridine ligands and the NPs surface could be envisaged, even though such a kind of interaction has never been reported in the literature. Finally, it is well stablished that ruthenium NP surfaces are halophilic [11], therefore making it reasonable to anticipate that the chlorine atom will interact with the surface of metal nanoparticles. Taking into account all these observations our objective was to set up a direct procedure to prepare a new hybrid nanomaterial, in order to open the door towards a new domain of research.

After a short general introduction on the synthesis and characterization of ruthenium nanoparticles commonly conducted in our group, (i) the synthesis of the novel hybrid nanomaterial, $([RuPMe]_n\text{-}RuNPs)^+(PF_6^-)_n$, and (ii) its full characterization, performed by using a combination of complementary characterization techniques as well as theoretical modeling, are described throughout this Chapter. We chose to present the results of the characterization according to the chronological order in which they have been obtained all along this study. As it will be seen, these fundamental studies provided very rich information on the feasibility to get innovative hybrid nanomaterials.

2. General features of ruthenium nanoparticles

Ruthenium nanoparticles are widely known for their catalytic properties. They have been involved in a large range of chemical transformations as reductions, mainly of C=C and C=O bonds, or oxidations of CO and alcohols, among others. Fischer-Tropsch, C-H activation, CO_2 transformation, dehydrogenation of amine boranes or water splitting are other reactions catalyzed by RuNPs [12]. Even though ruthenium is an expensive metal, which limits its application in large scale facilities, ruthenium nanoparticles allow performing fundamental studies in order to understand the structure-properties relationships that govern their reactivity.

The first ruthenium nanoparticles have been synthetized in water by the reduction of $RuCl_3 \cdot 3H_2O$ with sodium borohydride in the presence of different surfactants providing RuNPs in the size range of 10-150 nm [13]. From this pioneering work by Nakao and Kaeriyama, reduction of $RuCl_3 \cdot 3H_2O$, either by hydrides like $NaBH_4$, or by molecular hydrogen, and in the presence of surfactants or polymers, has been largely studied [12,14,15]. Polyol species can also be used to both reduce the $RuCl_3 \cdot 3H_2O$ salt and stabilize the resulting nanoparticles, within a size range of 1.5-6 nm [16,17]. The use of this precursor implies the presence of halogen species in the media that can eventually adsorb on the metal surface. Alternatively, olefinic organometallic precursors can be decomposed in mild conditions, usually dihydrogen pressure (1-3 bar) and often at room temperature, to yield ruthenium nanoparticles with narrow size distributions and controlled composition. The organometallic bis(2-methylallyl)(1,5-cyclooctadiene)ruthenium(II) compound, [Ru(cod)(2-methylallyl)$_2$], for instance, has been used for preparing RuNPs over black platinum [18] or in ionic liquids [19,20]. In our group, the prototypical precursor for the synthesis of ruthenium nanoparticles is (1,5-cyclooctadiene)(1,3,5-cyclooctatriene)ruthenium, commonly named as [Ru(cod)(cot)] (cod=1,5-cyclooctadiene; cot=1,3,5-cyclooctatriene) [21].

The controlled decomposition of [Ru(cod)(cot)] was firstly explored in the presence of polymers like polyvinylpyrrolidone (PVP) [22] as well as nitrocellulose and cellulose acetate [23], and later extended to other organic molecules like ligands commonly used in molecular chemistry. Alkylmines and alkylthiols [24], pyridine groups [25,26], carbenes [27], phosphines [8–10], carboxylic acids [28] or solvents like ionic liquids [29,30] and alcohols like methanol [31] or heptanol [32] are some examples of stabilizers employed in the organometallic approach for the synthesis of ruthenium nanoparticles.

The only byproduct that results from the treatment of [Ru(cod)(cot)] under hydrogen atmosphere is cyclooctane formed by reduction of the initial olefinic ligands of the complex. Cyclooctane is considered as an inert molecule towards the metal surface since it cannot coordinate to the surface of the nanoparticles. In addition, it is easily eliminated by evaporation of the volatiles under vacuum. This

facilitates the characterization of the resulting nanoparticles and allows for a better study of the influence of the ligands used as stabilizers on the final properties of the nanomaterial.

Ruthenium nanoparticles can be characterized by using the state-of-the-art techniques generally applied for metal nanoparticles such as Transmission Electron Microscopy (TEM), High Resolution Transmission Electron Microscopy or Wide-Angle X-Ray Scattering (WAXS) [33]. These techniques provide information on the morphology of the nanoparticles focusing mainly on the metallic core, like mean size (TEM/HRTEM), crystalline structure of the metal and coherence length (maximum metal-metal distance; WAXS). However, they don't provide valuable information on the stabilizing layer (ligands for example). Regarding the chemical composition of the nanoparticles, Energy-Dispersive X-Ray spectroscopy (EDX), Inductively Coupled Plasma (ICP) and elemental analysis are techniques of choice in order to determine the inorganic and organic proportions inside NPs. In the case of ruthenium-based nanomaterials, ICP analysis is not always reliable due to the difficulties met to get a full digestion of the metal, even in strongly acidic media, and the possible formation of the volatile specie RuO_4 that can lead to underestimation of the actual Ru content in the samples.

For the study of the stabilizing shell, Infrared (IR) spectroscopy can be used to identify the characteristic vibrations of the organic molecules present and eventually the binding modes [28].

Both liquid and solid-state Nuclear Magnetic Resonance (NMR) experiments have also been reported to be effective tools to study the coordination of ligands and in some cases their mobility around the surface of nanocrystals [34]. Ruthenium nanoparticles, which can be small, dispersible in aqueous or organic solvents, non-magnetic and known to display an almost-negligible Knight shift effect [7], are perfect candidates for NMR studies in order to determine the nanoparticle surface state [28,35]. However, it is important to note that liquid NMR measurements involving nanoparticles present some limitations that are not encountered for the characterization of molecular compounds. The interaction of a molecule with the surface of a bigger object like a metal nanoparticle affects its motion in solution. Consequently, its response to an applied magnetic field is altered. The reorientation ability of a spin in space is defined by its rotational correlation time, τ_c, namely the time a molecule takes to rotate one radian. This rotational correlation time is related to the dimension of the molecule and to its mobility in a given environment. Big molecules as well as dendrimers, polymers, proteins or nanoparticles among other large species have hindered mobility and as a consequence high τ_c. So, they present high T_1 (longitudinal relaxation time) and low T_2 (transverse relaxation time), as represented in Figure 1 [36,37].

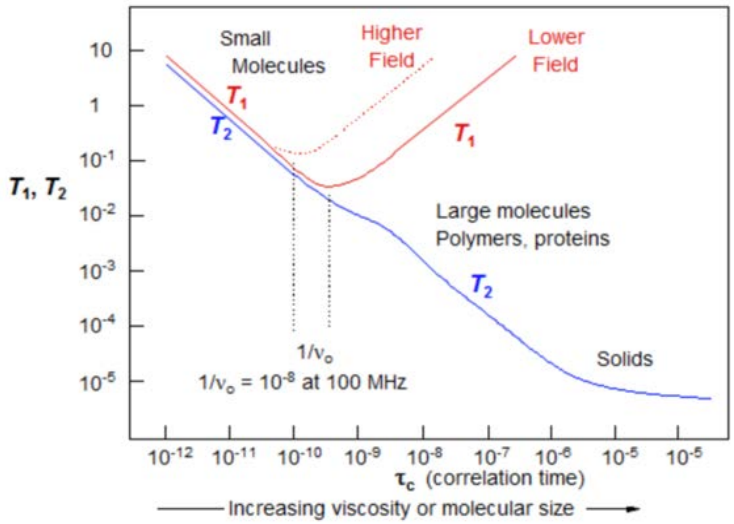

Figure 1. Evolution of T_1 and T_2 as a function of correlation time for spin ½ nuclei relaxing by the Dipole-Dipole mechanism, reproduced from ref. [38].

Having a low T_2, which is inversely proportional to the width at half-height of the signal observed in the NMR spectrum, produces a widening of such signal. In addition to that, field inhomogeneities, related to T_2* (or effective T_2), will also affect the signal. A same species in a heterogeneous chemical environment, such as the surface of metal-based nanoparticles, will appear as a set of slightly shifted signals and so in the form of a broad peak. High T_1 or slow longitudinal relaxation is reflected in a loss of peak intensity for a fixed acquisition time [37]. All of these facts combined result in a very difficult observation of the atoms directly connected to the surface of a metal nanoparticle by liquid NMR experiments. To circumvent this phenomenon, the Magic Angle Spinning (MAS), is a technique commonly used in solid-state NMR. This approach, which involves the high-speed mechanical rotation of the sample, allows minimizing some magnetic interactions involved in the broadening phenomenon and makes detectable some signals that were not visible by liquid-state NMR techniques. However, the signals generally remain broad and sometimes filtering sequences are required in order to access better defined spectra [39].

As a complementary tool to the experimental characterization techniques listed above, the development and optimization of Density Functional Theory (DFT) models for the study of small metal clusters has recently gained importance. For example, a Ru_{55} cluster model has been developed by the group of Pr. R. Poteau [40] to perform theoretical studies in parallel of experimental investigations in order to obtain information on the coordination modes of organic ligands [25,28]. The Ru_{55} model consists on a 55-atom hcp Ru cluster of ca. 1 nm and spherical shape, the surface of which has been shaped to simulate inhomogeneities that can be statistically found in a sample of small hcp nanoparticles. This average representation of a small RuNP presents (001) and (101) crystalline

planes and a corrugated facet, as well as a tip, which generates B_4 and B_5 sites (see Fig. 2, left). Since RuNPs are generally synthetized in our group through the decomposition of an organometallic precursor under dihydrogen pressure, the Ru_{55} model also considers a certain degree of hydride surface coverage. H_2 can easily adsorb at the surface, dissociate and coordinate to one (top sites, η), two (bridging sites, μ) or three (three-fold face capping sites, μ_3) Ru surface atoms (see Fig. 2, right) [40,41]. The energies related to the adsorption of hydride species on the Ru_{55} surface are in the -5.6 to -14.9 kcal/mol range.

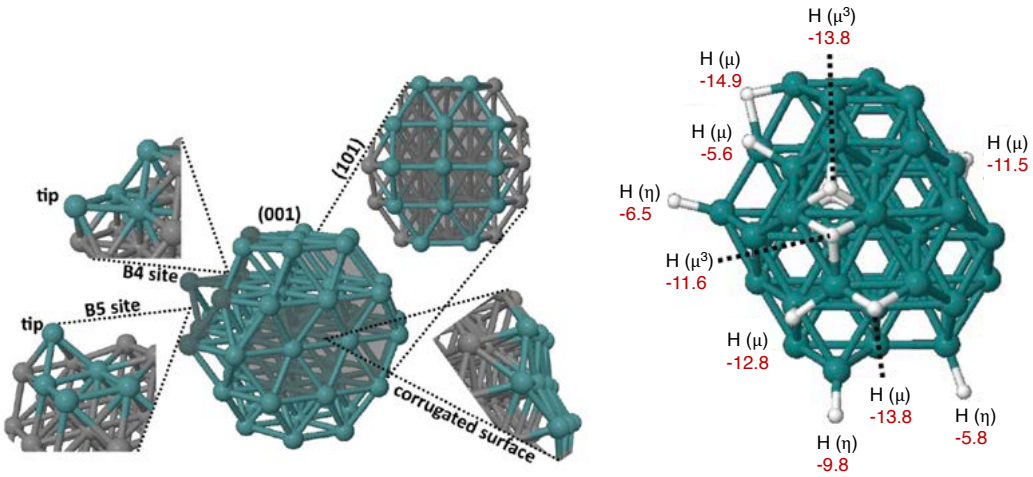

Figure 2. hcp-based Ru_{55} cluster and special sites at its surface (left) and different adsorption sites and related adsorption energies of H atoms at the Ru_{55} surface (right). Energies (red) are given in kcal/mol. Reproduced from ref. [40].

Such a combination of experimental/theoretical data appeared to be a highly valuable approach to get insights on the surface state of metal nanoparticles as well as on their interest for a given catalytic reaction [25,28].

3. Synthesis of the hybrid nanomaterial $([RuPMe]_n\text{-}RuNPs)^+(PF_6^-)_n$

In this pioneering study, the development and optimization of the experimental conditions in order to prepare controlled and stable nanohybrids, $([RuPMe]_n\text{-}RuNPs)^+(PF_6^-)_n$, consisting on $[RuPMe]^+PF_6^-$ complexes coordinated on the surface of ruthenium nanoparticles, will be described. The originality of this work is the use of the mononuclear transition metal complex $[RuPMe]^+PF_6^-$ as a direct stabilizing agent of RuNPs.

The synthesis of $[RuPMe]^+PF_6^-$ complex has been previously reported by Meyer and coworkers [42]. This synthesis has been modified to get higher isolated yield (see Experimental Section) [43].

Cis-Bis(2,2′-bipyridine)dichlororuthenium(II), *cis*-[Ru(bpy)$_2$Cl$_2$], used as precursor was dissolved in dry acetone (see Scheme 1). Sequentially, a low excess of thallium hexafluorophosphate, TlPF$_6$, and methyldiphenylphosphine, PPh$_2$Me, both in acetone, were added dropwise and the mixture was stirred for 12 h at 25 °C. After elimination of TlCl by filtration, purification through flash chromatography and washing with ether, a precipitate has been isolated under the form of a very fine orange powder (yield: 60%). The so-obtained product [RuPMe]$^+$PF$_6^-$ has been characterized by ^{1}H and ^{31}P NMR (see Experimental Section). For the synthesis of nanohybrids, the [RuPMe]$^+$PF$_6^-$ complex has been used after lyophilization.

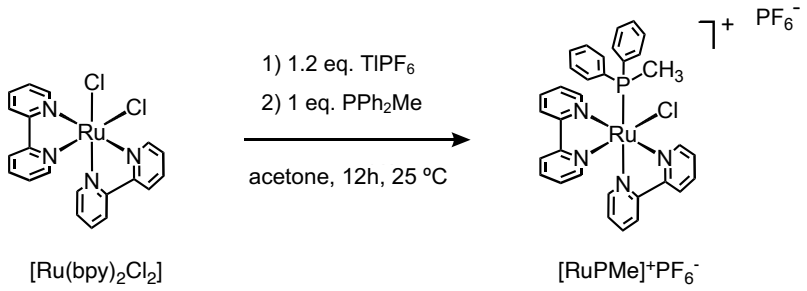

Scheme 1. Synthesis of the mononuclear cationic organophosphorus polypyridyl ruthenium complex, [(bpy)$_2$Ru(PPh$_2$Me)Cl]PF$_6$ ([RuPMe]$^+$PF$_6^-$).

In a first attempt, synthesis of the hybrid nanomaterial ([RuPMe]$_n$-RuNPs)$^+$(PF$_6^-$)$_n$ (see Scheme 2), was performed using the organometallic complex [Ru(cod)(cot)] as precursor of RuNPs and 0.1 molar equivalent (eq.). of the [RuPMe]$^+$PF$_6^-$ complex as stabilizer. Both were dissolved in freshly distilled and degassed tetrahydrofuran (THF) (1 mL per mg of [Ru(cod)(cot)]), inside a Fischer-Porter reactor and under argon atmosphere, providing an intense orange homogeneous solution. Note that in THF, [Ru(cod)(cot)] is pale yellow and the [RuPMe]$^+$PF$_6^-$ complex is dark orange. The reaction mixture was then pressurized with 3 bar of H$_2$ and then kept under vigorous stirring for 24 h at 25 °C. The initial orange solution turned black within a few minutes. After 24 h of reaction, excess H$_2$ was evacuated by pumping and the resulting black colloidal suspension was observed to be stable at least for one week but the stability was not checked further. The volatiles were then evaporated under vacuum which led to the formation of a black precipitate.

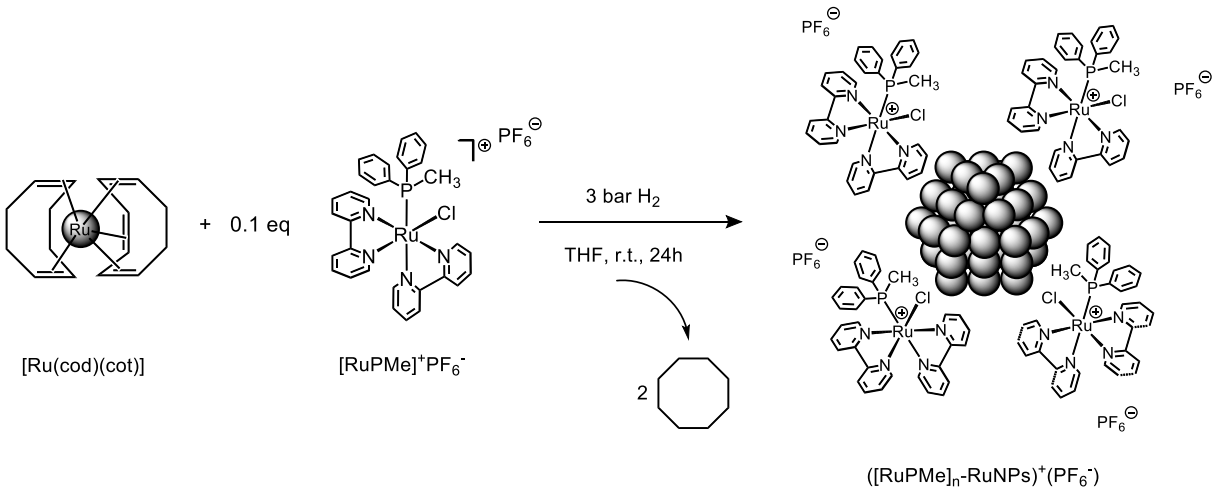

Scheme 2. Synthesis of the hybrid nanomaterial $([RuPMe]_n\text{-}RuNPs)^+(PF_6^-)_n$.

It is important to note that the fate of $[RuPMe]^+PF_6^-$ under H_2 pressure was previously checked. The $[RuPMe]^+PF_6^-$ complex was dissolved in THF and exposed to 3 bar of H_2 for 24 h. After evacuation of H_2 and evaporation of the solvent, the sample was analyzed by ^{31}P and ^1H NMR and no modification of the complex $[RuPMe]^+PF_6^-$ was observed.

In order to remove the by-products of the reaction, cyclooctane (resulting from the hydrogenation of [Ru(cod)(cot)]) and unreacted $[RuPMe]^+PF_6^-$, THF was added in the Fischer-Porter reactor and the orange supernatant was extracted after precipitation of the hybrid $([RuPMe]_n\text{-}RuNPs)^+(PF_6^-)_n$ in the form of a black powder. This procedure was repeated three times. Note that the third wash appeared colorless, indicating that excess of $[RuPMe]^+PF_6^-$ complex had been removed. Removal of free $[RuPMe]^+PF_6^-$ by THF washes favored the precipitation of the hybrid RuNPs and facilitated the purification step. The nanomaterial was dissolved into a minimum amount of acetonitrile in order to favor the dispersion of the sample and transferred into a vial before drying under vacuum. A second purification sequence, consisting on three additional washes with THF was then performed. The washing solution appeared slightly colored, indicating a release of $[RuPMe]^+PF_6^-$ that could not be removed before dispersion in acetonitrile. ^1H and ^{31}P NMR demonstrated that the species liberated during this last washing procedure was exclusively $[RuPMe]^+PF_6^-$.

Preliminary TEM analysis performed on two grids - one prepared from the crude colloidal suspension in THF and the second one obtained after dispersion of the purified black powder in acetonitrile - clearly evidenced some differences in terms of dispersion. From THF crude colloidal suspension, regular spherical aggregates of ca. 350 nm were visible on the TEM grid (Fig 3a). It can be observed on a zoomed TEM image (Fig 3b) that these aggregates are made of individual NPs. In the contrary, in acetonitrile dispersion, small and well-dispersed individual NPs are visible showing a fairly symmetrical size distribution centered at ca. 1.4 nm ± 0.6 (Fig. 3c and 3d). Although the rather wide

size distribution and the observation of a few larger NPs, it is important to note that a great majority of particles display a size close to the calculated mean size, which indicates that the reaction conditions applied led to a rather effective size control.

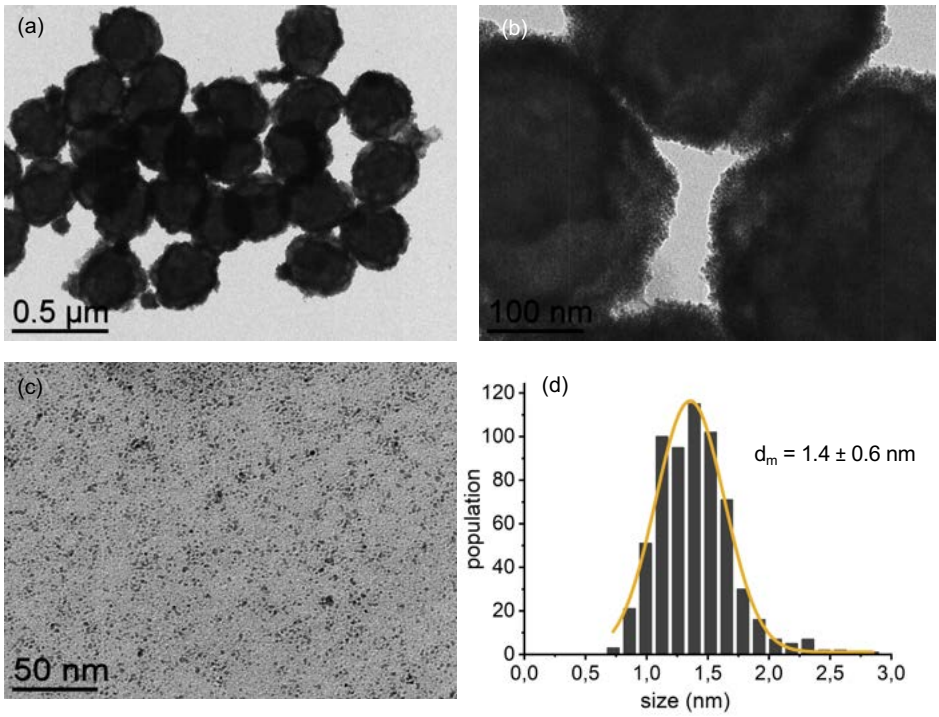

Figure 3. TEM pictures of $([RuPMe]_n\text{-}RuNPs)^+(PF_6^-)_n$: (a, b) in THF and (c) redispersed in acetonitrile. (d) Size histogram of $([RuPMe]_n\text{-}RuNPs)^+(PF_6^-)_n$ dissolved in acetonitrile.

The behavior observed in solution connotes a certain ionic-like character of the nanohybrids that spontaneously aggregate in a solvent of low polarity like THF, but that are well-dispersed in an organic polar solvent like acetonitrile. A parallel can be made with the behavior of the $[RuPMe]^+PF_6^-$ complex in the same solvents, since due to its ionic character it is more soluble in acetonitrile, a more polar solvent than THF.

A comparable behavior was observed by Mayer and coworkers for positively charged Ru(II)-polypiridyl-capped gold nanoparticles, which displayed similar solubility properties as common inorganic salts [44]. Their hybrid system was synthesized by a post-functionalization procedure, substituting the weakly stabilizing tetraoctylammonium bromide (TOAB) by a chlorine salt of a Ru(II)-polypyridyl complex bearing a phenanthroline grafting group. The resulting hybrids were water-soluble. Addition of an excess of NH_4PF_6 salt to the colloidal aqueous solution induced anion exchange and consequent precipitation of the hybrids, that could then be re-dispersed in acetonitrile. Substitution of PF_6^- again by Cl^-, which resulted in the formation of new flocculate in acetonitrile, allowed reversible transfer to aqueous media without apparent change of size of the AuNPs core.

Before pursuing the characterization studies, a series of reactions have been performed at a different $[RuPMe]^+PF_6^-$/ [Ru(cod)(cot)] ratio in order to optimize the experimental conditions leading to the hybrid RuNPs. First, the synthesis of $([RuPMe]_n\text{-}RuNPs)^+(PF_6^-)_n$ using 0.2 eq. of $[RuPMe]^+PF_6^-$ was envisaged. Phosphine-stabilized ruthenium nanoparticles previously synthesized in the group, such as PPh_3-RuNPs, in which the same ratio phosphine/[Ru(cod)(cot)] had been used were taken as a reference [8]. Also, ratios lower than 0.1 eq. (0.05 and 0.001) were tested. To be able to compare the results, the same post-treatment has been applied to all the samples of nanoparticles prepared, namely washing/precipitation by addition of THF and then redispersion in acetonitrile. Figure 4 shows TEM images recorded for $([RuPMe]_n\text{-}RuNPs)^+(PF_6^-)_n$ prepared with 0.2, 0.1, 0.01 and 0.005 eq. of $[RuPMe]^+PF_6^-$, from colloidal suspensions in acetonitrile.

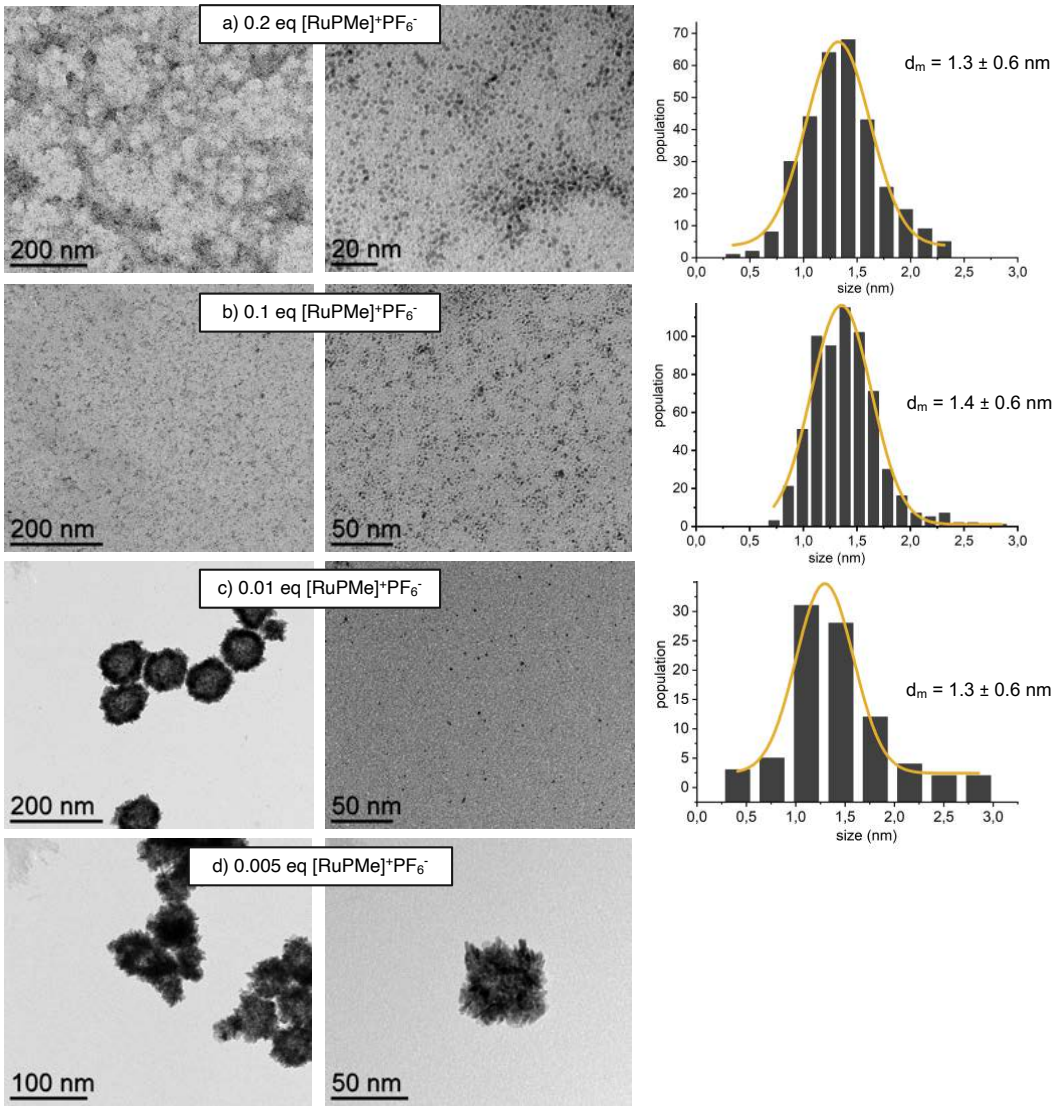

Figure 4. TEM pictures of $([RuPMe]_n\text{-}RuNPs)^+(PF_6^-)_n$ hybrid nanomaterials synthesized with 0.2, 0.1, 0.01, and 0.005 equivalent of $[RuPMe]^+PF_6^-$.

No significant difference of size, dispersion and homogeneity of the hybrid RuNPs was observed between 0.2 and 0.1 eq. of $[RuPMe]^+PF_6^-$. The only divergence is the color of the reaction solution, more intense for the synthesis performed with 0.2 eq. of complex, which points out a higher concentration of ungrafted $[RuPMe]^+PF_6^-$complex in the crude reaction mixture.

For a decreased ratio of 0.01 eq of $[RuPMe]^+PF_6^-$, large and non-dispersable aggregates are visible on the TEM grid. There are, however, few small and individual nanoparticles on the background of the grid, with similar size than that observed for the two previous systems. With 0.005 eq. of $[RuPMe]^+PF_6^-$ only big aggregates were observed indicating a lack of stabilization.

This series of syntheses provided evidence of the stabilizing effect of the $[RuPMe]^+PF_6^-$ complex at a molar ratio of 0.1 to 0.2 leading in both cases to small hybrid RuNPs of ca. 1.4 nm in size. However, the synthesis performed with 0.2 eq. showed that a large part of the introduced complex was not grafted. In order to minimize the excess of $[RuPMe]^+PF_6^-$ complex and reduce the purification process we decided to keep 0.1 eq. of $[RuPMe]^+PF_6^-$ to pursue our study.

As a conclusion of this part, our first results showed that the mononuclear cationic organophosphorus polypyridyl ruthenium complex, $[RuPMe]^+PF_6^-$, allows the stabilization of RuNPs, like the conventional stabilizers previously cited do.

4. Characterization of the hybrid nanomaterial $([RuPMe]_n\text{-}RuNPs)^+(PF_6^-)_n$

4.1. Physical characterization recorded by HRTEM, WAXS and ICP

As previously observed from TEM images (Fig. 3c and 3d) the sample seems rather heterogeneous in terms of size dispersion of the NPs. This was confirmed by HRTEM images recorded from sample $([RuPMe]_n\text{-}RuNPs)^+(PF_6^-)_n$ dispersed in acetonitrile (Fig. 5a). While the small nanoparticles (main population) seem amorphous, bigger NPs tend to display crystalline planes. The Fast Fourier Transformation (FFT) of a HRTEM image shows, for a ca. 2.6 nm nanoparticle, the presence of interplanar distances of 0.219 and 0.203 nm corresponding to the crystalline (002) and (101) planes of the hexagonal close-packed (hcp) structure of bulk ruthenium (Fig. 5b). Ru hcp is the recurring crystalline structure observed for RuNPs [45].

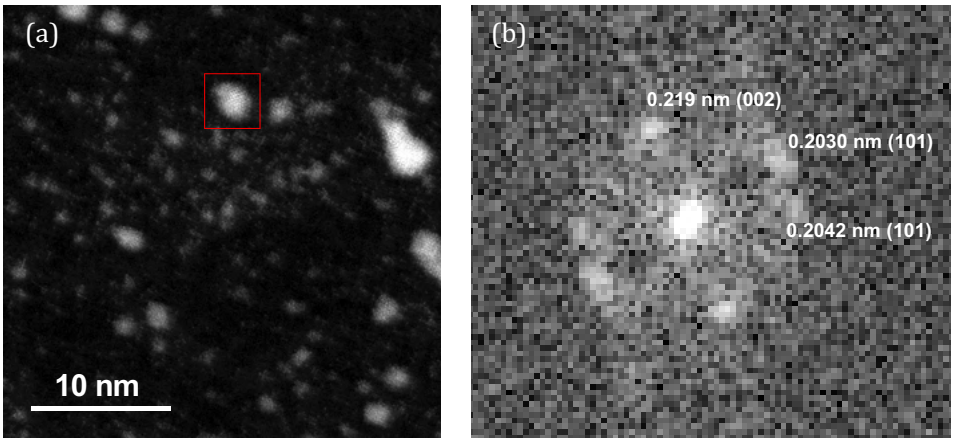

Figure 5. (a) HRTEM image of $([RuPMe]_n\text{-}RuNPs)^+(PF_6^-)_n$ dispersed in acetonitrile; (b) diffractogram of the selected RuNP.

Wide-Angle X-Ray Scattering (WAXS) analysis, performed on a 1 mm glass capillary filled with purified $([RuPMe]_n\text{-}RuNPs)^+(PF_6^-)_n$ black powder under argon atmosphere, complemented the results observed by HRTEM. The pattern obtained is consistent with that of the hcp ruthenium bulk. The diffractogram (Fig. 6a, black line) displays all the peaks corresponding to the crystalline Ru hcp structure (Fig. 6a, red pattern), as previously pointed by FFT of HRTEM images. The first peak observed, at ca. 2° could be attributed to partial sample aggregation.

Figure 6b shows the radial distribution function (RDF) of the $([RuPMe]_n\text{-}RuNPs)^+(PF_6^-)_n$ sample. A maximum coherence length of ca. 2.5 nm indicates the presence of crystalline domains close to the estimated size of big and crystalline RuNPs previously observed on HRTEM images (ca. 2.6 nm). The RDF profile is consistent with two populations of well crystallized RuNPs. Indeed, the best agreement was obtained using a dual size model simulation computed from the hcp network: small RuNPs displaying short interatomic distances (1.3 nm in size, green line) required for the fast decrease of the RDF at short distances and larger ones (2.5 nm in size, blue line) generating the longer distances. Besides, characteristic lengths of RuO_x species are not observed. These WAXS results confirm a certain dispersity in size but also the presence of hcp metallic ruthenium in the nanohybrids.

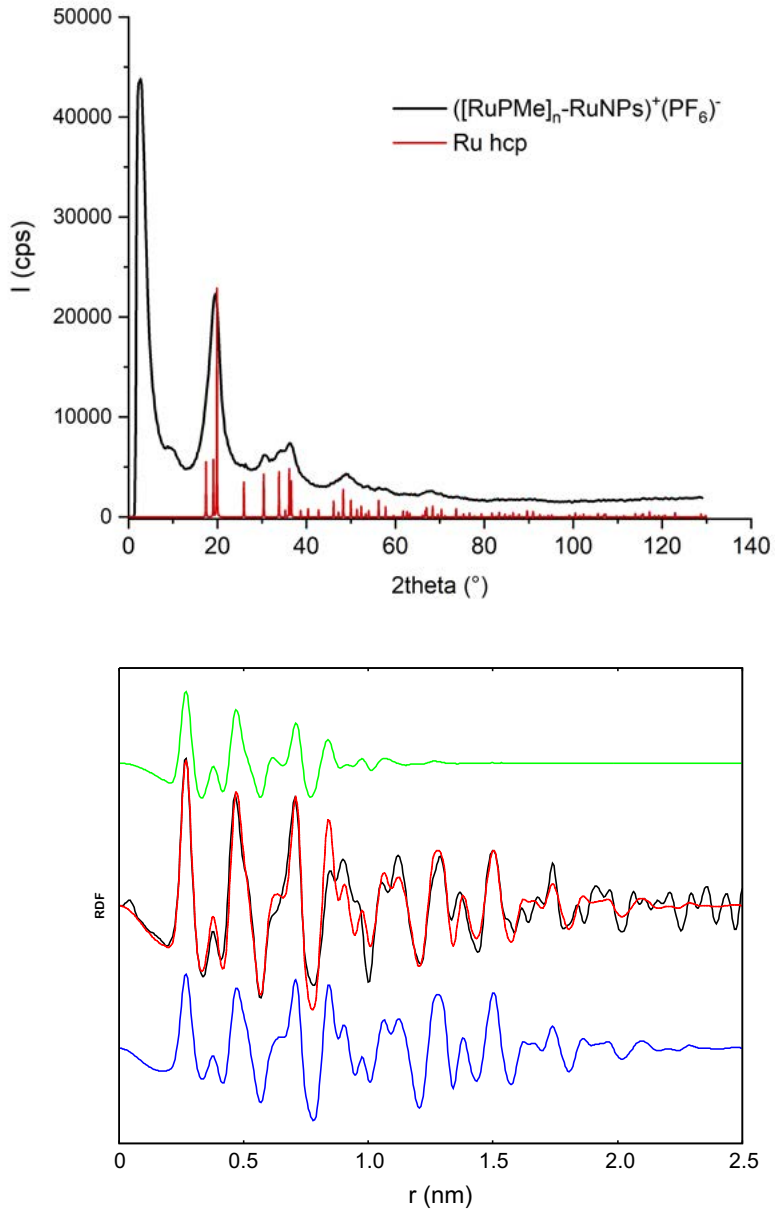

Figure 6. (top) WAXS diagram of $([RuPMe]_n\text{-}RuNPs)^+(PF_6^-)_n$ in comparison with diffraction pattern of bulk hcp Ru; (bottom) RDF: experimental function (black) with simulation from dual size model (red).

The purified sample of $([RuPMe]_n\text{-}RuNPs)^+(PF_6^-)_n$ was characterized by Inductive Coupled Plasma Optical Emission Spectrometry (ICP-OES), in order to get an estimation of the Ru and P contents in the material. The sample was digested at 80 °C for 6 days in an acidic HNO_3/HCl solution (1:3). As it was mentioned before, a complete digestion of ruthenium nanomaterials is difficult to attain and as a consequence, ICP results are sometimes poorly reproducible. Knowing this and in order to get a reliable mean value, samples of different synthesis batches were analyzed after the same acidic treatment. Mean values of ca. 62.2 wt% in ruthenium and of 2.1 wt% in phosphorus were obtained. These values are close to those calculated by considering a full integration of the initial quantities of

[Ru(cod)(cot)] and $[RuPMe]^+PF_6^-$ complex in the final $([RuPMe]_n\text{-}RuNPs)^+(PF_6^-)_n$ material, namely ca. 62 wt% and ca. 3.4 wt%, for Ru and P elements, respectively.

Table 1 reports both the average values of the results obtained by ICP analysis (first entry) and the estimated weight percentages, considering a total integration of the $[RuPMe]^+PF_6^-$ introduced for the synthesis in the final nanomaterial while keeping its integrity (second entry).

	weight % Ru	**weight % P**
experimental (ICP)	62.2	2.1
estimated	62.0	3.4

Table 1. Ru and P content of the $([RuPMe]_n\text{-}RuNPs)^+(PF_6^-)_n$ obtained considering the initial amounts used for the synthesis and the experimental ICP results.

Comparing the estimated and experimental P values it can be deduced that ca. 60% of the $[RuPMe]^+PF_6^-$ complex amount introduced for the synthesis of the hybrid is present in the nanohybrid, the excess being eliminated during the washing process. Note that the Ru weight % could not be used to support this estimation as Ru is an element present in both the organometallic precursor [Ru(cod)(cot)] and the $[RuPMe]^+PF_6^-$ complex used as stabilizer.

4.2. Characterization by liquid and solid-state NMR spectroscopy

Different NMR experiments have been recorded in order to gain further information on the composition of the metallic surface of the RuNPs of the $([RuPMe]_n\text{-}RuNPs)^+(PF_6^-)_n$ nanohybrids as well as on the nature of the interaction with $[RuPMe]^+PF_6^-$ complexes. As it will be seen hereafter, liquid NMR provided information on the fate of the $[RuPMe]^+PF_6^-$ complexes and their mobility when surrounding RuNPs. Solid-state NMR experiments complemented the results obtained in solution, especially on the identification of the characteristic fragments of the $[RuPMe]^+$ unit in close proximity to the metal surface. Both liquid and solid NMR analysis allowed us to propose a detailed picture on the arrangement of $[RuPMe]^+PF_6^-$ at the surface of RuNPs.

4.2.1. Liquid NMR spectroscopy

For comparison purpose, NMR data of the $[RuPMe]^+PF_6^-$ complex were taken as reference for the study of the nanohybrid. The ^1H NMR spectrum of $[RuPMe]^+PF_6^-$ complex recorded in deuterated acetonitrile, CD_3CN, is presented in Figure 7. The region of the aromatic protons (6-10 ppm) gathers the signals for the protons of the phenyl groups of the phosphine ligand (PPh_2Me) and those of the two bipyridine

ligands (peaks between 7.0 and 9.5 ppm). A second feature of $[RuPMe]^+PF_6^-$ is the doublet observed at 1.53 ppm, corresponding to the methyl protons of the PPh_2Me ligand, with a coupling constant $^2J_{P-H}$ = 8.5 Hz. Traces of acetone (δ = 2.08 ppm, solvent used for the synthesis of the complex), THF (δ = 1.80 and 3.64 ppm) and water (δ = 2.13 ppm) are also observed.

^{31}P NMR{^1H} (Fig. 8) spectrum of $[RuPMe]^+PF_6^-$ complex in acetonitrile-d_3 presents a singlet at 27.3 ppm corresponding to the phosphorus atom of the ligand PPh_2Me and a septuplet at -144.6 ppm for the PF_6^- anion. As observed in Figure 6b, the integration of the two ^{31}P signals corresponds to a 1:1 ratio, as expected.

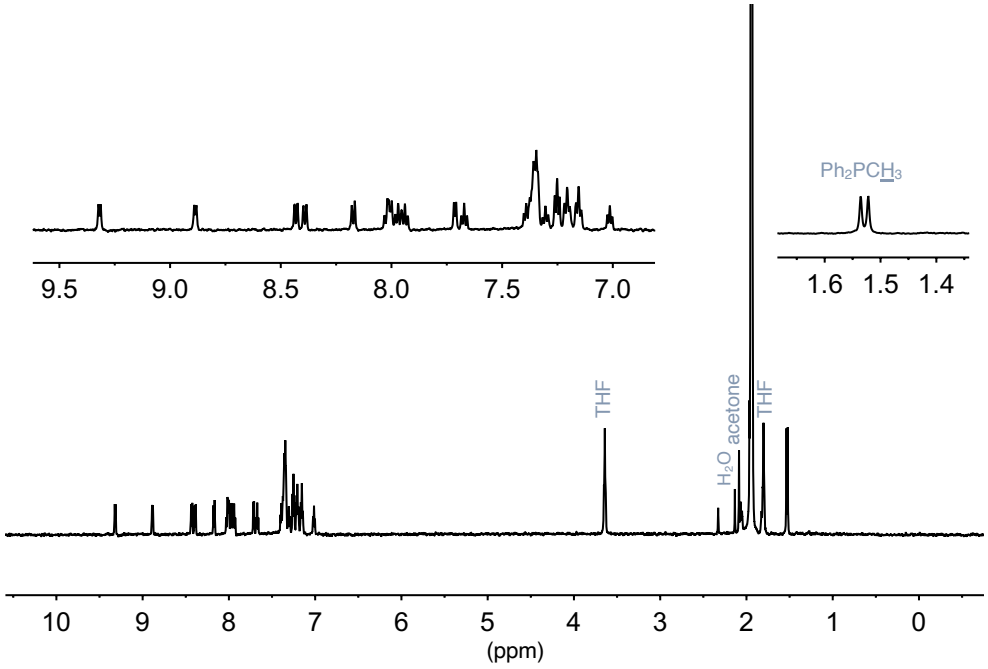

Figure 7. ^1H NMR spectra of $[RuPMe]^+PF_6^-$ in CD_3CN.

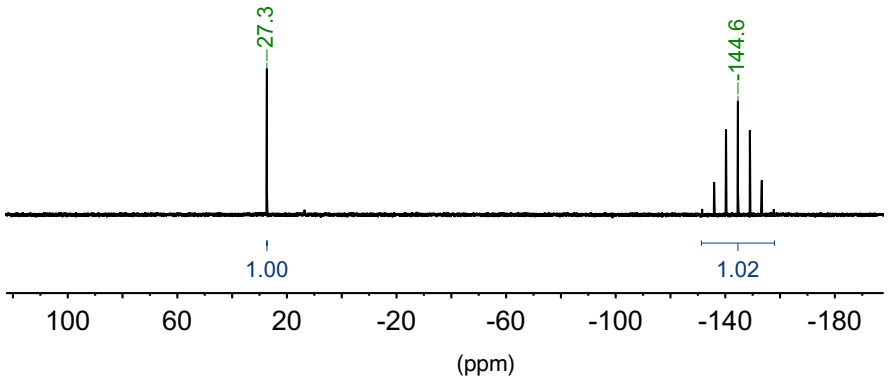

Figure 8. ^{31}P NMR{^1H} spectra of $[RuPMe]^+PF_6^-$ in CD_3CN.

In order to get more details on the formation of the $([RuPMe]_n\text{-}RuNPs)^+(PF_6^-)_n$ hybrid, its synthesis has been reproduced at a lower scale inside an NMR tube allowing to introduce hydrogen pressure (Young NMR tube). Thus, in a first step, a solution of [Ru(cod)(cot)] and $[RuPMe]^+PF_6^-$ (0.1 eq.) has been prepared in THF-d_8, transferred into the NMR tube and ^1H and ^{31}P NMR spectra were recorded. As shown in figures 9 and 10, ^1H and ^{31}P NMR spectra (t=0) present the typical signals of [Ru(cod)(cot)] and $[RuPMe]^+PF_6^-$, respectively, indicating that no reaction happened between the $[RuPMe]^+PF_6^-$ complex and [Ru(cod)(cot)] when mixed under argon atmosphere in THF-d_8 at 25 °C. When the NMR tube was pressurized with 3 bar of H_2, a singlet at δ = 1.5 ppm in ^1H NMR appeared immediately. This signal can be assigned to cyclooctane, the product released from the hydrogenation of [Ru(cod)(cot)]. The intensity of this singlet grew as the reaction proceeded, which is indicative of the progressive decomposition of the [Ru(cod)(cot)] metallic precursor. Regarding the fate of the complex $[RuPMe]^+PF_6^-$ no signals attributable to its evolution or degradation could be observed, but a gradual disappearance of its respective signals is visible, both in ^1H and ^{31}P NMR. This disappearance is attributed to (i) a decrease in concentration of $[RuPMe]^+PF_6^-$ in solution which can be explained by its interaction with the growing RuNP surface and (ii) continuous precipitation of the black solid formed which can be attributed to the small diameter of the NMR tube and the lack of stirring compared to the synthesis of $([RuPMe]_n\text{-}RuNPs)^+(PF_6^-)_n$ performed in a Fischer-Porter reactor. After 24 h of reaction, a solid and black product was present in the bottom of the NMR tube.

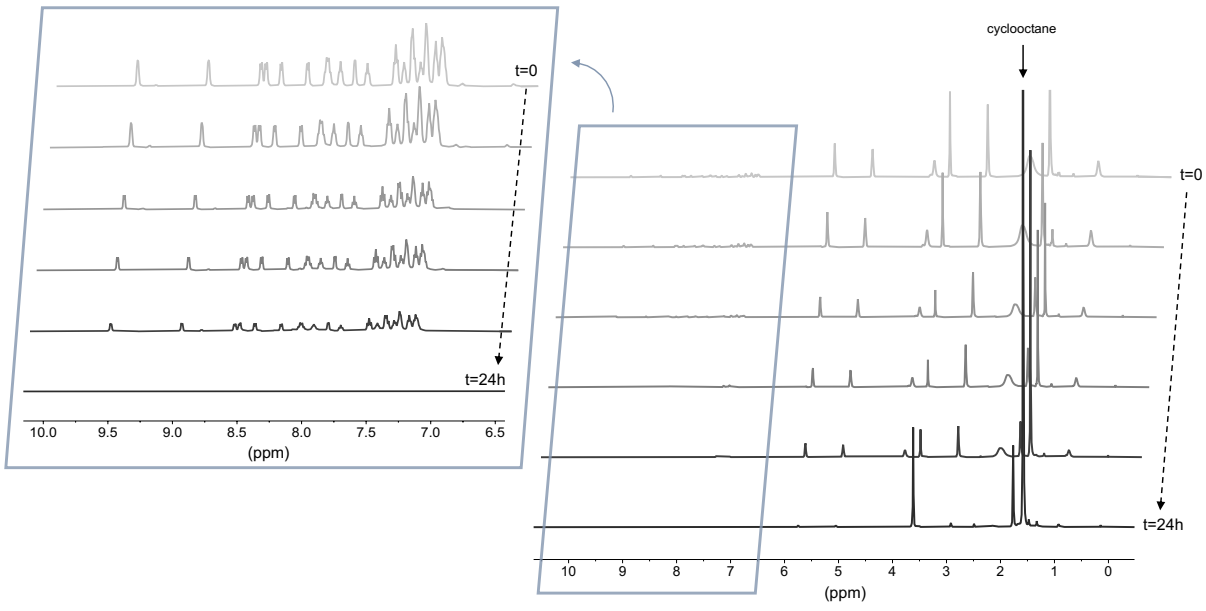

Figure 9. ^1H NMR spectra of the reaction of [Ru(cod)(cot)] with 0.1 eq of $[RuPMe]^+PF_6^-$ in THF-d_8 under 3 bar of H_2, as a function of time.

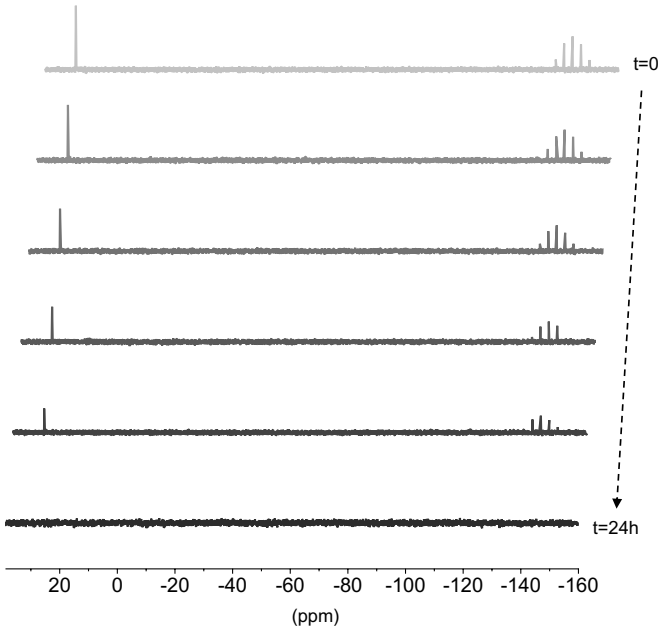

Figure 10. ^{31}P NMR spectra of the reaction of [Ru(cod)(cot)] with 0.1 eq of $[RuPMe]^+PF_6^-$ in THF-d_8 under 3 bar of H_2, as a function of time.

As mentioned before, when the $([RuPMe]_n\text{-}RuNPs)^+(PF_6^-)_n$ hybrid material is prepared in a Fischer-Porter reactor, TEM analysis of the crude colloidal suspension in THF revealed the presence of aggregates that could explain the formation of a precipitate. However, well-separated nanoparticles were detected by TEM after redispersion of the solid in acetonitrile. For solubility reasons, the following liquid NMR studies were then performed in CD_3CN.

Figure 11 shows the ^1H NMR spectrum of the purified $([RuPMe]_n\text{-}RuNPs)^+(PF_6^-)_n$ (Fig. 11b) together with that of the $[RuPMe]^+PF_6^-$ complex, used as a reference (Fig. 11a), both in CD_3CN. ^1H NMR spectrum of the purified $([RuPMe]_n\text{-}RuNPs)^+(PF_6^-)_n$ presents a very broad signal between 6.5 and 9.0 ppm, a region corresponding to that expected for the chemical shifts of the bipyridine ligands and phenyl groups of $[RuPMe]^+$ ligand from the complex. As mentioned previously, the observation of broad signals is usual in liquid NMR involving metal NPs. For instance, the ^1H NMR spectrum of PTA-stabilized RuNPs prepared in the group (PTA = 1,3,5-triaza-7-phosphaadamantane) showed an enlargement of the signals corresponding to the $N(CH_2)N$ protons of the PTA ligands, while the PCH_2N protons, which are closer to the RuNPs surface, were not observed [46]. Another example of signal broadening as consequence to the proximity of a ligand to a nanoparticle surface has been observed for the methylene protons (1.3 – 1.6 ppm) of hexadecylamine ligands stabilizing RuNPs [24]. The protons of the hexadecylamine methyl group were observed but the protons next to the nitrogen, and thus closer to the metal surface, were not detected by ^1H NMR.

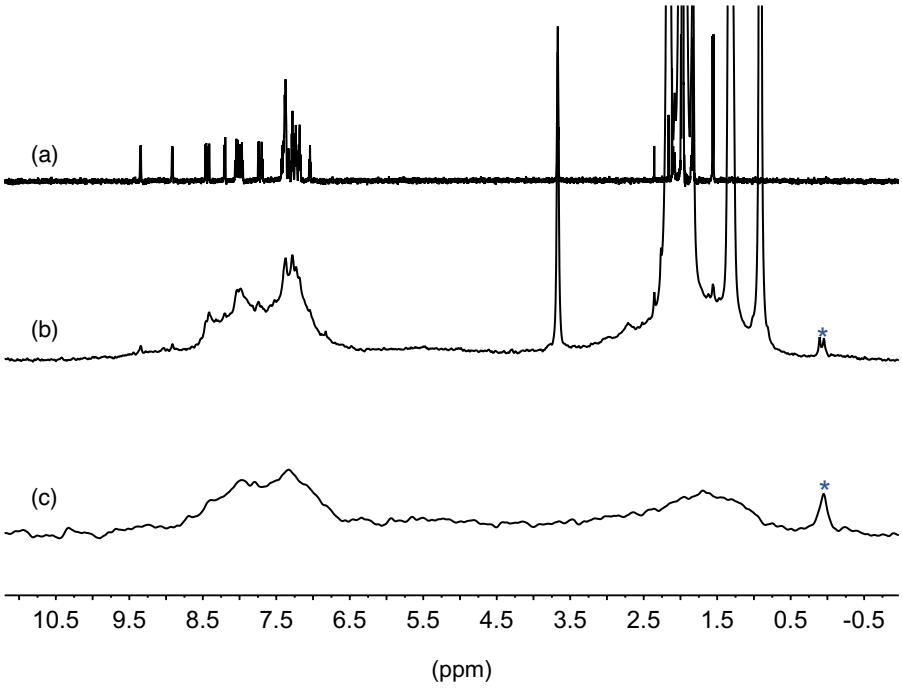

Figure 11. ^{1}H NMR spectra of (a) $[RuPMe]^{+}PF_6^{-}$, (b) purified $([RuPMe]_n\text{-}RuNPs)^{+}(PF_6^{-})_n$ and (c) diffusion-filtered $([RuPMe]_n\text{-}RuNPs)^{+}(PF_6^{-})_n$ in CD_3CN. *Grease.

Therefore, at first view, the ^{1}H NMR profile obtained for $([RuPMe]_n\text{-}RuNPs)^{+}(PF_6^{-})_n$ is indicative of the presence of $[RuPMe]^{+}$ in close proximity to the RuNPs, probably directly interacting with the surface and forming a layer around the RuNPs. Moreover, even if partial hydrogenation of $[RuPMe]^{+}$ during the synthesis cannot be excluded (see below), it suggests that the aromaticity of the complex is mostly preserved.

Along the broad signals, sharp peaks matching with $[RuPMe]^{+}$ complexes are also observed. Those peaks are too sharp to belong to $[RuPMe]^{+}$ directly coordinated to the RuNPs surface but, at the same time, they are significantly broader than those of the free $[RuPMe]^{+}$ complexes in solution. They may reasonably be attributed to $[RuPMe]^{+}$ species that stand in an external layer of the $([RuPMe]_n\text{-}RuNPs)^{+}(PF_6^{-})_n$ nanomaterial. The coexistence of different ligand shells or layers at different distances from the NP surface and displaying different interaction modes has been previously identified. An insightful study on the organization of various amines (hexadecylamine, dodecylamine and octylamine) around the surface of ZnO nanoparticles [47] allowed to identify at least three different modes of interaction: (i) amines in strong interaction with the ZnO surface, (ii) amines in weak interaction with the ZnO surface and (iii) amines in a second ligand shell, in a van der Waals interaction-type. The amines in weak interaction and those in the second shell were found to be in exchange with free amines in solution.

At this stage of our work, a reasonable hypothesis on the structure of the $([RuPMe]_n\text{-}RuNPs)^+(PF_6^-)_n$ hybrid was that the RuNPs were surrounded by two different layers of $[RuPMe]^+$ complexes. The first one, an "inner layer" made of $[RuPMe]^+$ in the close environment of the Ru surface. The second, an "outer layer" constituted of $[RuPMe]^+$ complexes, at a longer distance from the metal surface. Considering the ionic nature of the $[RuPMe]^+$ complexes we can propose that the complex entities that stand in the outer layer are in an electrostatic-type interaction with those present in the inner layer. To shed some light on this hypothesis, Diffusion Ordered NMR SpectroscopY (DOSY-NMR) experiments have been performed.

The diffusion-filtered ^1H NMR spectrum of the $([RuPMe]_n\text{-}RuNPs)^+(PF_6^-)_n$ hybrid is given on Figure 11c. This spectrum has been recorded in conditions where the contribution of molecules with fast diffusion coefficients are eliminated, namely molecules like solvents and $[RuPMe]^+PF_6^-$ molecules that are not directly coordinated to the surface of RuNPs. In these conditions, in comparison with spectrum 10b, the sharp signals with low intensity attributed to the $[RuPMe]^+$ in the outer layer, named as $[RuPMe]^+_{exch}$, are no longer visible and only two broad signals are observed. The first enlarged signal, in the range of 6.5 - 9.0 ppm, has been attributed to the polypyridyl and phenyl groups of $[RuPMe]^+$. The second large signal, between 0.5 and 2.5 ppm, is of lower intensity and became more visible after filtering of the CD_3CN peak. This second large signal could originate from acetonitrile coordinated to the RuNPs surface, the methyl group of $[RuPMe]^+$ or from the partial hydrogenation reaction of phenyl groups of $[RuPMe]^+$. Due to the reductive conditions applied and the fact that RuNPs are good hydrogenation catalysts of arenes [10], hydrogenation of aromatic groups during the synthesis of nanoparticles has already been observed in our group. For instance, on the surface of PPh_3-stabilized RuNPs, besides the ^{31}P MAS chemical shift corresponding to the PPh_3 ligand, a signal attributed to the hydrogenated phosphine was observed. The presence of hydrogenated species PCy_3 was confirmed by oxidation of the RuNPs surface species upon addition of H_2O_2, and ^{31}P NMR analysis of the resulting solution [8].

2D DOSY experiments were conducted in order to get information on the mobility of the different $[RuPMe]^+$ species present in solution. The corresponding plots are presented in Figure 12. The diffusion curve can be fitted with two diffusion coefficients, namely $D_1 = 4.0(\pm0.2)\cdot10^{-10}$ m^2/s and $D_2 = 10.0(\pm0.3)\cdot10^{-10}$ m^2/s, with a population ratio of $60/40(\pm5)$. The lowest value, D_1, corresponds to species that are poorly mobile and can thus be attributed to the hybrid nanomaterial $([RuPMe]_n\text{-}RuNPs)^+(PF_6^-)_n$ in which the $[RuPMe]^+$ complexes are directly coordinated to the surface of the RuNPs, forming an inner stabilizing layer. The second value, D_2, is higher to D_1 assigned to the nanohybrid but a bit lower than that obtained for the free $[RuPMe]^+PF_6^-$ in the same conditions ($D_{[RuPMe]PF6} = 1{,}3\cdot10^{-9}$ m^2/s, see Table 2). This second value, D_2, may thus be attributed to species of

higher mobility than the hybrid but not as mobile as the free complex. This indicates that $[RuPMe]^+$ entities other than those directly coordinated to the RuNP surface are present. Our previous hypothesis about the existence of two different layers of $[RuPMe]^+$ complexes around the RuNPs is thus supported by the 2D DOSY experiments data. As earlier proposed in this chapter, given the ionic character of the mononuclear organophosphorus polypyridyl $[RuPMe]^+$ complexes, one can reasonably propose an electrostatic interaction between the hybrid nanomaterial $([RuPMe]_n\text{-}RuNPs)^+(PF_6^-)_n$ and the entities named as $[RuPMe]^+_{exch}$, located in an outer layer. Such electrostatic interactions involve some dynamics and exchange of the $[RuPMe]^+_{exch}$ species between the outer layer and the solvent. However, it seems that the electrostatic interaction is strong enough to have limited the elimination of these $[RuPMe]^+_{exch}$ entities during the purification step of the sample (THF washings). Figure 12 (left) shows the ^1H NMR projections corresponding to the species diffusing at D_1 and D_2. The species diffusing at D_2, $[RuPMe]^+_{exch}$, display sharper signals, thus accounting for a main contribution of the weakly coordinating species. D_1 is associated to species directly coordinated to the RuNP surface, $([RuPMe]_n\text{-}RuNPs)^+(PF_6^-)_n$, with hindered mobility, and thus present a broader signal.

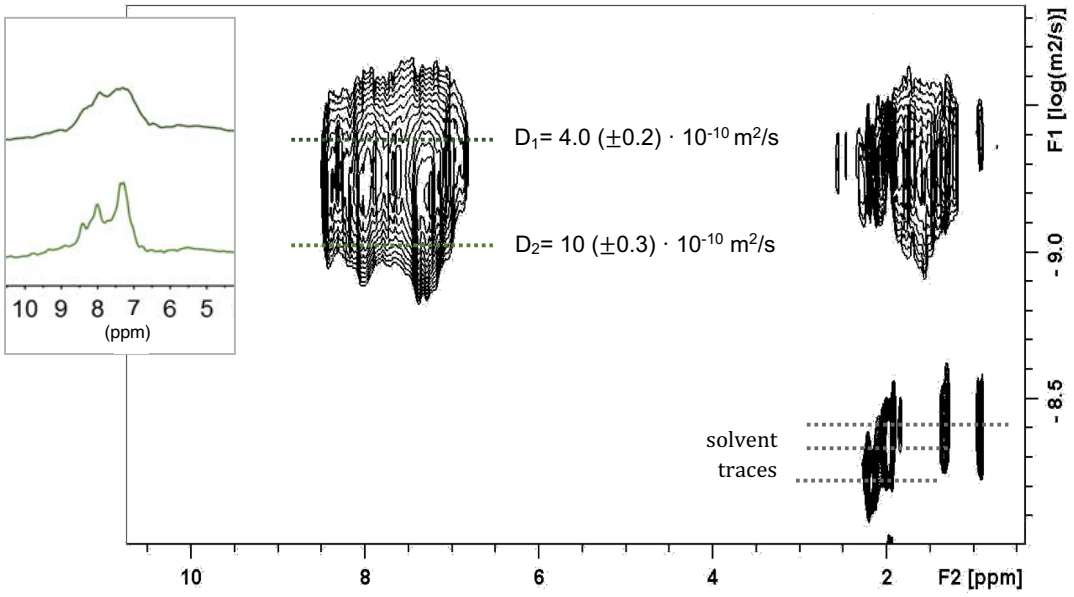

Figure 12. 2D DOSY plot of $([RuPMe]_n\text{-}RuNPs)^+(PF_6^-)_n$ in CD_3CN, with the ^1H NMR projections of the species in the inner layer (D_1) and outer layer (D_2).

By the Stockes-Einstein equation one can correlate the diffusion coefficient of an entity with its hydrodynamic radius, for a given solvent and temperature (see Experimental Section). Applying this equation, for the diffusion coefficient D_1, attributed to the $([RuPMe]_n\text{-}RuNPs)^+(PF_6^-)_n$ hybrid material where the $[RuPMe]^+$ complexes are strongly coordinated to the surface of the RuNPs, an hydrodynamic diameter of 3.0 nm can be estimated in acetonitrile. In the same way, the diffusion coefficient of the

free $[RuPMe]^+PF_6^-$ measured in the same conditions, corresponds to an hydrodynamic diameter of 0.85 nm (see Table 2).

	Species	Diffusion coefficient, D (m^2/s)	Hydrodynamic diameter, d_h (nm)
free	$[RuPMe]^+PF_6^-$	$1.3 \cdot 10^{-9}$	0.85
hybrid	$([RuPMe]_n\text{-}RuNPs)^+(PF_6^-)_n$ (RuNPs and directly coordinated $[RuPMe]^+$ species, D_1)	$4.0(\pm 0.2) \cdot 10^{-10}$	3.0
	$[RuPMe]^+_{exch}$ (outer layer, D_2)	$10.0(\pm 0.3) \cdot 10^{-10}$	-

Table 2. List of diffusion coefficients and hydrodynamic diameters obtained for the free $[RuPMe]^+PF_6^-$ complex, the hybrid $([RuPMe]_n\text{-}RuNPs)^+(PF_6^-)n$ and the $[RuPMe]^+_{exch}$ in the outer layer, in CD_3CN.

Given a mean size of ca. 1.4 nm corresponding to the ruthenium metal core determined from TEM analysis, the diameter of the hybrid $([RuPMe]_n\text{-}RuNPs)^+(PF_6^-)_n$, composed by the ruthenium core surrounded by a layer of $[RuPMe]^+$ complexes can be estimated. To the 1.4 nm metal core, the hydrodynamic diameter of $[RuPMe]^+$ corresponding to the stabilizer layer around the RuNP has been added (2 x 0.84 nm), which results in a total diameter of 3.1 nm for the $([RuPMe]_n\text{-}RuNPs)^+(PF_6^-)_n$ hybrid. So, the value of 3.0 nm calculated from the diffusion coefficient D_1 seems to be in good accordance with the value estimated above.

^{31}P NMR spectroscopy gave also valuable information on the structure of the hybrid. In the ^{31}P NMR$\{^1H\}$ spectrum of purified $([RuPMe]_n\text{-}RuNPs)^+(PF_6^-)_n$ the relative intensity of the two phosphorus signals is different from that of the $[RuPMe]^+PF_6$ free complex (1:1) (see Figure 13). The septuplet of PF_6^- at -144.6 ppm is well resolved. This indicates that this counteranion is totally solvated by acetonitrile, preserving its molecular dynamics and located away from the influence of the surface of the RuNPs. In marked contrast, the intensity of the phosphorus signal of the PPh_2Me ligand is considerably lowered. The small peak at 27.3 ppm, which matches well that of the $[RuPMe]^+PF_6^-$ complex, can be attributed to $[RuPMe]^+_{exch}$ species present in the outer layer of the $([RuPMe]_n\text{-}RuNPs)^+(PF_6^-)_n$ hybrid, as already observed by ^1H NMR.

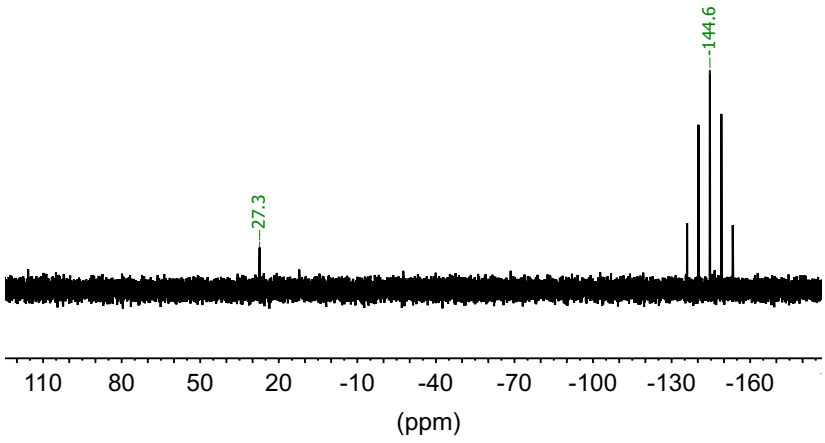

Figure 13. ^{31}P NMR spectrum of purified hybrid nanomaterial $([RuPMe]_n\text{-}RuNPs)^+(PF_6^-)_n$ in CD_3CN.

As it has been previously noted, the resonances of molecules in close interaction with nanoparticles are strongly influenced by their reduced dynamics and the heterogeneous chemical environment of the NP surface. The $[RuPMe]^+$ species directly coordinated to the RuNP surface, besides being in a very heterogeneous environment which makes the ^{31}P signal very broad, are in low concentration. The combination of these two cases complicates the observation of the ^{31}P of the PPh_2Me ligand close to the surface by the recording conditions applied. Even if a large number of scans was applied, the signal to noise ratio is still too high. It was possible, however, to observe the ^1H signals of the same species, since in this case the concentration of protons around the RuNPs is much higher than that of phosphorous.

At this stage of our studies, we can propose a representation of the hybrid $([RuPMe]_n\text{-}RuNPs)^+(PF_6^-)_n$ interacting with the $[RuPMe]^+_{exch}$ species as illustrated in Scheme 3.

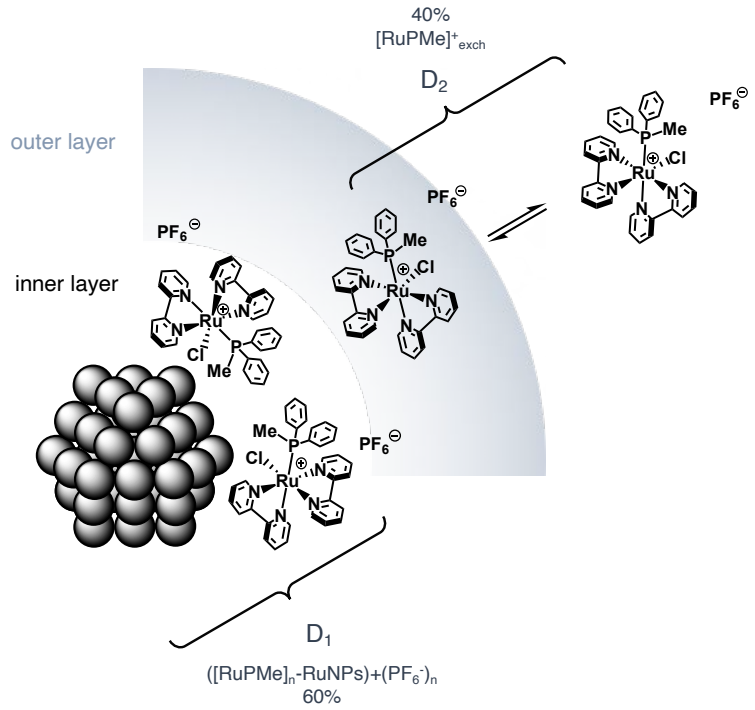

Scheme 3. Schematic representation of the organization of $[RuPMe]^+$ species around the metal cores in the hybrid material on the basis of NMR data.

4.2.2. Solid-state NMR spectroscopy

Even if the spectra recorded were significantly affected by signal broadening, liquid ^1H NMR techniques gave valuable information on the structure of the hybrid, (i) evidencing the presence of both $[RuPMe]^+$ complexes directly interacting with the NP surface and $[RuPMe]^+$ complexes standing in an outer sphere around the RuNPs, as well as (ii) on their respective dynamics in solution. ^{31}P nuclei are notably less concentrated in our sample and the information we could get from liquid ^{31}P NMR data was limited. In this section, the data obtained using solid state Magic Angle Spinning (MAS) solid-state NMR are discussed. ^{31}P and ^{13}C MAS solid-state NMR spectra were recorded at a mechanic high-speed rotation in order to minimize the effects of heterogeneity and low mobility of the hybrid sample.

To perform the solid-state NMR experiments some difficulties were met. Indeed, the purified $([RuPMe]_n\text{-}RuNPs)^+(PF_6^-)_n$ has a strong metallic character and an important electric arcing effect appeared when the radiofrequency pulse was applied to the sample, which shielded the NMR signal and did not allow to pursue the experiment. Such a phenomenon had already been observed for other measures on metal-riched ruthenium nanoparticles in the group. In order to be able to record solid-state NMR data, the nanohybrid material $([RuPMe]_n\text{-}RuNPs)^+(PF_6^-)_n$ was then deposited onto an inorganic support, a SiO_2 powder, by an impregnation technique. The SiO_2 support was impregnated with a colloidal solution of the purified hybrid and then dried under vacuum to eliminate the volatiles (see Experimental Section). This alternative, previously applied in the group to characterize RuNPs

capped with ethanoic acid [28] can be viewed as a dilution of the nanomaterial in an inorganic media which allowed to isolate the RuNPs from one to another and then minimize the arcing effect. The optimal concentration was found to be 8.5 mg of $([RuPMe]_n\text{-}RuNPs)^+(PF_6^-)_n$ per 100 mg of SiO_2. For comparison purposes, the free $[RuPMe]^+PF_6^-$ complex was also adsorbed onto the same SiO_2 powder in order to perform solid-state NMR experiments in the same conditions.

Compared to what has been observed in NMR experiments recorded in solution, solid-state ^{31}P MAS NMR of $([RuPMe]_n\text{-}RuNPs)^+(PF_6^-)_n$ in SiO_2 (Fig. 14b) have comparable features to those of the free $[RuPMe]^+PF_6^-$ complexes in SiO_2 (Fig. 14a) but with broader signals due to local chemical heterogeneity around the ^{31}P nucleus. As seen on Figure 14c, the Carr-Purcell-Meiboom-Gill (CPMG) sequence [48,49] was applied in order to improve the signal to noise ratio. This allowed to better detect an intense PF_6^- signal at ca. -144 ppm and another one of lower intensity standing out at 26 ppm. Due to its chemical shift and sharpness, the peak at 26 ppm can be attributed to $[RuPMe]^+_{exch}$ species located in the outer layer. Beneath this peak, a considerably broader band centered at 33 ppm is also identified and assigned to the organophosphorus PPh_2Me ligand of the $[RuPMe]^+$ complex directly attached to the RuNPs. The broadness of this signal is due to the fact that these $[RuPMe]^+$ entities are more affected by the heterogeneity of the NP surface, as previously observed for liquid NMR. Broad ^{31}P resonances for phosphine-stabilized metal nanoparticles have been commonly observed. IrNPs stabilized by secondary phosphine oxides [39] or PTA-stabilized RuNPs [46] are some examples. In those cases, the phosphorous atom of the ligand is directly coordinated to the surface of the nanoparticle, which explains signal enlargement. In our system, the phosphorous atom of the PPh_2Me ligand is not directly bound to the ruthenium surface, but the broad ^{31}P signal observed indicates that the organophosphorus fragment is very close to the surface. Therefore, the shape of this signal is largely influenced by the heterogeneous chemical environment of the RuNPs' surface.

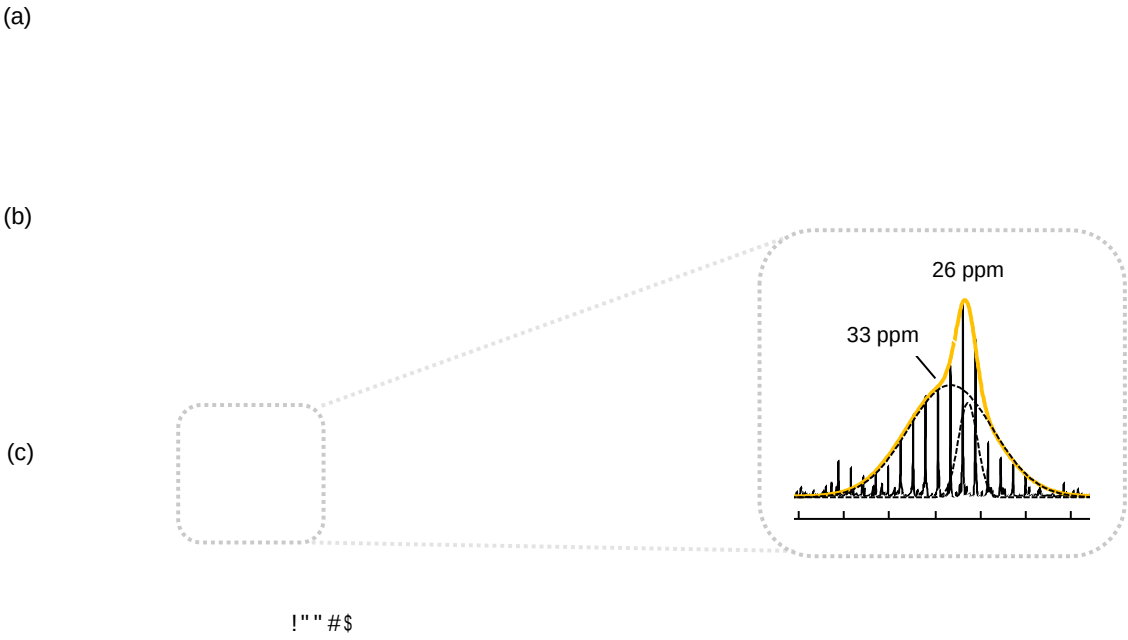

Figure 14. Solid-state ^{31}P MAS NMR of (a) free $[RuPMe]^+PF_6^-$ in SiO_2, (b) $([RuPMe]_n\text{-}RuNPs)^+(PF_6^-)_n$ in SiO_2 and (c) ^{31}P CPMG MAS NMR of $([RuPMe]_n\text{-}RuNPs)^+(PF_6^-)_n$ in SiO_2.

The ^{13}C MAS solid-state NMR spectrum of the hybrid (Figure 15b) displays aromatic signals in the range of 110-160 ppm similarly to that observed for the free complex $[RuPMe]^+PF_6^-$ (Figure 15a). Aliphatic carbons centered at ca. 28 ppm are also observed, that could correspond to the aliphatic protons already observed by liquid ^1H NMR. These aliphatic carbons could correspond to partially hydrogenated PPh_2Me organophosphorus fragments. This hypothesis is substantiated by previous studies in the group where hydrogenation of aromatic parts of phosphine ligands used to stabilize RuNPs has been detected by NMR. In the study previously cited [8], in which PPh_3 ligands were used to stabilize RuNPs, the ^{13}C MAS spectrum displayed two different groups of ^{13}C signals. A set of signals attributed to the aromatic groups of the PPh_3 ligand and centered at 129 ppm, and a second signal in the range of 26 ppm, assigned to the hydrogenation of the phenyl groups. Note that these chemical shift at 26 ppm for hydrogenated PPh_3 ligands is in the same area of that observed for the aliphatic carbons of the hybrid nanomaterial $([RuPMe]_n\text{-}RuNPs)^+(PF_6^-)_n$.

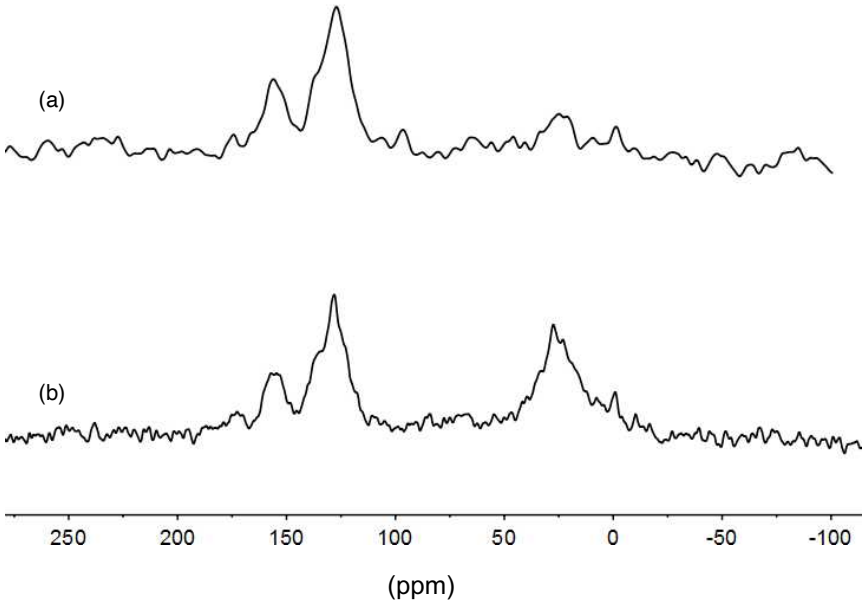

Figure 15. Solid-state ^{13}C MAS NMR of (a) free $[RuPMe]^+PF_6^-$ in SiO_2 and (b) $([RuPMe]_n\text{-}RuNPs)^+(PF_6^-)_n$ in SiO_2.

The combination of solid and liquid-state NMR experiments allowed to determine the presence of $[RuPMe]^+$ species on the surface of RuNPs. The results obtained are consistent with the existence of two different populations of $[RuPMe]^+$ species in the hybrid: a major population of $[RuPMe]^+$ species that lay at the close environment of the surface and form an inner layer, together with a minor fraction of $[RuPMe]^+$ species that are in electrostatic interaction with the hybrid $([RuPMe]_n\text{-}RuNPs)^+(PF_6^-)_n$ thus forming an outer layer. Due to its cationic character, the $[RuPMe]^+$ complex in the outer layer probably displays electrostatic interaction with its counterparts from the inner layer.

4.3. Quantification of hydrides and CO adsorption modes: a surface study on the $([RuPMe]_n\text{-}RuNPs)^+(PF_6^-)_n$ hybrid

4.3.1. Titration of hydrides at the surface of the hybrid nanomaterial

The reaction conditions used for the synthesis of RuNPs by the organometallic approach, namely a treatment under dihydrogen pressure, entail the adsorption of hydrides on the metal surface. These hydride species are known to take part in the stabilization of the growing surface and their quantification is taken as a standard to evaluate the coverage and accessibility of the RuNPs surface [6].

The method applied in our group for the quantification of hydrides present on the surface of nanoparticles, H_{reac}/Ru_{surf} (reacted hydride species per Ru surface atoms), is based on the reaction of

the metal NPs with 2-norbornene without addition of extra source of hydrogen (Scheme 4). Using this experimental procedure only hydrogen atoms coordinated on the surface of the NP surface can lead to hydrogenation of the olefinic bond of 2-norbornene. This procedure was firstly applied in the group [50] to quantify the reactive hydrides at a metal surface of RuNPs stabilized by PVP, HDA and dppd ligands (HDA = hexadecylamine; dppd = 1,10-bis(diphenylphosphino)decane). Values in the range of 1.1 – 1.3 H_{reac}/Ru_{surf} were obtained for those systems.

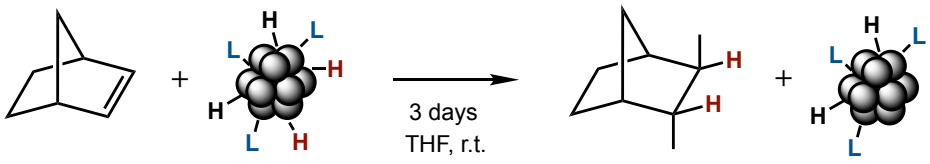

Scheme 4. Surface hydrides titration by the hydrogenation of 2-norbornene.

A batch of $([RuPMe]_n\text{-}RuNPs)^+(PF_6^-)_n$ hybrid was thus prepared by the usual method. Then, 5 cycles of vacuum/argon were applied to the crude colloidal solution, in order to evacuate the H_2 dissolved in the THF. Ca. 5 eq. of 2-norbornene per mol of [Ru(cod)(cot)] initially introduced for the synthesis of the nanohybrid material were added, and the mixture was stirred for 72 h at room temperature. Then, the hydrogenation of 2-norbornene into norbornane was analyzed by gas chromatography (see experimental section). The number of hydrides involved in the reduction reaction, coming from the surface of the RuNPs, is deduced from the mol of norbornane produced (2 mol of H_{reac}/mol norbornane) while taking into account the mean diameter of the nanoparticles as determined by TEM and the equations below.

Equation (1) was used to estimate the total number of atoms per nanoparticle, N_T

$$(1) \qquad N_T = \left(\frac{d_m}{2r_{Ru}b}\right)^3$$

Where d_m is the nanoparticle diameter (measured by TEM), r_{Ru} is the atomic radius of a Ru atom (146 pm) and b is the crystalline closed-packed parameter (b=1.105)

Equations (2) and (3) were used to estimate the number of shells per nanoparticle, n, and the number of surface atoms, N_{surf}, respectively

$$(2) \qquad N_T = \frac{1}{3}(10n^3 - 15n^2 + 11n - 3)$$

$$(3) \qquad N_{surf} = 10n^2 - 20n + 12$$

The amount of H atoms involved in the reduction of norbornene, n_H, was calculated by equation (4), considering the quantity of norbornane produced as determined by gas chromatography – mass spectrometry (GC-MS).

$$n_H = 2 \cdot n_{norbornane} \quad (4)$$

Finally, the ratio H_{reac}/Ru_{surf} is obtained by equation (5)

$$H_{reac}/Ru_{surf} = \left(\frac{n_H}{n_{Ru}}\right)\left(\frac{N_{surf}}{N_T}\right) \quad (5)$$

where n_{Ru} is the number of moles of ruthenium used for the synthesis.

An hcp RuNP of 1.4 nm is constituted of ca. 106 Ru atoms, of which ca. 70 stand on the surface, what makes a ratio of 0.66 Ru_{surf} /Ru (detailed calculations can be found in the Experimental Section). Dividing the number of reacted hydrides by the number of Ru_{surf} atoms leads to a value of 1.6 H_{reac} per Ru_{surf} for $([RuPMe]_n\text{-}RuNPs)^+(PF_6^-)_n$ hybrid nanomaterial.

Applying the same methodology, a value of 0.3 H_{reac}/Ru_{surf} was estimated for RuNPs stabilized with ethanoic acid [28], 1.1 H_{reac}/Ru_{surf} when using 4-phenylpyridine [25] and bis(diphenylphosphino)butane and 1.3 H_{reac}/Ru_{surf} with the polymer PVP [50]. Thus, our hybrid system seems to have a higher amount of surface hydrides than previous systems involving organic ligands as stabilizers of RuNPs. This might confirm an unusual surface coverage of the RuNPs in the presence of the $[RuPMe]^+$ complexes as only stabilizers. The H_{reac}/Ru_{surf} ratio obtained for the $([RuPMe]_n\text{-}RuNPs)^+(PF_6^-)_n$ system, besides underlining the particular effect of the $[RuPMe]^+$ stabilizer, will be considered for further theoretical discussions (see section 5 of this Chapter).

4.3.2. Adsorption of CO at the surface of the hybrid nanomaterial

Followed by IR-FT and NMR spectroscopies, coordination of CO has been commonly used in our group as a means to probe the accessibility of RuNPs surface atoms and the presence of potential active sites (free metal atoms besides those occupied by the stabilizing ligands or solvent molecules non exchanged by CO). This technique also allows to determine the location of the stabilizing ligands as their proximity with CO molecules adsorbed at the metal surface can be deduced from the CO characteristics (position and pattern observed) [6]. CO is a small molecule that strongly adsorbs on the surface of RuNPs, being able to coordinate in a terminal mode (CO_t) or in a bridging mode (CO_b) (see Fig. 16). It is commonly accepted that CO coordinates to edges and apexes in the terminal mode and to facets in the bridging mode [17]. There are, however, other considerations that must be taken into account. In a study conducted in our group [35], PVP-stabilized RuNPs were exposed to 0.5 bar of ^{13}CO

and the reaction was followed by ^{13}C solid-state NMR spectroscopy. A broad band centered at 245 ppm first appeared, assigned to CO_b. For longer exposure times, the band at 245 ppm disappeared and a sharper band at ca. 200 ppm, corresponding to CO_t, became predominant. These observations, which were similar for RuNPs-dppb systems (dppb = bisdiphenylphosphinobutane), indicate that the coordination mode of CO may also depend on the gas concentration and/or reaction time.

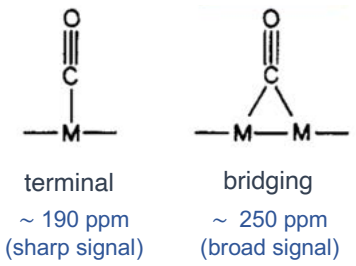

Figure 16. Different CO coordination modes on metal-based nanoparticle surfaces and their related ^{13}C solid-state NMR chemical shifts, reproduced from ref. [51].

Thus, $([RuPMe]_n\text{-}RuNPs)^+(PF_6^-)_n$ hybrid previously adsorbed on SiO_2 was exposed to 1 bar of ^{13}CO for 24 h in a Fischer-Porter bottle. The excess of CO was then evacuated under vacuum and the hybrid sample introduced in an NMR rotor to be analyzed by ^{13}C MAS solid-state NMR. The corresponding spectrum is given in Figure 17.

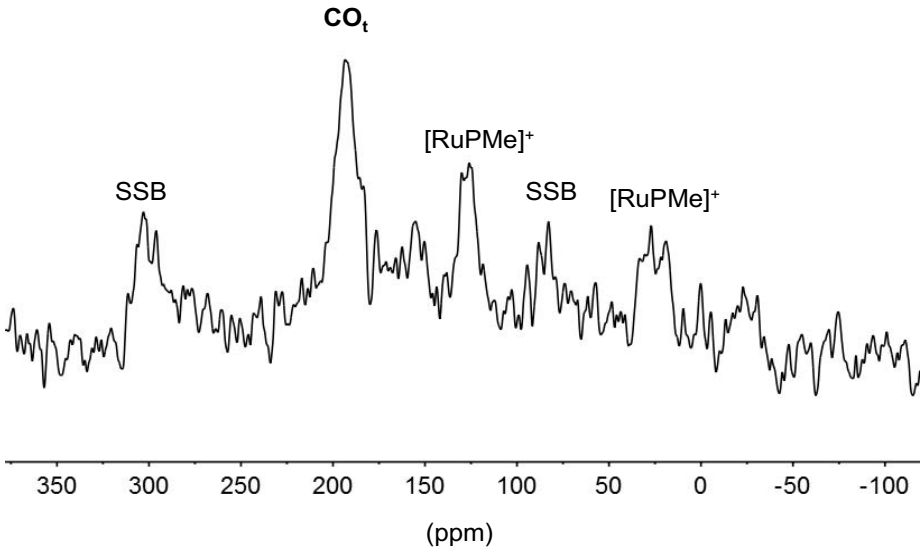

Figure 17. Solid-state ^{13}C CP MAS NMR of $([RuPMe]_n\text{-}RuNPs)^+(PF_6^-)_n$ onto SiO_2 after exposure to 1 bar ^{13}CO (SSB = Spinning side bands of the adsorbed ^{13}CO).

This spectrum shows several signals, among which, one can distinguish two broad chemical shifts centered at 125 and 25 ppm, that can be attributed to the aromatic and aliphatic carbons of the

[RuPMe]$^+$ species, respectively. The signal at 193 ppm is assigned to ^{13}CO molecules coordinated to the RuNP surface in a terminal mode. Close values of CO_t resonances were previously observed for RuNPs systems stabilized by betaine adduct ligands [52] and PPh_3 ligands [8] for example (CO_t at 199 ppm). The presence of spinning side bands (SSB) from either side of this signal indicates that these ^{13}CO molecules are bound in a relatively rigid mode compared to RuNPs stabilized by PVP [35], where the absence or low intensity of the SSBs is attributed to a fluxional character of the adsorbed ^{13}CO. CO is able to migrate on a metal surface free of strongly coordinating molecules. Indeed, PVP is often considered to weakly interact with the Ru surface, thus offering Ru_{surf} atoms free to accommodate CO with a high degree of freedom to move on the NP surface. On the contrary, lack of mobility of CO across the Ru surface is evidenced by intense SSB.

No signal indicating the presence of ^{13}CO in the bridging mode is observed for our system (expected signal at ca. 230 ppm). From these observations we can conclude that there are Ru surface atoms available for the coordination of ^{13}CO. With the experimental conditions used, only terminal ^{13}CO was detected, which can be due to the fact that (i) too high concentration of ^{13}CO was used and/or (ii) the surface of $([RuPMe]_n\text{-}RuNPs)^+(PF_6^-)_n$ is highly covered and ^{13}CO cannot coordinate in a bridging mode. Based on these data it would be reckless to attribute the CO_t coordination mode observed to facets, edges or apexes.

5. Theoretical calculations on the hybrid nanomaterial

With the experimental data in hands, Density Functional Theory (DFT) calculations were performed by close collaborators, Dr. I. del Rosal and Pr. R. Poteau (Laboratoire de Physique et Chimie des Nano-objects (LPCNO), Toulouse), who already participated to studies on RuNPs systems prepared by our group. The aim of these DFT calculations was to get a deeper insight in the nature of the coordination modes of the [RuPMe]$^+$ units on the surface of the ruthenium nanoparticles. The role of the PF_6^- counter ion was also studied and completed by additional NMR experiments.

5.1. Coordination of the [RuPMe]$^+$ complex at the RuNP surface

A Ru_{55} cluster model, which corresponds to a RuNP core of ca. 1 nm, has been chosen to perform the DFT calculations. As it has been previously mentioned, the Ru_{55} cluster is an optimized model that represents the characteristic surface sites of small hcp RuNPs. The DFT periodic calculations on the metal cluster have been performed using the Vienna *ab initio* simulation package (VASP) (spin polarized DFT and exchange–correlation potential approximated by the generalized gradient approach proposed by Perdew, Burke and Ernzerhof (PBE)). In a preliminary study and in order to

measure the compatibility of the method with the molecular structure, the experimental crystallographic parameters of the $[RuPMe]^+PF_6^-$ complex were compared to those calculated by the theoretical approximation employed (PBE-DFT). Figure 18 shows that the simulated geometry is in good agreement with the bond lengths obtained by X-ray diffraction (XRD). The use of the chosen DFT model is thus adequate for the study of the $([RuPMe]_n\text{-}RuNPs)^+(PF_6^-)_n$ system.

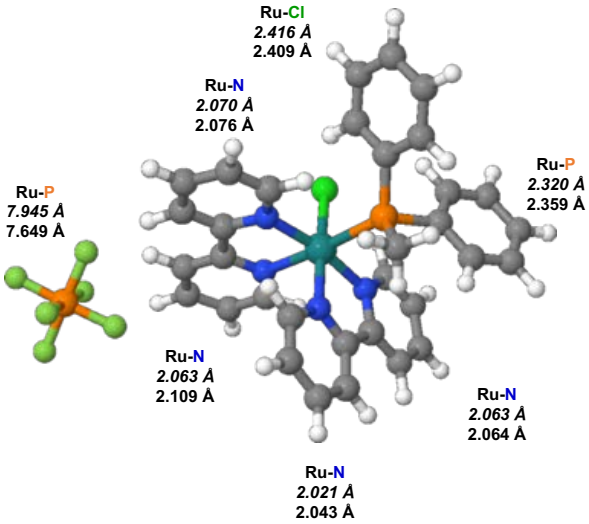

Figure 18. Comparison of the X-Ray (italic) and PBE-DFT geometries (plain) of $[RuPMe]^+PF_6^-$.

DFT calculations were then performed on the Ru_{55} model with a pre-stablished 0.8 hydride/Ru_{surf} ratio ($Ru_{55}H_{35}$). The simulations pointed to a favorable coordination of the $[RuPMe]^+$ complex at the RuNP surface through the σ-donation of the chlorine atom lone pair, thus forming a Ru-Cl-Ru bridge, an interaction mode which is commonly observed for some dimeric ruthenium complexes [53,54]. The adsorption energy of the $[RuPMe]^+$ complex through the chlorine ligand is ca. -33.8 kcal/mol (Fig. 19b). In the most favorable conformer (Fig. 19a), an additional aromatic π-type chelating interaction between one of the bipyridine ligands of the $[RuPMe]^+$ complex and an adjacent Ru surface atom stabilizes the structure by around 10 kcal/mol, and results in a total adsorption energy of -41.4 kcal/mol. The adsorption energy value of -33.9 kcal/mol obtained for $[RuPMe]^+$ simultaneously interacting with the RuNP by the chlorine and the π-electron density of one of the phenyl rings (Fig. 19c) is very similar to that calculated for the complex coordinated through the chlorine alone (-33.8 kcal/mol).

Interaction of $[RuPMe]^+$ complex by a phenyl ring (-29.5 kcal/mol, Fig. 19d) or one of the bipyridine ligands (-25.7 kcal/mol, Fig. 19e) has also been calculated, but the corresponding adsorption energies are significantly less favorable than the others.

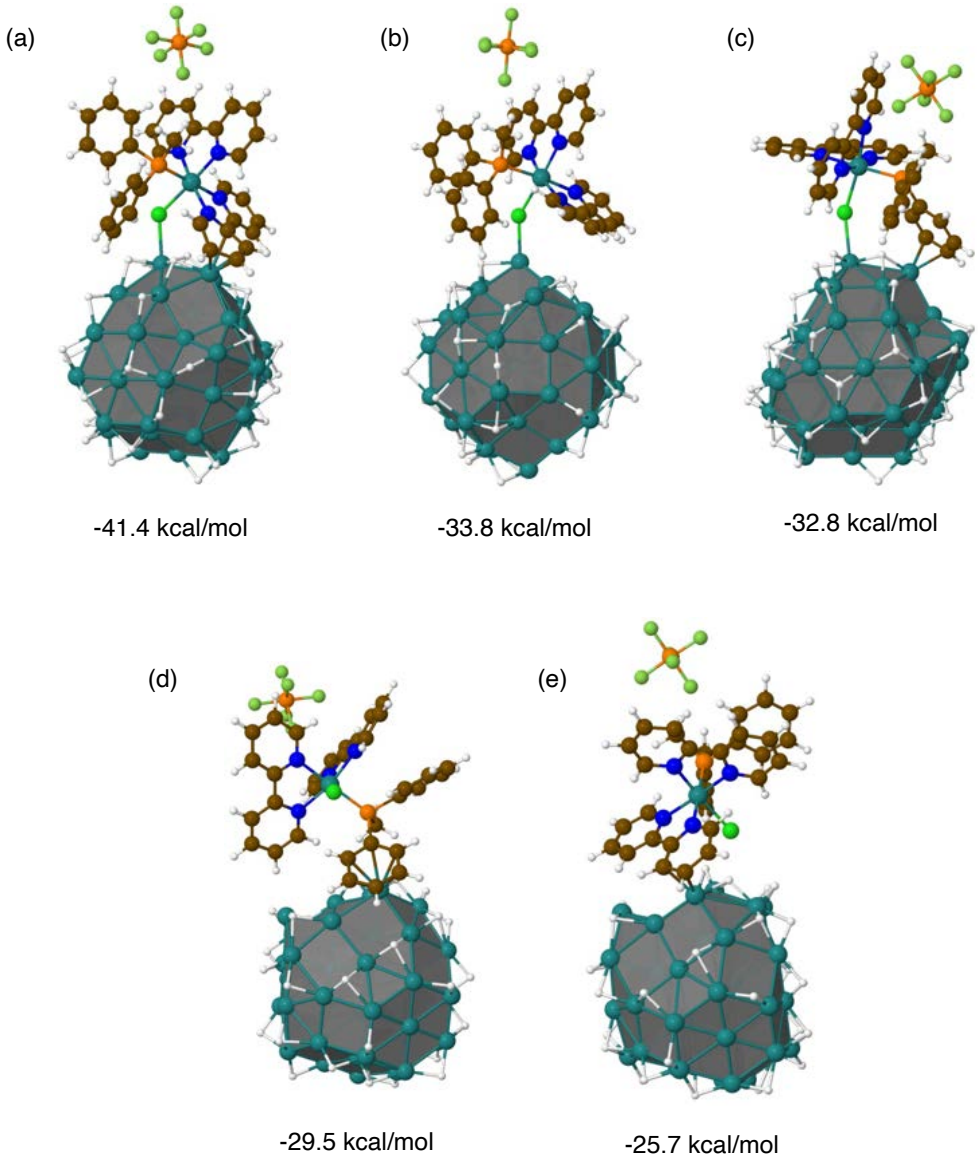

Figure 19. Stable coordination modes of the $[RuPMe]^+$ complex on the surface of a Ru_{55} cluster and related adsorption energies.

From a structural point of view, the coordination of the $[RuPMe]^+$ complex at the RuNP surface induces only slight geometrical modifications on the complex (Figure 20), such as the elongation of the Ru – Cl bond (by 0.05 Å) as well as the C – N and C – C bonds of the bipyridine ligand interacting with the surface (by 0.07 and 0.04 Å, respectively). A back-donation from the d-electron density of the Ru surface towards the π^*-antibonding orbitals of the pyridine cycle explains the elongation of the C – N and C – C bonds.

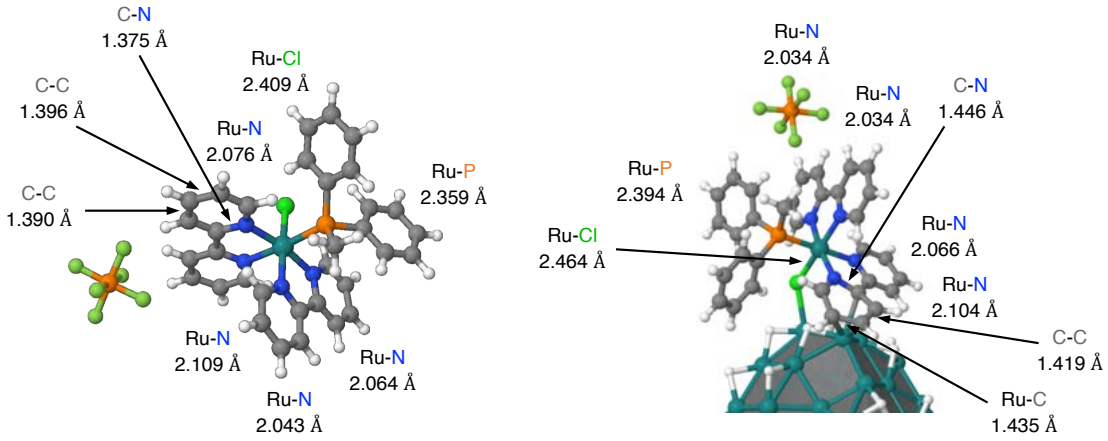

Figure 20. Characteristic bond lengths of $[RuPMe]^+$ free (left) and bound to the Ru_{55} cluster in the most stable coordination mode (right).

To confirm the preservation of the structure of the $[RuPMe]^+$ complex when coordinated to the surface, the activation of the Ru – Cl bond by the RuNP surface leading to the formation of a Ru – Ru bond and μ-Cl capping one edge of the RuNP has been considered. An adsorption energy of -40.3 kcal/mol is obtained for the resulting structure (see Figure 21a). The thermal energy related to this process is slightly endothermic (ΔE = 1.1 kcal/mol) regarding the most stable configuration (-41.4 kcal/mol, Fig. 19a), and this low energy difference could be questioned.

Further energy clues using a $Ru_{13}H_{17}$ model cluster were thus calculated. Such Ru_{13} cluster model allows faster calculi than Ru_{55}, while displaying the same surface cases [55]. Besides, the $Ru_{13}H_{17}$ cluster used presents a ratio of ca. 1.4 hydrides/Ru_{surf}, which is closer to the value obtained experimentally (ca. 1.6). In the two considered coordination modes (one very similar to the one depicted in Fig. 19a, whilst the second one could occur on sharp apexes) the undissociated $[RuPMe]^+$ complex is thermodynamically more stable than its dissociated counterpart by significant values of ca. 10 and 12.5 kcal/mol (Fig. 21b). It is thus assumed that the adsorbed $[RuPMe]^+$ keeps its structural integrity.

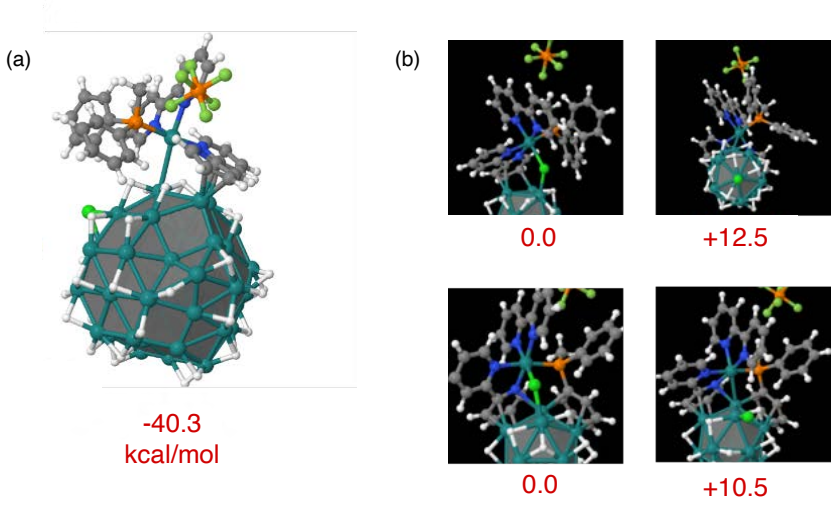

Figure 21. (a) Cleavage of the Ru-Cl bond of $[RuPMe]^+$ by the RuNP surface and related adsprtion energy. (b) Two possible coordination modes on a $Ru_{13}H_{17}$ scale model. Energy differences of the $[RuPMe]^+$ complex after Ru-Cl cleavage with respect to the undissociated complex are given in kcal/mol.

By performing the simulations on a Ru_{55} cluster with higher surface hydride concentration than the pre-stablished 0.8 ratio (experimental value is ca. 1.6 hydride/Ru_{surf}) one could expect the adsorption energies of $[RuPMe]^+$ to be slightly less exothermic. For instance, the adsorption of bis(diphenylphosphino)butane (dppb), on the surface of a bare Ru_{55} cluster is favored by -124.6 kcal/mol, while on a hydrogenated cluster, $Ru_{55}H_{64}$ (1.5 hydrides/Ru_{surf}), the adsorption energy on the same surface site is of ca. -51.4 kcal/mol [56]. This difference is attributed to the steric hindrance of the H atoms that impedes the π-interaction between the phenyl rings and the Ru surface, as well as to the weakening of the Ru-P bond. On the other hand, the higher the number of hydrides on the surface, the less favored the activation of the Ru – Cl bond of $[RuPMe]^+$ by the RuNP is (as seen for the simulations performed on the $Ru_{13}H_{17}$ cluster), which also supports the assumption that the $[RuPMe]^+$ complex preserves its integrity when coordinated to the RuNP.

The maximum surface coverage of a 1 nm cluster by $[RuPMe]^+$ units has been estimated on the basis of a molecular builder and steric considerations. An approximate value of 5 $[RuPMe]^+$ molecules was obtained.

5.2. On the role of the PF_6^- anion in the hybrid structure

In the liquid ^{31}P NMR studies we have performed, the signal of PF_6^- always appeared unperturbed, thus suggesting that the PF_6^- anion is totally solubilized in the media and not affected by the RuNPs. Nevertheless, we found necessary to confirm this hypothesis in order to be able to discard any bonding of the PF_6^- anion to the surface by fluorine atoms.

From the theoretical point of view, for the most stable $([RuPMe]_n\text{-}RuNPs)^+(PF_6^-)_n$ configuration, the difference between having the PF_6^- in electrostatic interaction with the hybrid (initial consideration) or grafted onto the ruthenium surface is of ca. +7 kcal/mol (see Fig. 22).

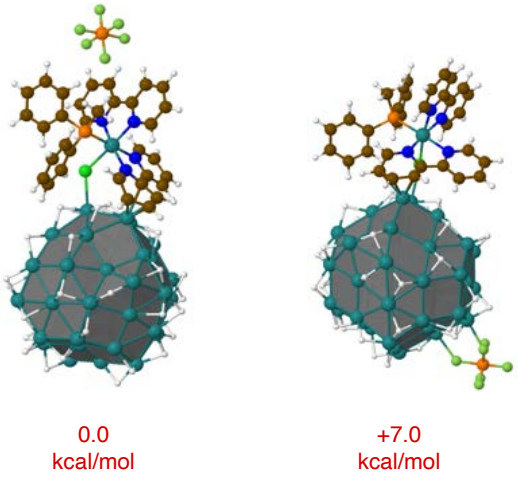

Figure 22. Adsorption energy differences of $[RuPMe]^+$ on Ru_{55} with PF_6^- in electrostatic interaction with the hybrid (left) or adsorbed on the surface (right).

Solid-state ^{19}F MAS NMR experiments were performed with the aim to conclude on the location of the PF_6^- anion in the nanohybrid material. For comparison purpose, a simulation on a Ru_6 cluster has been performed in order to predict the ^{19}F and ^{31}P NMR chemical shifts of the PF_6^- anion isolated (Fig. 23a) and adsorbed on a ruthenium surface in two different dispositions (Fig. 23b and 23c). For ^{19}F NMR of isolated PF_6^- no signal is expected at values lower than -100 ppm, while adsorption of the hexafluorophosphate anion on the Ru surface would give rise to ^{19}F resonances between -104 and -188 ppm.

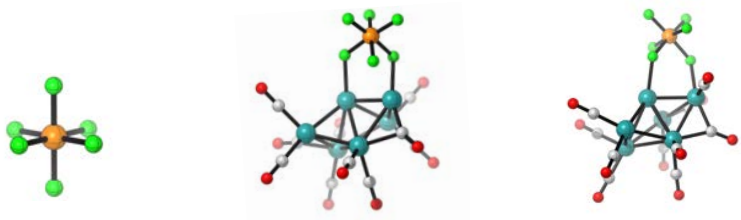

	(a)	(b)	(c)
^{19}F NMR	-76 ppm	-55 to -76 ppm -122 and -188 ppm	-63 to -79 ppm -104 and -124 ppm
^{31}P NMR	-145 ppm	-130 ppm	-124 ppm

Figure 23. Simulated ^{19}F and ^{31}P chemical shift values for a (a) free PF_6^- anion and (b) and (c) PF_6^- grafted on a Ru_6 cluster.

The experimental results obtained by solid-state ^{19}F MAS NMR are summarized in Figure 24. A KPF_6 salt has been used as a reference for the anion which provided a sharp doublet with a coupling constant $^1J_{P\text{-}F} \sim 720$ Hz. For $[RuPMe]^+PF_6^-$ and $[RuPMe]^+PF_6^-$ deposited onto SiO_2, signals centered at ca. -72 ppm together with a small doublet at -83 ppm ($^1J_{P\text{-}F} \sim 720$ Hz) were observed. Such behavior of the PF_6^- anion in $[RuPMe]^+PF_6^-$, not observed in KPF_6 and $([RuPMe]_n\text{-}RuNPs)^+(PF_6^-)_n$, could be attributed to different environments of the anion in the crystalline network of $[RuPMe]^+PF_6^-$ complex.

For $([RuPMe]_n\text{-}RuNPs)^+(PF_6^-)_n$ deposited onto SiO_2, only a broad signal centered at -73 ppm is observed (Fig. 24d) and there are no signals lower than -100 ppm. As suggested by the chemical shift simulations, these results allow to rule out the grafting of PF_6^- on the ruthenium surface. Interestingly, the PF_6^- signal in the ^{31}P CPMG MAS NMR described above (see section 4.2.2.) that is centered at ca. -144.6 ppm, is in strong agreement with the simulated one for free PF_6^- (- 145 ppm).

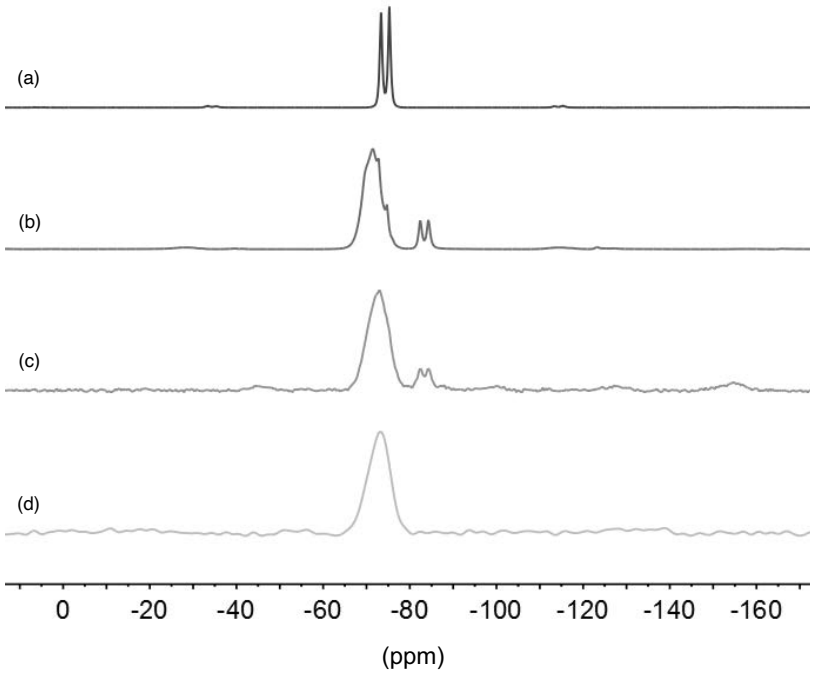

Figure 24. Solid-state ^{19}F MAS NMR of (a) KPF_6, (b) $[RuPMe]^+PF_6^-$, (c) $[RuPMe]^+PF_6^-$ on SiO_2 and (d) $([RuPMe]_n\text{-}RuNPs)^+(PF_6^-)_n$ on SiO_2.

The results of these ^{19}F solid state NMR studies combined with the simulations thus confirm the previously envisaged hypothesis from solution ^{31}P NMR experiments, that is, a PF_6^- anion which is far from the RuNP surface but in electrostatic interaction with the grafted complex. Additionally, the preparation of RuNPs using 0.2 eq. of $NaPF_6$ was attempted following usual RuNP synthesis conditions. This experiment wasn't successful and big precipitates were obtained. Only big aggregates were observed by TEM analysis and solution ^{31}P NMR on the supernatant revealed the only presence of the

usual signal of PF_6^- at -144.6 ppm. These last results indicate that, in the synthesis conditions applied, PF_6^- is not able to stabilize small RuNPs.

6. X-Ray Photoelectron Spectroscopy on $([RuPMe]_n\text{-}RuNPs)^+(PF_6^-)_n$

As DFT calculations gave us a valuable insight on the nature of the interaction between the $[RuPMe]^+$ complex and the RuNP surface, at this point, we complemented our experimental work by additional characterization using X-ray photoelectron spectroscopy (XPS). This study has been performed in collaboration with J. Esvan (CIRIMAT-ENSIACET, Toulouse).

XPS spectra were thus recorded from a powder of purified hybrid $([RuPMe]_n\text{-}RuNPs)^+(PF_6^-)_n$. Same measurement conditions (see below) were applied for the free $[RuPMe]^+PF_6^-$ complex, for direct comparison purposes. Taking into account the information gathered with the other characterization techniques, the focus was set on the Ru 3d, N 1s, Cl 2p, P 2p and F 1s regions of the spectra.

The first XPS measurements on $[RuPMe]^+PF_6^-$ and $([RuPMe]_n\text{-}RuNPs)^+(PF_6^-)_n$ were performed after deposition of the powders on a carbon scotch previously glued on a silicon wafer. KPF_6 and RuO_2 compounds were measured in the same conditions as references. The carbon contribution of the scotch used was not negligible and did not allow for a correct characterization nor quantification of the chemical species. This became particularly problematic to analyze the Ru3d contribution (278-290 eV) in the spectra which lays in the same region as the C1s responses (282-288 eV). Inhomogeneous distribution of the powder over the carbon scotch was also a source of imprecision.

A second set of measurements with $[RuPMe]^+PF_6^-$ and $([RuPMe]_n\text{-}RuNPs)^+(PF_6^-)_n$ were then performed from samples embedded onto an indium sheet (the sample powders were mechanically pressed to adhere to the indium foil). This second procedure for sample preparation allowed us to get better resolved XPS spectra with an increased signal to noise ratio. The spectra obtained, together with the tables summarizing the corresponding binding energies (BE) of the peaks observed, are presented hereafter.

As seen in Figure 25a, only one Ru chemical environment is detected for $[RuPMe]^+PF_6^-$, with peaks at 280.7 eV, 284.8 eV and 282.6 eV ($Ru3d_{5/2}$, $Ru3d_{3/2}$ and Ru3d satellite, respectively), that is reasonably attributed to Ru(II) metal center. In the same spectral region, 278-290 eV, the $([RuPMe]_n\text{-}RuNPs)^+(PF_6^-)_n$ hybrid displays different signals (Fig. 25b). First, two components are visible which can be assigned to metallic ruthenium: a $Ru3d_{5/2}$ peak at 279.8 eV, which is very close to the 280 eV reported value for Ru metallic [57], and a $Ru3d_{3/2}$ peak at 284 eV. Other peaks at 280.7 eV, 284.8 eV and 282.6 eV ($Ru3d_{5/2}$, $Ru3d_{3/2}$ and Ru3d satellite) can be attributed to the $[RuPMe]^+$ complex

since this latter displays itself these same three peaks. These results indicate that the integrity of the Ru(II) atom in the $[RuPMe]^+$ complex is preserved and that metallic RuNPs are present in the hybrid nanomaterial. However, a third Ru chemical environment is observed for $([RuPMe]_n\text{-}RuNPs)^+(PF_6^-)_n$, appearing at higher binding energies. Those energies, possibly related to Ru species in an electronegative environment, could thus be assigned to surface Ru-Cl bonds, as suggested by theoretical data.

Since the $([RuPMe]_n\text{-}RuNPs)^+(PF_6^-)_n$ powder was embedded onto the indium sheet under air, RuO_2 species could originate during the sample preparation. This was checked by determining the $Ru3d_{5/2}$ energy of a RuO_2 sample recorded as a reference (280.4 eV). At this stage of the study, if such RuO_2 species were present in the $([RuPMe]_n\text{-}RuNPs)^+(PF_6^-)_n$ sample their response would be difficult to detect as it would be covered by that of the $[RuPMe]^+$ complex (280.7 eV).

In both spectra (Fig. 25), signals for C1s carbon (287.7-284.6 eV) can derive from $[RuPMe]^+$ ligands or solvent traces (THF, CH_3CN).

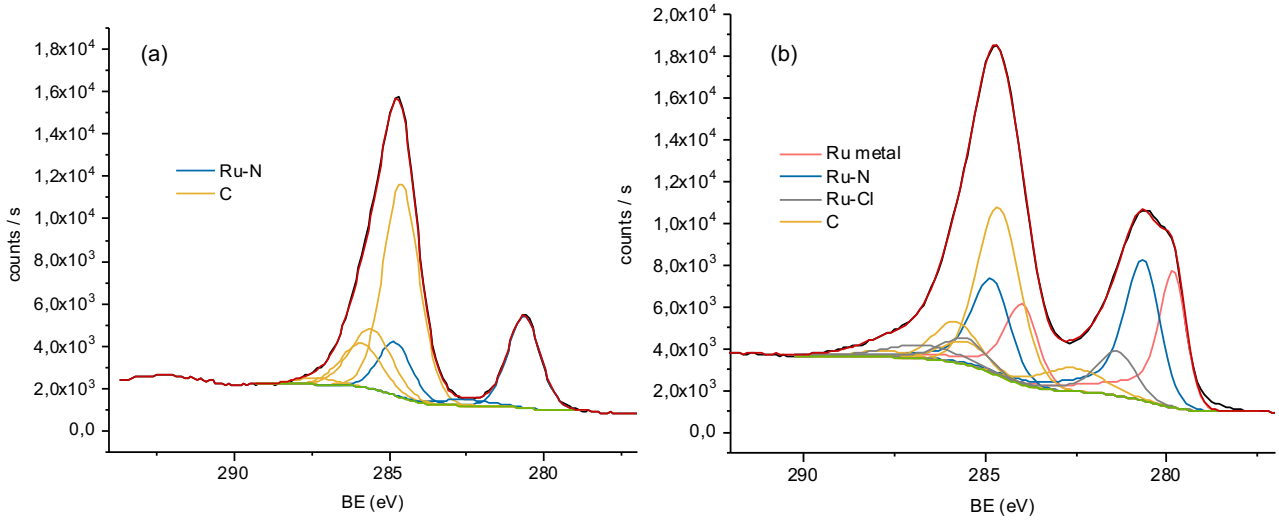

Figure 25. XPS spectra of Ru3d and C1s of (a) $[RuPMe]^+PF_6^-$ and (b) $([RuPMe]_n\text{-}RuNPs)^+(PF_6^-)_n$.

	$[RuPMe]^+PF_6^-$	$([RuPMe]_n\text{-}RuNPs)^+(PF_6^-)_n$
Ru		$Ru3d_{5/2}$ at 279.8 eV (Ru metal) $Ru3d_{3/2}$ at 284.0 eV (Ru metal)
	$Ru3d_{5/2}$ at 280.7 eV (Ru-N) Ru sat 282.6 eV (Ru-N) $Ru3d_{3/2}$ at 284.8 eV (Ru-N)	$Ru3d_{5/2}$ at 280.7 eV (Ru-N) Ru sat 282.6 eV (Ru-N) $Ru3d_{3/2}$ at 284.8 eV (Ru-N)
		$Ru3d_{5/2}$ at 281.4 eV (Ru-Cl) $Ru3d_{3/2}$ at 285.5 eV (Ru-Cl) Ru sat 286.7 eV (Ru-Cl)
C	C1s at 284.6 eV (CC, CH, sp^2) C1s at 285.9 eV (C-O, CN) C1s at 285.6 eV (sp^3, CN) C1s at 287.4 eV (C=O)	C1s at 284.6 eV (CC, CH, sp^2) C1s at 285.8 eV (C-O, CN) C1s at 285.5 eV (sp^3, others) C1s at 287.7 eV (C=O)

Table 3. XPS data on Ru3d and C1s of $[RuPMe]^+PF_6^-$ and $([RuPMe]_n\text{-}RuNPs)^+(PF_6^-)_n$.

In $[RuPMe]^+PF_6^-$, the N1s signal of the bipyridine ligands is located at 399.9 eV. Interestingly, the $([RuPMe]_n\text{-}RuNPs)^+(PF_6^-)_n$ displays a same peak at 399.9 eV together with a second peak at 398.0 eV which indicates a different chemical environment (Figure 26). As previously pointed by the DFT calculations, in the most stable hybrid configuration, one of the bipyridine rings of the $[RuPMe]^+$ complex is engaged in a π-type interaction with a Ru surface atom. This interaction of the one bipyridine with the surface could possibly be at the origin of the second N1s peak observed at lower binding energies for the $([RuPMe]_n\text{-}RuNPs)^+(PF_6^-)_n$ hybrid.

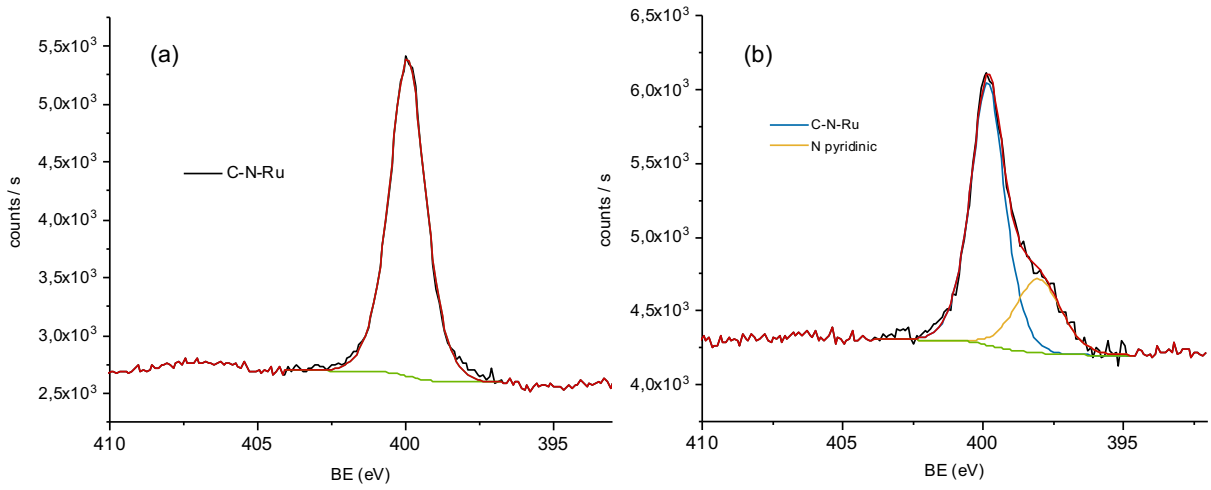

Figure 26. XPS spectra of N1s of (a) $[RuPMe]^+PF_6^-$ and (b) $([RuPMe]_n\text{-}RuNPs)^+(PF_6^-)_n$.

	$[RuPMe]^+PF_6^-$	$([RuPMe]_n\text{-}RuNPs)^+(PF_6^-)_n$
N	N1s at 399.9 eV (C-N-Ru)	N1s 398.0 eV (pyridinic) N1s at 399.9 eV (C-N-Ru)

Table 4. XPS data on the N1s of $[RuPMe]^+PF_6^-$ and $([RuPMe]_n\text{-}RuNPs)^+(PF_6^-)_n$.

The Cl 2p signals of $[RuPMe]^+PF_6^-$ and $([RuPMe]_n\text{-}RuNPs)^+(PF_6^-)_n$ are very similar (Figure 27). Two different Cl environments are observed in both cases: (i) peaks at 197.5 and 199.1 eV, assigned to a Cl-Ru environment (complex), and (ii) peaks at 198.4 and 200.0 eV, that could not be attributed. Given the results of the DFT calculations, which indicated a coordination of the Cl to the Ru surface *via* a σ-donation of one of its lone pairs, one could expect a Cl 2p shift to higher binding energies. This shift, however, has not been observed by our XPS measurements, and the Cl 2p binding energies of the $[RuPMe]^+$ on the RuNPs are the same as those displayed by the free $[RuPMe]^+PF_6^-$. At this stage of the study, no additional information can derive from the Cl 2p region data. To be able to propose further interpretations for the energies observed, a systematic study should be conducted by focusing on slight changes on the chemical environment of the Cl atom and analysis of the XPS response.

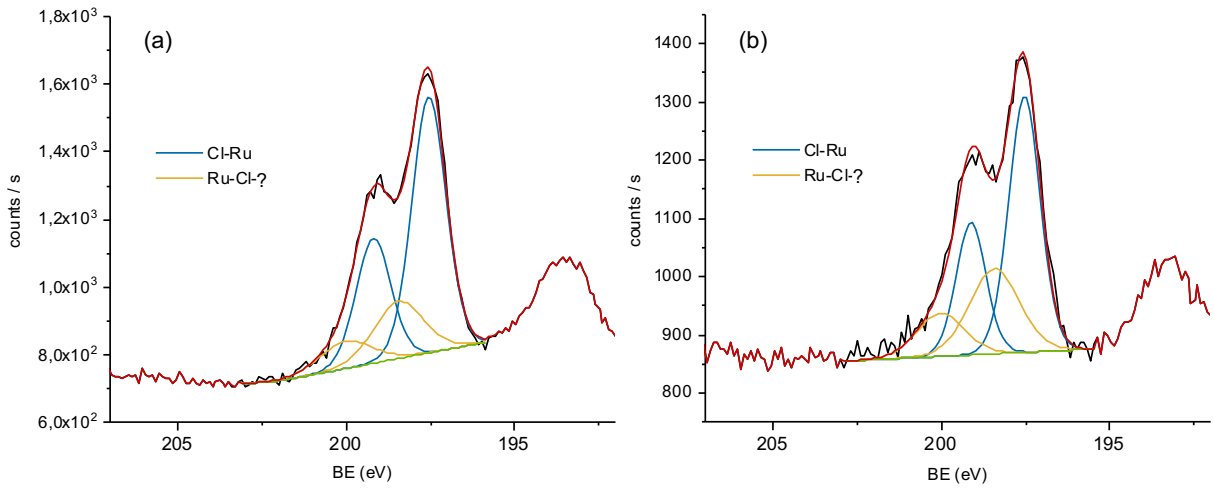

Figure 27. XPS spectra of Cl2p of (a) $[RuPMe]^+PF_6^-$ and (b) $([RuPMe]_n\text{-}RuNPs)^+(PF_6^-)_n$.

	$[RuPMe]^+PF_6^-$	$([RuPMe]_n\text{-}RuNPs)^+(PF_6^-)_n$
Cl	$Cl2p_{3/2}$ at 197.5 eV (Cl-Ru)	$Cl2p_{3/2}$ at 197.5 eV (Cl-Ru)
	$Cl2p_{1/2}$ at 199.2 eV (Cl-Ru)	$Cl2p_{1/2}$ at 199.1 eV (Cl-Ru)
	$Cl2p_{3/2}$ at 198.4 eV (Ru-Cl-?)	$Cl2p_{3/2}$ at 198.4 eV (Ru-Cl-?)
	$Cl2p_{1/2}$ at 200.0 eV (Ru-Cl-?)	$Cl2p_{1/2}$ at 200.0 eV (Ru-Cl-?)

Table 5. XPS data on the Cl2p of $[RuPMe]^+PF_6^-$ and $([RuPMe]_n\text{-}RuNPs)^+(PF_6^-)_n$.

The P 2p regions of the XPS spectra display two main phosphorous species (Figure 28a and 28b). The peak centered at ca. 131 eV is easily assigned to the P atom of the PPh_2Me ligand. Indeed, this peak can be deconvoluted in two main contributions, at same binding energies for $[RuPMe]^+PF_6^-$ and $([RuPMe]_n\text{-}RuNPs)^+(PF_6^-)_n$. In this sense, the P atom of the diphenylmethylphosphine ligand seems unperturbed by the coordination of the $[RuPMe]^+$ complex at the surface of the Ru nanoparticles.

At higher energies in the P 2p region and centered at ca. 136 eV, PF_6^- signals are observed. While for the $([RuPMe]_n\text{-}RuNPs)^+(PF_6^-)_n$ the PF_6^- response is composed by only one set of signals (135.8 and 136.7 eV), at least two different contributions are observed for the PF_6^- signal of the free $[RuPMe]^+PF_6^-$ complex (a first one matching the binding energies observed for the hybrid, 135.8 and 136.7 eV, and a second one at higher binding energies, 137.6 and 138.4 eV).

Similarly, when comparing the F 1s regions (Figure 28c and 28d), both $[RuPMe]^+PF_6^-$ and $([RuPMe]_n\text{-}RuNPs)^+(PF_6^-)_n$ display a peak at 686.2 eV. Also, the $[RuPMe]^+PF_6^-$ complex, displays an additional environment at 687.7 eV. This peak is similar to that observed for the KPF_6 salt deposited over a carbon scotch (F1s at 687.8 eV). Interestingly, a comparable behavior had already been observed by ^{19}F MAS NMR (see Fig. 24), where at least two different ^{19}F resonances were visible for $[RuPMe]^+PF_6^-$ while only one ^{19}F chemical shift was observed for the $([RuPMe]_n\text{-}RuNPs)^+(PF_6^-)_n$ hybrid. Again, these results could be explained by the different environments of the PF_6^- anion in the crystalline structure of the $[RuPMe]_+PF_6^-$ complex.

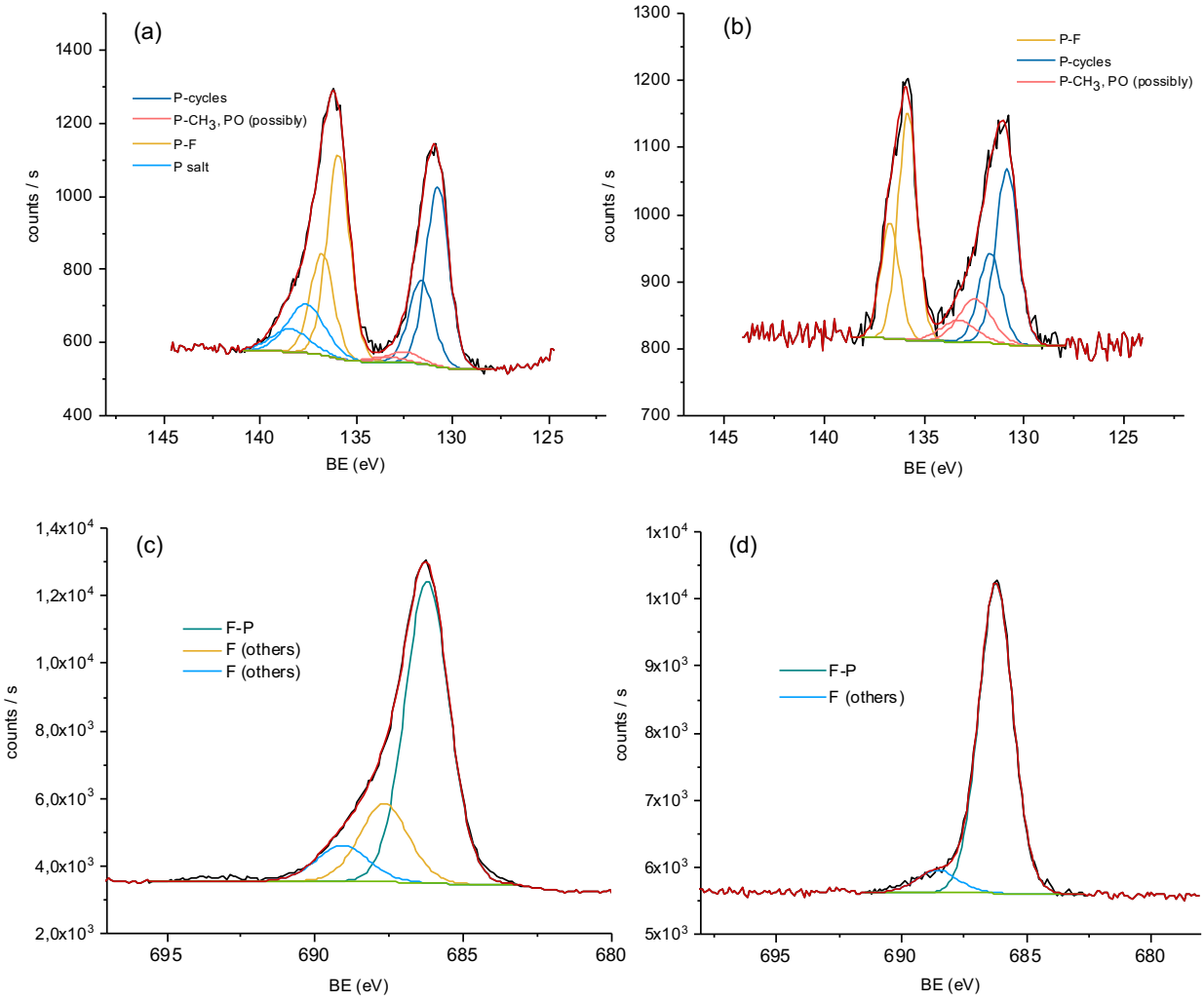

Figure 28. XPS spectra of P2p (a) $[RuPMe]^+PF_6^-$ and (b) $([RuPMe]_n\text{-}RuNPs)^+(PF_6^-)_n$ and F1s of (c) $[RuPMe]^+PF_6^-$ and (d) $([RuPMe]_n\text{-}RuNPs)^+(PF_6^-)_n$.

	$[RuPMe]^+PF_6^-$	**$([RuPMe]_n\text{-}RuNPs)^+(PF_6^-)_n$**
F	F1s at 686.2 eV (F-P) F1s at 687.7 eV (others) F1s at 689.1 eV (others)	F1s at 686.2 eV (F-P) F1s at 688.6 eV (others)

Table 6. XPS data on F1s of $[RuPMe]^+PF_6^-$ and $([RuPMe]_n\text{-}RuNPs)^+(PF_6^-)_n$.

	$[RuPMe]^+PF_6^-$	$([RuPMe]_n\text{-}RuNPs)^+(PF_6^-)_n$
P	$P2p_{3/2}$ at 130.9 eV (P-cycles) $P2p_{1/2}$ at 131.7 eV (P-cycles)	
	$P2p_{3/2}$ at 132.5 eV (P-CH_3, PO possibly) $P2p_{1/2}$ at 133.3 eV (P-CH_3, PO possibly)	$P2p_{3/2}$ at 130.9 eV (P-cycles) $P2p_{1/2}$ at 131.7 eV (P-cycles) $P2p_{3/2}$ at 132.5 eV (P-CH_3, PO possibly) $P2p_{1/2}$ at 133.3 eV (P-CH_3, PO possibly)
	$P2p_{3/2}$ at 135.8 eV (P-F) $P2p_{1/2}$ at 136.7 eV (P-F)	$P2p_{3/2}$ at 135.8 eV (P-F) $P2p_{1/2}$ at 136.7 eV (P-F)
	$P2p_{3/2}$ at 137.6 eV (P salt) $P2p_{1/2}$ at 138.4 eV (P salt)	

Table 7. XPS data on P2p of $[RuPMe]^+PF_6^-$ and $([RuPMe]_n\text{-}RuNPs)^+(PF_6^-)_n$.

In summary, the XPS data recorded allowed to compare the contribution of the Ru 3d, N 1s, Cl 2p, P 2p and F 1s signals observed in the $([RuPMe]_n\text{-}RuNPs)^+(PF_6^-)_n$ with those identified for the $[RuPMe]^+PF_6^-$ alone. Peaks for Cl2p or for P2p of the PPh_2Me ligand appeared unperturbed by the coordination of $[RuPMe]^+$ complex at the RuNP surface, but an additional chemical environment was observed in the N1s region, preliminarily attributed to a bipyridine ligand interacting with the RuNP surface as indicated by the theoretical results. In the Ru 3d region of the $([RuPMe]_n\text{-}RuNPs)^+(PF_6^-)_n$ spectrum, besides the Ru 3d peaks assigned to the $[RuPMe]^+$ stabilizer, ruthenium metallic species from the RuNPs core were also identified. To be able to assign more precisely the signals observed, a more systematic comparative study should be conducted on each of the elements of interest.

7. Conclusions

A novel type of hybrid nanomaterial made of metallic ruthenium nanoparticles efficiently stabilized by organophosphosphorous Ru(II)-polypyrdiyl complexes, $([RuPMe]_n\text{-}RuNPs)^+(PF_6^-)_n$, has been synthesized following the organometallic approach. This hybrid nanomaterial was fully characterized using a large combination of experimental analysis (TEM, HR-TEM, WAXS, ICP, NMR spectroscopy or XPS) together with theoretical calculations with Ru_{55}, Ru_{13} and Ru_6 models.

The $([RuPMe]_n\text{-}RuNPs)^+(PF_6^-)_n$ hybrid nanomaterial contains nanoparticles which have a metallic core of ca. 1.4 nm of diameter, corresponding to a Ru hcp structure, as confirmed by WAXS and HR-TEM techniques. Liquid and solid-state NMR experiments provided valuable information on the structure

of the hybrid nanomaterial, allowing to determine the location of the $[RuPMe]^+$ stabilizer regarding to the RuNPs surface. By liquid ^1H NMR and Diffusion-Ordered NMR spectroscopy, two types of $[RuPMe]^+$ species were identified:

(i) $[RuPMe]^+$ species directly coordinated to the RuNP surface forming an inner layer, which probably constitutes the driving force for the stabilization of the $([RuPMe]_n\text{-}RuNPs)^+(PF_6^-)_n$ hybrid material. DFT calculations using a 1 nm RuNP model evidenced that the coordination of the $[RuPMe]^+$ at the metal surface occurs *via* the chlorine atom of the complex which acts as a bridging ligand between the two entities of the hybrid nanomaterial. The stabilization of the hybrid is reinforced by an aromatic π −interaction between one of the bipyridine ligands of the $[RuPMe]^+$ species and the RuNP surface.

(ii) Dynamic $[RuPMe]^+$ species surrounding the $([RuPMe]_n\text{-}RuNPs)^+(PF_6^-)_n$ nanoobjects, $[RuPMe]^+_{exch}$, thus forming an outer layer. Given the cationic nature of the $[RuPMe]^+$ complex, an electrostatic-type interaction is proposed between $[RuPMe]^+_{exch}$ and $([RuPMe]_n\text{-}RuNPs)^+(PF_6^-)_n$ species.

DFT calculations suggested that 5 $[RuPMe]^+$ molecules saturated the RuNP surface. Note that DFT calculations are performed using vacuum conditions and that the solvent used in experimental conditions can have an important influence too. Considering that RuNPs of ca. 1.4 nm in size contain an average of 106 Ru atoms, the experimental data recorded on the overall population of the hybrid nanomaterial gave a number of 6 $[RuPMe]^+$ complexes per RuNP. This value has been estimated taking into account the results obtained by ICP, which indicated that the 60% of the $[RuPMe]^+PF_6^-$ complex used for the synthesis integrates the $([RuPMe]_n\text{-}RuNPs)^+(PF_6^-)_n$ hybrid. Considering that 2D DOSY NMR experiments pointed out a population ratio of $60/40(\pm 5)$ of directly coordinated $[RuPMe]^+$ and $[RuPMe]^+_{exch}$, 4 $[RuPMe]^+$ molecules are expected to coordinate at the RuNP surface. Therefore, we may consider that an average of 4 to 5 $[RuPMe]^+$ complexes are grafted at the surface of the RuNPs.

Liquid NMR results show that the PF_6^- counteranions do not interact with the surface of RuNPs; they are solubilized in the media and not affected by the influence of the RuNPs. This explains the ionic-like behavior of the $([RuPMe]_n\text{-}RuNPs)^+(PF_6^-)_n$ hybrid material. The $([RuPMe]_n\text{-}RuNPs)^+(PF_6^-)_n$ nanohybrid behaves like a cationic species, soluble in acetonitrile due to a good solvation and with a PF_6^- counteranions totally solvated.

Surface hydrides quantification performed by studying the hydrogenation of 2-norbornene as a substrate without additional hydrogen source apart the hydrides present at RuNP surface revealed a value of ca. 1.6 H per ruthenium surface atom. This value is the highest recorded to date compared to those observed for other RuNPs systems with classical ligands reported in the literature. This shows

that the RuNPs in the hybrid nanomaterial are able to accommodate a high amount of surface hydrogen atoms, which may be of interest for applicative studies involving hydrogen like hydrogenation reactions.

The ruthenium surface accessibility in the $([RuPMe]_n\text{-}RuNPs)^+(PF_6^-)_n$ hybrid nanomaterial has been probed by ^{13}CO adsorption. The solid state ^{13}C MAS NMR analysis of the hybrid sample revealed that there are still free surface sites available to interact. This confirms that the surface remains accessible for small molecules like CO.

Having a precise picture of the structure of this novel hybrid nanomaterial, the next step was to start studying its properties. Thus, an analysis of the electrochemical characteristics of these nanomaterials will be described in the next chapter, always keeping the free $[RuPMe]^+PF_6^-$ complex as a reference and trying to evaluate the influence of the RuNPs on its redox properties, and *vice versa.* Also, preliminary studies on the photocatalytic hydrogen evolution reaction (HER) and on the transformation of CO_2 into formic acid will be presented and compared to those obtained with other simple RuNPs.

8. References

1. Dixon, I.M.; Lebon, E.; Sutra, P.; Igau, A. Luminescent ruthenium–polypyridine complexes & phosphorus ligands: anything but a simple story. *Chem. Soc. Rev.* **2009**, *38*, 1621-1634.

2. Dixon, I.M.; Lebon, E.; Loustau, G.; Sutra, P.; Vendier, L.; Igau, A.; Juris, A. Broad HOMO–LUMO gap tuning through the coordination of a single phosphine, aminophosphine or phosphite onto a $Ru(tpy)(bpy)^{2+}$ core. *Dalton Trans.* **2008**, 5627-5635.

3. Lebon, E.; Sylvain, R.; Piau, R.E.; Lanthony, C.; Pilmé, J.; Sutra, P.; Boggio-Pasqua, M.; Heully, J.-L.; Alary, F.; Juris, A.; Igau, A. Phosphoryl Group as a Strong σ-Donor Anionic Phosphine-Type Ligand: A Combined Experimental and Theoretical Study on Long-Lived Room Temperature Luminescence of the $[Ru(tpy)(bpy)(Ph_2PO)]^+$ Complex. *Inorg. Chem.* **2014**, *53*, 1946–1948.

4. Sylvain, R.; Vendier, L.; Bijani, C.; Santoro, A.; Puntoriero, F.; Campagna, S.; Sutra, P.; Igau, A. Evidence of the unprecedented conversion of intermolecular proton to water bridging of two phosphoryl ruthenium complexes. *New J. Chem.* **2013**, *37*, 3543-3548.

5. Amiens, C.; Chaudret, B.; Ciuculescu-Pradines, D.; Collière, V.; Fajerwerg, K.; Fau, P.; Kahn, M.; Maisonnat, A.; Soulantica, K.; Philippot, K. Organometallic approach for the synthesis of nanostructures. *New J. Chem.* **2013**, *37*, 3374-3401.

6. Amiens, C.; Ciuculescu-Pradines, D.; Philippot, K. Controlled metal nanostructures: Fertile ground for coordination chemists. *Coord. Chem. Rev.* **2016**, *308*, 409–432.

7. Wang, P.-K.; Ansermet, J.-P.; Rudaz, S.L.; Wang, Z.; Shore, S.; Slichter, C.P.; Sinfelt, J.H. NMR Studies of Simple Molecules on Metal Surfaces. *Science* **1986**, *234*, 35–41.

8. Gutmann, T.; Bonnefille, E.; Breitzke, H.; Debouttière, P.-J.; Philippot, K.; Poteau, R.; Buntkowsky, G.; Chaudret, B. Investigation of the surface chemistry of phosphine-stabilized ruthenium nanoparticles – an advanced solid-state NMR study. *Phys. Chem. Chem. Phys.* **2013**, *15*, 17383–17394.

9. Ganji, P.; van Leeuwen, P.W.N.M. Phosphine Supported Ruthenium Nanoparticle Catalyzed Synthesis of Substituted Pyrazines and Imidazoles from α-Diketones. *J. Org. Chem.* **2017**, *82*, 1768–1774.

10. González-Gálvez, D.; Nolis, P.; Philippot, K.; Chaudret, B.; van Leeuwen, P.W.N.M. Phosphine-Stabilized Ruthenium Nanoparticles: The Effect of the Nature of the Ligand in Catalysis. *ACS Catal.* **2012**, *2*, 317–321.

11. Abo-Hamed, E.K.; Pennycook, T.; Vaynzof, Y.; Toprakcioglu, C.; Koutsioubas, A.; Scherman, O.A. Highly Active Metastable Ruthenium Nanoparticles for Hydrogen Production through the Catalytic Hydrolysis of Ammonia Borane. *Small* **2014**, *10*, 3145–3152.

12. Axet, M.R.; Philippot, K. Catalysis with Colloidal Ruthenium Nanoparticles. *Chem. Rev.* **2020**. *120, 2*, 1085-1145.

13. Nakao, Y.; Kaeriyama, K. Preparation of noble metal sols in the presence of surfactants and their properties. *J. Colloid. Interface Sci.* **1986**, *110*, 82–87.

14. Nowicki, A.; Zhang, Y.; Léger, B.; Rolland, J.-P.; Bricout, H.; Monflier, E.; Roucoux, A. Supramolecular shuttle and protective agent: a multiple role of methylated cyclodextrins in the chemoselective hydrogenation of benzene derivatives with ruthenium nanoparticles. *Chem. Commun.* **2006**, 296–298.

15. Yu, W.; Liu, M.; Liu, H.; Ma, X.; Liu, Z. Preparation, Characterization, and Catalytic Properties of Polymer-Stabilized Ruthenium Colloids. *J. Colloid Interface Sci.* **1998**, *208*, 439–444.

16. Viau, G.; Brayner, R.; Poul, L.; Chakroune, N.; Lacaze, E.; Fiévet-Vincent, F.; Fiévet, F. Ruthenium Nanoparticles: Size, Shape, and Self-Assemblies. *Chem. Mater.* **2003**, *15*, 486–494.

17. Martínez-Prieto, L.M.; Chaudret, B. Organometallic Ruthenium Nanoparticles: Synthesis, Surface Chemistry, and Insights into Ligand Coordination. *Acc. Chem. Res.* **2018**, *51*, 376–384.

18. Lee, C.E.; Tiege, P.B.; Xing, Y.; Nagendran, J.; Bergens, S.H. Hydrogenation of Ru(1,5-cyclooctadiene)(η^3-C_3H_5)$_2$ over Black Platinum. A Low-Temperature Reactive Deposition of Submonolayer Quantities of Ruthenium Atoms on Platinum with Real Time Control over Surface Stoichiometry. *J. Am. Chem. Soc.* **1997**, *119*, 3543–3549.

19. Prechtl, M.H.G.; Scariot, M.; Scholten, J.D.; Machado, G.; Teixeira, S.R.; Dupont, J. Nanoscale Ru(0) Particles: Arene Hydrogenation Catalysts in Imidazolium Ionic Liquids. *Inorg. Chem.* **2008**, *47*, 8995–9001.

20. Prechtl, M.H.G.; Campbell, P.S.; Scholten, J.D.; Fraser, G.B.; Machado, G.; Santini, C.C.; Dupont, J.; Chauvin, Y. Imidazolium ionic liquids as promoters and stabilising agents for the preparation of metal(0) nanoparticles by reduction and decomposition of organometallic complexes. *Nanoscale* **2010**, *2*, 2601-2606.

21. Lara, P.; Philippot, K.; Chaudret, B. Organometallic Ruthenium Nanoparticles: A Comparative Study of the Influence of the Stabilizer on their Characteristics and Reactivity. *ChemCatChem* **2013**, *5*, 28–45.

22. Bradley, J.S.; Millar, J.M.; Hill, E.W.; Behal, S.; Chaudret, B.; Duteil, A. Surface chemistry on colloidal metals: spectroscopic study of adsorption of small molecules. *Faraday Discuss.* **1991**, *92*, 255-268.

23. Duteil, A.; Queau, R.; Chaudret, B.; Mazel, R.; Roucau, C.; Bradley, J.S. Preparation of organic solutions or solid films of small particles of ruthenium, palladium, and platinum from organometallic precursors in the presence of cellulose derivatives. *Chem. Mater.* **1993**, *5*, 341–347.

24. Pan, C.; Pelzer, K.; Philippot, K.; Chaudret, B.; Dassenoy, F.; Lecante, P.; Casanove, M.-J. Ligand-Stabilized Ruthenium Nanoparticles: Synthesis, Organization, and Dynamics. *J. Am. Chem. Soc.* **2001**, *123*, 7584–7593.

25. Creus, J.; Drouet, S.; Suriñach, S.; Lecante, P.; Collière, V.; Poteau, R.; Philippot, K.; García-Antón, J.; Sala, X. Ligand-Capped Ru Nanoparticles as Efficient Electrocatalyst for the Hydrogen Evolution Reaction. *ACS Catal.* **2018**, *8*, 11094–11102.

26. Favier, I.; Massou, S.; Teuma, E.; Philippot, K.; Chaudret, B.; Gómez, M. A new and specific mode of stabilization of metallic nanoparticles. *Chem. Commun.* **2008**, 3296-3298.

27. Lara, P.; Rivada-Wheelaghan, O.; Conejero, S.; Poteau, R.; Philippot, K.; Chaudret, B. Ruthenium Nanoparticles Stabilized by N-Heterocyclic Carbenes: Ligand Location and Influence on Reactivity. *Angew. Chem. Int. Ed.* **2011**, *50*, 12080–12084.

28. González-Gómez, R.; Cusinato, L.; Bijani, C.; Coppel, Y.; Lecante, P.; Amiens, C.; Rosal, I. del; Philippot, K.; Poteau, R. Carboxylic acid-capped ruthenium nanoparticles: experimental and theoretical case study with ethanoic acid. *Nanoscale* **2019**, *11*, 9392–9409.

29. Campbell, P.S.; Santini, C.C.; Bouchu, D.; Fenet, B.; Philippot, K.; Chaudret, B.; Pádua, A.A.H.; Chauvin, Y. A novel stabilisation model for ruthenium nanoparticles in imidazolium ionic liquids: in situ spectroscopic and labelling evidence. *Phys. Chem. Chem. Phys.* **2010**, *12*, 4217–4223.

30. Gutel, T.; Santini, C.C.; Philippot, K.; Padua, A.; Pelzer, K.; Chaudret, B.; Chauvin, Y.; Basset, J.-M. Organized 3D-alkyl imidazolium ionic liquids could be used to control the size of in situ generated ruthenium nanoparticles? *J. Mater. Chem.* **2009**, *19*, 3624-3631.

31. Pelzer, K.; Vidoni, O.; Philippot, K.; Chaudret, B.; Collière, V. Organometallic Synthesis of Size-Controlled Polycrystalline Ruthenium Nanoparticles in the Presence of Alcohols. *Adv. Funct. Mater.* **2003**, *13*, 118–126.

32. Pelzer, K.; Philippot, K.; Chaudret, B. Synthesis of Monodisperse Heptanol Stabilized Ruthenium Nanoparticles. Evidence for the Presence of Surface Hydrogens. *Z. Für Phys. Chem.* **2003**, *217*, 1539–1548.

33. Mourdikoudis, S.; Pallares, R.M.; Thanh, N.T.K. Characterization techniques for nanoparticles: comparison and complementarity upon studying nanoparticle properties. *Nanoscale* **2018**, *10*, 12871–12934.

34. Coppel, Y.; Spataro, G.; Pagès, C.; Chaudret, B.; Maisonnat, A.; Kahn, M.L. Full Characterization of Colloidal Solutions of Long-Alkyl-Chain-Amine-Stabilized ZnO Nanoparticles by NMR Spectroscopy: Surface State, Equilibria, and Affinity. *Chem. – Eur. J.* **2012**, *18*, 5384–5393.

35. Novio, F.; Monahan, D.; Coppel, Y.; Antorrena, G.; Lecante, P.; Philippot, K.; Chaudret, B. Surface Chemistry on Small Ruthenium Nanoparticles: Evidence for Site Selective Reactions and Influence of Ligands. *Chem. – Eur. J.* **2014**, *20*, 1287–1297.

36. Bloembergen, N.; Purcell, E.M.; Pound, R.V. Relaxation Effects in Nuclear Magnetic Resonance Absorption. *Phys. Rev.* **1948**, *73*, 679–712.

37. *High-resolution NMR techniques in organic chemistry* ;Claridge, T.D.W. 3rd edition.; Elsevier: Amsterdam Boston Heidelberg London New York Oxford Paris, 2016; ISBN 978-0-08-099986-9.

38. 8-TECH-1 Relaxation in NMR Spectroscopy. Available online: https://www.chem.wisc.edu/areas/reich/nmr/08-tech-01-relax.htm.

39. Cano, I.; Martínez-Prieto, L.M.; Fazzini, P.F.; Coppel, Y.; Chaudret, B.; van Leeuwen, P.W.N.M. Characterization of secondary phosphine oxide ligands on the surface of iridium nanoparticles. *Phys. Chem. Chem. Phys.* **2017**, *19*, 21655–21662.

40. Cusinato, L.; Martínez-Prieto, L.M.; Chaudret, B.; del Rosal, I.; Poteau, R. Theoretical characterization of the surface composition of ruthenium nanoparticles in equilibrium with syngas. *Nanoscale* **2016**, *8*, 10974–10992.

41. del Rosal, I.; Mercy, M.; Gerber, I.C.; Poteau, R. Ligand-Field Theory-Based Analysis of the Adsorption Properties of Ruthenium Nanoparticles. *ACS Nano* **2013**, *7*, 9823–9835.

42. Sullivan, B.P.; Salmon, D.J.; Meyer, T.J. Mixed phosphine 2,2'-bipyridine complexes of ruthenium. *Inorg. Chem.* **1978**, *17*, 3334–3341.

43. Sylvain, R. Complexes polypyridyles de ruthénium dia- et paramagnétiques à ligands phosphorés fonctionnalisés pour des applications en transfert électronique et photovoltaïque. Doctoral Thesis, Université Paul Sabatier, Toulouse, 2013.

44. Mayer, C.R.; Dumas, E.; Sécheresse, F. 1,10-Phenanthroline and 1,10-phenanthroline-terminated ruthenium(II) complex as efficient capping agents to stabilize gold nanoparticles: Application for reversible aqueous–organic phase transfer processes. *J. Colloid. Interface Sci.* **2008**, *328*, 452–457.

45. Song, C.; Sakata, O.; Kumara, L.S.R.; Kohara, S.; Yang, A.; Kusada, K.; Kobayashi, H.; Kitagawa, H. Size dependence of structural parameters in fcc and hcp Ru nanoparticles, revealed by Rietveld refinement analysis of high-energy X-ray diffraction data. *Sci. Rep.* **2016**, *6*.

46. Debouttière, P.-J.; Coppel, Y.; Denicourt-Nowicki, A.; Roucoux, A.; Chaudret, B.; Philippot, K. PTA-Stabilized Ruthenium and Platinum Nanoparticles: Characterization and Investigation in Aqueous Biphasic Hydrogenation Catalysis. *Eur. J. Inorg. Chem.* **2012**, *2012*, 1229–1236.

47. Coppel, Y.; Spataro, G.; Collière, V.; Chaudret, B.; Mingotaud, C.; Maisonnat, A.; Kahn, M.L. Self-Assembly of ZnO Nanoparticles – An NMR Spectroscopic Study. *Eur. J. Inorg. Chem.* **2012**, *2012*, 2691–2699.

48. Harris, K.J.; Reeve, Z.E.M.; Wang, D.; Li, X.; Sun, X.; Goward, G.R. Electrochemical Changes in Lithium-Battery Electrodes Studied Using ^{7}Li NMR and Enhanced ^{13}C NMR of Graphene and Graphitic Carbons. *Chem. Mater.* **2015**, *27*, 3299–3305.

49. Wiench, J.W.; Lin, V.S.-Y.; Pruski, M. ^{29}Si NMR in solid state with CPMG acquisition under MAS. *J. Magn. Reson.* **2008**, *193*, 233–242.

50. García-Antón, J.; Axet, M.R.; Jansat, S.; Philippot, K.; Chaudret, B.; Pery, T.; Buntkowsky, G.; Limbach, H.-H. Reactions of Olefins with Ruthenium Hydride Nanoparticles: NMR Characterization, Hydride Titration, and Room-Temperature C-C Bond Activation. *Angew. Chem.* **2008**, *120*, 2104–2108.

51. Duncan, T.M.; Zilm, K.W.; Hamilton, D.M.; Root, T.W. Adsorbed states of carbon monoxide on dispersed metals: a high-resolution solid-state NMR study. *J. Phys. Chem.* **1989**, *93*, 2583–2590.

52. Martínez-Prieto, L.M.; Urbaneja, C.; Palma, P.; Cámpora, J.; Philippot, K.; Chaudret, B. A betaine adduct of N-heterocyclic carbene and carbodiimide, an efficient ligand to produce ultra-small ruthenium nanoparticles. *Chem. Commun.* **2015**, *51*, 4647–4650.

53. Ruiz-Ramírez, L.; Stephenson, A.; Switkes, E.S. New ruthenium(III) and ruthenium(II) complexes containing triphenyl-arsine and -phosphine and other ligands. *J. Chem. Soc., Dalton Trans.*, **1973**, 1770-1782.

54. Gilbert, D.; Baird, M.C.; Wilkinson, G. Thiocarbonyl and carbon disulphide complexes of ruthenium. *J. Chem. Soc. A*, **1968**, 2198-2201.

55. Taglang, C.; Martínez-Prieto, L.M.; del Rosal, I.; Maron, L.; Poteau, R.; Philippot, K.; Chaudret, B.; Perato, S.; Sam Lone, A.; Puente, C.; Dugave, C.; Rousseau, B.; Pieters, G. Enantiospecific C-H Activation Using Ruthenium Nanocatalysts. *Angew. Chem. Int. Ed.* **2015**, *54*, 10474–10477.

56. Cusinato, L.; del Rosal, I.; Poteau, R. Shape, electronic structure and steric effects of organometallic nanocatalysts: relevant tools to improve the synergy between theory and experiment. *Dalton Trans.* **2017**, *46*, 378–395.

57. Starr, D.E.; Bluhm, H. CO adsorption and dissociation on Ru(0001) at elevated pressures. *Surf. Sci.* **2013**, *608*, 241–248.

CHAPTER 3

1. Introduction

As reported in the literature reviewed in Chapter 1, by the assembly of metal nanoparticles and transition metal complexes, novel electrochemical, photophysical and catalytic properties might arise. In Chapter 2, we have described the synthesis and structural characterization of a novel hybrid nanomaterial $([RuPMe]_n\text{-}RuNPs)^+(PF_6^-)_n$, made with a mononuclear organophosphorus Ru(II)-polypyridyl complex, $[RuPMe]^+PF_6^-$, covalently bounded to the surface of ruthenium nanoparticles, RuNPs. Chapter 3 will now report on the study of the electrochemical properties emerging from this novel hybrid nanomaterial. Some very preliminary results issued from two different catalytic studies, with $([RuPMe]_n\text{-}RuNPs)^+(PF_6^-)_n$ hybrid nanomaterial will be presented as well.

As a first stage, the electronic properties of the $([RuPMe]_n\text{-}RuNPs)^+(PF_6^-)_n$ hybrid have been studied by electrochemical methods and compared to those of the free $[RuPMe]^+PF_6^-$ complex. While redox processes intrinsically associated with Ru(II)-polypyridyl type complexes are well-established [1], reports on the electrochemical characterization of metal nanoparticles (MNPs) are usually related to their application as electrocatalysts. In this context, the studies seek to understand the influence that nanoparticle size, shape and surface structure have on the electrocatalytic activity. For instance, Feliu and coworkers, reported the shape-dependent electrocatalytic oxidation of ammonia on PtNPs, significantly favored by the presence of Pt(100) surface domains [2]. In another study [3], they could assign the different signals obtained in the voltammograms of preferentially-oriented PtNPs (with core sizes of 4 to 11 nm) to specific surface sites, by correlation with the electrochemical responses of single-crystal Pt surfaces.

The development of nanoelectrochemical tools, namely nanoscale electrodes where single nanoparticles can be deposited in a way to be well isolated from each other, paves the way for establishing such structure-activity relationships [4,5]. In the study of populations of nanoparticles, which are polydisperse in size and might display different orientations towards the electrode, it is difficult to separate the observed electron transfers and attribute them to the different influencing parameters (size, crystallinity, etc.). In this case, the electrochemical responses obtained have to be considered as an average of the signals induced by the different particles present in the NP population. While the electrochemical behavior of colloidal Au nanoclusters (and in a lesser extent, of other noble metals like Ag, Pd and Pt) has been reported in several studies and can now be anticipated depending

on the cluster size [6], no references were found in the literature reporting on the redox behavior of small RuNPs. Therefore, additionally to the electrochemical measurements on the $([RuPMe]_n\text{-}RuNPs)^+(PF_6^-)_n$ hybrid nanomaterial, we also conducted a screening of the behavior of RuNPs stabilized by classical ligands (phosphine derivatives and bipyridines) aiming at identifying the electrochemical responses characteristic of the RuNP core.

In a second place, we preliminarily investigated the catalytic properties of the $([RuPMe]_n\text{-}RuNPs)^+(PF_6^-)_n$ hybrid nanomaterial regarding two important catalysis reactions, as follows:

(i) *The photocatalytic reduction of protons, as a part of the water-splitting process, for the production of hydrogen as a chemical fuel.* The studies have been performed in the group of Dr. Xavier Sala, SelOxCat, at the Autonomous University of Barcelona in the frame of a long-term collaboration of our team with this group. This objective was supported by the increasing interest gained by ruthenium-based nanomaterials as catalysts for the hydrogen evolution reaction (HER) [7,8]. For instance, ruthenium nanoparticles synthesized in our group displayed remarkable activities in the reduction of protons under electrocatalytic conditions, achieving, in acidic media, performances competitive to those of benchmarking Pt/C electrocatalysts [9,10]. In photocatalytic conditions, however, Ru nanocatalysts are less operative, which is attributed to a non-optimal electron transfer between Ru nanocatalysts and the widely used photosensitizer $[Ru(bpy)_3]^{2+}$ [7]. Due to their photochemical properties together with their chemical stability, excited-state lifetimes and reactivity, Ru(II)-polypyridyl complexes have been extensively used in photoinduced electron and energy transfer processes in multicomponent photocatalytic systems [11,12]. Given the photosensitive nature of the $[RuPMe]^+PF_6^-$ used as stabilizer of the $([RuPMe]_n\text{-}RuNPs)^+(PF_6^-)_n$ hybrid, we considered of interest to test the ability of our hybrid nanomaterial as photocatalyst in the HER.

(ii) *The transformation of CO_2 into formic acid, being a route to use this greenhouse gas as a raw material for the production of value-added products* [13]. This study has been conducted at the National University of Singapore, in the group of Pr. Ning Yan, Green Catalysis, in the frame of a mobility grant from the Université Fédérale Toulouse Midi-Pyrénées. While numerous ruthenium molecular complexes are known to display high activities towards the conversion of CO_2 into formic acid under H_2 pressure, there are very few examples of Ru nanocatalysts in the heterogeneous phase [14]. The use of ruthenium-based nanomaterials to catalyze this reaction is thus highly challenging, both in terms of reactivity and selectivity. In this context, we investigated the influence of the $[RuPMe]^+PF_6^-$ coordinated at the surface of RuNPs, in comparison to simple organic ligands, such as phosphine or pyridine derivatives.

2. Electrochemical properties of $([RuPMe]_n\text{-}RuNPs)^+(PF_6^-)_n$ and other RuNPs stabilized by classical ligands

2.1. Overview of the electrochemistry of organophosphorus Ru(II)-polypyridyl complexes

Ru(II)-polypyridyl complexes are well known for their characteristic electrochemical properties, notably, their reversible oxidation and reduction processes and the stability of their oxidized and reduced forms in the ground state [1]. The study of the redox properties of the prototypical tris(2,2'-bipyridine)ruthenium(II), $[Ru(bpy)_3]^{2+}$, was first reported by Bard *et. al*. [15] in acetonitrile (0.1 M tetrabutylammonium tetrafluoroborate, Bu_4NBF_4) and at a Pt disk microelectrode (Figure 1a, top). A reversible one-electron oxidation is observed at ca. 1.35 V (vs. SCE). As indicated by the schematic molecular orbital diagram of $[Ru(bpy)_3]^{2+}$ in the ground state (Figure 1b), this oxidation involves a metal-centered orbital (π_M) and it is formally attributed to the formation of $[Ru^{III}(bpy)_3]^{3+}$ species. In reduction, $[Ru(bpy)_3]^{2+}$ presents three successive monoelectronic reversible waves, at -1.33 V, -1.52 V and -1.76 V (vs SCE) (Figure 1a, bottom). In this case, the first reduction is localized on a ligand-centered orbital (π_L), and the resulting species is usually described as $[Ru^{II}(bpy)_2(bpy^{\cdot-})]^{2+}$. The following reduction processes correspond to successive reduction of the bpy ligands.

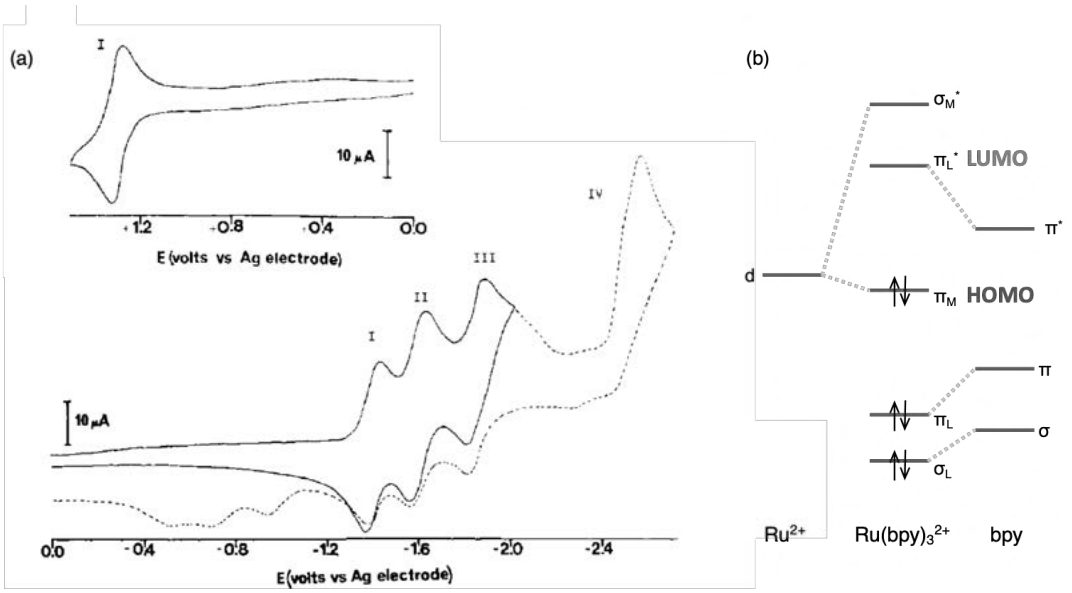

Figure 1. (a) Cyclic voltammograms of 1mM $[Ru(bpy)_3]^{2+}$ in CH_3CN (0.1 M Bu_4NBF_4) at a Pt electrode, reproduced from ref. [15], and (b) schematic molecular orbital diagram of $[Ru(bpy)_3]^{2+}$.

The electrochemistry of Ru(II)-polypyridyl derivatives has also been widely studied, commonly in non-aqueous aprotic solvents [1]. While the Ru^{3+}/Ru^{2+} redox couple falls in the potential range of 1.25 V (vs. SCE) with polypyridine ligands, when ligands of different nature are coordinated to the Ru(II)

center, depending on their electronic donating or withdrawing character, the oxidation potential of these Ru(II)-polypyridyl complexes can be strongly shifted. For instance, the oxidation of $[Ru(bpy)_2Cl_2]$ with two anionic σ-donating chlorine ligands, occurs at ca. 0.35 V (vs. SCE). In contrast, when strong π-acceptor ligands like CO are coordinated, as in $[Ru(bpy)_2(CO)_2]^{2+}$, the Ru^{2+}/Ru^{3+} oxidation potential shifts to ca. 1.90 V (vs. SCE). For comparison purposes, the potentials reported above have been normalized vs. SCE.

The electrochemical properties of Ru(II)-polypyridyl complexes incorporating an organophosphorus ligand in their coordination sphere have been recently investigated [16]. Coordination of organophosphorus ligands to the Ru(II)-polypyridyl fragment has proven to be a very powerful approach to modify the electronic properties of such complexes. By changing the σ and π abilities of the neutral phosphorous(III) ligands, a wide range of redox and spectroscopic properties have been achieved. As represented in Figure 2, the Ru^{2+}/Ru^{3+} oxidation potential of a Ru(II) terpyridine bipyridine complex, $[Ru(tpy)(bpy)L]^{2+}$, incorporating a strong σ-donor L-type ligand as the tricyclohexylphosphine, PCy_3, is 1.32 V. The Ru^{2+}/Ru^{3+} oxidation potential of the corresponding complex with L-type ligand displaying π-acceptor properties as the triphenylphosphite ligand, $P(OPh)_3$, is 1.61 V (vs. SCE, at r.t. and in CH_3CN) [17]. Interestingly, such an exceptional 290 mV range is attained for a same family of ligands coordinated through the same P heteroatom with the same oxidation state. It is noteworthy that a much narrower potential range is obtained by the coordination of neutral nitrogen ligands. Likewise, a broad range of electronic properties was obtained for symmetrical and asymmetrical $[Ru(bpy)_2L_2]^{2+}$ complexes depending on the coordinated P-ligand (such as Ph_2PH, $Ph_2P{=}O$, $Ph_2P\text{-}CH_3$ or $Ph_2P{=}S$, among others) [18]. In the case of the $[Ru(bpy)_2]^{2+}$ fragment the range of oxidation potential is extended, from 0.3 V to 1.80 V (vs. SCE).

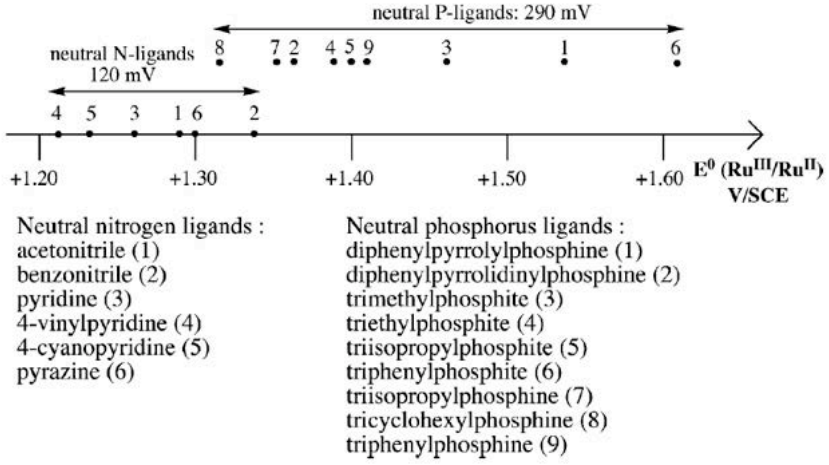

Figure 2. Accessible Ru^{2+}/Ru^{3+} oxidation potential range with neutral nitrogen and phosphorous ligands in $[Ru(tpy)(bpy)L]^{2+}$ complexes, reproduced from ref. [17].

In the frame of this PhD work, the electronic properties of the $[RuPMe]^{+}PF_6^{-}$ complex in the ground state were studied in acetonitrile solution by cyclic voltammetry (CV) using a glassy carbon (GC) electrode (3 mm diameter) and 0.1 M tetrabutylammonium hexafluorophosphate (Bu_4NPF_6) as supporting electrolyte. The cyclic voltammogram of $[RuPMe]^{+}PF_6^{-}$ is presented in Figure 3. A quasi-reversible oxidation peak is observed at $E_{1/2}$ = 0.94 V (vs SCE), that can be assigned to the Ru^{3+}/Ru^{2+} redox couple on the basis of our previous results for $[Ru(bpy)_2LL']^{2+}$ complexes [18]. The first quasi-reversible reduction wave at $E_{1/2}$ = -1.44 V (vs SCE) is attributed to the reduction of a bipyridine ligand. Further reductions at E_p = -1.67 V, -2.06 V and -2.17 V (vs SCE) are also observed. We can reasonably propose that they correspond to successive reduction processes on the bpy moieties.

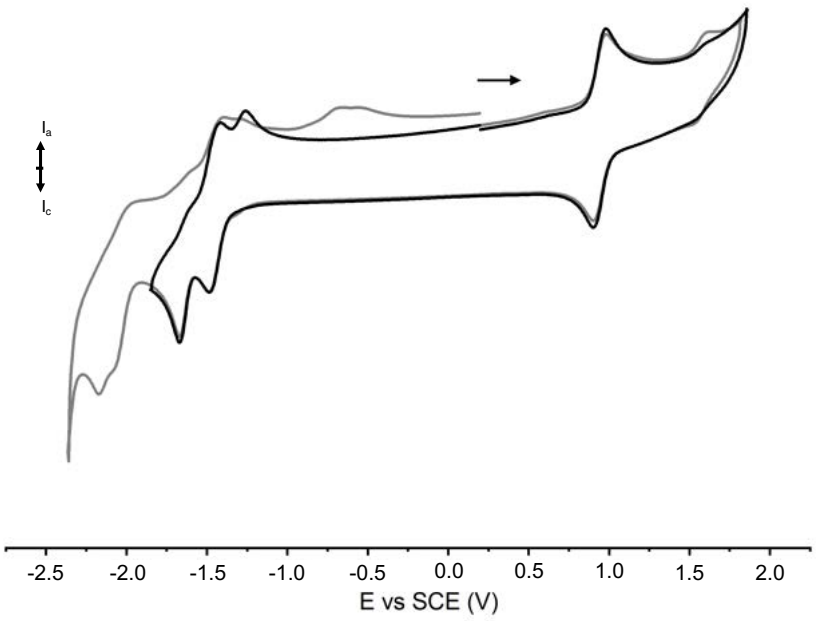

Figure 3. Cyclic voltammogram of $[RuPMe]^{+}PF_6^{-}$ in acetonitrile (1 mM $[RuPMe]^{+}PF_6^{-}$ in CH_3CN; 0.1 M NBu_4PF_6; GC electrode; 200 mV/s)

2.2. Overview of the electrochemistry of metal nanoparticles

The redox behavior of metal nanoparticles dispersed in a solvent and in the presence of an inert electrolyte can also be studied by electrochemical methods. When nanoparticles are dissolved in a conducting medium and surrounded by a dielectric layer of ligands, a double layer capacitance, C_{CLU}, arises upon electronic charging of the metal core (see Figure 4) [19,20]. As expressed in Equation 1, the capacitance of such system is strongly related to the nanoparticle radii, r_m, and the thickness of the stabilizing dielectric layer, d. The change in the electrochemical potential of the nanoparticle, ΔV, caused by the transfer of z electrons to or from the metal core is thus governed by the value of its C_{CLU} (see Equation 2).

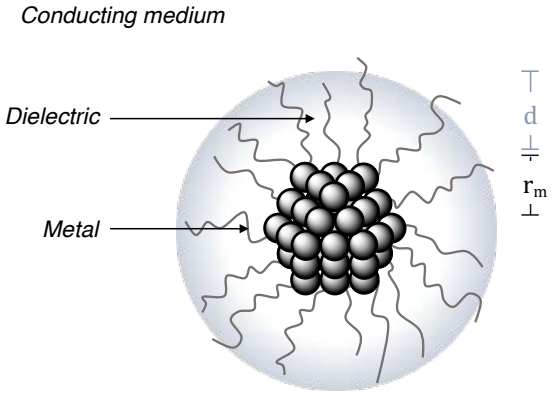

$$C_{CLU} = 4\pi\varepsilon\varepsilon_0 \frac{r_m}{d}(r_m + d) \quad (1)$$

r_m, nanoparticle radii
d, thickness of the stabilizing layer
ε, dielectric constant of stabilizing layer
ε_0, permitivity of free space

$$\Delta V = \frac{z \cdot e}{C_{CLU}} \quad (2)$$

z, electrons transfered from/to the metal core
e, electronic charge ($1.602 \cdot 10^{-19}$ C)

Figure 4. Concentric sphere capacitor model and equations used to describe the double layer capacitance of a MNP, C_{CLU}, in a conducting medium.

In his review, [6] R. W. Murray distinguished three different types of voltammetric regimes in order to describe the electrochemical responses of colloidal nanoparticles experimentally obtained, considering core sizes and, consequently, double layer capacitance (C_{CLU}) values. These three regimes are represented in Figure 5. In this classification, the variation of the observed electrochemical gap (i.e. difference between the first oxidation and the first reduction potentials, E_{ox}-E_{red}) as a function of the nanoparticle size is evidenced.

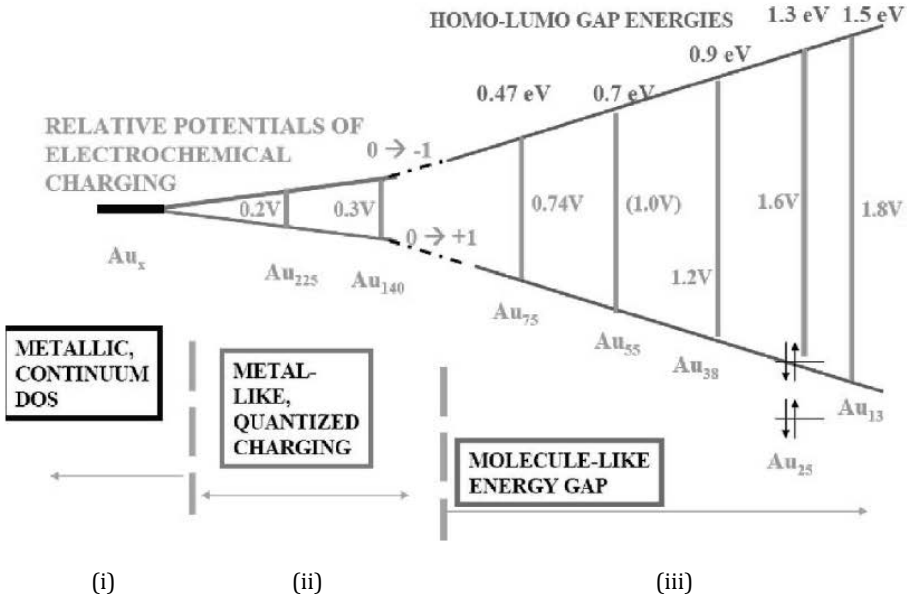

Figure 5. Summary of the electrochemical behavior of AuNPs as a function of their NP core size, showing estimated energy gaps (HOMO-LUMO gaps) and electrochemical energy gaps, reproduced from ref. [6].

(i) Typical of nanoparticles larger than 3-4 nm is the metallic or "bulk-continuum" regime. For this regime, successive electron transfers result in a continuous change in the nanoparticle charge, without

discontinuities attributable to single-electron processes. Accordingly, smooth current-potential curves are experimentally observed.

(ii) A second regime labeled as "quantized double layer charging" is characteristic of NPs that behave like quantum capacitors. When nanoparticles are sufficiently small (and so is their double layer capacitance, C_{CLU}), discrete changes in the electronic charge of the core can be experimentally observed. The successive single-electron charging of the nanoparticle will appear as a series of evenly distributed current peaks, commonly riding atop a continuous background current.

(iii) When scaling the core size down, clusters composed of few atoms (up to ca. 100 atoms) [21], a "molecule-like" behavior becomes predominant and larger electrochemical gaps become visible.

It is important to note that in order to distinguish and classify the different electrochemical behaviors of metal nanoparticles, stability in the measuring conditions and also highly monodisperse core sizes are ideally required [19,20]. The isolation and identification of atomically pure nanoclusters have been achieved owing to the development of optimized synthetic and purification procedures as well as the emergence of mass spectroscopy (MS) as a principal tool for their characterization. Because of their remarkable stabilities, advanced synthetical protocols and robustness under mass spectral conditions, Au clusters are the model systems of atomically precise clusters. To a lesser extent, well-defined nanocluster structures of noble metals such as Ag, Pt and Pd have been also reported [22,23]. Figure 6 shows the square wave voltammograms of highly-pure Au clusters of different sizes [24]. Larger clusters (Au_{102}, Au_{144} and Au_{333}) behave as quantized double layer charging capacitors, displaying rather small electrochemical gaps between the first oxidation and the first reduction followed by evenly spaced current peaks. For smaller Au clusters (Au_{25}, Au_{38} and Au_{67}) the "molecule-like" behavior appears, with strongly size-dependent electrochemical gaps (which increase from 0.75 V to 1.66 V by reducing core sizes from Au_{67} to Au_{25}).

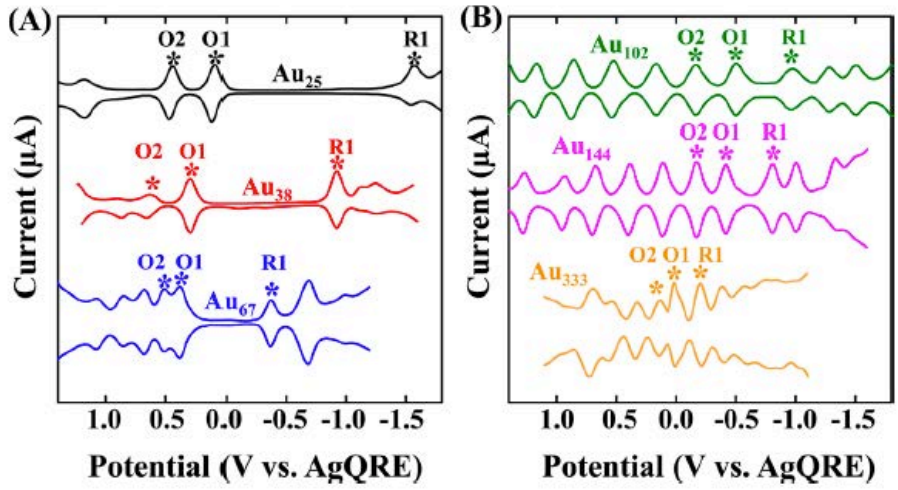

Figure 6. Square wave voltammograms of (a) Au_{25}, Au_{38} and Au_{67} clusters and (b) Au_{102}, Au_{144} and Au_{333} clusters in CH_2Cl_2, 0.1 M Bu_4NPF_6, reproduced from ref. [24].

A fourth (iv) electrochemical behavior includes nanoparticles with intrinsic redox-active groups on the surface (e.g. ferrocene, viologen or anthraquinone), whose own electrochemical responses will add to that of the nanoparticle core. For example, Schiffrin and coworkers [25] synthesized highly monodisperse hexanethiolate-capped gold nanoparticles of ca. 1.8 nm, which displayed, under cyclic voltammetry, a redox response typical of a double layer charging phenomenon (see Figure 6a).

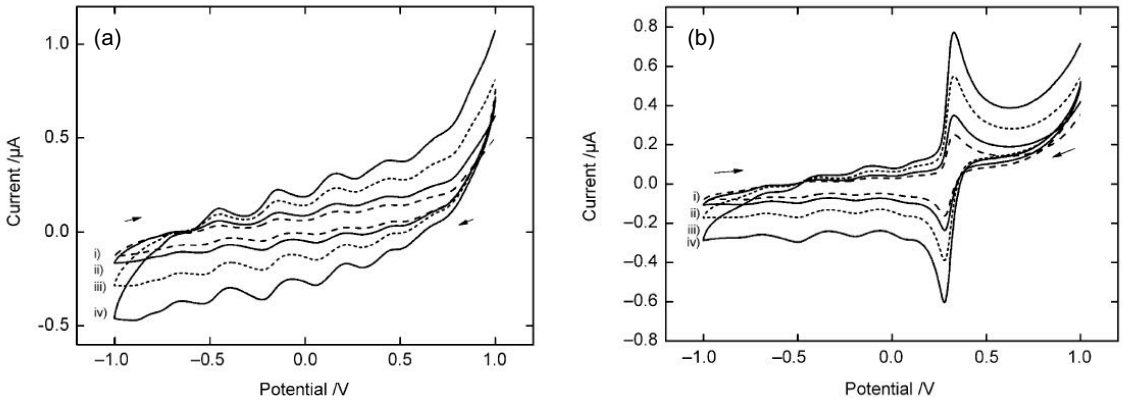

Figure 7. Cyclic voltammetry of (a) a 7 mg/mL solution of hexanethiolate-AuNPs and (b) 2 mg/mL of Fc-modified hexanethiolate-AuNPs, on Au electrode in 0.1 M $TBAPF_6$ in toluene:CH_3CN, reproduced from ref. [25]. Potentials are referred to Ag/Ag^+.

After post-functionalization with ferrocenyl (Fc) terminated hexanethiol, by a ligand exchange procedure, the gold nanoparticles preserved the charging events of the metal core (Figure 7b). In the example given, an average number of 10 Fc groups per AuNP were determined by NMR analysis, whose electrochemical response is observed in the voltammogram. The disappearance of the discrete

charging peaks at more positive potentials than the Fc^+/Fc redox couple is attributed to an inhibition of the electron transfer between the metal core and the electrode in presence of the positively charged Fc^+ groups. It was confirmed, however, that the capacitance value, C_{CLU}, of the AuNPs was maintained after the functionalization.

The electrochemical behavior of redox-active transition metal complexes, such as ferrocenyl or Ru(II)-polypyridyl groups, grafted on the surface of metal nanoparticles has also been studied. Generally, the redox properties of those transition metal complexes are preserved when they were connected to the MNP surface by alkyl spacers. For instance, cyclic voltammetry of gold nanoparticles (2 nm) modified with amido-ferrocenylalkylthiol displayed a reversible single wave at $E_{1/2}$ = 0.22 V (vs. Fc/Fc^+) [26]. The observation of a single Fc/Fc^+ wave indicates that the redox centers appear equivalent. Similarly, biferrocenyl-modified gold nanoparticles (2.2 ± 0.3 nm) [27] displayed two reversible oxidation waves at $E_{1/2}$ = 0.10 and 0.52 V (vs. Ag/Ag^+) and palladium nanoparticles (3.8 ± 0.8 nm) modified by the same biferrocenyl ligand [28] displayed reversible oxidations at $E_{1/2}$ = 0.17 and 0.58 V (vs. Ag/Ag^+) (see Figure 8, top).

Cyclic voltammetry measurements were also performed on $Ru(tpy)_3$ groups (tpy = terpyridine) connected to the surface of AuNPs (5.5 nm) by octanethiol spacers [29]. Two reduction peaks at $E_{1/2}$ = -1.52 and -1.71 V, centered on the tpy ligands, and an oxidation peak at $E_{1/2}$ = 0.93 V, for the Ru^{3+}/Ru^{2+} redox couple, were observed (vs. Ag/Ag^+).

Mayer *et al*. [30] studied the redox properties of Ru(II)-phen complexes (phen = phenanthroline) grafted to the surface of gold nanoparticles through a fully π-conjugated organic linker (see Figure 8, bottom). A single wave for the Ru^{3+}/Ru^{2+} redox couple was observed at $E_{1/2}$ = 0.99 V (vs. Ag/Ag^+) for the grafted complex, compared to that of the non-bonded free complex at $E_{1/2}$ = 1.02 V (vs. Ag/Ag^+). The authors attributed this slight lowering of the Ru^{2+}/Ru^{3+} oxidation potential by ca. 30 mV to a stabilization of the HOMO level of the Ru(II)-phenanthroline complex in the hybrid.

For comparison purposes, the potentials cited above have been normalized vs. SCE in Table 1, using the conversion constants tabulated in reference [31].

Hybrid system	Working electrode	Solvent	Reported potential	Potential (vs. SCE)	Ref.
Fc-AuNPs	Pt electrode	CH_2Cl_2	$E_{1/2}$ = 0.22 V (vs. Fc/Fc^+)	$E_{1/2}$ = 0.60 V	[26]
Fc_2-AuNPs	GC electrode	CH_2Cl_2	$E_{1/2}$ = 0.105 V $E_{1/2}$ = 0.52 V (vs. Ag/Ag^+)	$E_{1/2}$ = 0.40 V $E_{1/2}$ = 0.81 V	[27]
Fc_2-PdNPs	GC electrode	CH_2Cl_2	$E_{1/2}$ = 0.175 V $E_{1/2}$ = 0.58 V (vs. Ag/Ag^+)	$E_{1/2}$ = 0.47 V $E_{1/2}$ = 0.87 V	[28]
$[Ru(tpy)_2]^{2+}$-AuNPs	GC electrode	CH_3CN	$E_{1/2}$ = 0.93 V $E_{1/2}$ = -1.52 V $E_{1/2}$ = -1.71 V (vs. Ag/Ag^+)	$E_{1/2}$ = 1.27 V $E_{1/2}$ = -1.18 V $E_{1/2}$ = -1.37 V	[29]
$[Ru(phen)_3]^{2+}$-AuNPs	Pt disk	CH_3CN	$E_{1/2}$ = 0.995 V (vs. Ag/Ag^+)	$E_{1/2}$ = 1.29 V	[30]

Table 1. Normalized potentials vs SCE for the hybrid systems described in the literature.

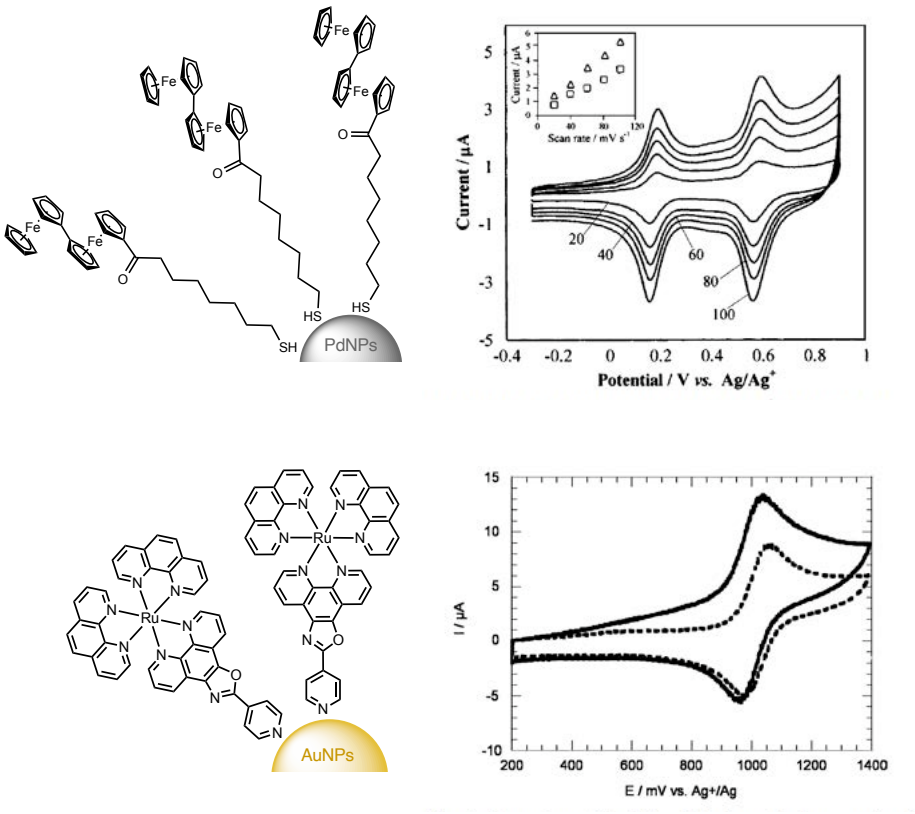

Figure 8. Cyclic voltammograms of (top) biferrocene-modified PdNPs at a GC disk in 0.1 M Bu_4NClO_4 in CH_2Cl_2 at different scan rates (vs. Ag/Ag^+) [28] and (bottom) Ru(II)-phenanthroline grafted on AuNPs (solid line) and free (dashed line) at a Pt electrode in CH_3CN [30].

The hybrid nanoparticles object of this study, $([RuPMe]_n\text{-}RuNPs)^+(PF_6^-)_n$, are composed of metallic Ru cores capped with intrinsically electroactive $[RuPMe]^+PF_6^-$ complexes. We can therefore expect to observe the redox response of the $[RuPMe]^+$ groups in addition to that of the metal nanoparticles. In Chapter 2, we were able to conclude on the existence of two different environments for the $[RuPMe]^+$ species conforming the hybrid nanomaterial. A major population (ca. 60%) of $[RuPMe]^+$ species are directly coordinated to the RuNP surface, forming an inner layer around the Ru metal core. In contrast to the examples abovementioned, the redox-active centers of the $[RuPMe]^+$ in the inner layer are directly coordinated to the RuNP surface by the chlorine atom of the complex, which acts as an unprecedented bridge between the two entities. The hybrid also contains a second type of $[RuPMe]^+$ species (ca. 40%), namely $[RuPMe]^+_{exch}$, that stand in electrostatic interaction with the $([RuPMe]_n\text{-}RuNPs)^+(PF_6^-)$ nanoobjects, forming an outer layer. While $[RuPMe]^+$ in the inner layer are strongly attached on the RuNPs surface through a covalent interaction and did not appear to be mobile, $[RuPMe]^+_{exch}$ species display exchange dynamics between the outer layer and the solvent (see NMR studies in Chapter 2).

Moreover, the amount of $[RuPMe]^+$ groups in the hybrid (ca. 6 total molecules of $[RuPMe]^+$ per RuNP, including directly coordinated $[RuPMe]^+$ and $[RuPMe]^+_{exch}$, as estimated by ICP analysis) is low in comparison to other hybrid systems described in the literature, which involve redox centers linked to the metal surface *via* organic spacer groups. For instance, ratios of ca. 20 biferrocene groups per AuNP [27], ca. 26 biferrocene groups per PdNP [28] or ca. 38 amidoferrocenyl groups per AuNP [26] were reported.

Taking into account previous electrochemical studies on MNPs and the unprecedented structure of the $([RuPMe]_n\text{-}RuNPs)^+(PF_6^-)_n$ hybrid, we decided to pursue electrochemical analysis to probe its redox properties.

2.3. Electrochemical studies on $([RuPMe]_n\text{-}RuNPs)^+(PF_6^-)_n$ and RuNPs stabilized by classical ligands

2.3.1. Experimental set-up and procedure

As previously mentioned, the number of $[RuPMe]^+$ redox active units in our nanohybrid is considerably lower than in other hybrid systems previously reported, whose redox properties could be studied in solution. In our case, despite electrochemical experiments with $([RuPMe]_n\text{-}RuNPs)^+(PF_6^-)_n$ dispersed in acetonitrile were essayed at very high concentrations (15 mg $([RuPMe]_n\text{-}RuNPs)^+(PF_6^-)_n$ /5 mL acetonitrile 0.1 M Bu_4NPF_6) only current peaks of low intensity were observed (see Figure 18, section 2.3.4 below).

To overcome these difficulties, and in order to minimize the amount of $([RuPMe]_n\text{-}RuNPs)^+(PF_6^-)_n$ per experiment while obtaining reliable and reproducible results from each electrochemical measurement, we set up a specific and optimized experimental procedure (see Figure 9).

$([RuPMe]_n\text{-}RuNPs)^+(PF_6^-)_n$ were then dissolved in dry acetonitrile under argon atmosphere (2 mg $([RuPMe]_n\text{-}RuNPs)^+(PF_6^-)_n$/mL). A drop (3 µL) of the RuNPs solution was then deposited on the surface of the GC electrode (3 mm diameter) and dried under argon flux. The best peak resolutions and intensities were obtained when this deposition protocol was repeated up to 4 times (4 x 3 µL). The electrochemical measurements were conducted in CH_3CN 0.1 M Bu_4NPF6, under Ar atmosphere in a 3-electrode cell system, using a glassy carbon (GC) disk as working electrode, a Pt wire as counterelectrode and a saturated calomel electrode (SCE) as reference.

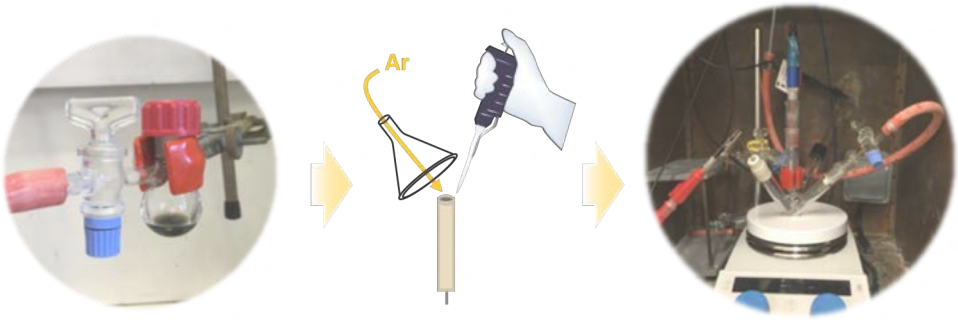

Figure 9. Schematic representation of the experimental procedure followed: solution of RuNPs (left), deposition of RuNPs on the GC electrode (middle) and 3-electrode cell system (right).

As a first attempt, cyclic voltammetry analyses of the $([RuPMe]_n\text{-}RuNPs)^+(PF_6^-)_n$ hybrid system deposited onto the GC electrode were performed. Very low-resolved voltammograms could be only recorded due to the presence of a strong capacitive current, reasonably arising from the deposition of $([RuPMe]_n\text{-}RuNPs)^+(PF_6^-)_n$ on the electrode surface. Such inconvenience was circumvented by using square wave voltammetry (SWV), which allowed obtaining better resolved current peaks and higher sensitivity. It is important to note that after the first potential sweep, the deposited NP layer leached to the solution and no more material remained at the electrode surface. This required to repeat the deposition process for every measurement performed in order to collect reproducible electrochemical data.

It is important to note that even though the experimental procedure to record the electrochemical data has been optimized to get reproducible measurements, the material deposited on the surface of the GC electrode surface can slightly vary from one experiment to the other. Therefore, the intensities, i(A), of the recorded square wave voltammograms have not been taken into account in the corresponding figures.

2.3.2. Electrochemistry of the $([RuPMe]_n\text{-}RuNPs)^+(PF_6^-)_n$ hybrid

Since the electrodes to study the behavior of the $([RuPMe]_n\text{-}RuNPs)^+(PF_6^-)_n$ were prepared by repeated deposition of the material on a GC electrode, the $[RuPMe]^+PF_6^-$ complex was also deposited on the surface of the GC electrode using the same experimental procedure in order to establish a reliable comparison. As shown in Figure 10, the redox potentials observed for the $[RuPMe]^+PF_6^-$ deposited on the GC electrode (solid line) were shifted by ca. -40 mV in comparison to those obtained for the same complex in solution (dashed line). The voltammetry data obtained for the $[RuPMe]^+PF_6^-$ complex were used as reference to analyze the redox behavior of the $([RuPMe]_n\text{-}RuNPs)^+(PF_6^-)_n$ hybrid.

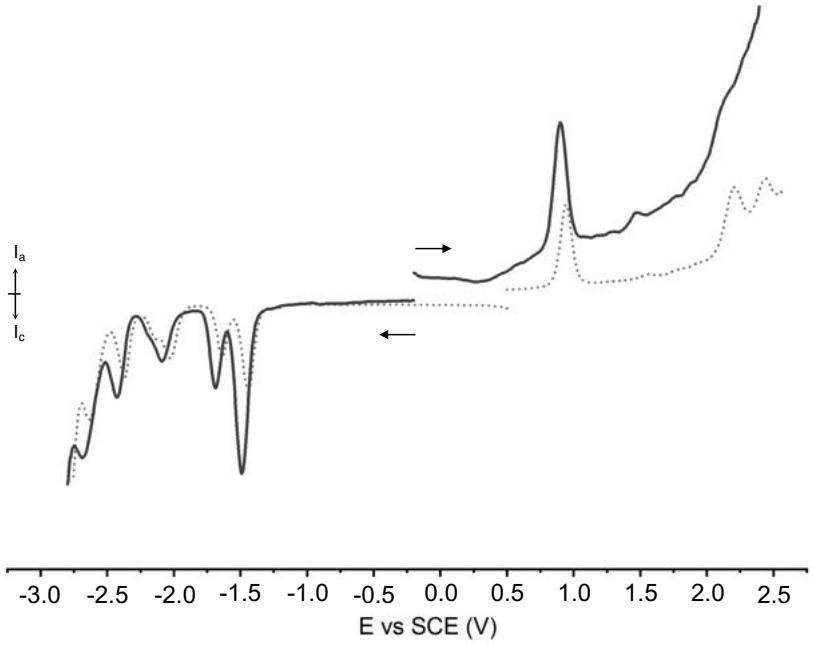

Figure 10. Square wave voltammograms of 1mM acetonitrile solution of $[RuPMe]^+PF_6^-$ (dashed line) and $[RuPMe]^+PF_6^-$ deposited on the surface of the GC electrode (solid line).

The square wave voltammograms of $([RuPMe]_n\text{-}RuNPs)^+(PF_6^-)_n$ and $[RuPMe]^+PF_6^-$ in oxidation are represented in Figure 11. The hybrid nanomaterial presents a first oxidation peak at ca. 0.88 V (vs SCE). Then, successive oxidations of similar intensities occur at ca. 1.06, 1.26, 1.53 and 1.71 V (vs SCE).

As the potential (0.88 V vs SCE) and the shape of the first oxidation peak observed for the hybrid nanomaterial are very close to those of the free $[RuPMe]^+PF_6^-$ complex (0.90 V vs SCE), one could attribute this peak in the hybrid to the oxidation of the $[RuPMe]^+$ complex, whether in the inner or the outer layer. The observed 20 mV shift could be a consequence of the proximity of the metal NP and the Ru(II) complex. By the peak position and resolution, this oxidation could be reasonably attributed to the $[RuPMe]^+_{exch}$ species present in the outer layer, which might preserve their original electrochemical behavior owing to the distance from the metal cores.

The second oxidation peak at 1.06 V (vs SCE), which is similar in shape and intensity to the first peak, could result from the oxidation of the $[RuPMe]^+$ groups in the inner layer. Given their close interaction with the RuNP surface by coordination of the chlorine atom, the electronic configuration of these $[RuPMe]^+$ species might be slightly modified, becoming more difficult to oxidize, and therefore, a higher oxidation potential is observed. By the slightly broader shape of the first oxidation peak with respect to the free $[RuPMe]^+PF_6^-$ complex, another hypothesis could be that the oxidation of both species (inner and outer layer $[RuPMe]^+$) integrate the same peak.

Besides this first peak attributed to the oxidation of $[RuPMe]^+$ species (either $[RuPMe]^+_{exch}$ or both $[RuPMe]^+_{exch}$ and $[RuPMe]^+$ directly coordinated), it is not straightforward to identify and assign the further oxidation waves. These oxidations are continuous and occur until high oxidative potentials, ca. 3 V (vs SCE), showing that the $([RuPMe]_n\text{-}RuNPs)^+(PF_6^-)_n$ hybrid material behaves as an electron-reservoir.

Note that the oxidation peak observed at ca. 0.32 V (*), considerably lower in intensity compared to the other oxidation peaks, could be related to other residual species adsorbed at the RuNP surface resulting from the synthesis conditions applied for $([RuPMe]_n\text{-}RuNPs)^+(PF_6^-)_n$, like solvent molecules or hydrides.

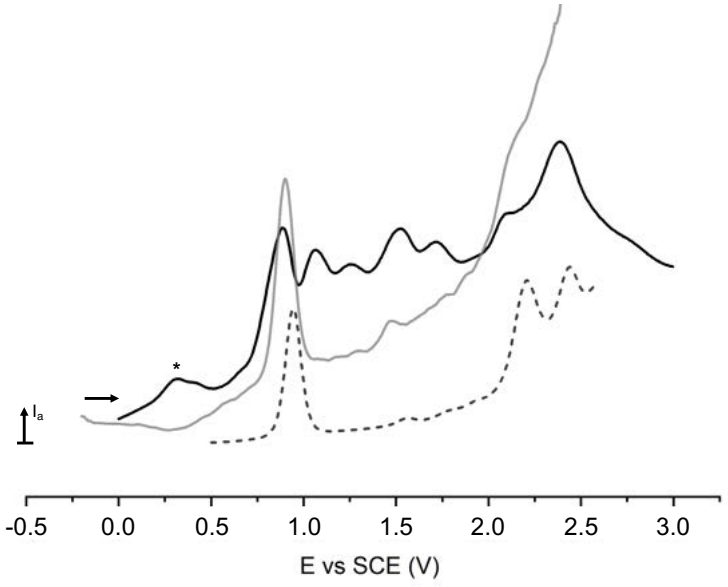

Figure 11. Square wave voltammogram of the oxidation of $([RuPMe]_n\text{-}RuNPs)^+(PF_6^-)_n$ (black), $[RuPMe]^+PF_6^-$ (grey) deposited on the GC electrode and $[RuPMe]^+PF_6^-$ in solution (dashed).

Figure 12 compares the reduction square wave voltammograms of $([RuPMe]_n\text{-}RuNPs)^+(PF_6^-)_n$ and the $[RuPMe]^+PF_6^-$ complex. For the free $[RuPMe]^+PF_6^-$ complex an intense reduction peak at -1.49 (vs SCE) V is observed, followed by a second reduction of lower intensity at -1.68 V (vs SCE).

$([RuPMe]_n\text{-}RuNPs)^+(PF_6^-)_n$ displays two broad reduction signals centered at ca. -1.55 and -1.80 V (vs SCE), each of it composed of two peaks. The relative intensities of the two peaks composing the broad signals, which are similar to those observed for the $[RuPMe]^+PF_6^-$ complex, suggest the reduction of two different Ru(II)-polypyridyl species occurred: (i) at -1.54 and -1.77 V (vs SCE) and (ii) at -1.61 and -1.87 V (vs SCE), marked as • and ♦ in figure 12, respectively. These two close reducing processes might be the signature of the $[RuPMe]^+$ complexes in the inner and the outer layer of the hybrid.

A reduction peak of low intensity and unknown origin is also observed at -0.85 V (vs SCE) (**). By analogy to the RuOx commercial sample which has been measured in the same experimental conditions, this peak can be reasonably attributed to RuOx surface species (see following section).

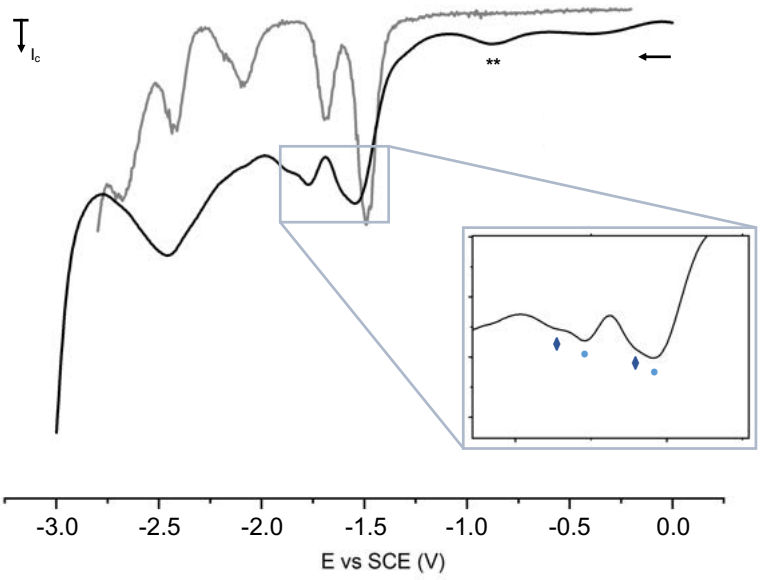

Figure 12. Square wave voltammograms of the reduction of $([RuPMe]_n\text{-}RuNPs)^+(PF_6^-)_n$ (black) and $[RuPMe]^+PF_6^-$ (grey) deposited on the GC electrode.

By the square wave voltammetry analysis of $([RuPMe]_n\text{-}RuNPs)^+(PF_6^-)_n$, it seems that the electrochemical characteristics of the $[RuPMe]^+PF_6^-$ complex are preserved in the $([RuPMe]_n\text{-}RuNPs)^+(PF_6^-)_n$ hybrid. Also, the redox behavior observed appears to be consistent with the inner/outer $[RuPMe]^+$ layer structure elucidated by NMR experiments and described in the previous Chapter.

The origin of the different oxidation peaks observed for the $([RuPMe]_n\text{-}RuNPs)^+(PF_6^-)_n$ hybrid, other than that assigned to $[RuPMe]^+$, is not ascertained. Since they are not inherent of the $[RuPMe]^+$ complex, they might arise from (i) the RuNP metal core itself or (ii) the combination of the two entities in $([RuPMe]_n\text{-}RuNPs)^+(PF_6^-)_n$. To shed some light on the origin of the various peaks observed for the

([RuPMe]$_n$-RuNPs)$^+$(PF_6^-)$_n$ system, additional electrochemical studies on RuNPs stabilized by ligands of different nature were performed, as it will be described in the following section.

2.3.3. Electrochemistry of RuNPs stabilized by classical ligands

In order to identify the redox properties of RuNP metal cores, RuNPs stabilized by triphenylphosphine (PPh_3), tricyclohexylphosphine (PCy_3) and 2,2'-bipyridine (bpy) ligands were synthesized following a similar experimental procedure than that used for the synthesis of the ([RuPMe]$_n$-RuNPs)$^+$(PF_6^-)$_n$ system. Additionally, 1,1'-bis(diphenylphosphino)ferrocene (dppf) ligand was also employed to stabilize RuNPs, in order to incorporate alternative redox groups on the nanoparticle surface. Ferrocene groups (Fc) are thermally and air stable, and the reversible oxidation of ferrocene to ferricenium occurs at moderate potentials (ca. 0.4 V vs SCE) [32]. Ferrocenyl phosphine derivatives have been previously used in the group as ligands for the stabilization of small RhNPs which showed interesting results in catalytic hydrogenation reactions [33].

For the synthesis of the series of ligand-capped RuNPs, [Ru(cod)(cot)] was dissolved in freshly distilled and degassed THF, and then decomposed under 3 bar of H_2 in the presence of 0.2 equivalents of PPh_3, PCy_3 or bpy or 0.1 equivalent of dppf (Scheme 1).

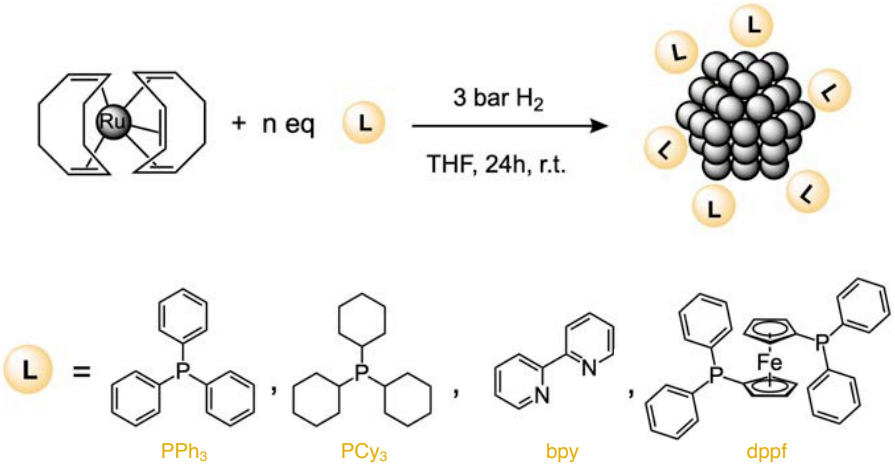

Scheme 1. Synthesis of RuNPs stabilized by PPh_3, PCy_3, bpy and dppf.

After 24 h of reaction at 25 °C, the remaining hydrogen pressure vas evacuated and an aliquot of the colloidal solution was collected in order to prepare a TEM grid. Three washings were then performed by addition of pentane and the supernatant was removed by canula. The diverse RuNPs were obtained under the form of a black solid after drying under vacuum.

The TEM micrographs and size histograms of PPh_3-RuNPs, PCy_3-RuNPs, bpy-RuNPs and dppf-RuNPs are presented in Figure 13. All of the systems display similar RuNP core-sizes to $([RuPMe]_n\text{-RuNPs})^+(PF_6^-)_n$, which will facilitate the comparison.

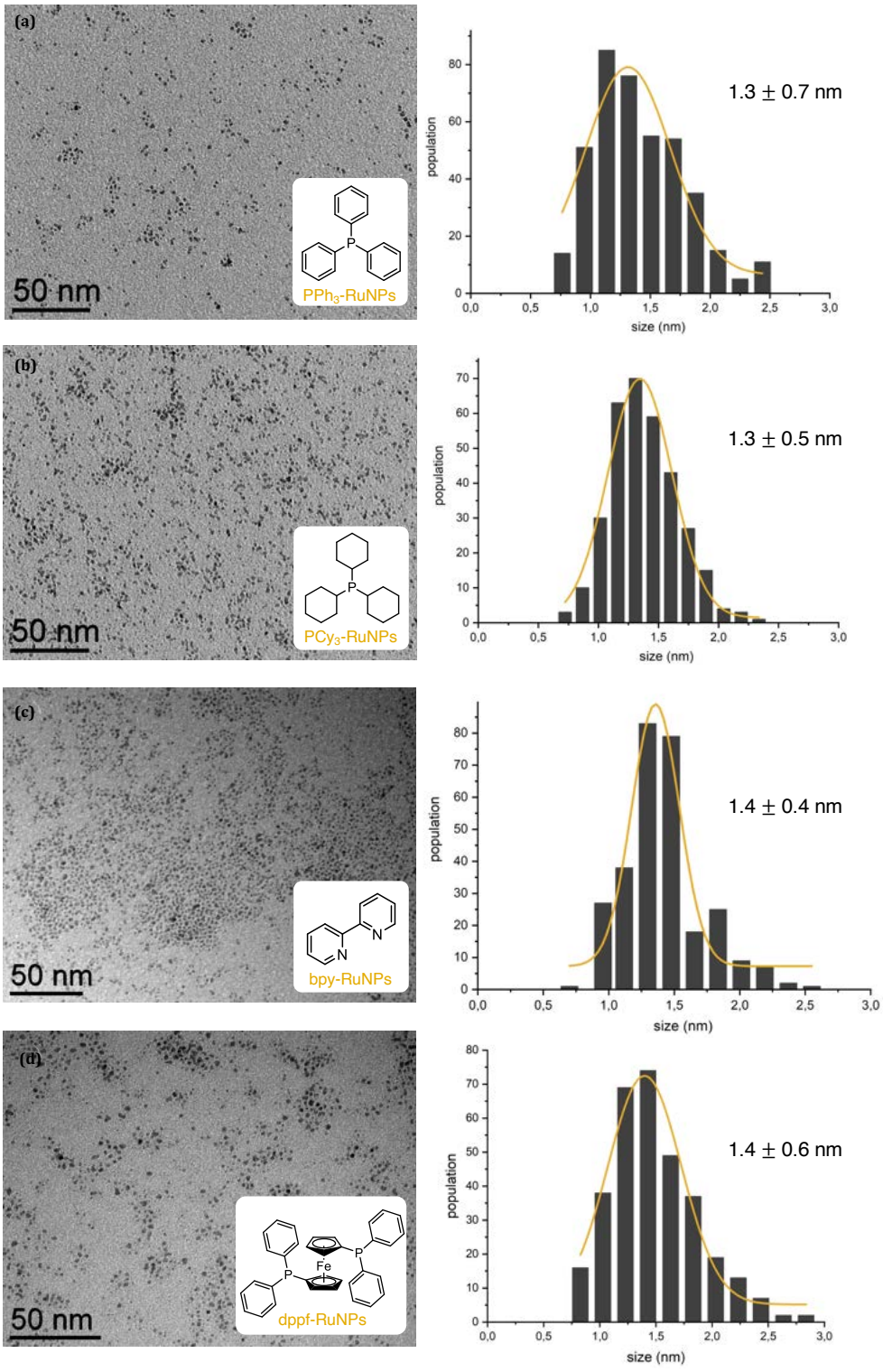

Figure 13. TEM pictures of the crude colloidal solutions of (a) PPh_3-RuNPs, (b) PCy_3-RuNPs, (c) bpy-RuNPs and (d) dppf-RuNPs and related size histograms.

The stabilization of RuNPs by PPh_3 ligands has been achieved before in the group [34], with core sizes of ca. 1.8 nm, and ^{31}P and ^{13}C solid-state NMR analyses revealed the presence of different phosphine ligands on the surface, that is, PPh_3 and PCy_3 species. On the PPh_3-RuNPs synthesized for this study, as well as PCy_3-RuNPs, bpy-RuNPs and dppf-RuNPs, no characterization other than TEM microscopy was performed due to time constraints.

The same procedure followed to measure the electrochemical responses of $([RuPMe]_n\text{-}RuNPs)^+(PF_6^-)_n$ system was applied for the other RuNPs. The voltammograms of PPh_3, bpy and dppf ligands in solution were also recorded for reference.

In the measurements involving bpy-RuNPs, PPh_3-RuNPs and PCy_3-RuNPs, we were not able to measure an equilibrium potential. We observed a slow continuous potential drift, caused by ongoing spontaneous electron transfer, which had not been experienced for $([RuPMe]_n\text{-}RuNPs)^+(PF_6^-)_n$. Indeed, the electrochemical behavior of RuNPs stabilized by bpy, PPh_3 and PCy_3 is very different from that observed for $([RuPMe]_n\text{-}RuNPs)^+(PF_6^-)_n$ under the same conditions (see Figures 14 and 15). Very broad and asymmetrical oxidation peaks of high intensity were observed, spanning, in the case of PCy_3-RuNPs, from -1.0 to +1.5 V (vs SCE). Similar behavior was observed for bpy-RuNPs and PPh_3-RuNPs but with a narrower amplitude (i.e. ca. 1 and 2 V large, respectively).

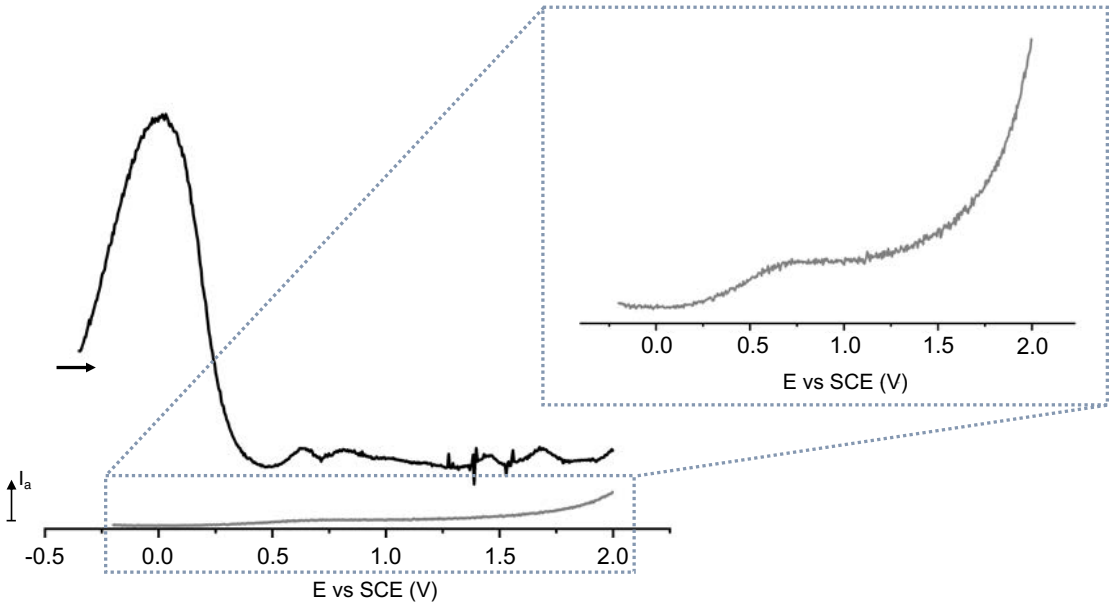

Figure 14. Square wave voltammogram of bpy-RuNPs (deposited; black) and free bpy (in solution; grey) on GC electrode.

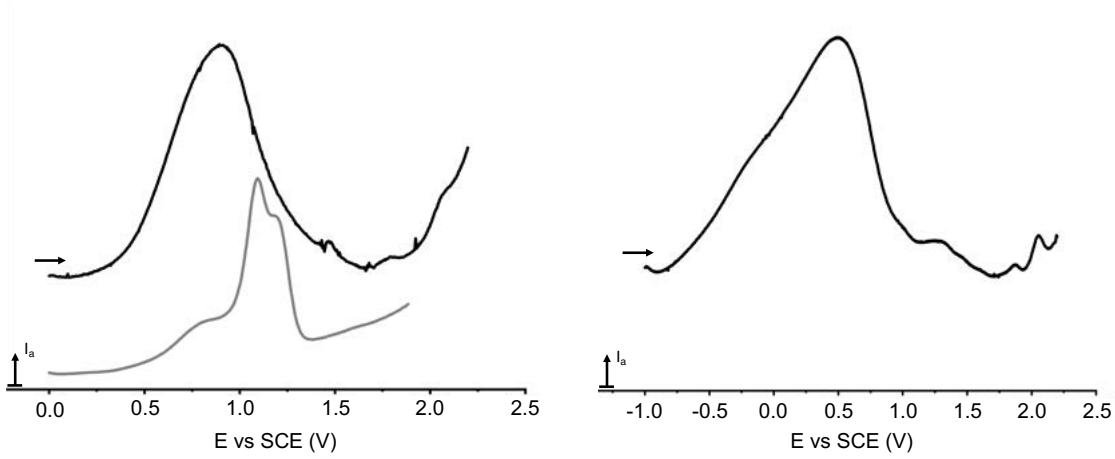

Figure 15. Square wave voltammogram of (left) deposited PPh_3-RuNPs (black) and free PPh_3 in solution (grey) and (right) PCy_3-RuNPs deposited on GC electrode.

The shape and broadness of the oxidation peaks presented in Figures 14 and 15 could be associated to a corrosion-like process, a phenomenon typically related to bulk metals. After electrochemical oxidation of PPh_3-RuNPs and PCy_3-RuNPs, a species was detected in solution by cyclic voltammetry, characterized by a quasi-reversible reduction wave centered $E_{1/2}$ = -0.87 V (vs SCE). Since corrosion of the RuNPs should induce metal leaching from the metal cores, we presumed the formation of ruthenium oxide species in solution. Thus, the cyclic voltammetry of a commercial sample of RuO_2 was recorded and appeared very similar to that obtained for the species present in solution after oxidation of RuNPs (see Figure 16). These results are thus consistent with the corrosion of the RuNPs, as suggested by the large oxidation asymmetrical waves and the instability of the equilibrium potential. To complete the characterization of the corrosion process experienced by the RuNPs, electrochemical impedance spectroscopy experiments should be performed as a perspective to this study.

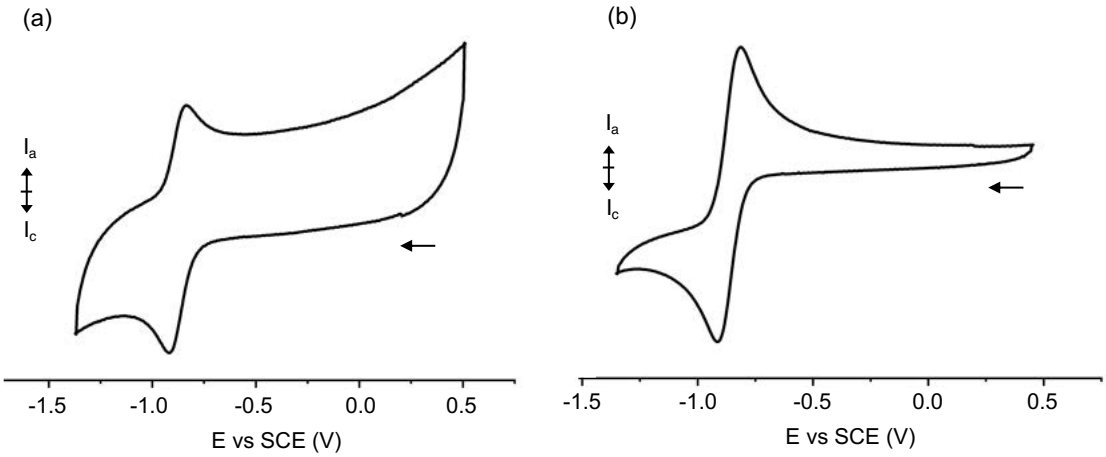

Figure 16. Cyclic voltammetry of (a) the solution after oxidation of PCy_3-RuNPs and (b) commercial RuO_2 sample.

In the case of dppf-RuNPs, the electrochemical behavior observed was similar to that of the $([RuPMe]_n\text{-}RuNPs)^+(PF_6^-)_n$ hybrid with no corrosion-like behavior. A first sharp oxidation wave is visible at 0.61 V (vs SCE), which is 20 mV shifted compared to that of the Fc/Fc^+ redox process of the free dppf ligand (0.59 V vs SCE) and a bit broader in shape. The second oxidation, initially at 1.16 V (vs SCE) is shifted to 1.05 V (vs SCE).

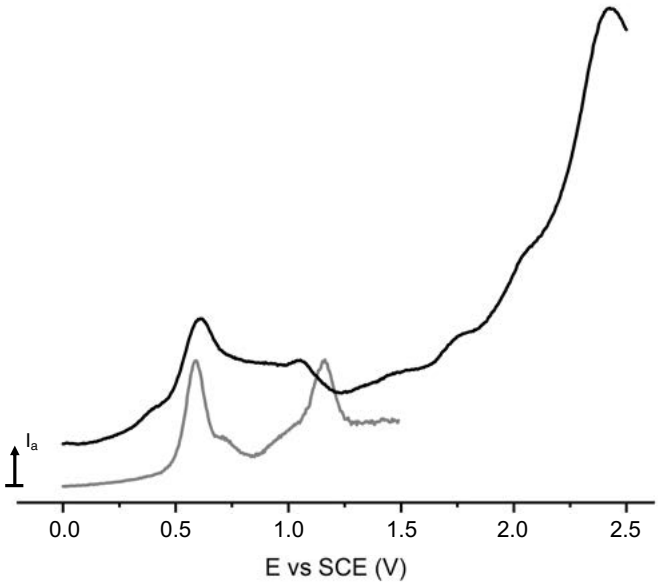

Figure 17. Square wave voltammograms of dppf-RuNPs (black) and dppf (grey) deposited on the GC electrode.

Up to now, the dppf-RuNPs system has not been fully characterized, with only size data of the RuNP cores determined from TEM analysis. Studies on the nature of the interaction between the dppf ligand and the RuNP have not been performed so far. Given the known ability of phosphine ligands to stabilize RuNPs *via* the phosphorous atoms [35], it is reasonable to propose also an interaction *via* the free electron pair of the diphenylphosphine groups in dppf. The distance between the Fc redox center and the surface of the nanoparticle would thus be shorter than in ferrocenyl-containing hybrid systems previously reported in the literature, where Fc groups are connected to AuNPs and PdPs by long alkylthiol spacers [26–28]. Even so, it is possible to observe the oxidation of the dppf ligands coordinated at the surface of RuNPs, as we could observe that of $[RuPMe]^+$ in our hybrid system.

2.3.4. Comparative analysis: $([RuPMe]_n\text{-}RuNPs)^+(PF_6^-)_n$ vs. RuNPs stabilized by classical ligands

The electrochemical analysis of the $([RuPMe]_n\text{-}RuNPs)^+(PF_6^-)_n$ hybrid compared to other RuNPs stabilized by classical ligands (PPh_3, PCy_3 and bpy) evidenced very different redox characters. While PPh_3-RuNPs, PCy_3-RuNPs and bpy-RuNPs presented very large redox waves, which were attributed to

a corrosion-like process as expected from bulk metals, the Ru hybrid displayed sharp redox peaks which are more comparable to successive electron transfer processes.

As a first remark, $([RuPMe]_n\text{-}RuNPs)^+(PF_6^-)_n$ exhibited a notable electrochemical gap of ca. 2.4 V (first oxidation at 0.88 V vs SCE and first reduction at -1.55 V vs SCE), typical of a complex/molecule-like behavior. The origin of the different peaks observed is, however, not straightforward to determine. Only the first oxidation peak was assigned, within reasonable limitations, to the $[RuPMe]^+_{exch}$ complexes present in the outer layer of the complexes surrounding the metal cores.

Second, the $([RuPMe]_n\text{-}RuNPs)^+(PF_6^-)_n$ hybrid can be successively oxidized in a form analogous to the staircase redox pattern observed for clusters that behave as quantum capacitors. This pattern is more clear when looking at the square wave voltammetry obtained for $([RuPMe]_n\text{-}RuNPs)^+(PF_6^-)_n$ in solution at high concentration (15 mg/5 mL), as presented in Figure 18.

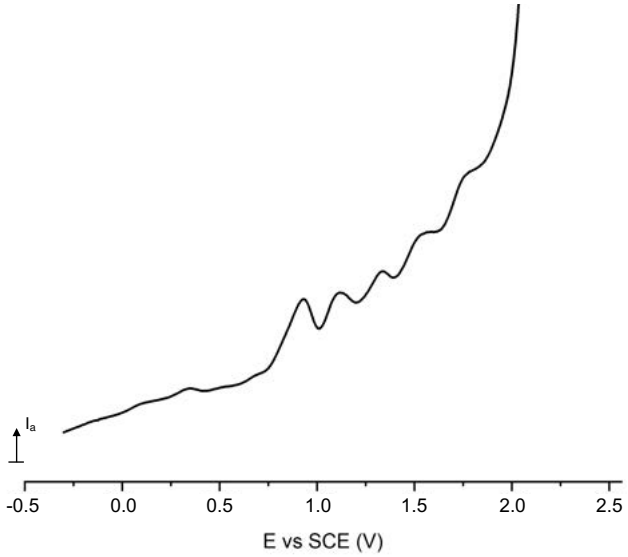

Figure 18. Square wave voltammogram of $([RuPMe]_n\text{-}RuNPs)^+(PF_6^-)_n$ in solution.

This specific behavior has not been experimentally observed for other RuNPs of similar size nor for the $[RuPMe]^+PF_6^-$ itself, which reflects the hybrid character of the $([RuPMe]_n\text{-}RuNPs)^+(PF_6^-)_n$ nanomaterial.

The dppf-RuNPs system contains redox active centers grafted to the surface of RuNP as it is the case for our hybrid nanomaterial $([RuPMe]_n\text{-}RuNPs)^+(PF_6^-)_n$. The dppf-RuNPs system does not manifest the corrosion-like process observed for phosphine ligand-stabilized RuNPs, even if the ferrocene fragment is coordinated *via* the diphenylphosphine ligand on the nanoparticle.

The fine characterization of dppf-RuNPs merits to be performed, since a further understanding of the structure of this nanomaterial is needed in order to come to a more detailed conclusion.

2.3.5. Theoretical calculations: pDOS, pCOHP and pMPA charges

In order to shed some light on the results experimentally obtained, the electronic properties of the $([RuPMe]_n\text{-}RuNPs)^+(PF_6^-)_n$ hybrid were studied by DFT calculations through a collaboration with Dr. I. del Rosal and Pr. R. Poteau (Laboratoire de Physique et Chimie des Nano-objets (LPCNO), Toulouse). The approach used, density of states (DOS), is defined as the number of all the levels or states in a given energy interval [36]:

$$\mathrm{DOS}(E)dE = \text{number of levels between } E \text{ and } E + dE$$

DOS curves describe the distribution of the electron density and the occupancy of the different states. The integral of the DOS up to the Fermi level is the total number of occupied molecular orbitals. The projected DOS (pDOS) shows the decomposition of the DOS into the contributions of the different molecular orbitals [36].

The pDOS representation has been performed for the free $[RuPMe]^+PF_6^-$ complex and for an hybrid structure composed by one molecule of $[RuPMe]^+$ directly coordinated to the surface of a $Ru_{55}H_{35}$ cluster, $([RuPMe]^+\text{-}Ru_{55}H_{35})PF_6^-$, in the most stable conformation (Figure 19).

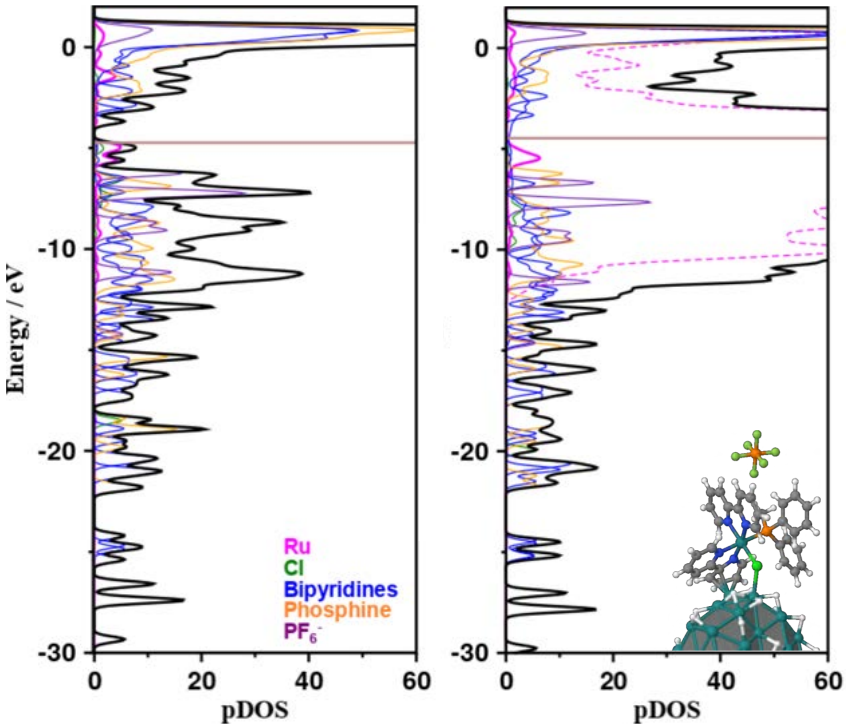

Figure 19. pDOS and profiles for $[RuPMe]^+PF_6^-$ (left) and $[RuPMe]^+\text{-}Ru_{55}H_{35}$ (right). Brown horizontal line: Fermi energy. Black line: total DOS.

The pDOS of ([RuPMe]$^{+}$-$Ru_{55}H_{35}$)PF_6^- denotes a very strong contribution from the d-orbitals of the Ru metal core (dashed pink line). Besides, we recognize the electronic signature of the [RuPMe]$^{+}$ complex, mostly unaffected by its coordination to the Ru_{55} cluster. Interestingly, the electronic density of Ru(II) center is close to the Fermi level, and slightly stabilized by its coordination to the Ru core. Previous studies on the pDOS of Ru_{55} clusters stabilized by organic ligands like CO [37] and ethanoates [38], namely $Ru_{55}(CO)_{66}$ and $Ru_{55}H_{33}(CH_3OO)_{16}$, showed that the highest occupied states laid essentially on Ru metal atoms. In these cases, the contributions of the CH_3OO^- and CO stabilizing ligands to the DOS are from ca. 3 to 6 eV lower than the Fermi level, respectively. By the profiles obtained for $Ru_{55}(CO)_{66}$ and $Ru_{55}H_{33}(CH_3OO)_{16}$, it seems thus reasonable to envisage a corrosion of the Ru metal core upon oxidation. In contrast, in ([RuPMe]$^{+}$-$Ru_{55}H_{35}$)PF_6^-, the states developed on the Ru(II) of the capping [RuPMe]$^{+}$ complexes are just below the Fermi energy of the hybrid (< 1 eV). In this case, it is difficult to predict in which of the states, d-orbitals of metal Ru (RuNP surface) or Ru(II) metal center, the oxidation will occur.

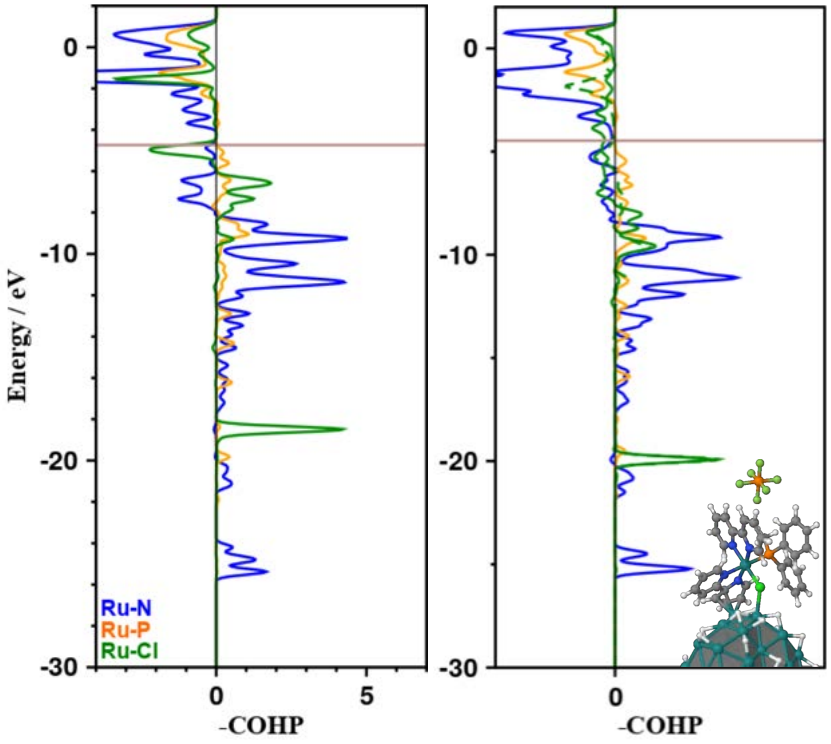

Figure 20. pCOHP profile of [RuPMe]$^{+}PF_6^-$ (left) and ([RuPMe]$^{+}$-$Ru_{55}H_{35}$)PF_6^- (right). Brown horizontal line: Fermi energy.

The projected crystal orbital Hamilton population (pCOHP) was also calculated (Figure 20). The pCOHP curves obtained plot the nature of specific bonds of the ([RuPMe]$^{+}$-$Ru_{55}H_{35}$)PF_6^- hybrid structure (positive regions are bonding and negative regions are anti-bonding). Close to the Fermi level, the nature of the Ru(II)-Cl and Ru(II)-bpy interaction is altered by their interaction with the

RuNP surface, becoming less antibonding. At lower energies, the nature of the bonds between the Ru(II) center and the other ligands in $[RuPMe]^+$, predictably those more distant from the RuNP surface, is preserved.

Finally, the projected Mulliken population analysis (pMPA) shows a slightly oxidized RuNP surface due to the adsorption of hydride species (Figure 21). Moreover, upon coordination of $[RuPMe]^+$ on the surface, a charge reorganization is observed. While the total charge of the free $[RuPMe]^+$ complex is initially ca. +1, in the hybrid, the charge of the $[RuPMe]^+$ grafted unit is of ca. +0.5. Consequently, the Ru_{55} core has a formal charge of ca. +0.4.

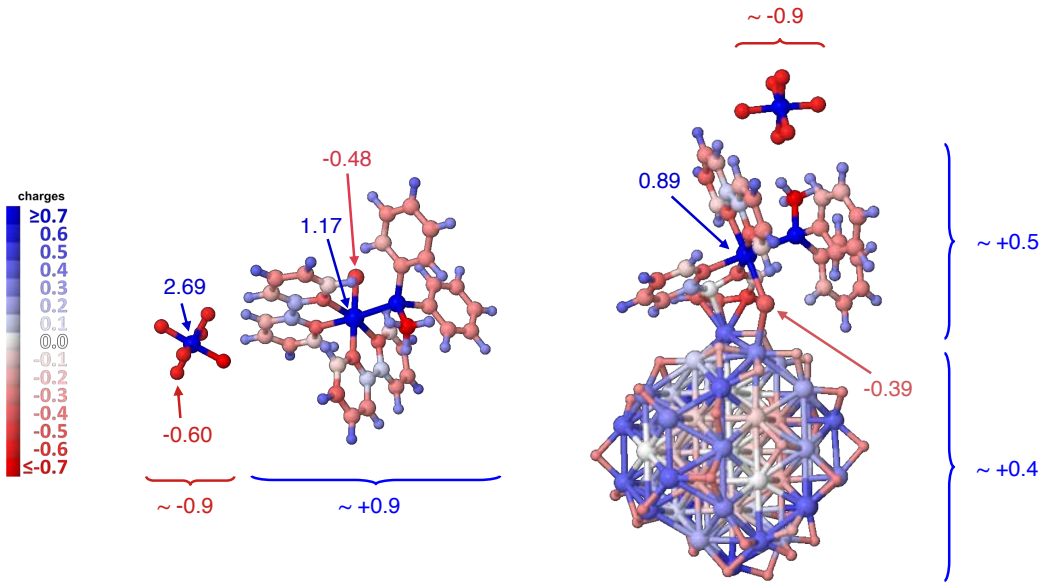

Figure 21. Atomic pMPA charges on $[RuPMe]^+PF_6^-$ (left) and $[RuPMe]^+$-$Ru_{55}H_{35}$ (right).

It is important to note that, due to the complexity of the calculations, the pDOS, pCOHP and pMPA of $([RuPMe]^+$-$Ru_{55}H_{35})PF_6^-$ incorporate only one $[RuPMe]^+$ molecule coordinated to the Ru_{55} cluster. It would thus be illustrative to study the electronic configuration of the system with a coverage of 4 or 5 $[RuPMe]^+$ molecules, a model that would be closer to the hybrid material $([RuPMe]_n$-RuNPs$)^+(PF_6^-)_n$. The first consequence would be an increase in intensity of all the contributions from the $[RuPMe]^+$ complex. Second, it would be interesting to evaluate how this change might affect the contribution of the d-orbitals from the RuNP surface, and consequently, the total DOS curve.

2.4. Conclusions on the electrochemical studies

The ensemble of data obtained by experimental and theoretical methods evidenced a marked difference in the electrochemical behavior of RuNPs stabilized by the electroactive $[RuPMe]^+PF_6^-$

complex compared to those observed for RuNPs capped by classic ligands, highlighting very different redox characters.

RuNPs stabilized by ligands like PPh_3, PCy_3 and bpy displayed large oxidation waves that were attributed to the corrosion of the Ru metal cores. Interestingly, the RuNPs stabilized by dppf and $[RuPMe]^+PF_6^-$ complex exhibited sharper peaks that could reasonably be attributed to the redox centers of the stabilizing surface groups. Most particularly, with a notable electrochemical gap of ca. 2.4 V, the $([RuPMe]_n\text{-}RuNPs)^+(PF_6^-)_n$ displays a molecule-like redox behavior. It also displays successive oxidations that could be related to a capacitor pattern. These observations allowed us to conclude on an unprecedented hybrid character of the $([RuPMe]_n\text{-}RuNPs)^+(PF_6^-)_n$ system.

The experimental data were supported by DFT calculations through the determination of the projected density of states (pDOS) of the $([RuPMe]_n\text{-}RuNPs)^+(PF_6^-)_n$ hybrid. In the pDOS profile obtained for this hybrid nanomaterial, a high occupied state (less than 1 eV below the Fermi level) is developed on a molecular orbital belonging to the Ru(II) metal center of the $[RuPMe]^+$ complex. Previous data obtained on Ru_{55} clusters stabilized by CH_3COO^- and CO ligands showed that the contributions of the ligands are far from the Fermi level of the resulting nanospecies, and, upon oxidation, electrons from the d-orbitals of the Ru nanoclusters would be supposedly retrieved. The presence of Ru(II) states from $[RuPMe]^+$ close to the Fermi level in the $([RuPMe]_n\text{-}RuNPs)^+(PF_6^-)_n$ hybrid might thus account for the different behavior observed experimentally.

In order to continue this work, it would be necessary to complete the characterization of the RuNPs stabilized by classical ligands and dppf, which so far have only been characterized by TEM analysis of the crude colloidal solution. For instance, WAXS analysis of the purified samples would be of interest to know about the crystallinity and agglomeration state of the RuNPs after the washing procedure. Also, TGA or elemental analysis to determine their composition (Ru wt%) and NMR experiments to shed some light on the fate of the ligands upon coordination to the RuNP surface would be revealing. These data will allow a more detailed and judicious comparison with the $([RuPMe]_n\text{-}RuNPs)^+(PF_6^-)_n$ nanohybrid system. Parallelly, DFT calculations on the electronic structure of RuNPs stabilized by simple ligands like PPh_3, PCy_3 or bpy would shed some light on the results experimentally obtained.

It is noteworthy that the electrochemical studies performed in the frame of this PhD work constitute a first achievement in our group. Previous essays performed in the past with other ligand-stabilized Ru and Pt NPs were not successful. Here, thanks to numerous efforts made in order to get exploitable signals, interesting information on the electronic behavior of a set of RuNPs could be obtained. This allowed evidencing that the redox responses obtained for the systems studied strongly depended on the nature of the stabilizer. Such a level of information might become very useful regarding

applications in catalysis, electron transfer processes or nanocapacitors devices, as possible examples, and this work will deserve to be thoroughly pursued by extending the scope of the capping molecules and/or of the nature of the metal nanoparticles.

3. Preliminary catalytic studies with $([RuPMe]_n\text{-}RuNPs)^+(PF_6^-)_n$

As it has been demonstrated above, the $([RuPMe]_n\text{-}RuNPs)^+(PF_6^-)_n$ hybrid nanomaterial displays different electrochemical properties than those observed for RuNPs stabilized by classical ligands. As reported, this nanohybrid presents successive oxidations that occur up to high oxidative potential (ca. 3 V (vs. SCE)). With this behavior, this nanomaterial may be envisaged as a potential electron reservoir, a property which can be of interest for catalytic reduction reactions. Besides the metallic core of the RuNPs, the $([RuPMe]_n\text{-}RuNPs)^+(PF_6^-)_n$ nanomaterial also contains organophosphorus Ru(II)-polypyridyl fragments surrounding the particles. The association of these two entities, which individually have interesting intrinsic properties, might lead to unusual surface reactivity. Also, given the photosensitive character of the organophosphorus Ru(II)-polypyridyl groups, the hybrid may promote photo-induced electron transfer processes.

Altogether, this encouraged us to evaluate the potential of our $([RuPMe]_n\text{-}RuNPs)^+(PF_6^-)_n$ nanohybrid in catalysis. For that purpose, we considered two reactions of interest for energy, environment and sustainability concerns, namely the production of hydrogen from water (hydrogen evolution reaction; see section 3.1.) and the transformation of carbon dioxide into formic acid (see section 3. 2).

The activity of $([RuPMe]_n\text{-}RuNPs)^+(PF_6^-)_n$ towards the photocatalytic hydrogen evolution reaction (HER) was studied at the Universitat Autònoma de Barcelona in the frame of a collaboration with the group of Dr. Xavier Sala. The performance of $([RuPMe]_n\text{-}RuNPs)^+(PF_6^-)_n$ as catalyst for the chemical reduction of CO_2 into formic acid was evaluated during a 4-week stay at the National University of Singapore, in the group of Pr. Ning Yan, with which our group has a collaborative ANR-NRF project centered on the valorization of CO_2. This stay was funded by a mobility grant received from the Université Fédérale Toulouse Midi-Pyrénées.

3.1. Photochemical reduction of H^+ for water splitting

3.1.1. Photochemical HER with ruthenium-based nanocatalysts

Ru(II)-polypyridyl complexes are well-known to present strong absorption in the visible spectral region, stability and tunable redox features in the excited-state. These properties account for their

extended use in energy and electron transfer processes, either as energy donor (Eq. 1), electron donor (Eq. 2) or electron acceptor (Eq. 3) [11].

$$[Ru(bpy)_3]^{2+*} + Q \rightarrow [Ru(bpy)_3]^{2+} + Q^* \quad \text{energy transfer} \quad (1)$$

$$[Ru(bpy)_3]^{2+*} + Q \rightarrow [Ru(bpy)_3]^{3+} + Q^- \quad \text{oxidative quenching} \quad (2)$$

$$[Ru(bpy)_3]^{2+*} + Q \rightarrow [Ru(bpy)_3]^{+} + Q^+ \quad \text{reductive quenching} \quad (3)$$

In photochemical systems related to the conversion of light into other forms of energy, Ru(II)-polypyridyl complexes play the role of light-harvesting units or photosensitizers, for instance, in dye-sensitized solar cells. Photoexcitation of the Ru(II)-polypyridyl dyes grafted to the surface of metal oxide nanoparticles, usually through carboxylate, hydroxamate or phosphonate functional groups, results in the injection of an electron to the conduction band of the metal oxide semiconductor [39]. In our group, $[Ru(bpy)_3]^{2+}$ complexes were grafted to the surface of heptanol-stabilized Co_3O_4 nanoparticles through phosphonate units, in order to photo-catalyze the oxidation of water into oxygen [40]. In this work it was demonstrated that the direct connection of the photo-sensitizer and the Co-based nanocatalyst favored the electronic communication between the two entities and allowed to get better yields in O_2 production than those obtained using the unbound counterparts under the same reaction conditions.

We will herein focus on the photocatalytic reduction of protons, namely hydrogen evolution reaction (HER), with metal nanoparticles. A conventional reaction for the photocatalytic HER is usually composed by a sacrificial electron-donor (e.g. ethylenediaminetetraacetic acid, EDTA), a photosensitizer such as $[Ru(bpy)_3]^{2+}$, an electron mediator to prevent back electron transfer (e.g. methyl viologen, MV^{2+}) and the hydrogen evolution catalyst (see Figure 22a) [41,42]. Platinum-based nanoparticles are the most efficient catalysts developed so far for this reaction. Nevertheless, a few recent publications report on the use of RuNPs in the photocatalytic HER.

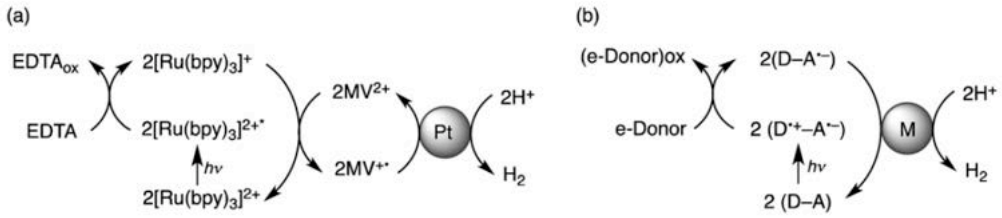

Figure 22. Catalytic cycle of (a) a conventional reaction system constructed by EDTA, $[Ru(bpy)_3]^{2+}$, MV^{2+} and PtNPs and (b) donor-acceptor linked dyad without electron mediator (M = Ru). Reproduced from [42].

The first example on the use of metal RuNPs for the efficient evolution of hydrogen under photocatalytic conditions was reported by Fukuzumi and coworkers [43]. The Ru catalyst was synthesized by thermal decomposition of $Ru_3(CO)_{12}$ using tri-*n*-octylamine as stabilizer, which was later exchanged by PVP to make the RuNPs water soluble. A donor-acceptor dyad, 2-phenyl-4-(1-naphthyl)-quinolinium ion ($QuPh^+$-NA), and reduced nicotinamide adenine dinucleotide (NADH), were used as photosensitizer and sacrificial electron-donor, respectively (Figure 22b). It was evidenced that the electron transfer rate from the reduced form of $QuPh^+$-NA to the RuNPs was faster than the rate of H_2 evolution at the nanoparticle surface. The catalytic activity observed with RuNPs of 4.1 nm optimal size was comparable to that of PtNPs under the same conditions. Longer catalyst life times were achieved by deposition of the RuNPs onto SiO_2 support, which prevented particle aggregation [44]. In another study, eosin Y (EY) dye was used to stabilize RuNPs, thus yielding an hybrid nanomaterial able to produce hydrogen under visible light irradiation in the presence of triethanolamine (TEOA) as sacrificial electron donor in aqueous media [45]. In this case, the authors attributed the efficiency of the electron transfer observed to the strong interaction between the OH and COO^- groups of the EY-dye and the RuNP surface.

There is only one efficient photocatalytic HER system where $[Ru(bpy)_3]^{2+}$ is employed as photosensitizer in combination with RuNPs acting as the hydrogen-evolution catalyst [46]. For an efficient electron transfer, 9-phenyl-10-methyl-acridinium ion (Ph–Acr^+–Mes) and EDTA were used as electron mediator and sacrificial electron donor, respectively.

3.1.2. Preliminary results with $([RuPMe]_n$-RuNPs$)^+(PF_6^-)_n$ hybrid

On the basis of the literature data summarized above, the hybrid structure of the $([RuPMe]_n$-RuNPs$)^+(PF_6^-)_n$ nanomaterial naturally led us to consider its evaluation in the HER. As presented on Scheme 2, we believed that the $[RuPMe]^+$ complex could act as light-harvester and then photoactivate the hydrogen-evolution catalyst, role played by the RuNPs.

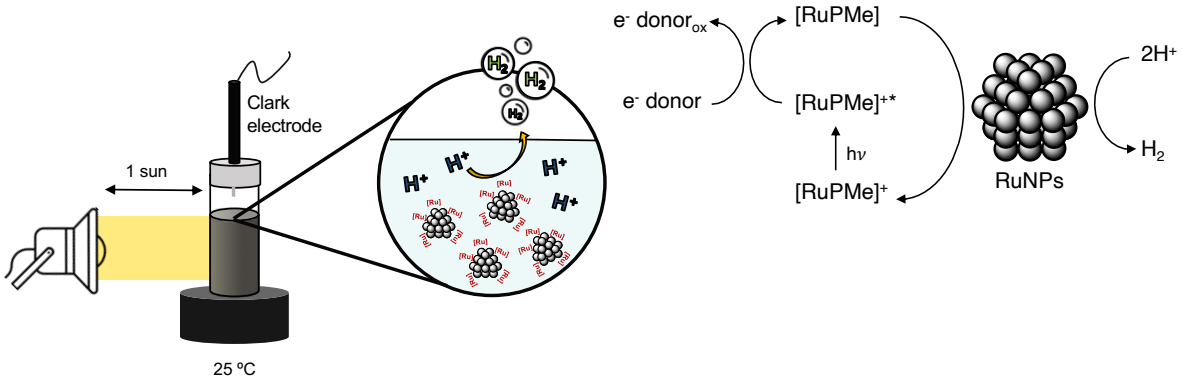

Scheme 2. Hypothetic mechanism for the photocatalyzed HER by $([RuPMe]_n$-RuNPs$)^+(PF_6^-)_n$.

The HER photocatalytic activity of $([RuPMe]_n\text{-}RuNPs)^+(PF_6^-)_n$ was evaluated under visible light irradiation (λ > 400 nm) calibrated to 1 sun intensity (1 kW/m^2), after dispersion of the hybrid nanomaterial in a 4 mL aqueous solution (pH 7, 25 °C) using TEOA as sacrificial electron donor (TEOA 0.2 M). The production of H_2 was measured by using a Clark hydrogen electrode (see Scheme 2). These reaction conditions had previously been optimized in the UAB group for the photocatalytic generation of H_2 using other Ru-based heterogeneous nanomaterials as catalysts [47].

In a first assessment of the photocatalytic activity of a colloidal solution of $([RuPMe]_n\text{-}RuNPs)^+(PF_6^-)_n$ no generation of H_2 was detected. Addition of $[RuPMe]^+PF_6^-$ and MV^{2+} to the reaction mixture didn't result in any improvement. At this stage we hypothesized that the low solubility of the hybrid material observed during the preparation of the catalytic medium in water, undesired back electron transfer, or a combination of the two, could be the cause of the inactivity of the system under the conditions applied.

In a recent work [47], the key role of TiO_2 in a ternary photocatalytic HER system composed by TiO_2-supported RuNPs and $[Ru(bpy)_3]^{2+}$ complexes bearing phosphonate anchoring groups has been evidenced. Time-resolved spectroscopic studies proved that TiO_2 acts as electron-mediator, ensuring the electronic communication between the Ru nanocatalysts and the photosensitive $[Ru(bpy)_3]^{2+}$ complex. Moreover, supporting RuNPs on TiO_2 prevents their aggregation during catalysis and facilitates their dispersion in aqueous media. Inspired by these positive results, $([RuPMe]_n\text{-}RuNPs)^+(PF_6^-)_n$ was then deposited onto TiO_2 by impregnation of the titania support from a colloidal solution of the hybrid in acetonitrile (9.3 mg of hybrid / 100 mg of TiO_2; see Table 2), in order to evaluate its activity in these supported conditions.

In addition, two other systems were prepared by the same procedure to use as references (Table 2). First, $[RuPMe]^+PF_6^-$ complex was adsorbed on TiO_2, leading to $[RuPMe]^+PF_6^-@TiO_2$ material in order to evaluate its own catalytic behavior in the absence of RuNP catalyst. Second, bpy-RuNPs were also supported on TiO_2, giving rise to bpy-RuNPs@TiO_2 material, to have a referent activity of RuNPs stabilized by classical ligands in the absence of any photosensitizer.

Material	Composition
$([RuPMe]_n\text{-}RuNPs)^+(PF_6^-)_n@TiO_2$	9.3 mg / 100 mg TiO_2
bpy-RuNPs@TiO_2	9.2 mg / 100 mg TiO_2
$[RuPMe]^+PF_6^-@TiO_2$	4.4 mg / 100 mg TiO_2

Table 2. Composition of the materials used for photocatalytic HER.

It is important to note that the activities of these different catalytic materials towards the photocatalytic HER can only be qualitatively discussed since the real Ru content of each material has not been analyzed. However, the experiments have shown reproducible catalytic behavior. Figure 23 represents the number of H_2 mol produced as a function of time, after introducing in the cell 4 mg of each TiO_2-supported material. The response of bare TiO_2 has been also evaluated in the same conditions for comparison purpose. Due to its photocatalytic properties, TiO_2 may also exhibit some activity [48].

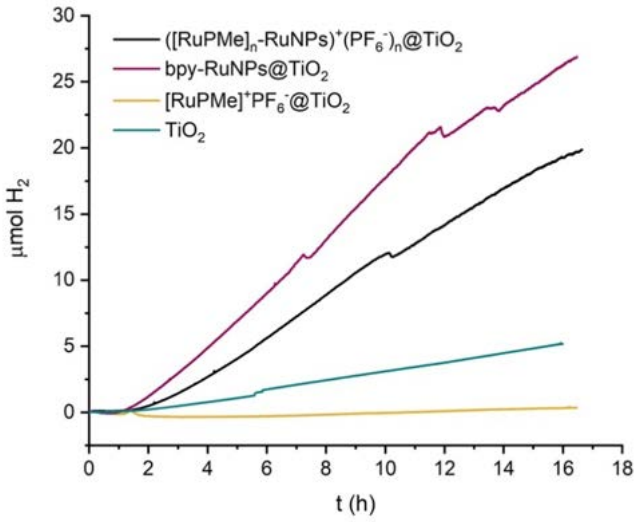

Figure 23. Photocatalytic hydrogen evolution (in a 4 mL TEOA 0.2 M aqueous solution) using as catalyst $([RuPMe]_n\text{-}RuNPs)^+(PF_6^-)_n@TiO_2$ (black curve) bpy-RuNPs@TiO_2 (violet curve), $[RuPMe]^+PF_6^-@TiO_2$ (yellow curve) and TiO_2 (green curve).

As shown on figure 23 (green curve), TiO_2 displayed a low activity by itself (ca. 4 µmol of H_2 evolved in 16 h) that was completely inhibited when $[RuPMe]^+PF_6^-$ was adsorbed on it (yellow curve). After 16 h of HER photocatalysis, 20 and 27 µmol of H_2 were generated in the presence of $([RuPMe]_n\text{-}RuNPs)^+(PF_6^-)_n@TiO_2$ and bpy-RuNPs@TiO_2, respectively. According to these qualitative results, the two $([RuPMe]_n\text{-}RuNPs)^+(PF_6^-)_n@TiO_2$ and bpy-RuNPs@TiO_2 materials seem to have comparable performances. However, note that the real Ru wt% of the bpy-RuNPs system, which is necessary to normalize the activity observed (mol H_2/mol Ru), has not yet been determined.

In the absence of more accurate data, the turnover number (TON) and turnover frequency (TOF) of the $([RuPMe]_n\text{-}RuNPs)^+(PF_6^-)_n@TiO_2$ material have been estimated on the basis of the Ru content determined for the hybrid material $([RuPMe]_n\text{-}RuNPs)^+(PF_6^-)_n$ by ICP analysis (see Chapter 2). By this way, a TON of 10 $mol_{H2} \cdot mol_{Ru}^{-1}$ and a TOF of 0.62 $mol_{H2} \cdot h^{-1} \cdot mol_{Ru}^{-1}$ values could be calculated over 16h of reaction. These values are considerably lower than those obtained for the ternary hybrid system cited above taken as model [47], i.e. TiO_2-supported RuNPs sensitized with $[Ru(bpy)_3]^{2+}$ complexes bearing phosphonate anchors, for which an activity 30 times superior has been achieved.

3.1.3. Conclusions on the activity of $([RuPMe]_n\text{-}RuNPs)^+(PF_6^-)_n$ towards the photocatalytic HER

The preliminary results obtained on the photocatalytic production of H_2 using as catalytic system the $([RuPMe]_n\text{-}RuNPs)^+(PF_6^-)_n$ hybrid, are disappointing, at least in the conditions applied. First, the estimated TON and TOF values are low and not competitive with those achieved by other catalytic systems previously reported. Second, compared to the bpy-RuNPs@TiO_2 system, we did not observe a significant improvement of the photocatalytic HER activity of RuNPs by their stabilization with photosensitive complexes, as we had initially envisaged for $([RuPMe]_n\text{-}RuNPs)^+(PF_6^-)_n$@$TiO_2$.

The low photocatalytic activity observed with the hybrid $([RuPMe]_n\text{-}RuNPs)^+(PF_6^-)_n$ could derive from an inefficient electron communication between the $[RuPMe]^+PF_6^-$ entities and the RuNPs. According to the results described in Chapter 2, the $[RuPMe]^+PF_6^-$ complex stabilizes the RuNPs being disposed in two different surrounding layers. If the photophysical properties of $[RuPMe]^+$ complexes covalently coordinated onto the RuNP surface (inner layer) have not been measured yet and might have been altered by the coordination to the nanoparticles, the $[RuPMe]^+$ complexes present in the outer layer, $[RuPMe]^+_{exch}$, which are supposed to electrostatically interact with their inner layer counterparts far from the RuNP surface, are expected to preserve their intrinsic electronic properties. However, the photocatalytic results obtained seem to indicate an inefficient electronic connection between the $[RuPMe]^+_{exch}$ complexes and the RuNPs. The electron transfer between the different entities composing the $([RuPMe]_n\text{-}RuNPs)^+(PF_6^-)_n$ hybrid system would merit to be studied by time-resolved optical spectroscopy measurements, in order to provide accurate conclusions on the photocatalytic behavior of our hybrid nanomaterial for HER in the conditions applied. Such studies should also help in the understanding of the parameters to be tuned within the aim to develop more performant photocatalysts.

3.2. Chemical reduction of CO_2 into formic acid

The capture and conversion of CO_2 into fuels and value-added chemicals have emerged as an attractive strategy to mitigate the CO_2 emissions to the atmosphere and to use these greenhouse gas as renewable C_1 chemical feedstock [13]. For instance, CO_2 can be used as building block for the production of carboxylates, esters, carbamates, urea, formic acid, carbon monoxide, methanol or hydrocarbons, as non-exhaustive examples [49].

A promising route for the use of CO_2 is the production of formic acid. Formic acid is a prominent chemical, feedstock in industrial processes and chemical syntheses (as an acid, a reductant and or

precursor) [50]. Formic acid is also recognized as an effective vector for the transport and storage of H_2 (Figure 24).

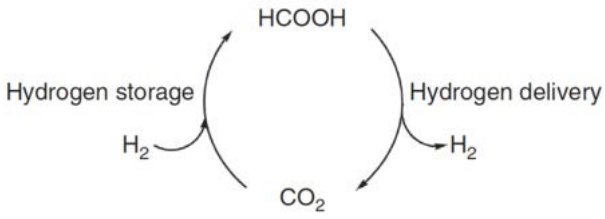

Figure 24. The formic acid/carbon dioxide cycle for hydrogen storage, reproduced from ref. [51].

Because of its high entropic contribution, the chemical reduction of CO_2 in the gas phase by H_2 has a positive ΔG value (+33 kJ mol^{-1}). The reaction is more favorable in basic aqueous solution, when the actual substrates are HCO_3- (ΔG = -35 kJ mol^{-1}) or CO_3^{2-}. The transformation of CO_2 into formic acid requires thus to use appropriate conditions and catalysts [51].

Given the recent examples reported on the interest of Ru-based nanomaterials for the production of formic acid and formates from CO_2 [14,52], we were interested in evaluating the catalytic behavior of our hybrid nanomaterial in this important reaction. Before presenting our first results, the next section will provide a short overview of the catalytic systems already reported for the reduction of CO_2 into HCOOH involving ruthenium-based nanocatalysts.

3.2.1. CO_2 transformation into formic acid ruthenium-based nanocatalysts

From one of the first reported studies on the direct synthesis of formic acid from CO_2 and H_2 by a combination of transition metal complexes, among which the $H_2Ru(PPh_3)_4$ [53], hydrogenation of CO_2 into formic by Ru homogeneous catalysts has been extensively developed. Many studies have been devoted to evaluate the effects of the electronic and steric properties of the coordinated ligands together with the optimal reaction conditions (solvent, temperature, addition of base in the reaction media), which allowed to achieve very efficient Ru metal complexes for the catalytic production of HCOOH [54–57].

In contrast to the highly active Ru homogeneous catalysts, moderate catalytic performances are observed in the transformation of CO_2 into formic acid by Ru-based heterogeneous catalysts [52]. A first example on the use of RuNPs for the hydrogenation of supercritical CO_2 to formic acid has been reported by Kojima and co-workers [58] where a TON ($mol_{FA} \cdot mol_{Ru}^{-1}$) of 6351 in 3 h (namely a TOF of 2117 h^{-1}), at 80 °C and in the presence of triethylamine as a base was achieved.

The activity of RuNPs dispersed in TiO_2 has also been evaluated in the presence or not of ionic liquids by Srivastava and co-workers [59]. Initially, a TOF of 28 h^{-1} ($mol_{FA} \cdot mol_{Ru}^{-1} \cdot h^{-1}$) was obtained at 80 °C and 40 bar H_2/CO_2 (1:1) for the most efficient system obtained. Addition of 1,3-di(*N,N*-dimethylaminoethyl)-2-methylimidazolium bis-(trifuoromethylsulfonyl)imide led to an increase of the activity to 47 h^{-1}. Ionic liquids are efficient for the adsorption of gases and, at the same time, improve the stability of the RuNPs. Immobilization of RuNPs by ionic liquids and further application in CO_2 hydrogenation was also essayed, achieving, in the best conditions (50 °C and 50 bar CO_2/H_2), a TOF value of 3300 h^{-1} [59].

3.2.2. Experimental results

Besides the evaluation of our nanohybrid material $([RuPMe]_n\text{-}RuNPs)^+(PF_6^-)_n$ in the transformation of CO_2 into formic acid, a series of RuNPs stabilized by classical ligands, PP, PPh_3, PCy_3 and bpy, eventually deposited onto TiO_2 as support has been also investigated (PP = 4-phenylpyridine). The catalytic studies have been performed following the conditions usually applied in Yan's group for other types of nanostructured catalysts [60,61].

In a typical reaction, the nanocatalyst was dispersed in a 1 M $NaHCO_3$ aqueous solution, $NaHCO_3$ being the source of CO_2. The mixture was sonicated to achieve an homogeneous dispersion and then introduced in a stainless-steel autoclave. The reactor was then pressurized with 20 bar H_2 before being plunged into an oil bath when heating (40 °C) was applied, at an optimized stirring rate of 800 rpm. After 1 or 2 h of reaction time, remaining H_2 was evacuated, the reaction mixture was filtered through a 0.45 μm PTFE (Teflon) filter and the solution was analyzed by high-performance liquid chromatography (HPLC) (see Experimental Section).

The obtained results are presented in Table 3. Note that these are only approximate results, based on an estimated Ru content of 70 wt% in each nanomaterial prepared. This value has been taken as an average from previous data from the group on RuNPs. As it can be observed from Table 3, the obtained results indicate low TON and TOF values but it is important to precise that no optimization has been performed. From these very first results, we can nevertheless discuss on the effect of the TiO_2 support and the nature of the stabilizer on the catalytic activities observed. The results will be discussed and compared through MTY values (metal time yield, right column), which are expressed in $\mu mol_{FA} \cdot s^{-1} \cdot mol_{metal}^{-1}$ [62].

When comparing PP-RuNPs and PP-RuNPs/TiO_2 systems (entries 1 and 2), it appears that the deposition of the PP-RuNPs onto the titania support improved the catalytic activity (from MTY 48 to MTY 101), probably due to a better dispersion and/or stability, thus limiting nanoparticle aggregation. Also, reaction time of 1 h provided a slightly higher activity than that obtained in 2 h (MTY 129 vs. 101)

which may indicate a lack of stability of the catalyst in the reaction conditions applied or eventually a certain reversibility of the reaction. Concerning the last hypothesis, the decomposition of formic acid into H_2 and CO_2 by Ru nanocatalysts, more precisely, PVP-stabilized RuNPs, has already been reported [63].

Unsupported PPh_3-RuNPs appeared slightly more active than PP-RuNPs (entry 4 vs. 1), which was proved when using the TiO_2-supported $RuPPh_3$ catalyst (entry 5 vs. 2). A phosphine positive effect appeared more evident in the presence of PCy_3 as stabilizer (entry 6 vs. 5), for TiO_2 supported RuNPs. With PCy_3 ligand, higher MTY value was also obtained at 1h of reaction time compared to 2 h (entry 7 vs. 6), following the same trend observed for PP-RuNPs. The better catalytic performance observed with PCy_3 could be attributed to the more electron donor character of this ligand compared to that of PPh_3 or PP ligands.

TiO_2-supported bpy-RuNPs appeared also active in this reaction, with a reactivity similar to that observed for phosphine-stabilized RuNPs (entry 8 vs. 5 and 6), after 2 h. Interestingly, these bpy-stabilized RuNPs appeared less active after 1 h than after 2 h. Considering the few data we have at our disposal, we cannot conclude about this last observation.

Finally, the best catalytic results were obtained with the non-supported $([RuPMe]_n\text{-}RuNPs)^+(PF_6^-)_n$ hybrid nanomaterial, with a MTY value of ca. 400 after 2 h of reaction at 40 °C. A first plausible explanation could derive from the better solubility of the $([RuPMe]_n\text{-}RuNPs)^+(PF_6^-)_n$ in water in comparison to the other RuNPs tested, due to the hydrophobic character of the stabilizers used which leads to less soluble RuNPs in aqueous media. The ionic character of $([RuPMe]_n\text{-}RuNPs)^+(PF_6^-)_n$ might give rise to a better dispersion in the aqueous solution and therefore, higher availability of active sites to react with the $NaHCO_3$ substrate. A second reason for the higher reactivity observed for $([RuPMe]_n\text{-}RuNPs)^+(PF_6^-)_n$ might derive from a synergic effect with the hybrid, arising from the coordination of the transition metal complex, $[RuPMe]^+PF_6^-$, at the surface of the RuNPs. This assumption is sustained by the catalytic results obtained for the free $[RuPMe]^+PF_6^-$ in the same conditions (entry 15), which did not display any activity towards the transformation of $NaHCO_3$ into $HCOO^-$.

Compared to other nanocatalysts tested, the activity of the $([RuPMe]_n\text{-}RuNPs)^+(PF_6^-)_n$ hybrid was drastically disfavored when supported on TiO_2, leading to a decrease on the MTY value from 405 to 208 at 40 °C (entry 10 vs. 11).

The activity of unsupported $([RuPMe]_n\text{-}RuNPs)^+(PF_6^-)_n$ has also been evaluated at room temperature (entries 12 and 13). Lower catalytic performances have been observed in these conditions, with MTY values of 254 and 267 after 1 and 2 h of reaction, respectively (vs. 405 at 40 °C after 2 h). Higher

temperatures seem to favor the rate of HCOOH production by $([RuPMe]_n\text{-}RuNPs)^+(PF_6^-)_n$, either by a better solubility of the nanocatalyst in the reaction mixture and/or a decrease of the necessary activation energy. Importantly, even if unsupported $([RuPMe]_n\text{-}RuNPs)^+(PF_6^-)_n$ catalysts exhibited lower activities at r.t. than at 40 °C, they still presented better results than to those obtained for RuNPs stabilized by classical ligands at 40 °C.

		Time (h)	**Temp.** (°C)	**TON**	**TOF** (h^{-1})	**MTY** ($\mu mol_{FA} \cdot s^{-1} \cdot mol_{metal}^{-1}$)
1	PP-RuNPs	2	40	0.3	0.2	48
2	PP-RuNPs/TiO_2	2	40	0.7	0.4	101
3	PP-RuNPs/TiO_2	1	40	0.5	0.5	129
4	PPh_3-RuNPs	2	40	1.0	0.5	138
5	PPh_3-RuNPs/TiO_2	2	40	0.8	0.4	113
6	PCy_3-RuNPs/TiO_2	2	40	0.9	0.4	124
7	PCy_3-RuNPs/TiO_2	1	40	0.6	0.6	161
8	bpy-RuNPs/TiO_2	2	40	0.9	0.5	128
9	bpy-RuNPs/TiO_2	1	40	0.2	0.2	64
10	$([RuPMe]_n\text{-}RuNPs)^+(PF_6^-)_n$	2	40	2.9	1.5	405
11	$([RuPMe]_n\text{-}RuNPs)^+(PF_6^-)_n$ /TiO_2	2	40	1.5	0.7	208
12	$([RuPMe]_n\text{-}RuNPs)^+(PF_6^-)_n$	2	r.t.	1.8	0.9	254
13	$([RuPMe]_n\text{-}RuNPs)^+(PF_6^-)_n$	1	r.t.	1.0	1.0	267
14	$([RuPMe]_n\text{-}RuNPs)^+(PF_6^-)_n$ /TiO_2	2	r.t.	1.3	0.6	178
15	$[RuPMe]^+PF_6^-$	2	r.t.	-	-	-

Table 3. Activities obtained for the different Ru-based nanocatalysts tested in 1 M aqueous solution of $NaHCO_3$ under 20 bar of H_2. TON, TOF and MTY values have been estimated on the basis of a Ru content of 70 wt%.

3.2.3. Conclusions on the activity of $([RuPMe]_n\text{-}RuNPs)^+(PF_6^-)_n$ and RuNPs stabilized by simple ligands on the catalytic formation of HCOOH

In this section, we have reported the very first results we have obtained in the transformation of CO_2 into HCOOH using Ru-based nanoparticles as catalysts, in mild reaction conditions. If the presented results are quite poor both in terms of parameter influence studies and of TON and TOF values, it is important to remind that only a few examples of Ru-based heterogeneous and nanoscale catalysts are

reported in the literature for this reaction so far. Considering that ruthenium is a metal of interest for industrial catalytic applications, the development of active Ru-nanocatalysts able to perform catalytic CO_2 transformation in mild conditions is an encouraging and challenging task. Moreover, from a fundamental point of view, the understanding of the key-parameters which govern the behavior of Ru-based catalysts is highly motivating, as this can provide helpful responses in order to progress in the synthesis of more performant catalysts. The study presented above lies in this context.

Comparing a set of RuNPs stabilized by different ligands (PP, PPh_3, PCy_3, bpy), some interesting results on the effect of the stabilizing ligand have been obtained. It appeared that phosphine ligands (PPh_3 and PCy_3) have a positive effect compared to a phenylpyridine ligand (PP), which appeared more pronounced with PCy_3, probably due to the higher electron donating character of this phosphine. The activity observed for bipyridine-stabilized RuNPs appeared also of interest. However, an extended study would be necessary in order to have more accurate data and get a better understanding of the ligand effect on the catalytic activity of the tested RuNPs. For these ligand-capped RuNPs, the deposition of the RuNPs onto TiO_2, support provided, in general, higher catalytic performances. Higher dispersion of the RuNPs when deposited at TiO_2 surface and increase of the stability in the reaction conditions applied, by limiting nanoparticle aggregation and loss of active surface sites, might account for the positive effect when using TiO_2-supported RuNPs. Higher catalytic performances were observed at shorter reaction times, maybe due to a certain deactivation of the nanocatalysts studied in the reaction conditions applied and/or a certain reversibility of the reaction. This point, i.e. regeneration of CO_2 from the produced HCOOH, will merit to be deeply studied.

Remarkably, at 40 °C, the best catalytic results were obtained with the non-supported $([RuPMe]_n\text{-}RuNPs)^+(PF_6^-)_n$ hybrid nanomaterial. Even if with a lower performance, this nanocatalyst remained active when reactions were carried at room temperature, and even more important, presented higher activity than the other RuNPs at 40 °C.

To conclude, the preliminary studies performed show that the performance of the $([RuPMe]_n\text{-}RuNPs)^+(PF_6^-)_n$ hybrid towards the catalytic transformation of HCO_3^- into $HCOO^-$ under H_2 pressure is higher than those observed with RuNPs stabilized by classical ligands, at least under the conditions applied. If a solubility effect cannot be discarded, we believe this difference derives from synergistic properties that might arise upon coordination of the $[RuPMe]^+$ complex onto the surface of the RuNPs. The evaluation of the $([RuPMe]_n\text{-}RuNPs)^+(PF_6^-)_n$ hybrid in this reaction will thus deserve to be pursued.

Altogether, the results obtained encourage us to pursue this line of research. Changing different reaction parameters like temperature, pressure, pH, nature of the stabilizer, solvent, solid support or

CO_2 source, in order to get accurate information on the role they play in the activity of the Ru nanocatalysts is now the primary objective.

4. Conclusions

In this chapter, we reported the studies of the electrochemical properties and catalytic properties in HER and CO_2 reduction of the $([RuPMe]_n\text{-}RuNPs)^+(PF_6^-)_n$ hybrid nanomaterial.

We designed an optimized experimental procedure for the collection of reliable and reproducible electrochemical data on hybrid RuNPs, as well as on RuNPs stabilized by classical ligands, which allowed us to investigate their fine redox properties.

Experimental and theoretical data highlighted the different electrochemical behavior of $[RuPMe]^+$-stabilized RuNPs compared to those of RuNPs capped by classical ligands, which displayed very different redox characters. Most specifically, with a notable electrochemical gap of ca. 2.4 V, the $([RuPMe]_n\text{-}RuNPs)^+(PF_6^-)_n$ hybrid displays a molecule-like redox behavior. It also displays successive oxidations that could be related to a capacitor pattern. According to the classification of Murray [6] that we presented in the introduction of this chapter, we may propose that our hybrid nanomaterial displays both regime II and III behaviors; namely "molecule-like" (regime III) and "quantized charging" (regime II) redox behaviors. This allowed us to conclude on unprecedented hybrid electrochemical properties of the $([RuPMe]_n\text{-}RuNPs)^+(PF_6^-)_n$ system.

A similar behavior was observed with dppf-RuNPs system, but further characterization is required to understand the intimate reasons of these structure-properties relationship.

In marked contrast, PPh_3-RuNPs, PCy_3-RuNPs and bpy-RuNPs systems showed large redox waves, which were attributed to a corrosion-like process, as observed for bulk metals. This behavior could correspond, according to Murray's classification, to the "bulk-continuum" regime (regime I).

Further structural characterization is needed on the dppf-RuNPs system, as well as for PPh_3-RuNPs, PCy_3-RuNPs and bpy-RuNPs, to be able to obtain more accurate conclusions on the reason of the electrochemical responses experimentally obtained.

These results allowed evidencing that the redox responses obtained for the systems studied strongly depended on the nature of the stabilizer. Such a level of information might become very useful regarding applications in catalysis or in other domains of interest, as in electron transfer applications or nanocapacitors, for example. This work will deserve to be exhaustively pursued by extending the scope of the nature of the stabilizers and/or metal nanoparticles.

The preliminary results obtained on the photocatalytic production of H_2 using $([RuPMe]_n\text{-}RuNPs)^+(PF_6^-)_n$ hybrid as photocatalyst showed TON and TOF values far lower than the best catalytic systems reported in the literature. The low photocatalytic activity observed with the hybrid $([RuPMe]_n\text{-}RuNPs)^+(PF_6^-)_n$ could derive from an inefficient electron transfer between the $[RuPMe]^+PF_6^-$ entities and the RuNPs or a poor photoactivation of the hybrid nanomaterial.

Regarding CO_2 hydrogenation, the preliminary studies performed showed that the performance of the $([RuPMe]_n\text{-}RuNPs)^+(PF_6^-)_n$ hybrid towards the catalytic transformation of HCO_3^- into $HCOO^-$ under H_2 pressure is higher than those observed with a set of ligand-capped RuNPs. If a solubility effect cannot be discarded, we believe this difference derives from synergistic properties that might arise upon coordination of the $[RuPMe]^+$ complex onto the surface of the RuNPs. The evaluation of the $([RuPMe]_n\text{-}RuNPs)^+(PF_6^-)_n$ hybrid in this reaction will thus deserve to be pursued.

5. References

1. Juris, A.; Balzani, V.; Barigelletti, F.; Campagna, S.; Belser, P.; von Zelewsky, A. Ru(II) polypyridine complexes: photophysics, photochemistry, eletrochemistry, and chemiluminescence. *Coord. Chem. Rev.* **1988**, *84*, 85–277.

2. Vidal-Iglesias, F.J.; Solla-Gullón, J.; Rodríguez, P.; Herrero, E.; Montiel, V.; Feliu, J.M.; Aldaz, A. Shape-dependent electrocatalysis: ammonia oxidation on platinum nanoparticles with preferential (100) surfaces. *Electrochem. Commun.* **2004**, *6*, 1080–1084.

3. Vidal-Iglesias, F.J.; Arán-Ais, R.M.; Solla-Gullón, J.; Herrero, E.; Feliu, J.M. Electrochemical Characterization of Shape-Controlled Pt Nanoparticles in Different Supporting Electrolytes. *ACS Catal.* **2012**, *2*, 901–910.

4. Kleijn, S.E.F.; Lai, S.C.S.; Koper, M.T.M.; Unwin, P.R. Electrochemistry of Nanoparticles. *Angew. Chem. Int. Ed.* **2014**, *53*, 3558–3586.

5. Mirkin, M.V.; Sun, T.; Yu, Y.; Zhou, M. Electrochemistry at One Nanoparticle. *Acc. Chem. Res.* **2016**, *49*, 2328–2335.

6. Murray, R.W. Nanoelectrochemistry: Metal Nanoparticles, Nanoelectrodes, and Nanopores. *Chem. Rev.* **2008**, *108*, 2688–2720.

7. Creus, J.; De Tovar, J.; Romero, N.; García-Antón, J.; Philippot, K.; Bofill, R.; Sala, X. Ruthenium Nanoparticles for Catalytic Water Splitting. *ChemSusChem* **2019**, *12*, 2493–2514.

8. Han, S.; Yun, Q.; Tu, S.; Zhu, L.; Cao, W.; Lu, Q. Metallic ruthenium-based nanomaterials for electrocatalytic and photocatalytic hydrogen evolution. *J. Mater. Chem. A* **2019**, *7*, 24691–24714.

9. Drouet, S.; Creus, J.; Collière, V.; Amiens, C.; García-Antón, J.; Sala, X.; Philippot, K. A porous Ru nanomaterial as an efficient electrocatalyst for the hydrogen evolution reaction under acidic and neutral conditions. *Chem. Commun.* **2017**, *53*, 11713–11716.

10. Creus, J.; Drouet, S.; Suriñach, S.; Lecante, P.; Collière, V.; Poteau, R.; Philippot, K.; García-Antón, J.; Sala, X. Ligand-Capped Ru Nanoparticles as Efficient Electrocatalyst for the Hydrogen Evolution Reaction. *ACS Catal.* **2018**, *8*, 11094–11102.

11. Campagna, S.; Puntoriero, F.; Nastasi, F.; Bergamini, G.; Balzani, V. Photochemistry and Photophysics of Coordination Compounds: Ruthenium. In *Photochemistry and Photophysics of Coordination Compounds I*; Balzani, V., Campagna, S., Eds.; Topics in Current Chemistry; Springer Berlin Heidelberg: Berlin, Heidelberg, 2007; pp. 117–214 ISBN 978-3-540-73347-8.

12. Meyer, T.J. Chemical approaches to artificial photosynthesis. *Acc. Chem. Res.* **1989**, *22*, 163–170.

13. Leitner, W. Carbon Dioxide as a Raw Material: The Synthesis of Formic Acid and Its Derivatives from CO_2. *Angew. Chem. Int. Ed. Engl.* **1995**, *34*, 2207–2221.

14. Yan, N.; Philippot, K. Transformation of CO_2 by using nanoscale metal catalysts: cases studies on the formation of formic acid and dimethylether. *Curr. Opin. Chem. Eng.* **2018**, *20*, 86–92.

15. Tokel-Takvoryan, N.E.; Hemingway, R.E.; Bard, A.J. Electrogenerated chemiluminescence. XIII. Electrochemical and electrogenerated chemiluminescence studies of ruthenium chelates. *J. Am. Chem. Soc.* **1973**, *95*, 6582–6589.

16. Dixon, I.M.; Lebon, E.; Sutra, P.; Igau, A. Luminescent ruthenium–polypyridine complexes & phosphorus ligands: anything but a simple story. *Chem. Soc. Rev.* **2009**, *38*, 1621-1634.

17. Dixon, I.M.; Lebon, E.; Loustau, G.; Sutra, P.; Vendier, L.; Igau, A.; Juris, A. Broad HOMO–LUMO gap tuning through the coordination of a single phosphine, aminophosphine or phosphite onto a $Ru(tpy)(bpy)^{2+}$ core. *Dalton Trans.* **2008**, 5627-5635.

18. Shang, C. Synthesis of ruthenium-phosphorus dyes and their incorporation in ZnO transparent conducting oxide and ZnO semi-conductor thin films for photovoltaic application. Doctoral Thesis, Université Paul Sabatier, Toulouse, 2013.

19. Templeton, A.C.; Wuelfing, W.P.; Murray, R.W. Monolayer-Protected Cluster Molecules. *Acc. Chem. Res.* **2000**, *33*, 27–36.

20. Chen, S.; Murray, R.W.; Feldberg, S.W. Quantized Capacitance Charging of Monolayer-Protected Au Clusters. *J. Phys. Chem. B* **1998**, *102*, 9898–9907.

21. Hesari, M.; Workentin, M.S.; Ding, Z. Highly Efficient Electrogenerated Chemiluminescence of Au_{38} Nanoclusters. *ACS Nano* **2014**, *8*, 8543–8553.

22. Chakraborty, I.; Pradeep, T. Atomically Precise Clusters of Noble Metals: Emerging Link between Atoms and Nanoparticles. *Chem. Rev.* **2017**, *117*, 8208–8271.

23. Jin, R.; Zeng, C.; Zhou, M.; Chen, Y. Atomically Precise Colloidal Metal Nanoclusters and Nanoparticles: Fundamentals and Opportunities. *Chem. Rev.* **2016**, *116*, 10346–10413.

24. Kwak, K.; Thanthirige, V.D.; Pyo, K.; Lee, D.; Ramakrishna, G. Energy Gap Law for Exciton Dynamics in Gold Cluster Molecules. *J. Phys. Chem. Lett.* **2017**, *8*, 4898–4905.

25. Cabo-Fernández, L.; Bradley, D.F.; Romani, S.; Higgins, S.J.; Schiffrin, D.J. Quantized Electron-Transfer Pathways at Nanoparticle-Redox Centre Hybrids. *ChemPhysChem* **2012**, *13*, 2997–3007.

26. Labande, A.; Astruc, D. Colloids as redox sensors: recognition of $H_2PO_4^-$ and HSO_4^- by amidoferrocenylalkylthiol–gold nanoparticles. *Chem. Commun.* **2000**, 1007–1008.

27. Horikoshi, T.; Itoh, M.; Kurihara, M.; Kubo, K.; Nishihara, H. Synthesis, redox behavior and electrodeposition of biferrocene-modified gold clusters. *J. Electroanal. Chem.* **1999**, *473*, 113–116.

28. Yamada, M.; Quiros, I.; Mizutani, J.; Kubo, K.; Nishihara, H. Preparation of palladium nanoparticles functionalized with biferrocene thiol derivatives and their electro-oxidative deposition. *Phys. Chem. Chem. Phys.* **2001**, *3*, 3377–3381.

29. Ito, M.; Tsukatani, T.; Fujihara, H. Preparation and characterization of gold nanoparticles with a ruthenium-terpyridyl complex, and electropolymerization of their pyrrole-modified metal nanocomposites. *J. Mater. Chem.* **2005**, *15*, 960-964.

30. Mayer, C.R.; Dumas, E.; Miomandre, F.; Méallet-Renault, R.; Warmont, F.; Vigneron, J.; Pansu, R.; Etcheberry, A.; Sécheresse, F. Polypyridyl ruthenium complexes as coating agent for the formation of gold and silver nanocomposites in different media. Preliminary luminescence and electrochemical studies. *New J. Che.m* **2006**, *30*, 1628–1637.

31. Pavlishchuk, V.V.; Addison, A.W. Conversion constants for redox potentials measured versus different reference electrodes in acetonitrile solutions at 25°C. *Inorganica Chim. Acta* **2000**, *298*, 97–102.

32. Astruc, D. Why is Ferrocene so Exceptional? *Eur. J. Inorg. Chem.* **2017**, *2017*, 6–29.

33. Ibrahim, M.; Wei, M.M.; Deydier, E.; Manoury, E.; Poli, R.; Lecante, P.; Philippot, K. Rhodium nanoparticles stabilized by ferrocenyl-phosphine ligands: synthesis and catalytic styrene hydrogenation. *Dalton Trans.* **2019**, *48*, 6777–6786.

34. Gutmann, T.; Bonnefille, E.; Breitzke, H.; Debouttière, P.-J.; Philippot, K.; Poteau, R.; Buntkowsky, G.; Chaudret, B. Investigation of the surface chemistry of phosphine-stabilized ruthenium nanoparticles – an advanced solid-state NMR study. *Phys. Chem. Chem. Phys.* **2013**, *15*, 17383–17394.

35. Lara, P.; Philippot, K.; Chaudret, B. Organometallic Ruthenium Nanoparticles: A Comparative Study of the Influence of the Stabilizer on their Characteristics and Reactivity. *ChemCatChem* **2013**, *5*, 28–45.

36. Hoffmann, R. *Solids and surfaces: a chemist's view of bonding in extended structures*. **1988**, Wiley-VCH: New York, NY, 2002; ISBN 978-0-471-18710-3.

37. Cusinato, L.; Martínez-Prieto, L.M.; Chaudret, B.; del Rosal, I.; Poteau, R. Theoretical characterization of the surface composition of ruthenium nanoparticles in equilibrium with syngas. *Nanoscale* **2016**, *8*, 10974–10992.

38. González-Gómez, R.; Cusinato, L.; Bijani, C.; Coppel, Y.; Lecante, P.; Amiens, C.; Rosal, I. del; Philippot, K.; Poteau, R. Carboxylic acid-capped ruthenium nanoparticles: experimental and theoretical case study with ethanoic acid. *Nanoscale* **2019**, *11*, 9392–9409.

39. Grätzel, M. Solar Energy Conversion by Dye-Sensitized Photovoltaic Cells. *Inorg. Chem.* **2005**, *44*, 6841–6851.

40. De Tovar, J.; Romero, N.; Denisov, S.A.; Bofill, R.; Gimbert-Suriñach, C.; Ciuculescu-Pradines, D.; Drouet, S.; Llobet, A.; Lecante, P.; Colliere, V.; Freixa, Z.; McClenaghan, N.; Amiens, C.; García-Antón, J.; Philippot, K.; Sala, X. Light-driven water oxidation using hybrid photosensitizer-decorated Co_3O_4 nanoparticles. *Mater. Today Energy* **2018**, *9*, 506–515.

41. Kiwi, J.; Graetzel, M. Projection, size factors, and reaction dynamics of colloidal redox catalysts mediating light induced hydrogen evolution from water. *J. Am. Chem. Soc.* **1979**, *101*, 7214–7217.

42. Fukuzumi, S.; Yamada, Y. Catalytic activity of metal-based nanoparticles for photocatalytic water oxidation and reduction. *J. Mater. Chem.* **2012**, *22*, 24284-24296.

43. Yamada, Y.; Miyahigashi, T.; Kotani, H.; Ohkubo, K.; Fukuzumi, S. Photocatalytic Hydrogen Evolution under Highly Basic Conditions by Using Ru Nanoparticles and 2-Phenyl-4-(1-naphthyl)quinolinium Ion. *J. Am. Chem. Soc.* **2011**, *133*, 16136–16145.

44. Yamada, Y.; Shikano, S.; Fukuzumi, S. Robustness of Ru/SiO_2 as a Hydrogen-Evolution Catalyst in a Photocatalytic System Using an Organic Photocatalyst. *J. Phys. Chem. C* **2013**, *117*, 13143–13152.

45. Kong, C.; Li, Z.; Lu, G. The dual functional roles of Ru as co-catalyst and stabilizer of dye for photocatalytic hydrogen evolution. *Int. J. Hydrog. Energy* **2015**, *40*, 5824–5830.

46. Yamada, Y.; Yano, K.; Fukuzumi, S. Photocatalytic Hydrogen Evolution Using 9-Phenyl-10-methyl-acridinium Ion Derivatives as Efficient Electron Mediators and Ru-Based Catalysts. *Aust. J. Chem.* **2013**, *65*, 1573–1581.

47. Romero, N.; Guerra, R.; Gil, L.; Drouet, S.; Salmeron, I.; Illa, O.; Philippot, K.; Natali, M.; García-Antón, J.; Sala, X. TiO_2-Mediated Visible-Light-Driven Hydrogen Evolution by Ligand-Capped Ru Nanoparticles. *ChemSusChem* Submitted.

48. Naldoni, A.; Altomare, M.; Zoppellaro, G.; Liu, N.; Kment, Š.; Zbořil, R.; Schmuki, P. Photocatalysis with Reduced TiO_2: From Black TiO_2 to Cocatalyst-Free Hydrogen Production. *ACS Catal.* **2019**, *9*, 345–364.

49. Aresta, M.; Dibenedetto, A.; Angelini, A. The changing paradigm in CO_2 utilization. *J. CO_2 Util.* **2013**, *3–4*, 65–73.

50. Gunasekar, G.H.; Park, K.; Jung, K.-D.; Yoon, S. Recent developments in the catalytic hydrogenation of CO_2 to formic acid/formate using heterogeneous catalysts. *Inorg. Chem. Front.* **2016**, *3*, 882–895.

51. Moret, S.; Dyson, P.J.; Laurenczy, G. Direct synthesis of formic acid from carbon dioxide by hydrogenation in acidic media. *Nat. Commun.* **2014**, *5*.

52. Axet, M.R.; Philippot, K. Catalysis with Colloidal Ruthenium Nanoparticles. *Chem. Rev.* **2020**. *120*, 2, 1085-1145

53. Inoue, Y.; Izumida, H.; Sasaki, Y.; Hashimoto, H. Catalytic fixation of carbon dioxide to formic acid by transition-metal complexes under mild conditions. *Chem. Lett.* **1976**, *5*, 863–864.

54. Wang, W.-H.; Feng, X.; Bao, M. *Transformation of Carbon Dioxide to Formic Acid and Methanol*; SpringerBriefs in Molecular Science; Springer Singapore: Singapore, **2018**; ISBN 978-981-10-3249-3.

55. Federsel, C.; Jackstell, R.; Boddien, A.; Laurenczy, G.; Beller, M. Ruthenium-Catalyzed Hydrogenation of Bicarbonate in Water. *ChemSusChem* **2010**, *3*, 1048–1050.

56. Ono, T.; Qu, S.; Gimbert-Suriñach, C.; Johnson, M.A.; Marell, D.J.; Benet-Buchholz, J.; Cramer, C.J.; Llobet, A. Hydrogenative Carbon Dioxide Reduction Catalyzed by Mononuclear Ruthenium Polypyridyl Complexes: Discerning between Electronic and Steric Effects. *ACS Catal.* **2017**, *7*, 5932–5940.

57. Munshi, P.; Main, A.D.; Linehan, J.C.; Tai, C.-C.; Jessop, P.G. Hydrogenation of Carbon Dioxide Catalyzed by Ruthenium Trimethylphosphine Complexes: The Accelerating Effect of Certain Alcohols and Amines. *J. Am. Chem. Soc.* **2002**, *124*, 7963–7971.

58. Umegaki, T.; Enomoto, Y.; Kojima, Y. Metallic ruthenium nanoparticles for hydrogenation of supercritical carbon dioxide. *Catal. Sci. Technol.* **2016**, *6*, 409–412.

59. Upadhyay, P.R.; Srivastava, V. Selective hydrogenation of CO_2 gas to formic acid over nanostructured Ru-TiO_2 catalysts. *RSC Adv.* **2016**, *6*, 42297–42306.

60. Zhang, Z.; Zhang, L.; Hülsey, M.J.; Yan, N. Zirconia phase effect in Pd/ZrO_2 catalyzed CO_2 hydrogenation into formate. *Mol. Catal.* **2019**, *475*, 110461.

61. Zhang, Z.; Zhang, L.; Yao, S.; Song, X.; Huang, W.; Hülsey, M.J.; Yan, N. Support-dependent rate-determining step of CO_2 hydrogenation to formic acid on metal oxide supported Pd catalysts. *J. Catal.* **2019**, *376*, 57–67.

62. Mondelli, C.; Puértolas, B.; Ackermann, M.; Chen, Z.; Pérez-Ramírez, J. Enhanced Base-Free Formic Acid Production from CO_2 on Pd/g-C_3N_4 by Tuning of the Carrier Defects. *ChemSusChem* **2018**, *11*, 2859–2869.

63. Liu, H.; Mei, Q.; Wang, Y.; Liu, H.; Han, B. N-vinyl pyrrolidone promoted aqueous-phase dehydrogenation of formic acid over PVP-stabilized Ru nanoclusters. *Sci. China Chem.* **2016**, *59*, 1342–1347.

CHAPTER 4

1. Introduction

In Chapter 2, an effective way to synthesize, in one-pot conditions, ruthenium nanoparticles stabilized by a mononuclear organophosphorus Ru(II)-polypyridyl complex, $[RuPMe]^+PF_6^-$, has been described. A fine characterization of the resulting hybrid nanomaterial, $([RuPMe]_n\text{-}RuNPs)^+(PF_6^-)_n$, by means of a combination of diverse and complementary experimental and theoretical methods, which allowed to determine precisely its structure, has been performed. In Chapter 3, electrochemical studies highlighted the unprecedented hybrid character of the $([RuPMe]_n\text{-}RuNPs)^+(PF_6^-)_n$ nanomaterial. Also, even if extended work is required in order to complete the preliminary catalytic studies in HER and CO_2 reduction, our results evidenced the potential interest of this hybrid nanomaterial in catalysis. Altogether, we are convinced that our fundamental work may open new avenues for the development of new hybrid nanomaterials. It is of great interest now to vary the two components, namely the stabilizing complex and/or the metal nanoparticles. In this Chapter, we will thus report preliminary results on the synthesis of other hybrid nanomaterials: (i) Ru-based nanoparticles stabilized by Ru(II)-polypyridyl complexes incorporating new type of phosphorus fragments and (ii) metal nanoparticles of other metals, Co and Pt, synthesized by using the organophosphorus Ru(II)-polypyridyl complexes as stabilizers.

It has already been demonstrated that organophosphorus Ru(II)-polypyridyl complexes allow to tune their electrochemical and photophysical properties to a very large extent. The coordination of various type of organophosphorus ligands to the $[Ru(bpy)(tpy)]^{2+}$ and the $[Ru(bpy)_2]^{2+}$ fragments has been widely investigated [1–3]. By the accurate choice of the P-based ligand, a wide range of electrochemical and photophysical properties can be attained. Also, the reactivity of these complexes can be modified by changing the different substituents on the P atom. For instance, incorporation of the hydrogen-bond acceptor ability $Ph_2P{=}O$ ligand in the coordination sphere of a polypyridine ruthenium(II) complex allowed the formation of proton-bridged and water-bridged dimeric complexes [4]. Given their versatile properties and their coordination ability onto a metal surface, organophosphorus Ru(II)-polypyridyl derivatives are good candidates in order to explore the resulting structure, surface reactivity, electrochemical and photophysical properties of the corresponding hybrids, in comparison to those of $([RuPMe]_n\text{-}RuNPs)^+(PF_6^-)_n$ hybrid described in Chapters 2 and 3.

The organometallic approach has proven to be an efficient method to provide small and well-controlled hybrid ruthenium nanoparticles. As previously mentioned, ruthenium was our first choice

to develop the $([RuPMe]_n\text{-}RuNPs)^+(PF_6^-)_n$ hybrid nanomaterials owing to the experience of the group in the synthesis of RuNPs, which facilitated their study by comparison with other RuNP systems. Moreover, RuNPs allow access to liquid and solid-state NMR experiments, and the organometallic precursor used for their synthesis, [Ru(cod)(cot)], releases only inert byproducts that do not coordinate to the metal surface.

The first part of this chapter is thus dedicated to the use of selected functionalized organophosphorus Ru(II)-polypyridyl complexes other than the initial $[RuPMe]^+PF_6^-$ to test their ability to stabilize Ru-based nanoparticles in order to prepare their corresponding Ru-based hybrid nanomaterials. In the second part, preliminary results in the organometallic synthesis of cobalt and platinum-based hybrid nanomaterials by using organophosphorus Ru(II)-polypyridyl complexes will be described.

2. Stabilization of RuNPs with selected functionalized organophosphorus Ru(II)-polypyridyl complexes

Hybrid nanomaterials based on two other mononuclear organophosphorus Ru(II)-polypyridyl complexes and RuNPs have been synthesized, following the procedure previously developed for the $([RuPMe]_n\text{-}RuNPs)^+(PF_6^-)_n$ hybrid nanomaterial. For this purpose, organophosphorus Ru(II)-polypyridyl complexes of similar structure as that of $[RuPMe]^+PF_6^-$ complex have been chosen.

On the one hand, we chose the mononuclear functionalized organophosphorus Ru(II)-polypyridyl complex $[(bpy)_2Ru(PPh_2H)Cl]PF_6$ complex, $[RuPH]^+PF_6^-$, which is structurally analogous to $[RuPMe]^+PF_6^-$, but bears a P-H bond instead of a P-Me. On the other hand, we used the functionalized organophosphorus Ru(II)-polypyridyl complex $[(bpy)_2Ru(P(O)Ph_2)MeCN]PF_6$, $[RuPO]^+PF_6^-$, where the phosphine ligand has been oxidized into a phosphoryl group, $Ph_2P{=}O$. Also, in this $[RuPO]^+PF_6^-$ complex, the Cl ligand coordinated to the Ru(II) metal center, as in $[RuPMe]^+PF_6^-$, has been substituted by an acetonitrile molecule.

The resulting nanomaterials obtained using these two complexes as stabilizers for the synthesis of RuNPs, $([RuPH]_n\text{-}RuNPs)^+(PF_6^-)_n$ and $([RuPO]_n\text{-}RuNPs)^+(PF_6^-)_n$, have been preliminarily characterized.

2.1. Synthesis and characterization of the $([RuPH]_n\text{-}RuNPs)^+(PF_6^-)_n$ hybrid nanomaterial

As mentioned above, the functionalized organophosphorus Ru(II)-polypyridyl complex $[(bpy)_2Ru(PPh_2H)Cl]PF_6$, $[RuPH]^+PF_6^-$, holds a diphenylphosphine, Ph_2PH, ligand. Interestingly, the deprotonation of the P-H group by the use of strong bases such as butyllithium [5] or potassium *tert*-

butoxide [6] has been reported for the preparation of their corresponding phosphanide transition metal complexes which are expected to be highly nucleophilic. They can undergo rapid alkylation into Ph_2PR, by reaction with, for instance, alkyl halides RX. They can also be easily oxidized into the corresponding phosphoryl group, Ph_2PO, when exposed to air. Therefore, by using the $[RuPH]^+$ complex as stabilizer of the RuNPs, we may envisage the fine-tuning of the hybrid nanomaterial by post-functionalization reactions on the P-H substituent.

2.1.1. Synthesis of the $[RuPH]^+PF_6^-$ complex

The synthesis of the functionalized organophosphorus Ru(II)-polypyridyl complex $[RuPH]^+PF_6^-$ has been performed following a protocol which has been set up by A. Igau and P. Sutra, starting from *cis*-$[Ru(bpy)_2Cl_2]$ (Scheme 1) [3]. Sequentially, a low excess of thallium hexafluorophosphate, $TlPF_6$, and 5 eq. of diphenylphosphine, PPh_2H, both dissolved in dry acetone, were added dropwise to an acetone solution of *cis*-$[Ru(bpy)_2Cl_2]$, and the mixture was magnetically stirred for 12 h at 25 °C (r.t.). After elimination of TlCl by filtration, purification through flash chromatography and washing with ether, a precipitate has been isolated under the form of a very fine orange powder (yield: 42%). The product $[RuPH]^+PF_6^-$ has been identified by ^1H and ^{31}P NMR (see Experimental Section).

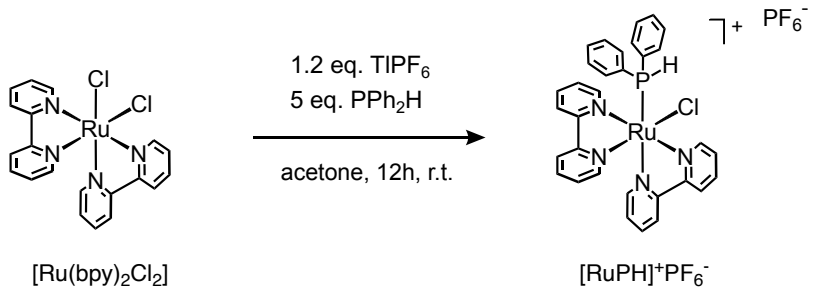

Scheme 1. Synthesis of $[(bpy)_2Ru(PPh_2H)Cl]PF_6$, $[RuPH]^+PF_6^-$.

The ^1H NMR spectrum of $[RuPH]^+PF_6^-$ complex is presented in Figure 1. The region of the aromatic protons gathers the signals for the protons of the phenyl groups of the phosphine ligand (PPh_2H) and those of the two bipyridine ligands (peaks between 7.0 and 9.5 ppm). The doublet centered at δ = 6.8 ppm with a $^1J_{P\text{-}H}$ = 356 Hz coupling constant corresponds to the P-H function of the PPh_2H ligand.

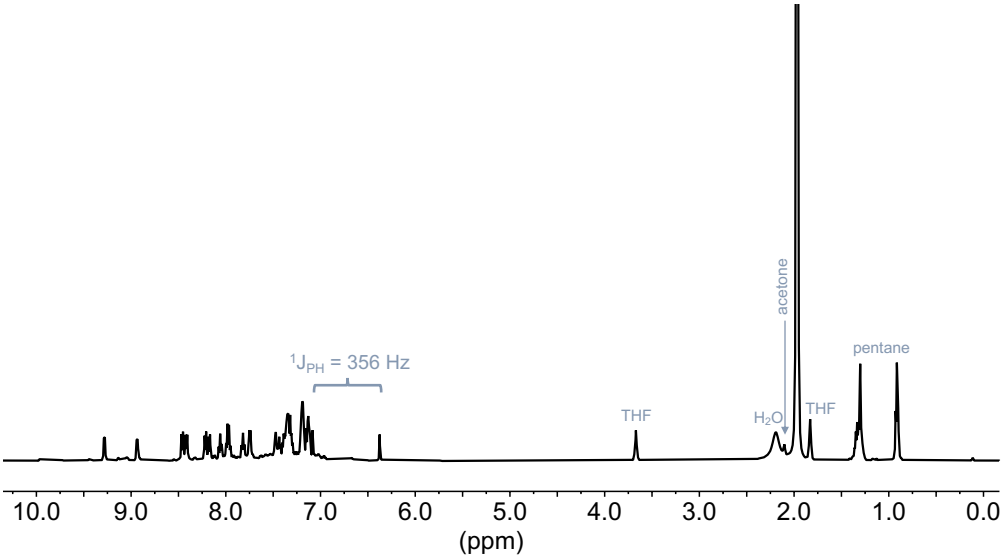

Figure 1. ^{1}H NMR spectrum of $[RuPH]^+PF_6^-$ in CD_3CN.

Traces of acetone (δ = 2.08 ppm), THF (δ = 1.80 and 3.64 ppm), water (δ = 2.13 ppm) and pentane (δ = 0.90, 1.29 and 1.31 ppm) are also observed. For the synthesis of nanohybrids, the $[RuPH]^+PF_6^-$ complex has been dried by lyophilization.

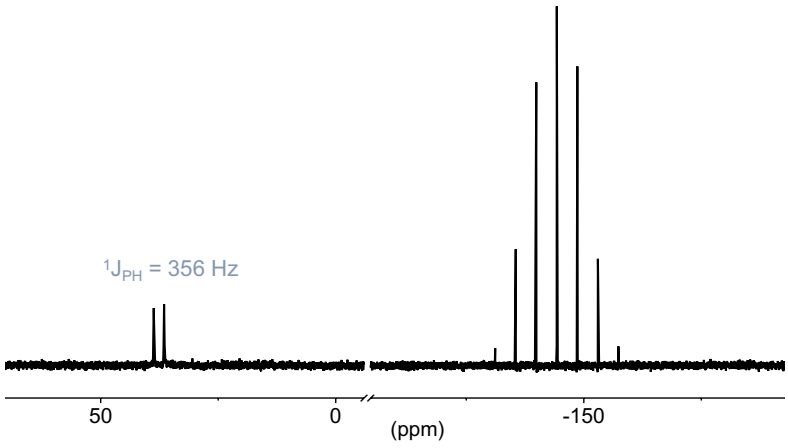

Figure 2. ^{31}P NMR spectrum of $[RuPH]^+PF_6^-$ in CD_3CN.

The ^{31}P NMR spectrum of $[RuPH]^+PF_6^-$ (Figure 2) presents a doublet centered at 37.5 ppm ($^1J_{P\text{-}H}$ = 356 Hz), corresponding to the Ph_2PH ligand, and a septuplet at -144.3 ppm which is characteristic of the PF_6^- counteranion.

2.1.2. Synthesis of the $([RuPH]_n\text{-}RuNPs)^+(PF_6^-)_n$ hybrid nanomaterial

Note that a blank test has been performed with the aim to check the stability of $[RuPH]^+PF_6^-$ complex when exposed to the conditions applied for the RuNP synthesis. After exposure of a THF solution of

$[RuPH]^+PF_6^-$ under 3 bar of H_2 in THF at 25 °C for 24 h, NMR analysis did not show any chemical and structural evolution of the functionalized organophosphorus Ru(II)-polypyridyl complex.

Like for $([RuPMe]_n\text{-}RuNPs)^+(PF_6^-)_n$, the synthesis of the hybrid nanomaterial $([RuPH]_n\text{-}RuNPs)^+(PF_6^-)_n$ (Scheme 2), has been performed using the organometallic complex [Ru(cod)(cot)] as precursor of RuNPs and 0.1 molar eq. of the $[RuPH]^+PF_6^-$ complex as stabilizer. Both were dissolved in freshly distilled and degassed THF (1 mL per mg of [Ru(cod)(cot)]), inside a Fischer-Porter reactor and under argon atmosphere, providing an intense orange homogeneous solution. The reaction mixture was then pressurized with 3 bar of H_2 and kept under vigorous stirring for 24 h at 25 °C. The initial orange solution turned black within a few minutes. After 24 h of reaction, excess H_2 was evacuated by pumping. The volatiles were then evaporated under vacuum which led to the formation of a black precipitate.

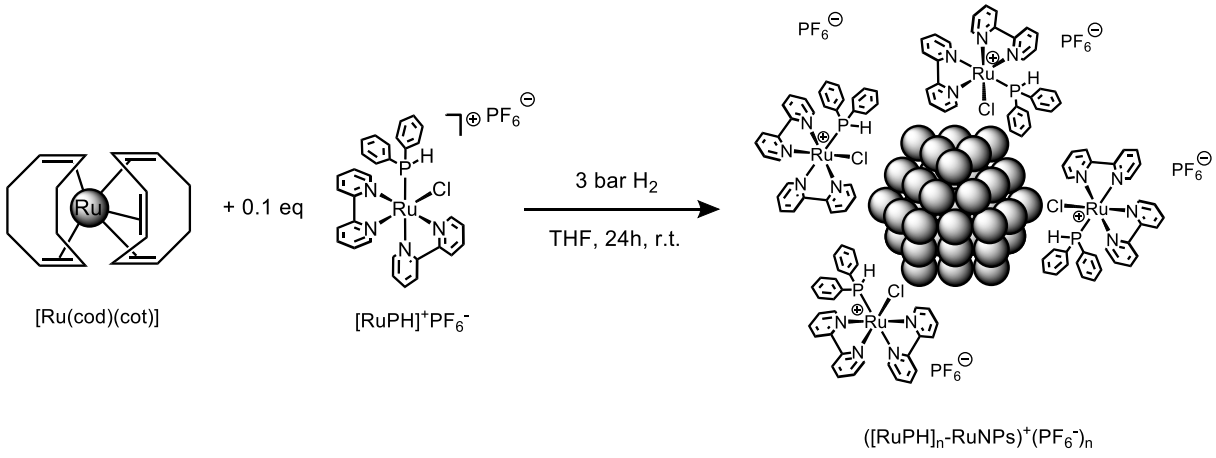

Scheme 2. Synthesis of the hybrid nanomaterial $([RuPH]_n\text{-}RuNPs)^+(PF_6^-)_n$.

In order to remove potentially unreacted $[RuPH]^+PF_6^-$, THF was added in the Fischer-Porter reactor. This led to an orange supernatant that was removed *via* canula after precipitation of the hybrid $([RuPH]_n\text{-}RuNPs)^+(PF_6^-)_n$ in the form of a black powder. This procedure was repeated three times, as previously done for the first hybrid nanomaterial. The obtained black powder was then dissolved into a minimum amount of acetonitrile in order to favor the dispersion of the sample transferred into a vial before drying under vacuum. Three additional washings with THF were again performed. The resulting washing solution appeared slightly colored. The washing solution was evaporated by pumping and the resulting solid was redissolved in CD_3CN for analysis by ^1H and ^{31}P NMR (see Figures 3 and 4). The ^1H and ^{31}P NMR data showed different signals than those expected for the initially introduced complex, $[RuPH]^+PF_6^-$.

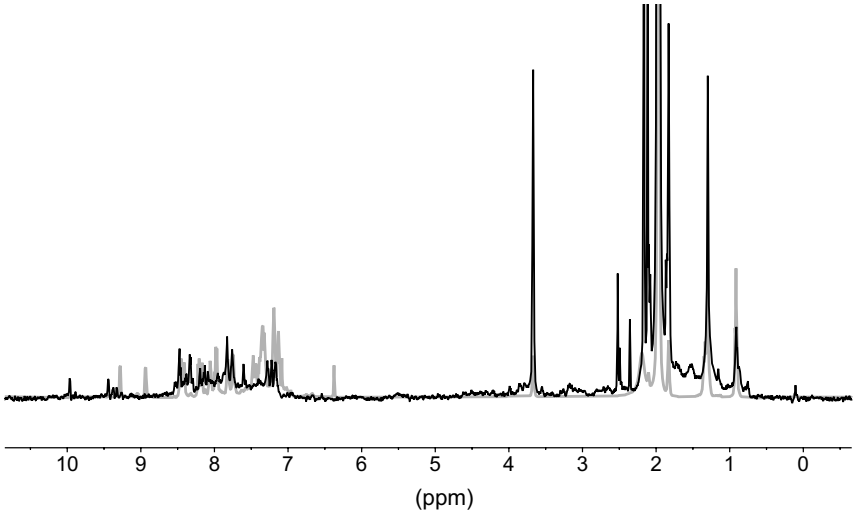

Figure 3. ^{1}H NMR spectra of the species extracted by THF washings (black) and of the original $[RuPH]^{+}PF_6^{-}$ (grey), in CD_3CN.

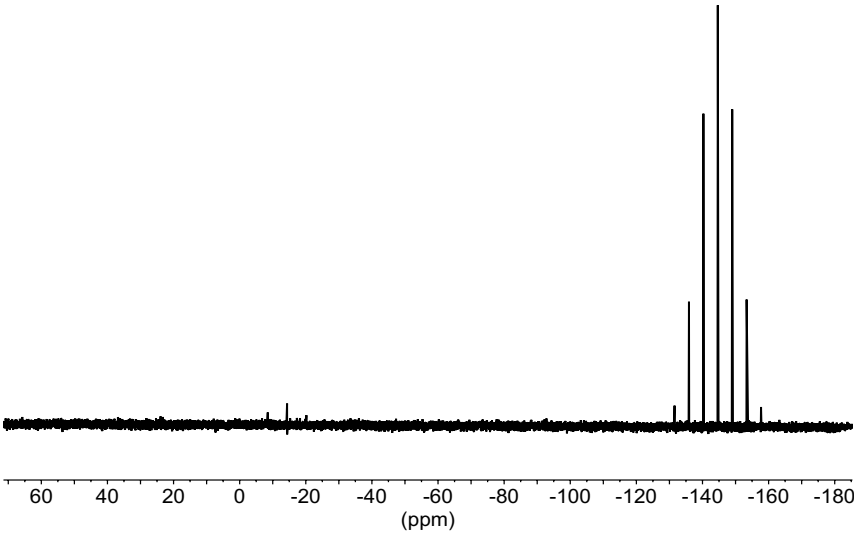

Figure 4. ^{31}P NMR spectra of the specie extracted by THF washings in CD_3CN.

Residual aromatic signals are observed in the ^{1}H NMR spectrum of the washings (Fig. 3). In ^{31}P NMR (Fig. 4), no characteristic peak of the Ph_2PH resonance at 37.5 ppm is observed. Only the PF_6^- septuplet and a triplet at -14.4 ppm are visible, the latter being attributed to difluorophosphate species, $PO_2F_2^-$, product of the partial hydrolysis of PF_6^- [7].

2.1.3. Characterization of the $([RuPH]_n\text{-}RuNPs)^+(PF_6^-)_n$ hybrid nanomaterial

TEM analysis has been performed from two grids, one prepared from the crude colloidal suspension in THF (Fig. 5a and 5b) and the second one from the re-dispersion of the purified black powder in acetonitrile (Fig. 5c). From THF crude colloidal suspension, regular spherical aggregates of ca. 1000 nm are visible on the TEM images. As already observed for the $([RuPMe]_n\text{-}RuNPs)^+(PF_6^-)_n$ material, these aggregates are composed of individual NPs. From re-dispersion in acetonitrile, small and individual NPs are observed, with a rather symmetrical size distribution centered at ca. 1.2 nm $\pm$ 0.3 (Fig. 5d). As previously discussed about $([RuPMe]_n\text{-}RuNPs)^+(PF_6^-)_n$, the different behavior of $([RuPH]_n\text{-}RuNPs)^+(PF_6^-)_n$ hybrid material in THF and acetonitrile may owe to an ionic-like character coming from the stabilizing complex. Concerning the size of the nanoparticles formed, the mean value determined by TEM appears very close to that previously observed for $([RuPMe]_n\text{-}RuNPs)^+(PF_6^-)_n$ hybrid material.

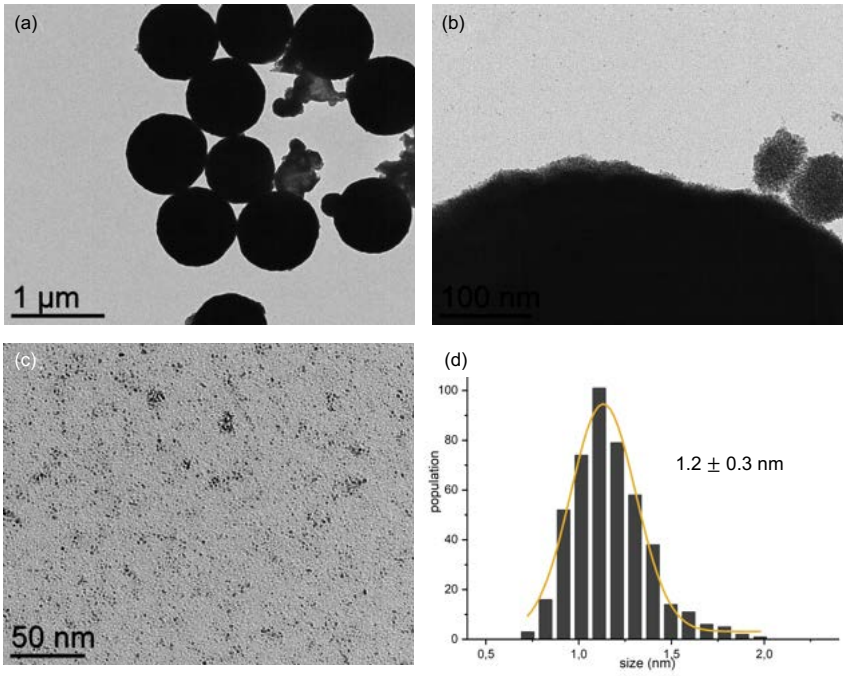

Figure 5. TEM images of $([RuPH]_n\text{-}RuNPs)^+(PF_6^-)n$: (a, b) in THF and (c) after redispersion in acetonitrile. (d) Size histogram of $([RuPH]_n\text{-}RuNPs)^+(PF_6^-)_n$ dissolved in acetonitrile.

WAXS analysis, on the purified $([RuPH]_n\text{-}RuNPs)^+(PF_6^-)_n$ powder (1 mm glass capillary, argon atmosphere) indicated metallic RuNPs with hcp crystalline structure and a coherence length estimated to ca. 2.5 nm (slightly higher than the core sizes measured by TEM (ca. 1.2 nm)) (Fig. 6).

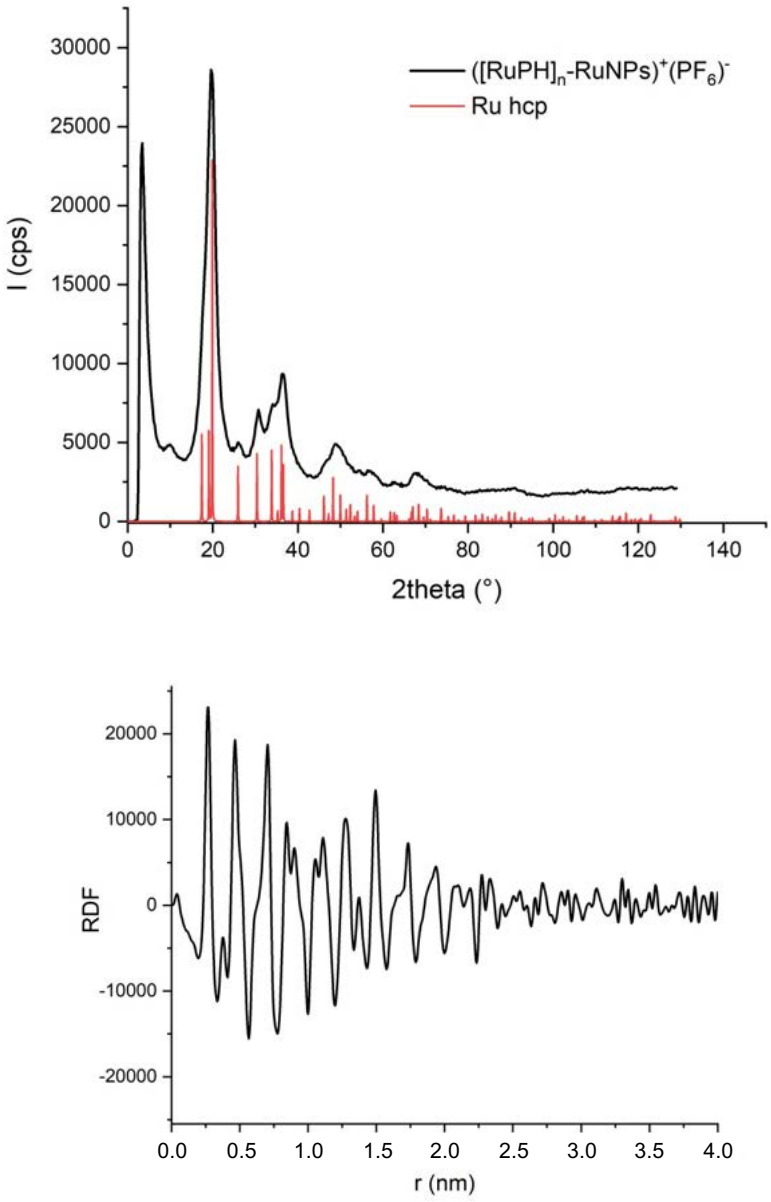

Figure 6. (top) WAXS diagram of $([RuPH]_n\text{-}RuNPs)^+(PF_6^-)_n$ (black) in comparison with diffraction pattern of bulk hcp (red) and (bottom) RDF of $([RuPH]_n\text{-}RuNPs)^+(PF_6^-)_n$.

Both TEM and WAXS analyses of the $([RuPH]_n\text{-}RuNPs)^+(PF_6^-)_n$ hybrid revealed comparable situation to that observed for $([RuPMe]_n\text{-}RuNPs)^+(PF_6^-)_n$ counterpart with similar metallic Ru core sizes and same crystalline structure.

Complementary liquid and solid-state NMR studies have been performed in order to shed some light on the structure of the $([RuPH]_n\text{-}RuNPs)^+(PF_6^-)_n$ hybrid. The purified hybrid nanomaterial was dissolved in CD_3CN in order to record liquid ^1H and ^{31}P NMR spectra. Figure 7 shows the ^1H NMR spectrum of the purified $([RuPH]_n\text{-}RuNPs)^+(PF_6^-)_n$ (Fig. 7b) and that of the $[RuPH]^+PF_6^-$ complex, as a reference (Fig. 7a). On spectrum 7b, a very broad signal is observed in the range of 6-9 ppm. Such a broad signal can result from the proximity of the phenyl and bipyridine protons of the $[RuPH]^+$ unit

with the RuNPs surface. Over this broad signal, sharper peaks are also visible at positions which are close to those expected for the free $[RuPH]^+PF_6^-$.

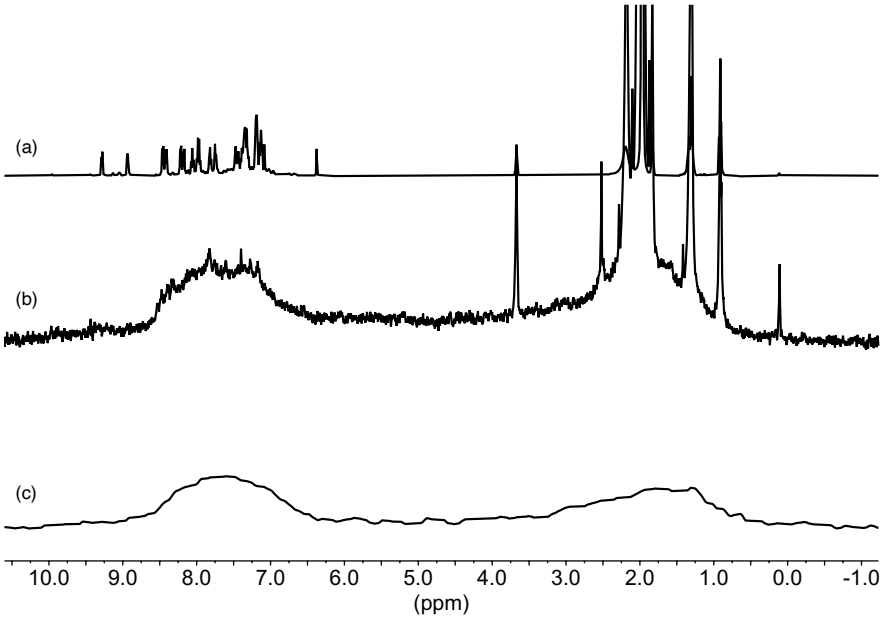

Figure 7. ^1H NMR spectra of (a) $[RuPH]^+PF_6^-$, (b) purified $([RuPH]_n\text{-}RuNPs)^+(PF_6^-)_n$ and (c) diffusion-filtered $([RuPH]_n\text{-}RuNPs)^+(PF_6^-)_n$ in CD_3CN.

The diffusion-filtered ^1H NMR profile of $([RuPH]_n\text{-}RuNPs)^+(PF_6^-)_n$ (Fig. 7c) revealed two broad signals (at ca. 1-3 and 6-9 ppm), reasonably attributed to $[RuPH]^+$ species in close interaction with the RuNP surface. By analogy with the previous $([RuPMe]_n\text{-}RuNPs)^+(PF_6^-)_n$ hybrid material, we can propose the presence of two types of complexes: 1) strongly grafted $[RuPH]^+$ species onto the RuNP surface which form an inner stabilizing layer and 2) weakly interacting $[RuPH]^+$ species, *via* electrostatic interaction with their inner layer counterparts, thus forming an outer layer. At this stage it is difficult to know, however, if the $[RuPH]^+$ complex used for the stabilization preserved its original structure when coordinated to the surface of the RuNPs.

Two different diffusion coefficients, D, have been determined by a bi-exponential analysis of the diffusion curve: D_1 ($4.1\cdot10^{-10}$ m^2/s,) attributed to the hybrid nanostructures, namely RuNPs and directly coordinated $[RuPH]^+$ species; and D_2 ($11.1\cdot10^{-10}$ m^2/s) very similar to that of the $[RuPH]^+PF_6^-$ free complex, and attributed to the $[RuPH]^+$ species in the outer layer, $[RuPH]^+_{exch}$ (see Table 1).

	Species	Diffusion coefficient, D (m^2/s)	Hydrodynamic diameter, d_h (nm)
free	$[RuPH]^+PF_6^-$	$11.6 \cdot 10^{-10}$	0.95
hybrid	$([RuPH]_n\text{-}RuNPs)^+(PF_6^-)_n$ (RuNPs and directly coordinated $[RuPH]^+$ species)	$4.1 \cdot 10^{-10}$	3.2
	$[RuPH]^+_{exch}$ (outer layer)	$11.1 \cdot 10^{-10}$	-

Table 1. List of diffusion coefficients and hydrodynamic diameters obtained for the free $[RuPH]^+PF_6^-$ complex, the hybrid $([RuPH]_n\text{-}RuNPs)^+(PF_6^-)_n$ and the $[RuPH]^+_{exch}$ in the outer layer, measured in CD_3CN.

In order to shed some light on the fate of the $[RuPH]^+$ complex when coordinated onto the surface of RuNPs, ^{31}P MAS NMR was recorded (Figure 8). As reported in Chapter 2, in order to avoid undesired electric arcing during the solid-state NMR experiments, the $([RuPH]_n\text{-}RuNPs)^+(PF_6^-)_n$ purified sample was diluted in an inert support, by impregnation of SiO_2 with a colloidal solution of the hybrid in acetonitrile (8.5 mg of $([RuPMe]_n\text{-}RuNPs)^+(PF_6^-)_n$ per 100 mg of SiO_2). For comparison purposes, the free $[RuPH]^+PF_6^-$ complex was also deposited onto the same SiO_2 powder.

Figure 8a shows the ^{31}P MAS NMR of free $[RuPH]^+PF_6^-$ in SiO_2. In order to get a better signal to noise ratio and more defined ^{31}P peaks, a Carr-Purcell-Meiboom-Gill (CPMG) sequence was applied. $[RuPH]^+PF_6^-$ complex (Fig. 8b) presents two peaks, one at -144 ppm and another one at 33 ppm corresponding to PF_6^- and to the Ph_2PH ligand, respectively. In the hybrid nanomaterial (Fig. 8c), the PF_6^- signal appears unaltered. On the basis of previous conclusions regarding the $([RuPMe]_n\text{-}RuNPs)^+(PF_6^-)_n$ nanomaterial, the unaltered PF_6^- signal indicates that the counteranion is far from the RuNP surface. In the 0-160 ppm range, a very broad signal composed of two main population of phosphorus groups is observed. One phosphorus group presents a chemical shift centered at 33 ppm, consistent with the signal of Ph_2PH ligand in the $[RuPH]^+$ complex. The second one, of lower intensity, spans between 80 to 160 ppm. Such deshielded ^{31}P chemical shift is characteristic of P-oxidized species, thus pointing out to an evolution of the Ph_2PH ligand in the complex towards higher oxidation state.

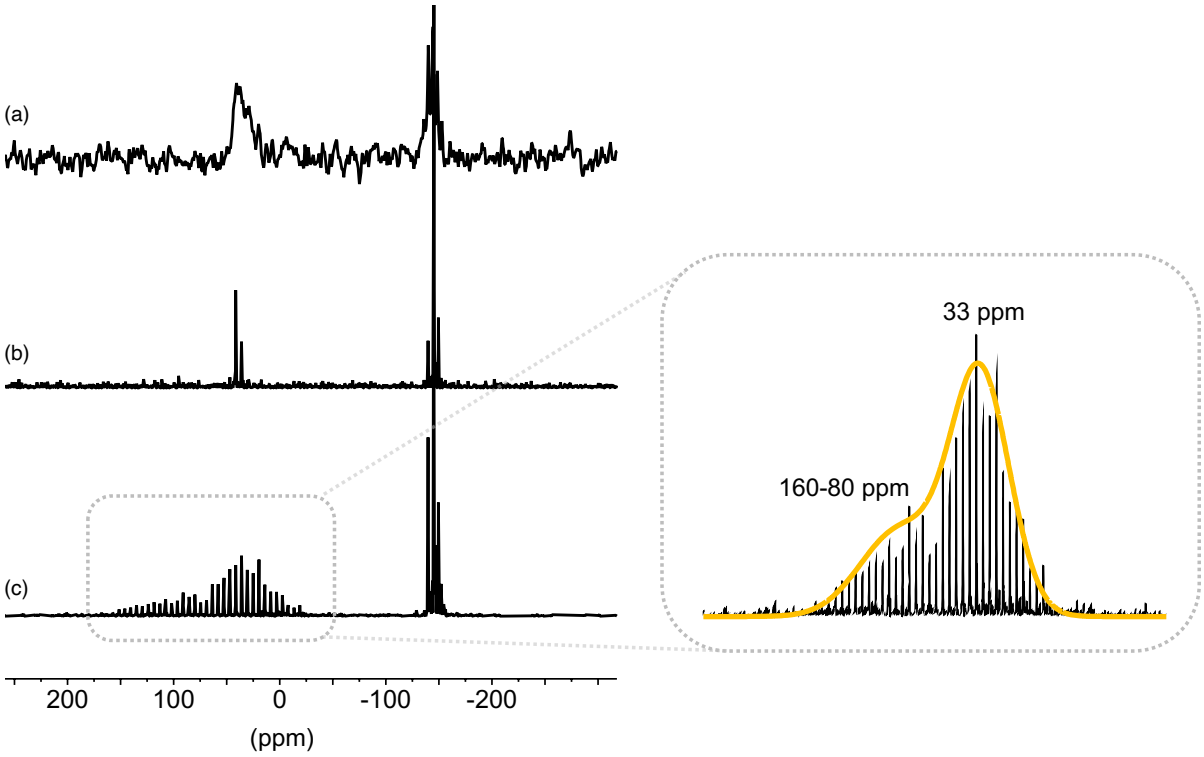

Figure 8. Solid-state ^{31}P MAS NMR of (a) free $[RuPH]^+PF_6^-$ in SiO_2 and ^{31}P CPMG MAS NMR of (b) $[RuPH]^+PF_6^-$ in SiO_2 and (c) of $([RuPH]_n\text{-RuNPs})^+(PF_6^-)_n$ in SiO_2.

As previously mentioned, the P-H function of the diphenylphosphine ligand in $[RuPH]^+PF_6^-$ can be deprotonated in the presence of an appropriate base [2,5,6]. It is a known fact that, by the experimental conditions applied for the nanoparticle synthesis, hydrides are present on the surface of RuNPs. In the case of the $([RuPMe]_n\text{-RuNPs})^+(PF_6^-)_n$ hybrid system, a ratio of 1.6 hydrides per Ru surface atom was determined (see Chapter 2). Partial deprotonation of the $[RuPH]^+$ species by those hydrides can be envisaged, followed by oxidation with traces of oxygen yielding to P-O species, consistent with chemical shifts observed in the region of 80-160 ppm. In this way, P-oxidized and $[RuPH]^+$ species may co-exist on the surface of the $([RuPH]_n\text{-RuNPs})^+(PF_6^-)_n$ hybrid nanomaterial.

2.2. Synthesis and characterization of $([RuPO]_n\text{-RuNPs})^+(PF_6^-)_n$ hybrid nanomaterial

The other functionalized organophosphorus Ru(II)-polypyridyl complex chosen for the stabilization of RuNPs is the $[(bpy)_2Ru(Ph_2PO)MeCN]PF_6$ complex, $[RuPO]^+PF_6^-$. It has been previously shown, the phosphoryl Ph_2PO ligand coordinated to a Ru(II) terpyridine bipyridine complex is a good hydrogen-bond acceptor that allows the formation of dimeric complexes [4]. Theoretical calculations on the

nature of the phosphoryl–Ru(II) bond revealed a strong anionic character located on the oxygen atom [8]. This Ph_2PO ligand can thus be described as an L-type phosphine ligand with an anionic charge centered on the oxygen atom (P-O^-), as represented in Figure 9.

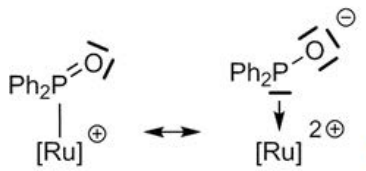

Figure 9. Two extreme canonical structures (left) and bonding description of the P-metallated phosphoryl ligand in $[Ru(tpy)(bpy)P(O)Ph_2]^+$ (right), reproduced from ref. [8].

2.2.1. Synthesis of the $[RuPO]^+PF_6^-$ complex

The synthesis of the $[RuPO]^+PF_6^-$ complex from the diphenylphosphine derivative, $[RuPH]^+PF_6^-$, was set up by A. Igau and P. Sutra [3]. To a solution of $[RuPH]^+PF_6^-$ in acetonitrile, a low excess of silver(I) oxide, Ag_2O, has been added (Scheme 3) and the reaction mixture magnetically left under stirring for 12 h at 25 °C. Addition of Ag(I) allowed abstraction of the Cl ligand and formation of the corresponding solvated complex. After elimination of AgCl by filtration, a fine orange product is obtained by precipitation with ether (yield: 58%). The product $[RuPO]^+PF_6^-$ has been identified by ^1H and ^{31}P NMR (see Experimental Section).

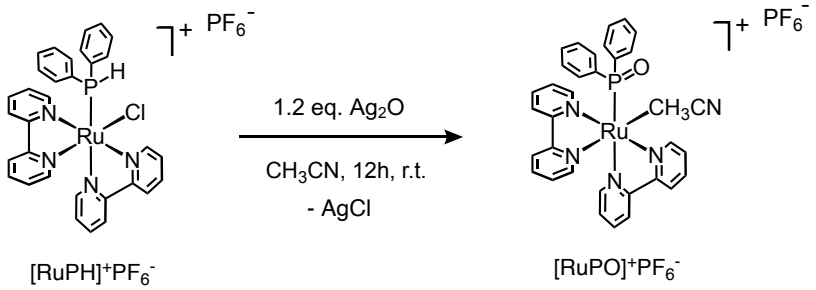

Scheme 3. Synthesis of $[(bpy)_2Ru(P(O)Ph_2)CH_3CN]PF_6$, $[RuPO]^+PF_6^-$.

The ^1H NMR spectrum of $[RuPO]^+PF_6^-$ complex is presented in Figure 10. The region of the aromatic protons (6-10 ppm) gathers the signals for the aromatic protons of the phenyl groups of the phosphine ligand (Ph_2PO) and those of the two bipyridine ligands. The methyl protons of the acetonitrile molecule coordinated to the Ru metal center (Ru-$NCCH_3$) appear as a singlet at δ = 1.91 ppm. Traces of acetone (δ = 2.08 ppm) and diethyl ether (δ = 1.12 and 3.42 ppm) are also observed.

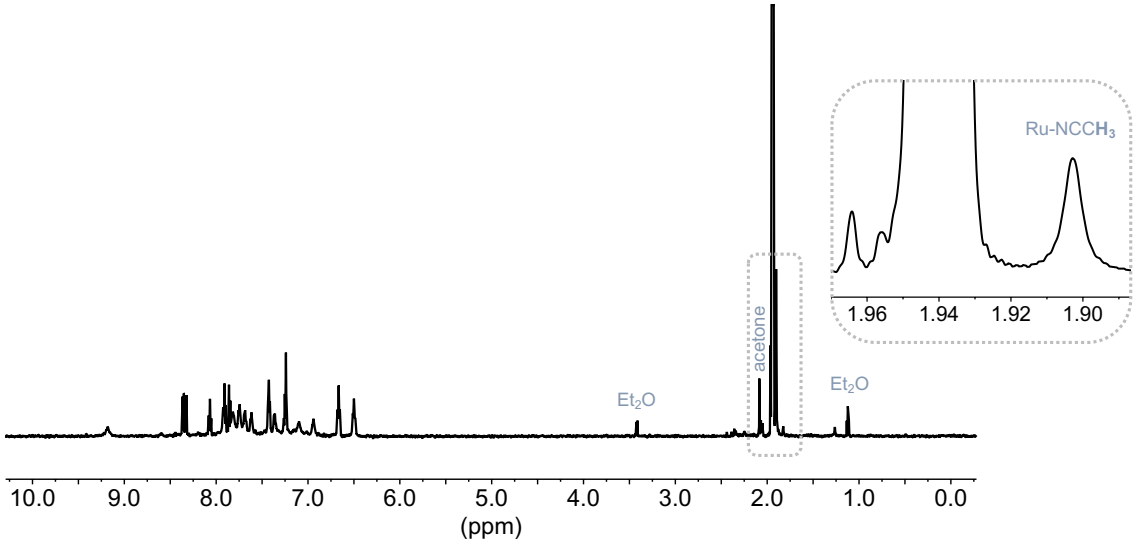

Figure 10. ^{1}H NMR spectrum of $[RuPO]^{+}PF_6^{-}$ in CD_3CN.

The ^{31}P NMR spectrum of $[RuPO]^{+}PF_6^{-}$ (Figure 11) shows two signals, namely a broad peak of low intensity centered at 78.3 ppm and a septuplet at -144.7 ppm, that corresponds to the Ph_2PO ligand and the PF_6^{-} counteranion, respectively.

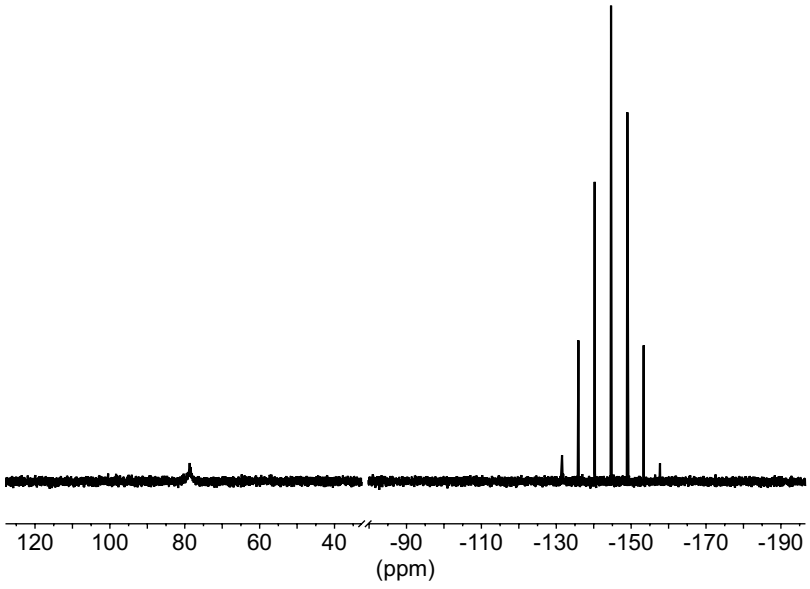

Figure 11. ^{31}P NMR spectrum of $[RuPO]^{+}PF_6^{-}$ in CD_3CN.

For the synthesis of the corresponding nanohybrid, the $[RuPO]^{+}PF_6^{-}$ complex has been dried by lyophilization.

2.2.2. Synthesis of the $([RuPO]_n\text{-}RuNPs)^+(PF_6^-)_n$ hybrid nanomaterial

Like for $([RuPMe]_n\text{-}RuNPs)^+(PF_6^-)_n$, the synthesis of the hybrid nanomaterial $([RuPO]_n\text{-}RuNPs)^+(PF_6^-)_n$ (Scheme 4), has been performed using the organometallic complex [Ru(cod)(cot)] as precursor of RuNPs and 0.1 molar eq. of the $[RuPO]^+PF_6^-$ complex as stabilizer. Both were dissolved in freshly distilled and degassed THF (1 mL per mg of [Ru(cod)(cot)]), inside a Fischer-Porter reactor and under argon atmosphere, providing an intense orange homogeneous solution. Due to the low solubility of $[RuPO]^+PF_6^-$ in THF, the reactor was sonicated for 5 min to reach an homogeneous solution. The reaction mixture was then pressurized with 3 bar of H_2 and kept under vigorous stirring for 24 h at 25 °C. The initial orange solution turned black within a few minutes. After 24 h of reaction, excess H_2 was evacuated by pumping. The volatiles were then evaporated under vacuum which led to the formation of a black precipitate.

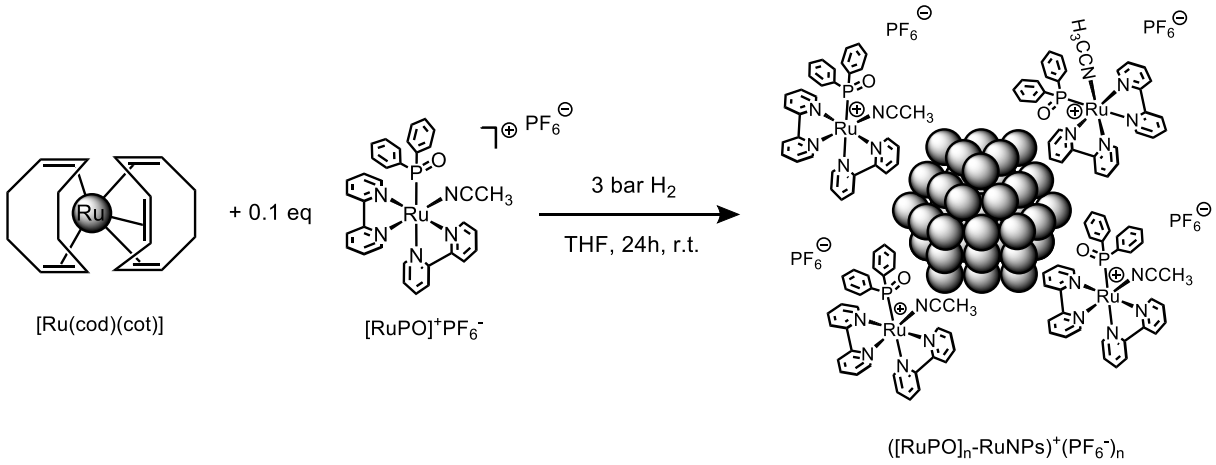

Scheme 4. Synthesis of the hybrid nanomaterial $([RuPO]_n\text{-}RuNPs)^+(PF_6^-)_n$.

The washing procedure optimized for the purification of $([RuPMe]_n\text{-}RuNPs)^+(PF_6^-)_n$ and $([RuPH]_n\text{-}RuNPs)^+(PF_6^-)_n$ hybrid nanomaterials has been applied. THF was added on the black precipitate and the obtained orange supernatant was removed *via* canula, and the operation was repeated three times. The washed black powder was then dissolved into a minimum amount of acetonitrile, transfer into a vial and dried under vacuum. Three additional washings with THF have been then performed before drying the sample under vacuum.

^1H and ^{31}P NMR spectra recorded from the orange product extracted by THF washing matched the structure of the $[RuPO]^+PF_6^-$ introduced as stabilizer.

2.2.3. Characterization of the $([RuPO]_n\text{-}RuNPs)^+(PF_6^-)_n$ hybrid nanomaterial

A TEM grid was prepared from an acetonitrile solution of the purified $([RuPO]_n\text{-}RuNPs)^+(PF_6^-)_n$ nanomaterial (Fig. 12a) showing small and individual nanoparticles of ca. 1.5 ± 0.6 nm core sizes (Fig. 12b). It is a very similar value to that obtained for RuNPs stabilized by the $[RuPMe]^+PF_6^-$ and $[RuPH]^+PF_6^-$ complexes.

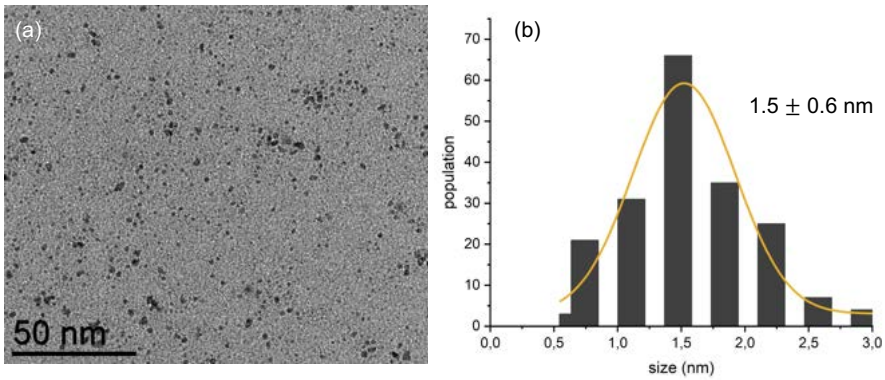

Figure 12. (a) TEM image (a) and size histogram of purified $([RuPO]_n\text{-}RuNPs)^+(PF_6^-)_n$ dispersed in acetonitrile.

WAXS data obtained from the purified sample of $([RuPO]_n\text{-}RuNPs)^+(PF_6^-)_n$ are consistent with a Ru hcp pattern (Fig. 13). In comparison with the results obtained for $([RuPH]_n\text{-}RuNPs)^+(PF_6^-)_n$, the $([RuPO]_n\text{-}RuNPs)^+(PF_6^-)_n$ sample seems to contain less crystallized RuNPs. The coherence length is estimated to ca. 2.5 nm (Fig. 14).

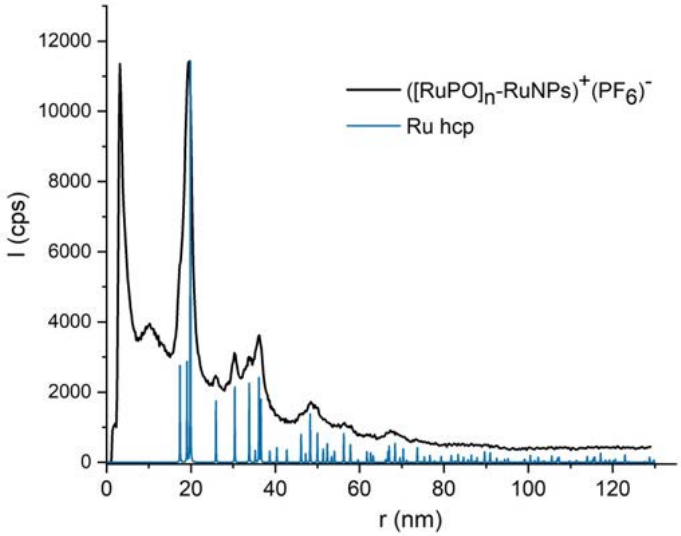

Figure 13. WAXS diagram of $([RuPO]_n\text{-}RuNPs)^+(PF_6^-)_n$ (black), in comparison with the diffraction pattern of hcp Ru bulk (blue).

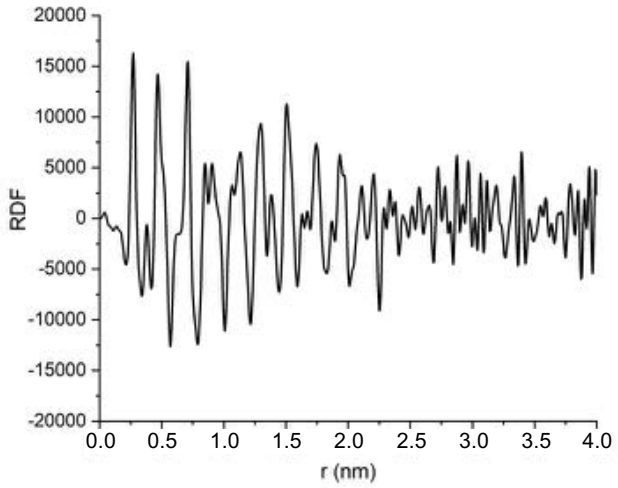

Figure 14. RDF of $([RuPO]_n\text{-}RuNPs)^+(PF_6^-)_n$.

The purified $([RuPO]_n\text{-}RuNPs)^+(PF_6^-)_n$ hybrid material was then dissolved in CD_3CN in order to perform liquid ^1H and ^{31}P NMR studies. Figure 15b shows the ^1H NMR spectrum of the purified $([RuPO]_n\text{-}RuNPs)^+(PF_6^-)_n$ and figure 15a that of the $[RuPO]^+PF_6^-$ complex, for comparison purpose. As it has been already observed for $([RuPMe]_n\text{-}RuNPs)^+(PF_6^-)_n$ and $([RuPH]_n\text{-}RuNPs)^+(PF_6^-)_n$, the ^1H NMR spectrum of $([RuPO]_n\text{-}RuNPs)^+(PF_6^-)_n$ displays a very broad signal in the range of 6-9 ppm, reasonably indicative of the proximity of the phenyl and bipyridine protons of the $[RuPO]^+$ units with the RuNP surface. Over the broad signal, sharp peaks are also observed that here match well those of the $[RuPO]^+$ complex. As mentioned before, the solubility of the $[RuPO]^+PF_6^-$ complex in THF, the solvent used for the washing procedure, is rather low, and given the sharpness of the peaks observed, they can correspond to free $[RuPO]^+PF_6^-$ complex which was not eliminated during the purification process. In the diffusion-filtered ^1H NMR spectrum (Fig. 15c), where the contribution of the fast diffusing species has been removed (i.e. solvent molecules and $[RuPO]^+$ species not directly coordinated to the RuNP surface), only a broad signal attributable to $[RuPO]^+$ species in strong interaction with the RuNP surface is observed.

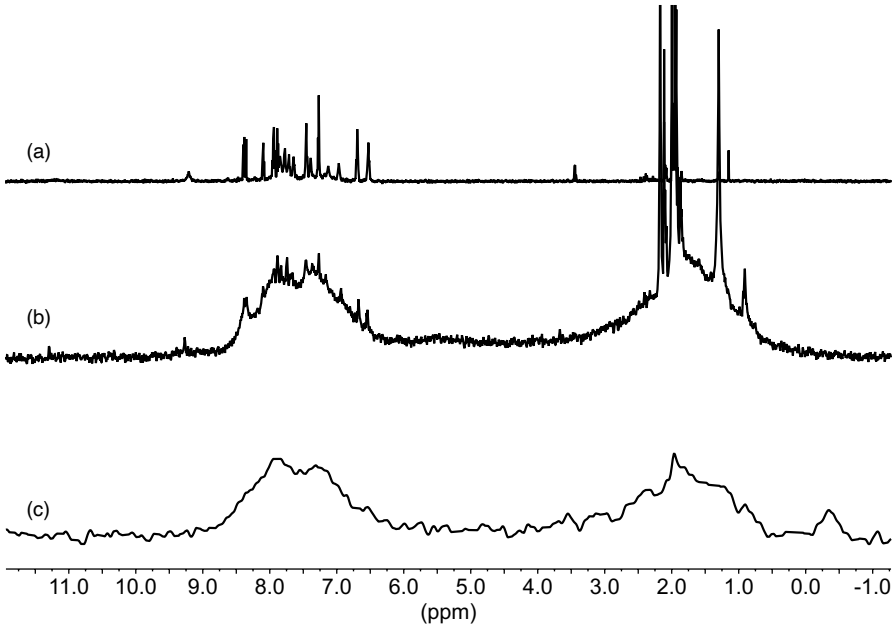

Figure 15. ^{1}H NMR spectra of (a) $[RuPO]^{+}PF_6^{-}$, (b) purified $([RuPO]_n\text{-}RuNPs)^{+}(PF_6^{-})_n$ and (c) diffusion-filtered $([RuPO]_n\text{-}RuNPs)^{+}(PF_6^{-})_n$ in CD_3CN.

2D DOSY experiments have been performed on the $([RuPO]_n\text{-}RuNPs)^{+}(PF_6^{-})_n$ hybrid in CD_3CN. In this case, the fitting of the diffusion curve appeared more complicated than in the previous cases. Indeed, different essays with different batches of $([RuPO]_n\text{-}RuNPs)^{+}(PF_6^{-})_n$ hybrid have been performed but they led to different results. With some samples, the curve could be fitted with two different diffusion coefficients (namely a slow diffusing species, $D_1 = 3.6 \cdot 10^{-10}$ m^2/s, and a fast diffusion species, $D_2 = 8.9 \cdot 10^{-10}$ m^2/s). With other samples, the diffusion curve matched a single-exponential fitting, with a $D \approx 6.0 \cdot 10^{-10}$ m^2/s. It is important to note that the diffusion coefficient of the original $[RuPO]^{+}PF_6^{-}$ measured in the same conditions is of $11.6 \cdot 10^{-10}$ m^2/s, which does not correspond to any of the values observed in the different batches of hybrid measured. Due to the differences observed when using different batches $([RuPO]_n\text{-}RuNPs)^{+}(PF_6^{-})_n$ hybrid, the obtained results do not enable conclusions. It will thus be necessary to repeat 2D DOSY NMR studies.

In order to shed some light on the fate of the $[RuPO]^{+}$ complex in the synthesis conditions applied for the synthesis of the RuNPs, ^{31}P MAS NMR was recorded. As it was done for the other hybrid systems, SiO_2 powder was impregnated with a colloidal solution of purified $([RuPO]_n\text{-}RuNPs)^{+}(PF_6^{-})_n$ in acetonitrile. The solvent was then evaporated under vacuum, yielding a dry powder (ca. 8.5 mg of $([RuPO]_n\text{-}RuNPs)^{+}(PF_6^{-})_n$ per 100 mg of SiO_2). For comparison purposes, the free $[RuPO]^{+}PF_6^{-}$ complex was also adsorbed onto the same SiO_2 powder.

Figure 16a and 16b show the ^{31}P MAS NMR and the ^{31}P CPMG MAS NMR spectra of free $[RuPO]^{+}PF_6^{-}$ in SiO_2, respectively. A peak at ca. -144 ppm, corresponding to PF_6^{-} and another one at ca. 78 ppm,

assigned to the Ph_2PO ligand are visible. The ^{31}P CPMG MAS NMR spectrum of the hybrid $([RuPO]_n\text{-}RuNPs)^+(PF_6^-)_n$ (Fig. 16c), displays a very broad signal in the range 0-160 ppm. This broad signal is in fact composed of two main signals centered at 100 ppm and 32 ppm.

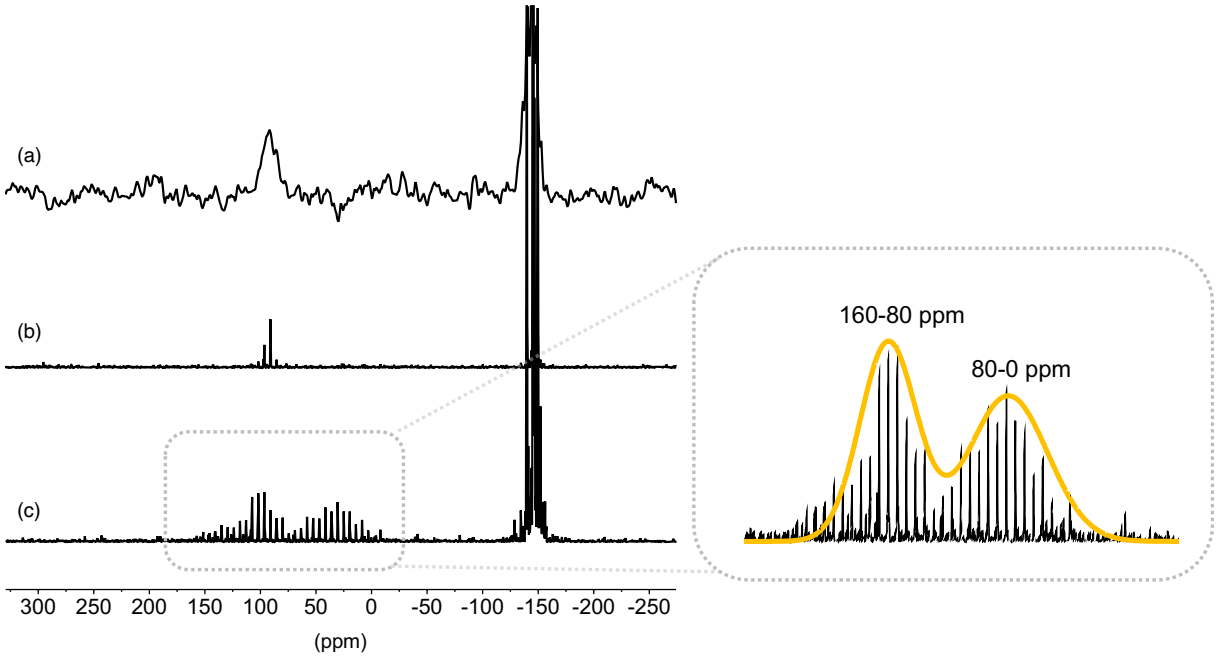

Figure 16. Solid-state ^{31}P MAS NMR of (a) free $[RuPO]^+PF_6^-$ in SiO_2 and ^{31}P CPMG MAS NMR of (b) $[RuPO]^+PF_6^-$ in SiO_2 and (c) of $([RuPO]_n\text{-}RuNPs)^+(PF_6^-)_n$ in SiO_2.

The broad signal which spans from 80 to 160 ppm can be assigned to $[RuPO]^+PF_6^-$ species in the inner and outer layers of the RuNP. It is important to note that the $[RuPO]^+PF_6^-$ complex does not bear any Cl ligand that could directly coordinate to the surface of the RuNPs, as $[RuPMe]^+$ and $[RuPH]^+$ ligands do in the previously described hybrids. The ionic character of the P-O bond in the $[RuPO]^+PF_6^-$ complex, with the anionic charge localized on the oxygen atom, led us to propose that the phosphoryl ligand acts as a bridging ligand between the mononuclear polypyridyl ruthenium complex of the inner layer and the RuNP surface. As it is observed for the other hybrid systems, the $[RuPO]^+PF_6^-$ complexes in the outer layer are in electrostatic interactions with those in the inner layer. Considering the broad signal spanning from 0 to 80 ppm we may envisage that reduction of the P-O occurred during the formation of the hybrid nanomaterial. Further experimental and theoretical studies are needed to fully establish the nature of the interaction between the $[RuPO]^+$ complex and the surface of the RuNPs.

2.3. Conclusions on the stabilization of RuNPs with $[RuPH]^+PF_6^-$ and $[RuPO]^+PF_6^-$ complexes

In this section, the direct stabilization of small RuNPs using, as stabilizers, two functionalized organophosphorus Ru(II)-polypyrdyl complexes, $[RuPH]^+$ and $[RuPO]^+$, has been described. The resulting hybrid nanomaterials, $([RuPH]_n\text{-RuNPs})^+(PF_6^-)_n$ and $([RuPO]_n\text{-RuNPs})^+(PF_6^-)_n$, have been preliminary characterized by a combination of physical techniques (TEM and WAXS) and chemical techniques (liquid- and solid-state NMR spectroscopy). While the RuNP cores displayed common characteristics for all the hybrid systems synthetized, namely similar ruthenium core sizes and same hcp crystalline structure, the $[RuPH]^+PF_6^-$ and $[RuPO]^+PF_6^-$ complexes present different behaviors towards the Ru surface compared to $[RuPMe]^+PF_6^-$, as the result of their different chemical properties.

On the basis of the NMR data and theoretical results obtained for $([RuPMe]_n\text{-RuNPs})^+(PF_6^-)_n$, which pointed to the formation of a Cl-bridge between the $[RuPMe]^+$ and the RuNP surface, a coordination of the $[RuPH]^+$ complex to the RuNP through its Cl atom is also proposed. However, the $[RuPH]^+$ complex is not as chemically inert as the $[RuPMe]^+$ analogue, and NMR data indicate a partial evolution to its oxidized form during the synthesis process.

Regarding the $[RuPO]^+PF_6^-$ complex, no apparent modification of its structure has been detected by NMR. However, the coordination mode of this complex onto the RuNP surface needs to be further studied. On the basis of NMR data and previous fundamental studies in the group, as a first hypothesis, we can propose this complex interacts with the RuNP surface *via* the oxygen atom of the phosphoryl ligand, which is known to hold a high anionic charge. If this hypothesis is true, this would mean that the phosphoryl ligand of the $[RuPO]^+PF_6^-$complex forms a bridge with the RuNP surface through its oxygen atom.

The preliminary results described in this section evidenced that the synthesis and stabilization of small RuNPs using other Ru(II) phosphorus polypyridyl complexes than the $[RuPMe]^+PF_6^-$ complex described in Chapter 2 are feasible. Given that such complexes can contain different phosphorus ligands, namely with functional groups, different coordination modes can occur. Ultimately different reactivity and catalytic properties can be expected.

3. First results on the stabilization of CoNPs and PtNPs with organophosphorus Ru(II)-polypyridyl complexes

In this section, hybrid nanomaterials based on the stabilization of cobalt and platinum nanoparticles by organophosphorus Ru(II)-polypyridyl complexes has been attempted, following the procedure developed for the $([RuPMe]_n\text{-}RuNPs)^+(PF_6^-)_n$ hybrid nanomaterial described in Chapter 2.

Both CoNPs [9] and PtNPs [10] systems have already been synthetized in the group by following the organometallic approach. Like [Ru(cod)(cot)], the precursors employed for the synthesis of CoNPs and PtNPs, (1,5-cyclooctadiene)(cyclooctadienyl)cobalt(I) and tris(norbornene)platinum(0), respectively, can be decomposed under mild conditions (r.t., 3 bar H_2). Cyclooctane and norbornane molecules, only byproducts resulting from their decomposition, do not coordinate to the NP surface. The resulting hybrids, named as $([RuPH]_n\text{-}CoNPs)^+(PF_6^-)_n$ and $([RuPMe]_n\text{-}PtNPs)^+(PF_6^-)_n$, could present properties of interest in fields like magnetism or catalysis.

3.1. Synthesis and preliminary characterization of $([RuPH]_n\text{-}CoNPs)^+(PF_6^-)_n$

The synthesis of the hybrid nanomaterial $([RuPH]_n\text{-}CoNPs)^+(PF_6^-)_n$ (Scheme 5), has been performed using the organometallic complex (1,5-cyclooctadiene)(cyclooctadienyl)cobalt(I), [Co(cod)(coe)], as precursor of CoNPs and 0.1 molar eq. of the $[RuPH]^+PF_6^-$ complex as stabilizer. The two complexes were dissolved in freshly distilled and degassed THF (1 mL per mg of [Co(cod)(coe)]), inside a Fischer-Porter reactor and under argon atmosphere, providing an intense black solution. The reaction mixture was then pressurized with 3 bar of H_2 and kept under vigorous stirring for 24 h at 25 °C. After 24 h of reaction, excess H_2 was evacuated by pumping. The volatiles were then evaporated under vacuum which led to the formation of a black precipitate.

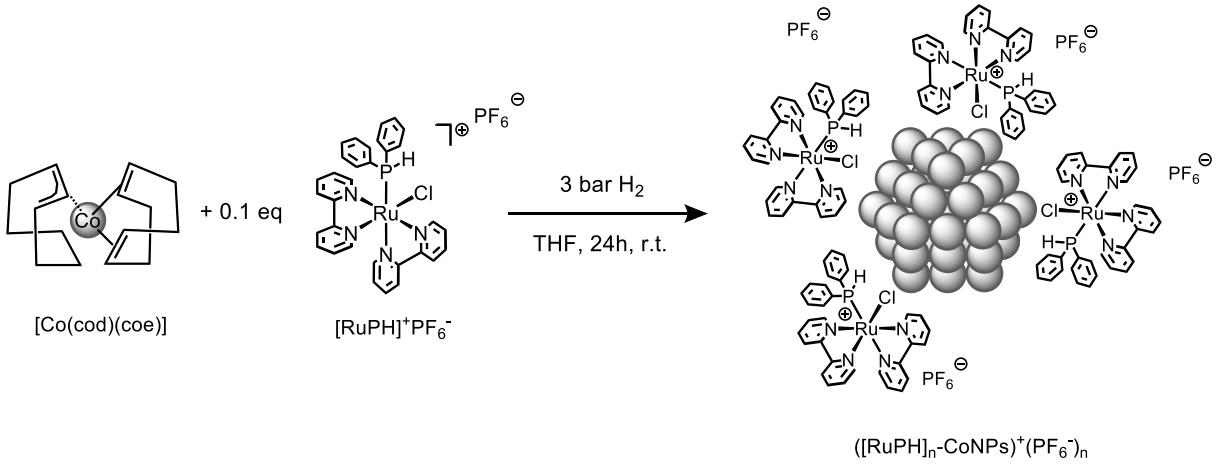

Scheme 5. Synthesis of the hybrid nanomaterial $([RuPH]_n\text{-}CoNPs)^+(PF_6^-)_n$.

In order to remove potentially unreacted $[RuPH]^+PF_6^-$, THF was added in the Fischer-Porter reactor. This led to an orange supernatant which has been removed *via* canula, after precipitation of the black $([RuPH]_n\text{-}RuNPs)^+(PF_6^-)_n$ powder. This procedure was repeated three times, as previously done for the other hybrid materials studied. For $([RuPH]_n\text{-}CoNPs)^+(PF_6^-)_n$ material, a faster precipitation was observed during the THF washings compared to $([RuPH]_n\text{-}RuNPs)^+(PF_6^-)_n$ system. Also, a spontaneous deposition of the material on the magnetic stirrer was noticed, reasonably attributed to the magnetic nature of the formed CoNPs, as previously observed in the group. The obtained black powder was dissolved into a minimum amount of acetonitrile in order to favor the dispersion of the sample and its transfer into a vial before drying under vacuum. Three additional washings with THF have been again performed. The resulting washing solution appeared slightly colored, indicating another release of $[RuPH]^+PF_6^-$ that could not be removed before dispersion in acetonitrile. Note that NMR data of the washing solutions could not be recorded due to the presence of paramagnetic species.

TEM analysis performed on a grid prepared from the crude colloidal suspension in THF (Fig. 17a), revealed the presence of aggregates of 200-300 nm, as already observed for the other hybrid nanomaterials. After re-dispersion in acetonitrile and deposition of the solution on a new TEM grid, individual nanoparticles were cleanly visible (Fig. 17b and 17c), with a mean size of 2.1 ± 0.7 nm (Fig. 17d).

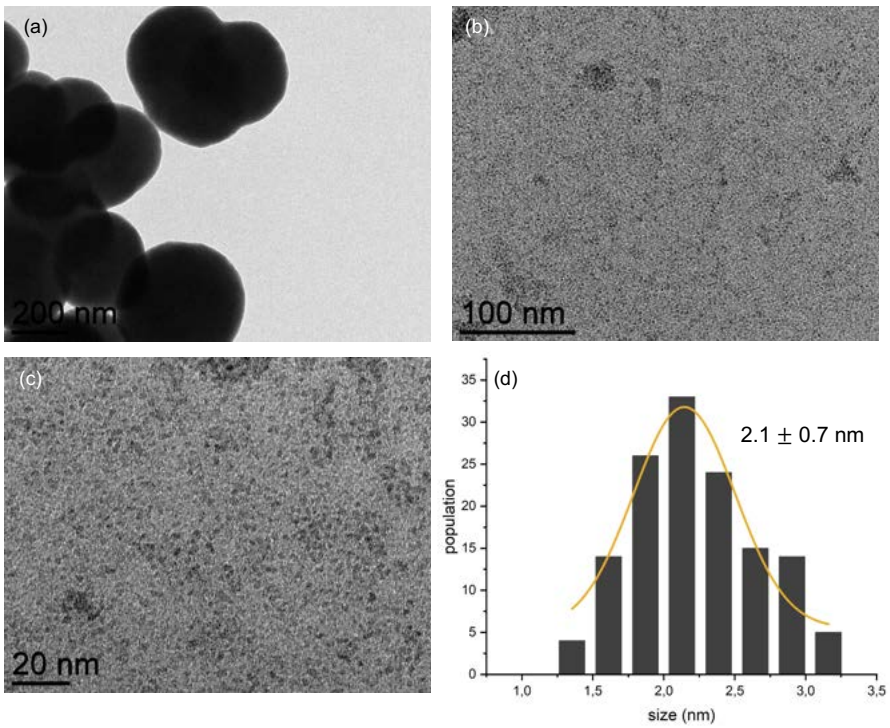

Figure 17. TEM images of $([RuPH]_n\text{-}CoNPs)^+(PF_6^-)_n$: (a) in THF and (b,c) redispersed in acetonitrile. (d) Size histogram of $([RuPH]_n\text{-}RuNPs)^+(PF_6^-)_n$ dissolved in acetonitrile.

HRTEM study was also performed on $([RuPH]_n\text{-}CoNPs)^+(PF_6^-)_n$. On the micrograph (Figure 18), CoNPs that displaying crystalline plans are visible, together with brighter small dots around the NPs. Such a difference of contrast observed can be attributed to the difference in atomic mass of ruthenium and cobalt elements. So, the brighter dots that surround the cobalt cores reasonably correspond to Ru(II) centers of the $[RuPH]^+$ complexes used for the stabilization of the CoNPs. This hypothesis is supported by EDX analysis which confirmed the presence of both Co and Ru elements in the nano-objects (Fig. 18 right).

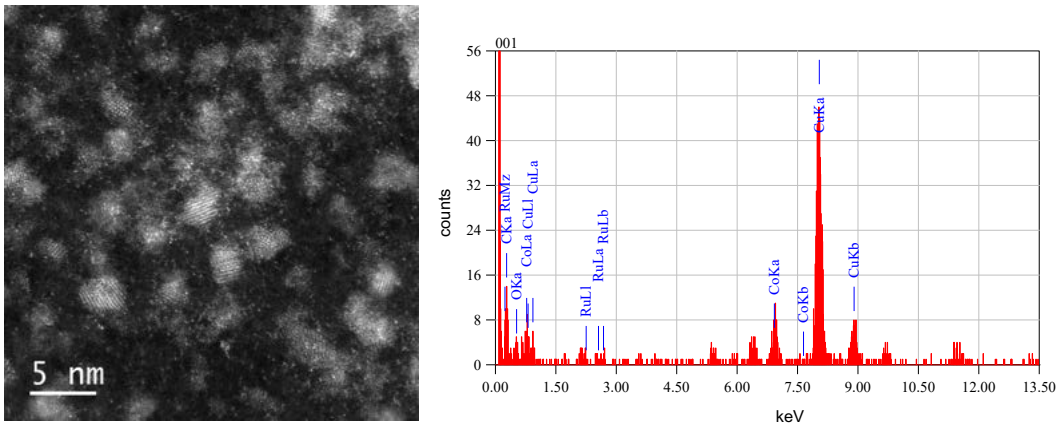

Figure 18. HRTEM micrograph of purified $([RuPH]_n\text{-}CoNPs)^+(PF_6^-)_n$ dispersed in acetonitrile (left) and EDX analysis (right).

If crystalline plans are observed on the cobalt cores, it was not possible to define precisely the crystalline structure by measuring the plan distances since HRTEM grid are exposed to air before introduction in the microscope. Given the very small size of the nanoparticles, we can expect their oxidation due to the high oxophilic character of cobalt. If this oxidation is not total, it can lead to a mixture of different metal-metal distances difficult to attribute.

WAXS analysis was performed on a glass capillary filled with purified $([RuPH]_n\text{-}CoNPs)^+(PF_6^-)_n$ powder under argon atmosphere, thus preserving the original crystalline structure of the NPs. The pattern observed is consistent with a Co epsilon (ε) structure (Fig 19 top), thus indicating the metallic character of the nanoparticles non exposed to air. Such ε-Co phase is considered metastable and its synthesis has only been achieved by solution-phase chemistry processes [11]. The ability of CoNPs to adopt different crystalline structures allows the modulation of their magnetic properties [12]. ε-Co structures are good precursors to obtain α-Co NPs, which display magnetic storage properties.

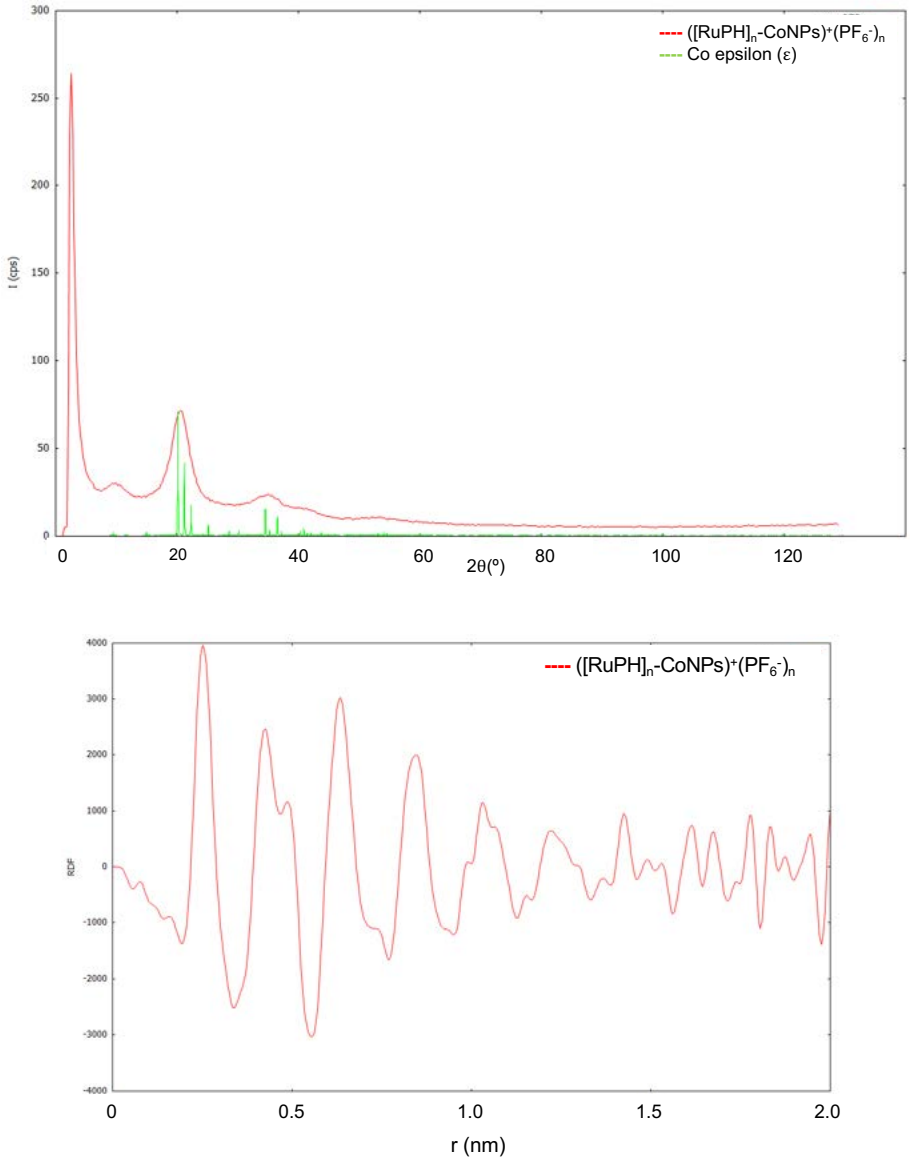

Figure 19. (top) WAXS diagram of $([RuPH]_n\text{-}CoNPs)^+(PF_6^-)_n$ (red) in comparison with diffraction pattern of *ε*-Co (green) and (bottom) RDF of $([RuPH]_n\text{-}CoNPs)^+(PF_6^-)_n$.

Given the encouraging results obtained for the stabilization of CoNPs with the $[RuPH]^+PF_6^-$ complex, further characterization needs to be pursued in order to determine more accurately the structure of the hybrid material $([RuPH]_n\text{-}CoNPs)^+(PF_6^-)_n$ and to study its potential applications.

3.2. Synthesis of $([RuPMe]_n\text{-}PtNPs)^+(PF_6^-)_n$

The synthesis of the hybrid nanomaterial $([RuPMe]_n\text{-}PtNPs)^+(PF_6^-)_n$ (Scheme 6), has been performed using the organometallic complex tris(norbornene)platinum(0), $[Pt(nbe)_3]$, as precursor of PtNPs and 0.1 molar eq. of the $[RuPMe]^+PF_6^-$ complex as stabilizer. Both were dissolved in freshly distilled and degassed THF (1 mL per mg of $[Pt(nbe)_3]$), inside a Fischer-Porter reactor and under argon

atmosphere. The reaction mixture was then pressurized with 3 bar of H_2 and kept under vigorous stirring for 24 h at 25 °C. The initial orange solution turned black within a few seconds. After 24 h of reaction, excess H_2 was evacuated by pumping. A precipitate was quickly formed after the stirring was stopped.

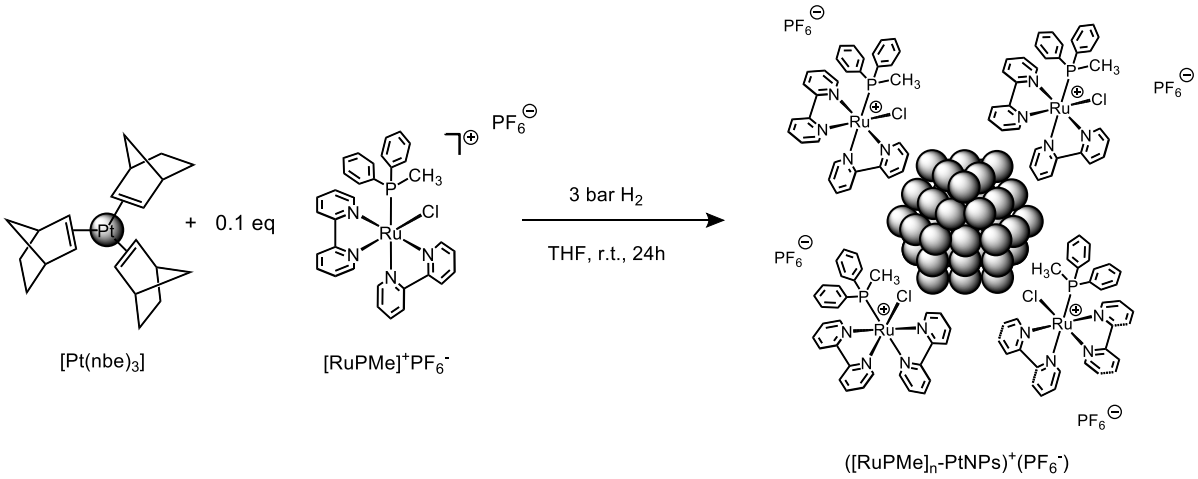

Scheme 6. Synthesis of the hybrid nanomaterial $([RuPMe]_n\text{-}PtNPs)^+(PF_6^-)_n$.

The resulting yellow supernatant was then removed by extraction, and three THF washings were performed. The black solid was then redispersed in acetonitrile for preparing a TEM grid.

TEM images from the crude colloidal suspension (Figure 20) revealed the presence of irregular structures made of individual nanoparticles. Figure 21 shows the HRTEM images of $([RuPMe]_n\text{-}PtNPs)^+(PF_6^-)_n$ in acetonitrile. Unlike the hybrid nanomaterials described so far, it was impossible to obtain individual and well-dispersed PtNPs after dissolution in acetonitrile.

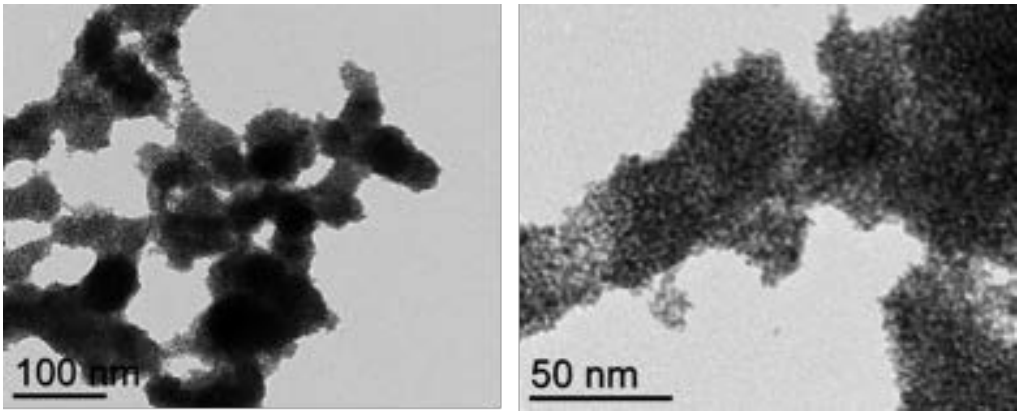

Figure 20. TEM images of crude colloidal suspension of $([RuPMe]_n\text{-}PtNPs)^+(PF_6^-)_n$ in THF.

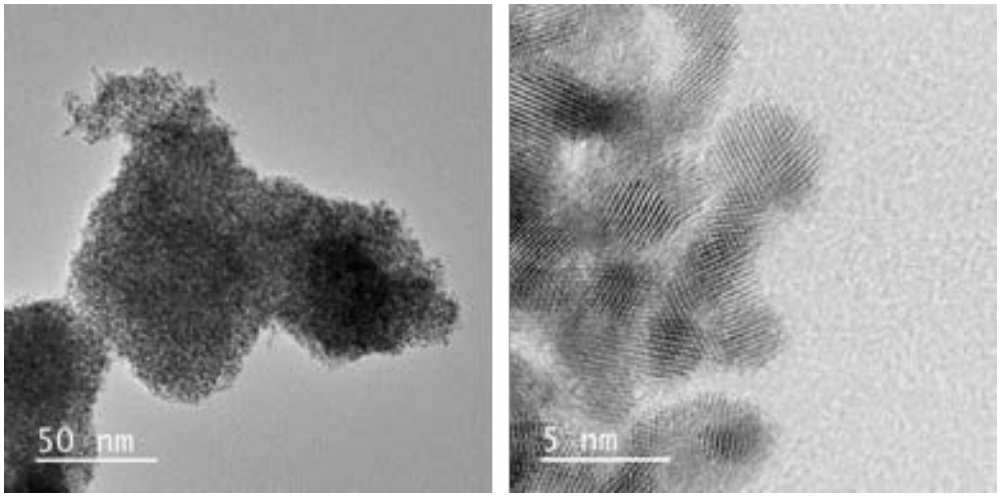

Figure 21. HRTEM images of a suspension of purified($[RuPMe]_n$-PtNPs)$^+(PF_6^-)_n$ in acetonitrile..

Even if the ($[RuPMe]_n$-PtNPs)$^+(PF_6^-)_n$ nanomaterial could not be re-dispersed, well crystallized PtNPs of ca. 2 nm are visible in the HRTEM pictures.

3.3. Conclusions on the Co and Pt-based hybrid systems

The preliminary TEM results above indicate that the synthesis conditions applied did not allow to get small and dispersed PtNPs stabilized by the $[RuPMe]^+PF_6^-$ complex. A different reactivity of Pt compared to that of Co or Ru towards the organophosphorus Ru(II)-polypyridyl complex might account for the different behavior observed. Therefore, the reaction conditions would need to be optimized before concluding on the adequation of the couple $[RuPMe]^+PF_6^-$/$[Pt(nbe)_3]$ to reach our target objective. Reaction times or reactant ratios are, for instance, parameters to be adjusted.

In contrast, the same reaction conditions used for the Ru-nanohybrids positively led to the formation of small and individual CoNPs stabilized by the $[RuPH]^+PF_6^-$ complex. Studies on the structure and properties of the resulting ($[RuPH]_n$-CoNPs)$^+(PF_6^-)_n$ nanomaterial are future perspectives.

4. Conclusions

In the first section of this chapter, we have shown that other organophosphorus Ru(II)-polypyridyl complexes than the $[RuPMe]^+PF_6^-$ complex (as reported in Chapters 2 and 3) can stabilize small RuNPs by the same direct synthesis procedure. If the fine characterization of the hybrid systems obtained needs to be completed by using other analytical techniques and theoretical methods, the preliminary NMR results already evidenced that the different chemical properties of the stabilizing complexes can lead to different coordination modes at the ruthenium surface.

The coordination of the $[RuPH]^+$ complex onto the RuNP surface is believed to occur similarly to that of $[RuPMe]^+PF_6^-$ complex. We propose that an inner stabilization layer is made with complexes interacting with the RuNP surface through the Cl atom thus forming a bridge between the two components of the hybrid nanomaterial; a second stabilization layer is formed through electrostatic interaction between complex counterparts. The $[RuPH]^+$ complex is not as chemically inert as the $[RuPMe]^+$ analogue and it might have undergone a partial evolution to its oxidized form during the synthetical process, as indicated by NMR data. Therefore, we may expect to observe a mixture of non-oxidized and oxidized complexes surrounding the RuNPs. This hypothesis needs to be further studied.

Regarding the $[RuPO]^+PF_6^-$ complex, no apparent evolution of its structure has been detected by NMR. Since the $[RuPO]^+$ complex does not hold any Cl ligand able to coordinate to the RuNPs surface, its interaction with the nanoparticle needs to be further investigated. On the basis of the NMR data, as a first hypothesis, we can propose that this complex interacts with the RuNP surface *via* the oxygen atom of the phosphoryl ligand. The oxygen atom of the P=O function holds a high anionic charge that could act as a bridge between the $[RuPO]^+$ unit and the RuNP surface.

In the studied series, TEM and WAXS data indicate a similar mean size and same hcp crystalline structure for the MNPs. Once their characterization will be completed, $([RuPH]_n\text{-RuNPs})^+(PF_6^-)_n$ and $([RuPO]_n\text{-RuNPs})^+(PF_6^-)_n$ will be nanomaterials of interest to study their physicochemical properties, and to compare the influence of the organophosphorus Ru(II) complexes used as stabilizers.

In the second section, we observed that the organophosphorus Ru(II)-polypyridyl complex $[RuPMe]^+PF_6^-$ does not stabilize the formation of PtNPs in the reaction conditions applied. The variation of the reaction parameters is thus a perspective on the future studies concerning the $([RuPMe]_n\text{-PtNPs})^+(PF_6^-)_n$ nanomaterial.

In very preliminary studies that have not been presented in this manuscript, we observed by TEM analysis that the same organophosphorus complex $[RuPMe]^+PF_6^-$ did allow the synthesis of small CoNPs. Due to time constraints, our efforts were devoted to the characterization of the Co-based hybrid nanomaterial stabilized by the $[RuPH]^+PF_6^-$ complex, $([RuPH]_n\text{-CoNPs})^+(PF_6^-)_n$. Even if very preliminary, these results are encouraging enough to pursue studies on the formation of novel hybrid nanomaterials associating phosphorus polypyridyl complexes to metal nanoparticles. For example, the small CoNPs obtained can be of interest due to the magnetic properties they may display as the result of their particular ε-Co crystalline structure. Also, being highly sensitive to air, their controlled oxidation (into Co_3O_4 or $Co(OH)_2$ species, for example) could lead to nanomaterials of interest as nanocatalysts in oxygen evolution reaction, the bottle-neck of the water splitting process.

5. References

1. Lebon, E. Synthèse et étude des propriétés électroniques et photophysiques de complexes polypyridyles de ruthénium à ligands phosphorés. Doctoral Thesis, Université Paul Sabatier, Toulouse, 2010.

2. Shang, C. Synthesis of ruthenium-phosphorus dyes and their incorporation in ZnO transparent conducting oxide and ZnO semi-conductor thin films for photovoltaic application. Doctoral Thesis, Université Paul Sabatier, Toulouse, 2013.

3. Sylvain, R. Complexes polypyridyles de ruthénium dia- et paramagnétiques à ligands phosphorés fonctionnalisés pour des applications en transfert électronique et photovoltaïque. Doctoral Thesis, Université Paul Sabatier, Toulouse, 2013.

4. Sylvain, R.; Vendier, L.; Bijani, C.; Santoro, A.; Puntoriero, F.; Campagna, S.; Sutra, P.; Igau, A. Evidence of the unprecedented conversion of intermolecular proton to water bridging of two phosphoryl ruthenium complexes. *New J. Chem.* **2013**, *37*, 3543-3548.

5. Lin, J.T.; Wang, S.Y.; Chou, Y.C.; Gong, M.L.; Shiow, Y.-M. Diphenylphosphine derivatives of $Co(NO)(CO)_3$, $Fe(NO)_2(CO)_2$ and $Mn(NO)(CO)_4$. *J. Organomet. Chem.* **1996**, *508*, 183–193.

6. Buhro, W.E.; Zwick, B.D.; Georgiou, Savas.; Hutchinson, J.P.; Gladysz, J.A. Synthesis, structure, dynamic behavior, and reactivity of rhenium phosphido complexes (η^5-C_5H_5)Re(NO)(PPh_3)(PR_2): the "gauche effect" in transition-metal chemistry. *J. Am. Chem. Soc.* **1988**, *110*, 2427–2439.

7. Fernandez-Galan, R.; Manzano, B.R.; Otero, A.; Lanfranchi, M.; Pellinghelli, M.A. ^{19}F and ^{31}P NMR evidence for silver hexafluorophosphate hydrolysis in solution. New palladium difluorophosphate complexes and x-ray structure determination of [Pd(η^3-2-Me-C_3H_4)(PO_2F_2)(PCy_3)]. *Inorg. Chem.* **1994**, *33*, 2309–2312.

8. Lebon, E.; Sylvain, R.; Piau, R.E.; Lanthony, C.; Pilmé, J.; Sutra, P.; Boggio-Pasqua, M.; Heully, J.-L.; Alary, F.; Juris, A.; et al. Phosphoryl Group as a Strong σ-Donor Anionic Phosphine-Type Ligand: A Combined Experimental and Theoretical Study on Long-Lived Room Temperature Luminescence of the [Ru(tpy)(bpy)(Ph_2PO)]$^+$ Complex. *Inorg. Chem.* **2014**, *53*, 1946–1948.

9. Osuna, J.; de Caro, D.; Amiens, C.; Chaudret, B.; Snoeck, E.; Respaud, M.; Broto, J.-M.; Fert, A. Synthesis, Characterization, and Magnetic Properties of Cobalt Nanoparticles from an Organometallic Precursor. *J. Phys. Chem.* **1996**, *100*, 14571–14574.

10. Martínez-Prieto, L.M.; Rakers, L.; López-Vinasco, A.M.; Cano, I.; Coppel, Y.; Philippot, K.; Glorius, F.; Chaudret, B.; van Leeuwen, P.W.N.M. Soluble Platinum Nanoparticles Ligated by Long-Chain N-Heterocyclic Carbenes as Catalysts. *Chem. - Eur. J.* **2017**, *23*, 12779–12786.

11. de la Peña O'Shea, V.A.; Moreira, I. de P.R.; Roldán, A.; Illas, F. Electronic and magnetic structure of bulk cobalt: The α, β, and ε-phases from density functional theory calculations. *J. Chem. Phys.* **2010**, *133*, 024701.

12. *Advances in organometallic chemistry and catalysis: the silver/gold jubilee International Conference on Organometallic Chemistry celebratory book*; Pombeiro, A.J.L., Ed.; Wiley: Hoboken, New Jersey, 2014; ISBN 978-1-118-51014-8.

Experimental Section

1. Generalities

1.1. Operation conditions

For the synthesis of the organophosphorus Ru(II)-polypyridyl complexes the reactions were performed under an argon atmosphere by using standard Schlenk techniques. Concerning of the nanoparticles all operations for their synthesis were carried out by using standard Schlenk tubes, Fisher-Porter bottle techniques or in a glovebox (MBraun) under argon.

1.2. Reactants

1.2.1. Solvents and gases

Tetrahydrofurane (THF; CarloErba) was purified by filtration on an adequate column inside a purification apparatus (MBraun) and degassed before use according to a freeze–pump–thaw process.

Acetonitrile (CH_3CN; CarloErba) was purified by distillation on P_2O_5 and degassed before use by argon bubbling.

Acetone (CarloErba) was purified by distillation on $MgSO_4$ and degassed before use according to a freeze–pump–thaw process.

Pentane (CarloErba) was purified by filtration on an adequate column inside a purification apparatus (MBraun) and degassed before use according to a freeze–pump–thaw process.

Dichloromethane (CH_2Cl_2; CarloErba) and diethyl ether (Et_2O; CarloErba) were used as received for the purification of the organophosphorus Ru(II)-polypyridyl complexes.

Deuterated solvents (CD_3CN and THF-d_8) for NMR studies were purchased from Eurisotop and stored on activated molecular sieves inside a glove box.

Argon (classe 2, U 1006) and hydrogen (Alphagaz) were purchased from Air Liquide and ^{13}CO from Eurisotop.

1.2.2. Metal complexes, ligands and inorganic salts

Metal complexes, ligands and inorganic salts were used as received, unless additional information provided.

Type	Name	Formula or structure	Supplier
Metal complexes	*cis*-Dichlorobis(2,2'-bipyridine)ruthenium(II)	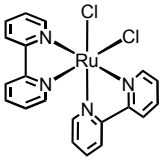	Aldrich (97%)
	1,1'-Bis(diphenylphosphino) ferrocene (DPPF)	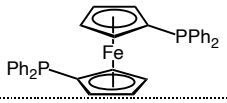	Strem Chemicals (99%)
Ligands	Methyldiphenylphosphine	Ph_2PCH_3	Aldrich (99%)
	Diphenylphosphine	Ph_2PH	Aldrich (98%)
	Triphenylphosphine	PPh_3	Aldrich (99%)
	Tricyclohexylphosphine	PCy_3	Aldrich
	2,2'-bipyridine	bpy	Aldrich (≥99%)
Inorganic salts	Silver(I) oxide	Ag_2O	Aldrich (≥99,99%)
	Thallium(I) hexafluorophosphate	$TlPF_6$	Alfa aesar (97%)
	Sodium hexafluorophosphate	$NaPF_6$	Aldrich (98%)

Table 1. Metal complexes, ligands and inorganic salts used in this work.

1.2.3. Organometallic precursors

The organometallic precursors used for the synthesis of metal nanoparticles were purchased from Nanomeps Toulouse and stored in a glove-box.

Name	Structure	Formula
(1,5-cyclooctadiene)(1,3,5-cyclooctatriene) ruthenium(0) [Ru(cod)(cot)]	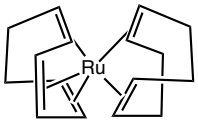	$Ru(\eta^4\text{-}C_8H_{12})$ $(\eta^6\text{-}C_8H_{10})$
(1,5-cyclooctadiene)(cyclooctadienyl) cobalt (I) [Co(cod)(coe)]	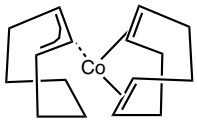	$Co(\eta^3\text{-}C_8H_{13})$ $(\eta^4\text{-}C_8H_{12})$
tris(norbornene) platinum(0) [$Pt(nbe)_3$]	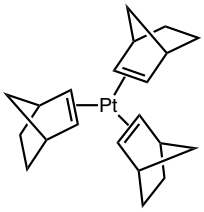	$Pt(C_7H_{10})_3$

Table 2. Organometallic precursors used for the synthesis of MNPs.

2. Syntheses

2.1. Synthesis of organophosphorus ruthenium(II) polypyridyl complexes

The syntheses of the organophosphorus ruthenium(II) polypyridyl complexes described below has been previously optimized and the products finely characterized [1].

2.1.1. Synthesis of $[(bpy)_2Ru(Ph_2PMe)Cl]PF_6$, $[RuPMe]^+PF_6^-$

A solution of 10 mL of $TlPF_6$, (83.8 mg; 0.24 mmol) in acetone was added to *cis*-$[Ru(bpy)_2Cl_2]$, (100 mg; 0.2 mmol) dissolved in 30 mL of dry acetone. Methyldiphenylphosphine, Ph_2PMe, (40 mg; 0.2 mmol) dissolved in 10 mL of acetone was then added dropwise and the mixture was stirred for 12 h at 25 °C. TlCl was removed by filtration and the remaining solution was purified by CombiFlash chromatography, using dichloromethane and acetone as eluents. The product was then precipitated by adding ether, and finally isolated under the form of a very fine orange powder (isolated yield: 60%).

NMR ^{31}P {^{1}H} (243 MHz, CD_3CN, 25 °C): δ (ppm) = 27.3 (s, $\underline{P}Ph_2Me$), -144.6 (sept, $^{1}J_{P-F}$ = 705 Hz, PF_6^-).

NMR ^{1}H (600 MHz, CD_3CN, 25 °C): δ (ppm) = 9.31 (d, 1H), 8.87 (d, 1H), 8.42 (d, 1H), 8.38 (d, 1H), 8.16 (d, 1H), 8.02-7.98 (m, 2H), 7.97-7.92 (m, 2H), 7.70 (d, 1H), 7.66 (t, 1H), 7.39-7.33 (m, 7H), 7.29 (t, 1H), 7.24 (t, 2H), 7.20 (t, 2H), 7.14 (t, 2H), 7.00 (t, 1H), 1.52 (d, $^{2}J_{P-H}$ = 8.2 Hz, 3H, PC$\underline{H}_3$).

2.1.2. Synthesis of $[(bpy)_2Ru(Ph_2PH)Cl]PF_6$, $[RuPH]^+PF_6^-$

A solution of 10 mL of $TlPF_6$, (83.8 mg; 0.24 mmol) in acetone was added to a solution of *cis*-$[Ru(bpy)_2Cl_2]$, (100 mg; 0.2 mmol) in dry acetone (30 mL). Diphenylphosphine, Ph_2PH, (192 mg; 1 mmol) dissolved in 10 mL of acetone was then added dropwise and the mixture was stirred for 12 h at 25 °C. TlCl was removed by filtration and the resulting solution purified by CombiFlash chromatography, using dichloromethane and acetone as eluents. The product was precipitated by adding ether, and isolated under the form of a very fine orange powder (isolated yield: 42 %).

NMR ^{31}P (162 MHz, acetone-d_6, 25 °C): δ (ppm) = 37.5 (d, $^{1}J_{P-H}$ = 356 Hz, $\underline{P}Ph_2H$), -144.2 (sept, $^{1}J_{P-F}$ = 705 Hz, PF_6^-).

NMR ^{1}H (400 MHz, acetone-d_6, 25 °C): δ (ppm) = 9.40 (d, 1H), 9.07 (d, 1H), 8.70 (d, 1H), 8.66 (d, 1H), 8.50 (d, 1H), 8.47 (d, 1H), 8.18-8.05 (m, 3H), 8.01-7.92 (m, 2H), 7.64 (d, 1H), 7.51 (td, 2H), 7.46-7.32 (m, 6H), 7.32-7.16 (m, 8H), 6.80 (d, $^{1}J_{P-H}$ = 356 Hz, 1H, $Ph_2P\underline{H}$).

2.1.3. Synthesis of $[(bpy)_2Ru(P(O)Ph_2)CH_3CN]PF_6$, $[RuPO]^+PF_6^-$

To a solution of 30 mL of $[RuPH]^+PF_6^-$ in acetonitrile (244 mg, 0.31 mmol), a low excess of silver(I) oxide, Ag_2O, was added (87 mg; 0.38 mmol) and the reaction mixture was stirred for 12 h at 25 °C. After elimination of AgCl by filtration, a fine orange product is obtained by precipitation with ether, isolated yield: 58 %.

NMR ^{31}P (243 MHz, CD_3CN, 25 °C): δ (ppm) = 78.3 (s, $\underline{P}(O)Ph_2$), -144.7 (sept, $^{1}J_{P-F}$ = 705 Hz, PF_6^-).

NMR ^{1}H (600 MHz, CD_3CN, 25 °C): δ (ppm) = 11.24 (broad, 1H), 9.28 (d, 1H), 8.38 (d, 1H), 8.36 (d, 1H), 8.09 (td, 1H), 7.94 (m, 2H), 7.89-7.83 (m, 4H), 7.77 (m, 2H), 7.71 (t, 1H), 7.64 (t, 1H), 7.45 (t, 2H), 7.37 (t, 1H), 7.27 (m, 2H), 7.16 (t, 1H), 6.94 (t, 1H), 6.69 (t, 2H), 6.54 (t, 2H), 1.92 (s, 3H, NCCH3).

2.2. Synthesis of metal nanoparticles

2.2.1. Synthesis of hybrid nanoparticles

As a general procedure, in a glove-box, [Ru(cod)(cot)] (30.0 mg; 0.095 mmol) and the chosen organophosphorus Ru(II)-polypyridyl complex (0.0095 mmol) were introduced in a Fisher-Porter reactor and dissolved in 30 mL of freshly degassed THF, leading to an intense orange solution. The reactor was then pressurized with 3 bar of hydrogen (H_2) at 25 °C under stirring. The initial orange solution turned black into a few minutes. Vigorous stirring and H_2 pressure were maintained for 24 h. The excess of H_2 was then evacuated and solvent evaporated under vacuum giving rise to the formation of a black precipitate. This solid was washed three times with THF (3x15mL), dried under vacuum and then re-dissolved in acetonitrile, providing an homogeneous colloidal dispersion. This colloidal dispersion was then transferred into a vial before drying under vacuum. The solid was again washed three times with THF and finally dried under vacuum overnight, which led to a dark black fine powder.

The same procedure was followed to prepare the hybrid nanomaterials based on CoNPs and PtNPs, using [Co(cod)(coe)] and [$Pt(nbe)_3$] as organometallic precursors, respectively.

2.2.2. Synthesis of RuNPs stabilized by ligands

As a typical example, [Ru(cod)(cot)] (30.0 mg; 0.095 mmol) and n eq. of L (L = bpy, PPh_3, PCy_3 (n = 0.2 eq.) or dppf (n = 0.1 eq.)) were dissolved in 30 mL of THF in a Fisher-Porter reactor inside a glove-box. After pressurization of the reactor with 3 bar of H_2 at 25 °C under vigorous magnetic stirring, the initial yellow solution turned dark brown in a few minutes. Vigorous stirring and the H_2 pressure were maintained for 24 h. After this reaction time, the remaining H_2 pressure was evacuated under vacuum. Precipitation of a black solid was induced by partial evaporation of the solvent and addition of pentane. The supernatant solution was extracted and pentane washings were repeated three times. A dark powder was finally isolated by evaporation to dryness under vacuum.

3. Characterization techniques

3.1. Electron microscopy

Samples for transmission electron microscopy (TEM) and high-resolution HR-TEM analyses were prepared by deposition of a drop of colloidal solution, either the crude or the purified colloidal solution, onto a holey carbon-covered copper grid followed by slow evaporation.

TEM analysis were performed on a MET JEOL JEM 1400 microscope operating at 120 kV with a resolution point of 0.45 nm. For HR-TEM, a JEOL JEM-ARM 200F microscope working at 200 kV with a resolution point of 0.19 nm was used. TEM allowed evaluating the particle morphology, size and size distribution. Enlarged micrographs were used for treatment with ImageJ software to obtain statistical size distributions (nanoparticles were manually measured) and nanoparticle mean diameters. FFT treatments of HR-TEM images were carried out with Digital Micrograph (Version 1.80.70) in order to determine the crystalline structure and lattice parameters of the metal nanoparticles.

3.2. ICP-OES

ICP-OES analyses were performed on a Thermo iCAP 6300 duo system at the "Service d'analyse élémentaire" at LCC-CNRS in Toulouse, after mineralization of the samples in aqua regia (HNO_3/HCl, 1:3) at 80 °C during 6 days.

3.3. Wide-Angle X-Ray Scattering

Wide-Angle X-Ray Scattering (WAXS) measurements were performed at CEMES-CNRS in Toulouse by Pierre Lecante. Samples of purified metal nanoparticles were sealed in 0.5 or 1.0 mm diameter Lindemann glass capillaries, under argon atmosphere. The samples were irradiated with graphite monochromatized molybdenum Kα (0.071069 nm) radiation and the X-ray scattering intensity measurements were performed using a dedicated two-axis diffractometer. Radial distribution functions (RDF) were obtained after Fourier transformation of the corrected and reduced data.

3.4. Nuclear Magnetic Resonance (NMR) Spectroscopy

Preparation of the samples for liquid NMR experiments was carried out under argon in a glove box using CD_3CN as a solvent. Liquid proton (^1H) and phosphorous (^{31}P) NMR were performed on a Bruker Avance 400 spectrometer or a Bruker Avance NEO 600 spectrometer at 296 K.

DOSY measurements were acquired with a diffusion delay (Δ) of 130.0 ms and a gradient pulse length (δ) of 2.0 ms. The diffusion dimension was processed with bi-exponential analysis involving least-squares fitting or by the Laplace inversion routine CONTIN (Topspin software). The hydrodynamic diameters were calculated with the Stockes Einstein Gierer-Wirtz estimation method.

Hydrodynamic diameters were estimated from the diffusion coefficients measured in 2D-DOSY experiments by following the Stokes–Einstein equation for spherical particles:

$$D = \frac{k_B T}{6\pi\eta r_H}$$

Where D is the diffusion coefficient, k_B is the Boltzmann constant, T is the temperature, η is the viscosity of the solvent and r_H is the hydrodynamic radius of the spherical particle. The DOSY experiments were performed at 296 K in acetonitrile (η=0.334 mPa·s).

Solid-state NMR analysis was accomplished on a Bruker Avance III HD 400 wide-bore spectrometer. In order to avoid electric arching, RuNPs were dispersed in mesoporous silica (60 Å). The silica matrix was impregnated with a colloidal solution in acetonitrile, and the solvent then evaporated under vacuum. Ca. 8.5 mg of nanoparticle powder were used per 100 mg of silica support. Filling of the rotors (zirconia; diameter 3.2 mm) with the samples was performed in a glove-box. Rotors were spun at 16 kHz at 298 K. ^{19}F and ^{31}P MAS NMR experiments were performed with recycle delays of 5 s and 2 s, respectively. ^{31}P MAS NMR data were recorded with Hahn-echo and CPMG pulse sequences. ^{13}C CPMAS spectra were acquired with a recycle delay of 2 s and a contact time of 3 ms.

3.5. X-Ray Photoelectron Spectroscopy

X-Ray Photoelectron Spectroscopy (XPS) measurements were performed at CIRIMAT-ENSIACET, Toulouse, by Jerome Esvan. The samples were prepared by embedding the powder of nanoparticles on an indium support.

The photoelectron emission spectra were recorded using a monochromatised Al Kalpha (hν = 1486.6 eV) source on a ThermoScientific K-Alpha system. The X-ray Spot size was 400 µm. The Pass energy was fixed at 30 eV with a step of 0.1 eV for core levels and 160 eV for surveys (step 1eV). The spectrometer energy calibration was done using the Ag3d5/2 (368.2 ± 0.1 eV) photoelectron lines. XPS spectra were recorded in direct mode N (Ec) and the background signal was removed using the Shirley method. XPS High Resolution spectra were recorded in order to extract the chemical environments of the studied species.

4. Surface reactivity studies

4.1. Hydride quantification

4.1.1. Reaction with norbornene and GC-MS detection

The synthesis of nanoparticles was performed in THF as previously described. To a freshly prepared colloidal solution, five cycles of vacuum/bubbling of argon (1 minute each) were applied in order to eliminate dissolved hydrogen. Then, 5 equivalents of 2-norbornene were added (5 mol 2-norbornene/mol [Ru(cod)(cot)]), and the mixture was stirred for 72 h at r.t. The reaction mixture was then filtered through silica in order to get a nanoparticle-free solution.

The obtained filtrate was analyzed on a GCMS-QP2010 Ultra instrument equipped with a flame ionization detector and a Zebron ZB-5MSplus column (30 mL x 0.25 mm ID x 0.25 µm df) 5% polysilarylene – 95% polydimethylsiloxane. Helium was used as carrier gas. Analysis was performed using a temperature set from 30 to 250 °C (15 °C·min^{-1}).

The quantity (mmol) of norbornane generated was calculated using a calibration curve previously optimized, on the basis of the necessary number of surface hydrides to convert the olefin into alkane (2 mol hydrides/mol norbornane).

4.1.2. Calculation of R_{surf}/Ru ratio and of reacted hydrides

To obtain the total number of Ru atoms per nanoparticle, we used the equation reported by Janiak and coworkers [2], where d_m is the nanoparticle diameter, r_{Ru} is the atomic radii of a Ru atom (r_{Ru} = 134 pm) and b = 1.105 for fcc and hcp structures.

$$N_T = \left(\frac{d_m}{2r_{Ru}b}\right)^3$$

RuNPs of 1.4 nm are thus composed of 106 atoms (N_T).

Number of shells (n)	Number of atoms (N_T)	Surface atoms (N_{surf})	d_m (nm)
1	13	12	0.7
2	55	42	1.1
3	147	92	1.6
4	309	162	2.0

Table 3. Number of surface atoms related to the total number of atoms in full shell clusters and corresponding cluster diameter [3].

The number of shells per nanoparticle, n, can be thus deduced as follows:

$$N_T = \frac{1}{3}(10n^3 - 15n^2 + 11n - 3)$$

The value of n for 1.4 nm RuNPs (n = 3.6) is then used to obtain the number of Ru surface atoms, N_{surf}.

$$N_{surf} = 10n^2 - 20n + 12$$

The two equations used above were originally described to determine the number of shells for a PdNP of cuboctahedron geometry [4].

From this method, ca. 70 Ru surface atoms were estimated for RuNPs of 1.4 nm, which results in a mean value of 66 Ru_{surf}/RuNP.

The number of reacted hydrides (H_{reac}) has been deduced from the amount of norbornane produced (obtained by GC), since 2 hydrides are necessary to reduce a C=C bond, divided by the number of moles of introduced ruthenium, as represented in the following equation

$$H_{reac}/Ru_{surf} = \left(\frac{n_H}{n_{Ru}}\right)\left(\frac{n_{Ru}}{n_{Ru_{surf}}}\right)$$

4.2. ^{13}CO adsorption

The RuNPs supported on silica as prepared for solid-state NMR experiments (see section 3.4.) were introduced in a Fischer-Porter reactor that was pressured with 1 bar of ^{13}CO. After 24 h under magnetic stirring at r.t., excess of ^{13}CO was evacuated under vacuum and the powder introduced in the NMR rotor for analysis.

5. Electrochemical studies

Voltammetric measurements were carried out with a potentiostat Autolab PGSTAT100 (ECO Chemie, The Netherlands) controlled by GPES 4.09 software. Experiments were performed at r.t. in a home-made airtight three-electrode cell connected to a vacuum/argon line. The reference electrode consisted of a saturated calomel electrode (SCE) separated from the solution by a bridge compartment. A platinum wire of ca. 1 cm^2 of apparent surface was used as counter electrode. The working electrode was a glassy carbon (GC) disk (3 mm diameter Bio-logic SAS). The 0.1 M in supporting electrolyte Bu_4NPF_6 was used as received (Fluka, +99% puriss electrochemical grade). Acetonitrile was freshly distilled prior to use and degassed by argon bubbling for 10 min.

Before each measurement, a 3 µL drop of RuNPs colloidal solution was deposited on the polished surface of the GC electrode. This process was repeated up to four times (4 x 3 µL). After each measurement, the GC electrode was polished with a polishing machine (silicon carbide P2400, Presi P230).

Typical instrumental parameters for recorded square-wave voltammograms were: SW frequency f =20 Hz, SW step potential = 5 mV and SW modulation amplitude = 20 mV.

6. Catalytic reactions

6.1. HER

TiO_2-supported Ru-nanocatalysts were prepared by adding TiO_2 powder (P-25 anatase/rutile, from Sigma Aldrich) to an acetonitrile colloidal solution of RuNPs (ca. 9 mg of RuNPs per 100 mg of TiO_2). The reaction mixture was stirred at r.t. for 24h and the solvent was evaporated under

vacuum, yielding a grey powder. 4 mg of supported material were used for each catalytic reaction.

The photocatalytic HER reactions were performed at the Universitat Autònoma de Barcelona, in the group of Dr. Xavier Sala, SelOxCat.

The evolution of hydrogen was measured by means of a Clark hydrogen electrode (Unisense H2-NP-9463). The photocatalytic hydrogen evolution reaction was performed in a 6 ml glass cell thermostatically controlled at 25 °C and containing 4 ml of TEOA 0.2 M as SED, where the catalyst is dispersed. The cell was sealed with a septum and grease and the Clark electrode tip was introduced at the headspace of the cell. The solution was degassed by Ar bubbling for at least 10 min until stabilization of the signal. Flat signal was recorded for at least 2 min. The cell was then irradiated with a solar simulator (Abet 10500) equipped with a Xe lamp placed at 1 sun (100 mW/cm^2) distance. After each hydrogen evolution catalytic test, the cell was degassed by Ar bubbling and a calibration was performed by injecting known volumes of H_2 (50, 100, 200, 300 and 400 μL) with a Hamilton syringe for gases.

6.2. CO_2 hydrogenation

The CO_2 hydrogenation reactions were performed at the National University of Singapore, in the group of Green Catalysis headed by Pr. Nin Yang.

The CO_2 hydrogenation to formic acid was conducted in a stainless-steel autoclave. In a typical reaction, sodium bicarbonate (168 mg, 2 mmol), employed as CO_2 source, was dissolved in 2 mL H_2O in a 10 mL glass vial whose dimeter corresponds to the internal diameter of the reactor. The catalyst was added and the mixture was sonicated for 10 min before introducing the vial inside the reactor. The reactor was then purged three times with N_2, charged with 20 bar of H_2, sealed and placed in a pre-heated oil bath (if indicated) at a 800 rpm stirring rate. After the chosen reaction time, the reaction was quenched by plunging the reactor in cold water before evacuating the H_2. The reaction mixture was then filtered before analysis by high performance liquid chromatography (HPLC, SHIMADZU, Singapore) equipped with a Hi-plex column and RID detector.

7. Computational details

DFT calculations were performed by Romuald Poteau and Iker del Rosal, at the LPCNO, Toulouse.

Periodic DFT calculations of metal clusters.

Software: Vienna ab initio simulation package, VASP [5,6]; spin polarized DFT; exchange-correlation potential approximated by the generalized gradient approach proposed by Perdew, Burke, and Ernzerhof (PBE) [7]; projector augmented waves (PAW) full-potential reconstruction; PAW data sets for metal atoms treating the (n-1)p, (n-1)d and ns states (14 valence electrons for Ru); kinetic energy cutoff: 525 eV; Γ-centered calculations; Gaussian smearing of 0.02 eV width; geometry optimization threshold: residual forces on any direction less than 0.02 eV/Å; supercell size: 40×39.5×39 Å for Ru55 clusters and 28×28.25×25.5 Å for Ru_{13} nanoclusters (set to ensure a vacuum space of ca. 16 Å between periodic images of metal clusters). The harmonic vibrational modes were systematically calculated in order to distinguish minima and saddle points by using the dynamical matrix code implemented in VASP as well as the VASPTST tools also developed in Henkelman's group.

NMR Calculations

Software: Gaussian09; geometries fully optimized without any geometry constraints; B3PW91 hybrid functional; Chemical shielding tensors: Gauge Including Atomic Orbital (GIAO) method. Relativistic effective core potentials developed by the Stuttgart group and their associated basis sets have been used for Ru - augmented with an f polarization function (ζf : 1.235); P, F, C and O: 6-31G(d,p) basis set. The optimized structures were used for ^{31}P and ^{19}F NMR calculations. Typically, in order to compare the calculations with experimental values, ^{31}P and ^{19}F chemical shieldings were converted to chemical shifts using the usual equation $\delta_{iso} = \sigma_{iso,ref} - \sigma_{iso,sample}$, where $\sigma_{iso,ref}$ is the isotropic chemical shielding of ^{31}P in 85% phosphoric acid or of ^{19}F in trichlorofluoromethane. In our case, $\sigma_{iso,ref}$ (^{31}P) = 330.24 ppm and $\sigma_{iso,ref}$ (^{19}F) = 186.87 ppm.

Following a computational strategy successfully used for computing ^{1}H, ^{13}C and ^{15}N chemical shits, a [Ru6] carbonyl cluster was first used as a model for RuNPs. The ^{31}P and ^{19}F chemical shifts were calculated by DFT studies and compared with the observed ones. When PF_6^- bridges two adjacent Ru atoms, the estimated ^{19}F chemical shifts are between -104 ppm and -188 ppm for the F atom directly coordinated to the Ru cluster surface and between -55 ppm and -79 ppm for the other ones. In the same way, the coordination of the PF_6^- anion is expected to unshield

the phosphorus chemical shift by around 25 ppm with respect to the free PF_6^- anion. In summary, according to the theoretical calculations, when the PF_6^- anion is coordinated at the RuNP surface the Fluor atoms interacting with the surface are more shielded (by around 50 ppm) while a deshielding is observed for phosphorus (by around 17 ppm). Thus, in view of these results, DFT calculations corroborate that the PF_6^- anion does not interact with the RuNP surface.

8. References

1. Sylvain, R. Complexes polypyridyles de ruthénium dia- et paramagnétiques à ligands phosphorés fonctionnalisés pour des applications en transfert électronique et photovoltaïque. Doctoral Thesis, Université Paul Sabatier, Toulouse, 2013.

2. Hosseini-Monfared, H.; Meyer, H.; Janiak, C. Dioxygen oxidation of 1-phenylethanol with gold nanoparticles and N-hydroxyphthalimide in ionic liquid. *J. Mol. Catal. Chem.* **2013**, *372*, 72–78.

3. Gonzalez Gomez, R. Développement de nanoparticules de ruthénium comme modèles de catalyseurs pour le craquage de l'eau: approches expérimentale et théorique. Doctoral Thesis, Université Paul Sabatier, Toulouse, 2019.

4. Wilson, O.M.; Knecht, M.R.; Garcia-Martinez, J.C.; Crooks, R.M. Effect of Pd Nanoparticle Size on the Catalytic Hydrogenation of Allyl Alcohol. *J. Am. Chem. Soc.* **2006**, *128*, 4510–4511.

5. Kresse, G.; Furthmüller, J. Efficiency of ab-initio total energy calculations for metals and semiconductors using a plane-wave basis set. *Comput. Mater. Sci.* **1996**, *6*, 15–50.

6. Kresse, G.; Furthmüller, J. Efficient iterative schemes for *ab initio* total-energy calculations using a plane-wave basis set. *Phys. Rev. B* **1996**, *54*, 11169–11186.

7. Perdew, J.P.; Burke, K.; Ernzerhof, M. Generalized Gradient Approximation Made Simple. *Phys. Rev. Lett.* **1996**, *77*, 3865–3868.

General Conclusion

In this PhD manuscript, the design of novel hybrid nanomaterials synthesized by the direct stabilization of metal nanoparticles with organophosphorus Ru(II) polypyridyl complexes has been presented. The objective of our fundamental studies was to finely determine the structure of the resulting hybrid nanomaterials, and to start evaluating the properties that might arise from the assembly of the two components. In order to do so, we took advantage of coordination chemistry and nanochemistry toolboxes.

After a brief introduction on the main properties of metal nanoparticles, the state-of-the-art in the domain of hybrid nanomaterials consisting on the assembly of transition metal complexes (TMCs) and metal nanoparticles (MNPs) was overviewed in Chapter 1. Interestingly, most of the publications regarding this research field have been reported during the last two decades, and mainly concern gold nanoparticles and applications in sensing and catalysis. The objective of this bibliographic review was to present the synthetic strategies applied for the building of TMC-MNPs nanohybrids and the techniques used for their characterization. This allowed highlighting that the most widely reported strategy for synthesis of TMCs-MNPs is, by far, through the use of pendant ligands, thus leading to TMCs connected to the surface of MNPs *via* organic spacers of various lengths. Note that most of the studies report multi-step synthetical procedures and poor descriptions on the nature of the interaction between the TMCs and the MNPs.

In Chapter 2, a first nanohybrid material made of ruthenium nanoparticles (RuNPs) stabilized by a mononuclear organophosphorus Ru(II)-polypyridyl complex, $[Ru(bpy)_2(PPh_2CH_3)Cl]PF_6$ (named as $[RuPMe]^+PF_6^-$) was successfully synthesized in a one-pot experimental procedure. This hybrid nanomaterial, $([RuPMe]_n\text{-}RuNPs)^+(PF_6^-)_n$, was fully characterized by a combination of experimental analytical techniques as well as *in silico* studies. Stable, small and well-dispersed nanoparticles were obtained, with ruthenium core mean sizes of ca. 1.4 nm and hcp structure. Advanced liquid and solid NMR experiments allowed to precisely determine the interaction modes of the stabilizing $[RuPMe]^+$ complex at the RuNP surface. Interestingly, two different populations of $[RuPMe]^+$ cationic organophosphorus complexes surrounding the RuNPs were observed:

A major population (ca. 60%) of $[RuPMe]^+$ is directly coordinated to the RuNP surface, forming an inner stabilizing layer. Theoretical calculations performed on the most stable hybrid conformer revealed an unprecedented coordination between the chlorine atom of the $[RuPMe]^+$ in the inner layer and the Ru surface atoms of the nanoparticle. This coordination leads to a Ru-Cl-Ru bridge between the $[RuPMe]^+$ and the RuNP. To the best of our knowledge, such an interaction between a transition metal complex and a metal nanoparticle was never reported in the literature.

A second population of $[RuPMe]^+$ species (ca. 40%), interacts electrostatically with their counterparts of the inner stabilizing layer, thus forming an outer layer.

The ionic character of the $[RuPMe]^+PF_6^-$ complex which act as stabilizer appeared to have strong effects on the solubility and stability of the hybrid nanomaterial in solution, with higher solubility in CH_3CN than in THF, as it is observed for the free complex itself. This solubility effect was a first evidence of the transfer of properties of the complex to the hybrid material.

The complex-like character of the hybrid nanomaterial was also evidenced by electrochemical studies, described in Chapter 3. Indeed, the $([RuPMe]_n\text{-}RuNPs)^+(PF_6^-)_n$ hybrid displayed an electrochemical gap (E_{ox}-E_{red}) of ca. 2.4 V, characteristic of a molecule-like redox behavior. Moreover, after the first oxidation peak, successive oxidations were also observed, which were related to a quantized charging phenomenon typical of quantum capacitors. These observations were drastically different from the electrochemical responses observed for other RuNPs stabilized with classical organic ligands, such as phosphine or bipyridine derivatives. Upon oxidation, these latter RuNPs undergo corrosion-like processes typical of bulk metals.

As the nanohybrid displays oxidations that occur up to high oxidative potentials (ca. 3 V (vs SCE)), the $([RuPMe]_n\text{-}RuNPs)^+(PF_6^-)_n$ nanomaterial can be considered as a potential electron reservoir, a property of interest for catalytic reduction reactions. Preliminary studies on the photocatalytic hydrogen evolution reaction and the transformation of carbon dioxide into formic acid were thus performed. While the results on the photoinduced hydrogen production were disappointing, positive and encouraging results on the hydrogenation of CO_2 into formic acid were obtained. Even if low activities were observed, the $([RuPMe]_n\text{-}RuNPs)^+(PF_6^-)_n$ hybrid used as nanocatalyst in the production of formic acid proved to achieve higher rates than those obtained by RuNPs stabilized by simple organic ligands (PPh_3, PCy_3 bpy or PP). Further efforts will be devoted to improve the CO_2 conversion by the

($[RuPMe]_n$-RuNPs)$^+$(PF_6^-)$_n$ by evaluating the influence of the different reaction parameters (temperature, solvent, reaction time or carbon dioxide source, as examples).

Based on the results obtained during this PhD, we believe that this work strongly contributes to the field of hybrid TMC-MNPs, because of the versatility of the synthesis strategy developed to achieve the ($[RuPMe]_n$-RuNPs)$^+$(PF_6^-)$_n$ nanohybrid. In the last part of this PhD work, it has been demonstrated that different hybrid structures can be also accessed, by either changing the nature of the metal nanoparticle cores (Co, Pt) or the functions on P-atom of the organophosphorus Ru(II)-polypyridyl complexes used as stabilizers. This thus opens new avenues for the development of a large variety of TMC-NPs hybrid nanomaterials towards future applications in fields such as electronics, electro(photo)catalysis or energy storage.

Résumé en français

Au cours des dernières décennies, d'importants progrès ont été réalisés en nanochimie pour l'élaboration de nanoparticules métalliques (MNPs) de morphologie, taille, et composition contrôlées. La synthèse de MNPs bien définies permet d'obtenir de meilleures informations sur les paramètres, pouvant affecter leurs propriétés physico-chimiques. L'un de ces paramètres ayant un fort effet sur les caractéristiques des MNPs, est l'agent stabilisant (polymère, tensioactif ou ligand, par exemple). Lorsque des ligands sont utilisés pour la stabilisation des MNPs, les interactions qui ont lieu entre ces ligands et les atomes métalliques de surface peuvent être comparées à l'interaction du ligand avec le centre métallique d'un complexe de métal de transition. On peut parler ainsi de coordination des ligands aux sites métalliques de surface des MNPs. Les ligands, qui se placent à l'interface entre le milieu extérieur et la surface des MNPs et possèdent des propriétés électroniques et stériques spécifiques, ont un rôle déterminant sur les propriétés – solubilité, stabilité chimique et thermique, réactivité - des MNPs.

Les propriétés physicochimiques des nanoparticules métalliques étant fortement influencées par les espèces présentes à leur surface, pourquoi alors ne pas envisager d'utiliser des complexes de métaux de transition (TMCs) porteurs de nouvelles fonctionnalités et les associer à des nanoparticules métalliques pour construire de nouveaux matériaux. Pour mettre en œuvre ce type assemblages, un choix rationnel du fragment TMC peut conférer aux nanoparticules des groupements redox, des propriétés photophysiques ou bien encore enrichir leur réactivité catalytique par la présence de différents centres métalliques. On peut anticiper que ces nanomatériaux hybrides ainsi formés pourraient trouver des applications dans des domaines comme la détection, la catalyse, l'imagerie biomédicale ou l'électronique.

Ce travail de thèse porte sur le développement de nouveaux nanomatériaux hybrides consistant en l'assemblage covalent d'un complexe de métal de transition (TMC) avec des nanoparticules métalliques (MNPs). On peut attendre de tels nanomatériaux hybrides des propriétés différentes de celles observées pour chaque entité indépendante.

Au cours des deux dernières décennies, la synthèse de nanomatériaux hybrides incorporant des MNPs et des TMCs avec diverses caractéristiques et pour différentes applications a été rapportée dans la littérature. Ce champ de recherche est largement dominé par les

nanoparticules d'or. Les principales raisons de ce développement sont (i) la stabilité chimique des AuNPs et leur préparation relativement simple, mais aussi (ii) des propriétés optiques remarquables qui peuvent trouver des applications dans des domaines tels que la détection et l'optique non linéaire. Pour des intérêts similaires, mais dans une moindre mesure, plusieurs travaux décrivent également l'assemblage de TMCs avec des AgNPs. Seuls quelques exemples décrivent la préparation de nanohybrides qui associent des NPs de cobalt, de palladium, de rhodium, de cuivre et de fer-platine à des TMCs.

Une analyse précise des nanomatériaux hybrides TMC-MNPs rapportés à ce jour nous a permis de constater qu'ils peuvent être classés selon quatre stratégies différentes de formation des assemblages entre TMCs et MNPs, comme le montre la figure 1: (a) greffage des TMC à la surface des MNPs *via* des groupes d'ancrage pendants sur les TMCs, (b) complexation des TMCs à la surface des MNPs *via* des groupes d'ancrage pendants provenant de la couche stabilisante des MNPs, (c) association des deux composants par interaction électrostatique et (d) systèmes divers (par exemple π-stacking, interactions hôte-invité).

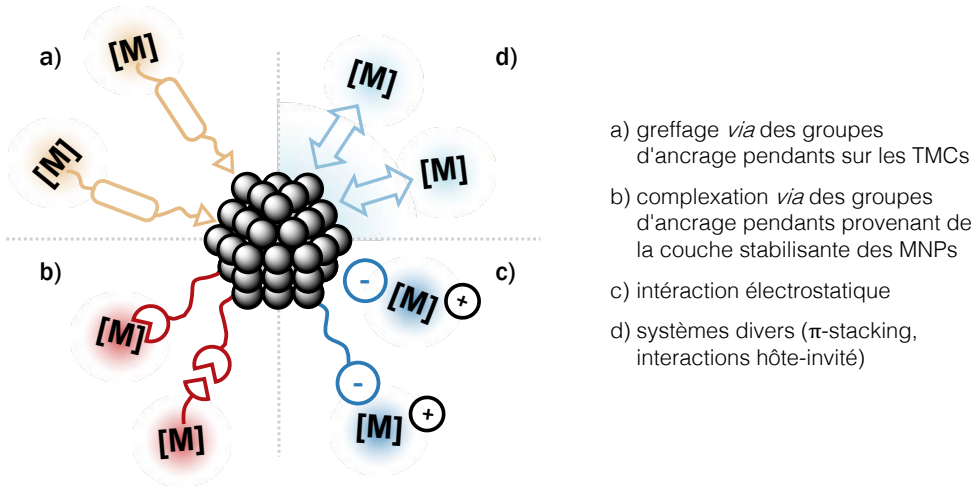

Figure 1. Représentation schématique des quatre modes de connexion entre les nanoparticules métalliques (MNPs) et les complexes de métaux de transition (TMCs).

Dans ce travail de thèse, la préparation des MNPs a été menée selon l'approche organométallique développée dans le groupe, qui consiste en la décomposition de précurseurs organométalliques en solution et dans des conditions de réaction douces. Le déplacement de ligand ou la réduction de précurseurs organométalliques ou métalloorganiques à valence nulle/basse, généralement en appliquant une température douce et/ou une pression de H_2 ou de CO, entraine la libération des atomes métalliques en solution ce qui induit le processus de

nucléation. La nucléation et la croissance des nanoparticules sont contrôlées par l'ajout d'un agent stabilisant dès le début du processus de synthèse, qui peut se coordonner à la surface des noyaux en croissance et ainsi la stopper (ligand) ou bien la limiter stériquement (polymère), les deux empêchant l'agrégation des particules en un matériau massif. Des ligands ou polymères organiques, des petites molécules comme le monoxide de carbone, CO, ou le méthanol, CH_3OH, des liquides ioniques ou des supports hétérogènes (silice, alumine, nanotubes de carbone, etc.) peuvent être utilisés pour stabiliser des MNPs synthétisées par cette méthode. Un choix adéquat du précurseur métallique, des conditions de réaction (solvant, température et / ou pression) et de la nature du stabilisant, une grande variété de nano-objets peuvent être ainsi synthétisés, avec un bon contrôle de taille, forme et environnement de surface.

Par comparaison avec les nanoparticules étudiées auparavant dans notre groupe, le caractère innovant de ce travail consiste en l'utilisation de complexes organophosphorés polypyridyles de ruthénium comme agent stabilisant des MNPs.

Les complexes polypyridyles de ruthénium sont robustes thermiquement et chimiquement et présentent des propriétés électrochimiques et photophysiques très riches, ce qui explique leur application dans des domaines comme le photovoltaïque ou la photocatalyse. La coordination des ligands organophosphorés au fragment ruthénium polypyridyle est une approche très puissante pour modifier les propriétés électroniques de tels complexes. En modifiant les capacités de donneur et d'accepteur des ligands organophosphorés, une large gamme de propriétés redox et spectroscopiques peut être obtenue. Par exemple, le potentiel d'oxydation Ru^{2+}/Ru^{3+} d'un complexe terpyridine bipyridine ruthénium incorporant un ligand tricyclohexylphosphine, PCy_3, est de 1,32 V, et celui du complexe correspondant avec un ligand triphénylphosphite, $P(OPh)_3$, est de 1,61 V (par rapport à SCE, à température ambient et dans l'acétonitrile). Il est remarquable qu'une gamme de 290 mV si exceptionnelle est atteinte en utilisant des ligands d'une même famille qui sont coordonnés par le même hétéroatome P avec le même état d'oxydation. La coordination des ligands phosphoryles aux fragments ruthénium polypyridyle entraîne également des changements dans les propriétés photophysiques de tels complexes, et la capacité d'accepteur de protons de l'unité P=O offre de nouvelles opportunités pour explorer les interactions intermoléculaires comme la liaison hydrogène. En résumé, les complexes Ru(II)-polypyridine portant des ligands organophosphorés coordonnés au centre métallique présentent une réactivité réglable et des propriétés électroniques, ce qui les rend très intéressants à combiner avec des nanoparticules métalliques.

Les nanoparticules de ruthénium (RuNPs) ont été choisies pour mener ces études fondamentales en raison (i) de la possibilité d'utiliser un complexe organométallique de ruthénium comme source d'atomes métalliques ne libérant que des sous-produits de type alcane qui sont inertes vis-à-vis de la surface métallique, (ii) des compétences accumulées dans le groupe pour la synthèse de RuNPs, permettant ainsi une comparaison des nanomatériaux hybrides formés avec d'autres systèmes de RuNPs, et (iii) la possibilité que le ruthénium offre d'effectuer des expériences de RMN liquide et solide, contrairement à d'autres métaux tels que le palladium ou le platine qui présentent des effets Knight Shift prononcés.

Le travail décrit est centré sur l'utilisation d'un complexe organophosphoré polypyridyl ruthénium cationique mononucléaire, $[(bpy)_2Ru(PPh_2Me)Cl]PF_6$, désigné par la suite $[RuPMe]^+PF_6^-$, comme agent stabilisant des RuNPs, et la caractérisation fine du nanomatériau hybride résultant, $([RuPMe]_n\text{-}RuNPs)^+(PF_6^-)_n$, grace à une combinaison de techniques analytiques complémentaires accompagnée d'une étude théorique.

La synthèse du nanomatériau hybride $([RuPMe]_n\text{-}RuNPs)^+(PF_6^-)_n$ (voir schéma 1), a été réalisée en utilisant le complexe organométallique [Ru(cod)(cot)] comme précurseur de RuNPs et 0,1 équivalent molaire (éq.) du complexe $[RuPMe]^+PF_6^-$ comme stabilisant. Ces deux espèces ont été dissoutes dans du tétrahydrofurane (THF) fraîchement distillé et dégazé dans un réacteur Fischer-Porter sous atmosphère d'argon. Le mélange réactionnel a ensuite été mis sous pression de H_2 (3 bar) puis maintenu sous agitation vigoureuse pendant 24 h à 25 ° C. Après ce temps de réaction, l'excès de H_2 a été évacué par pompage. A partir de la suspension colloïdale noire brute, les composés volatils ont été évaporés sous vide ce qui a conduit à la formation d'un précipité noir. Ce solide noir a été lavé trois fois avec du THF, redispersé dans de l'acétonitrile et transféré dans un flacon avant séchage sous vide. La poudre noire résultante a été à nouveau lavée trois fois avec du THF et séchée sous vide pendant une nuit.

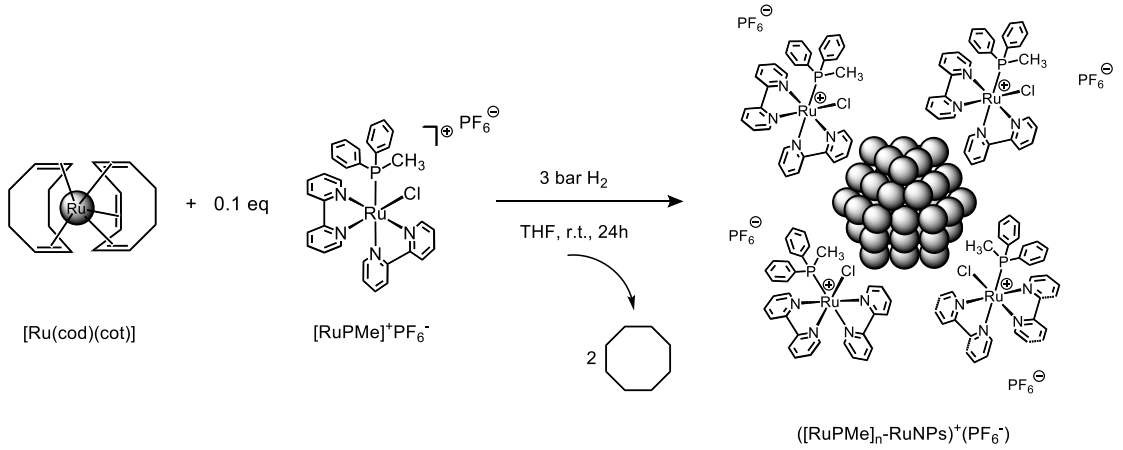

Schéma 1. Synthèse du nanomatériau hybride $([RuPMe]_n\text{-}RuNPs)^+(PF_6^-)_n$.

Il est important de noter qu'aucune modification du complexe n'a été observée par RMN ^{31}P et ^1H après avoir soumis le complexe $[RuPMe]^+PF_6^-$ sous H_2 durant plusieurs heures à 3 bar de pression.

Une analyse TEM comparative effectuée sur deux grilles - l'une préparée à partir de la suspension colloïdale brute dans le THF et la seconde obtenue après dispersion de la poudre noire purifiée dans l'acétonitrile - a clairement mis en évidence des différences en termes de dispersion des NPs formées. À partir de la suspension colloïdale brute dans le THF, des agrégats sphériques réguliers d'environ 350 nm ont été observés sur la grille TEM (Fig 2a). Une image TEM zoomée (figure 2b) montre que ces agrégats sont constitués de NPs individuelles. Au contraire, la dispersion d'acétonitrile, contient des NPs individuelles petites et bien dispersées, avec une distribution en tailles assez symétrique et centrée à environ 1,4 nm $\pm$ 0,6 (Fig. 2c et 2d). Bien que la distribution en tailles soit assez large avec observation de quelques NPs plus grandes, il est important de noter qu'une grande majorité de particules présentent une taille proche de la taille moyenne calculée, ce qui indique que les conditions de réaction appliquées ont conduit à un contrôle de taille efficace.

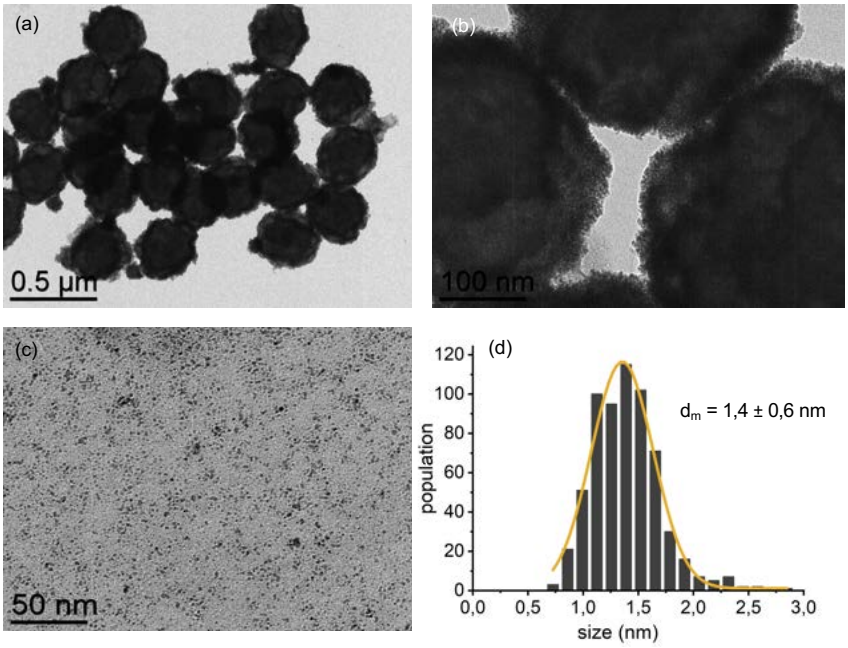

Figure 2. Images TEM de $([RuPMe]_n\text{-}RuNPs)^+(PF_6^-)_n$: (a, b) dans le THF et (c) après redispersion dans l'acétonitrile. (d) Histogramme de taille de $([RuPMe]_n\text{-}RuNPs)^+(PF_6^-)_n$ dissous dans l'acétonitrile.

Le comportement observé en solution indique un certain caractère ionique des espèces nanohybrides formées qui ont tendance à s'agréger spontanément dans un solvant de faible polarité comme le THF, mais qui sont au contraire bien dispersées dans un solvant polaire organique comme l'acétonitrile. Ce comportement est similaire à celui du complexe $[RuPMe]^+PF_6^-$ dans les mêmes solvants qui, en raison de son caractère ionique, est plus soluble dans l'acétonitrile, un solvant plus polaire que le THF.

Les images HRTEM enregistrées à partir d'échantillons $([RuPMe]_n\text{-}RuNPs)^+(PF_6^-)_n$ dispersés dans l'acétonitrile (Fig. 3a) montrent des petites RuNPs amorphes et quelques-unes plus grosses qui ont tendance à afficher des plans cristallins. Comme le montre la Fig. 3b, la transformation de Fourier rapide (FFT) de l'image HRTEM d'une RuNP de ca. 2,6 nm montre des distances interplanaires de 0,219 et 0,203 nm correspondant aux plans cristallins (002) et (101) de la structure hexagonale compacte (hcp) du ruthénium massif, cette structure cristalline étant observée de manière récurrente pour des RuNPs.

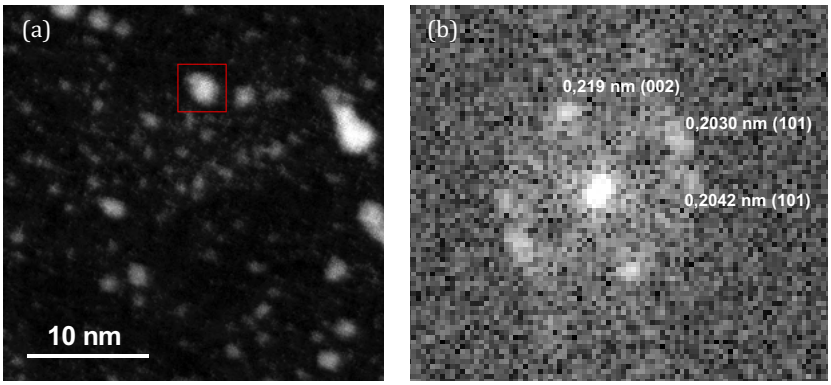

Figure 3. (a) Image HRTEM de $([RuPMe]_n\text{-}RuNPs)^+(PF_6^-)_n$ dispersé dans l'acétonitrile; (b) diffractogramme d'une une RuNP (cadre rouge).

L'analyse par diffusion des rayons X aux grands angles (WAXS), effectuée sur un échantillon solide purifié de $([RuPMe]_n\text{-}RuNPs)^+(PF_6^-)_n$ et sous atmosphère d'argon, a complété les résultats obtenus par HRTEM. La signature obtenue est cohérente avec celle du ruthénium massif hcp. La figure 6b montre la fonction de distribution radiale (RDF) de l'échantillon $([RuPMe]_n\text{-}RuNPs)^+(PF_6^-)_n$. Une longueur de cohérence maximale d'env. 2,5 nm indique la présence de domaines cristallins de dimensions proches de la taille estimée pour les RuNPs de grandes tailles et cristallines précédemment observées sur les images HRTEM (~ 2,6 nm).

Différentes expériences de RMN ont permis d'obtenir de plus amples informations sur la composition de la surface métallique des RuNPs au sein du nanohybride $([RuPMe]_n\text{-}RuNPs)^+(PF_6^-)_n$ ainsi que sur la nature de l'interaction existant entre les RuNPs et le complexe $[RuPMe]^+PF_6^-$. Comme nous le verrons par la suite, la RMN liquide a fourni des informations sur l'état des complexes $[RuPMe]^+PF_6^-$ et leur mobilité autour des RuNPs et proximité ou pas avec leur surface. Des expériences de RMN à l'état solide ont complété les études en solution, notamment pour l'identification des fragments caractéristiques de l'unité $[RuPMe]^+$ à proximité immédiate de la surface métallique. Les analyses RMN liquide et solide ont permis de proposer un schéma détaillé de la disposition des entités $[RuPMe]^+PF_6^-$ à la surface des RuNPs (voir ci-après).

La figure 4 compare le spectre RMN ^1H du $([RuPMe]_n\text{-}RuNPs)^+(PF_6^-)_n$ (Fig. 4b) avec celui du complexe $[RuPMe]^+PF_6^-$, utilisé comme référence (Fig. 4a), tous deux dans CD_3CN. Le spectre RMN ^1H de l'hybride $([RuPMe]_n\text{-}RuNPs)^+(PF_6^-)_n$ présente un signal très large entre 6,5 et 9,0 ppm, région correspondante à celle des déplacements chimiques des ligands bipyridiniques et des substituants phényles du ligand du fragment organophosphoré du complexe $[RuPMe]^+$. Le profil RMN ^1H de l'hybride $([RuPMe]_n\text{-}RuNPs)^+(PF_6^-)_n$ indique la présence de $[RuPMe]^+$ à

proximité immédiate des RuNPs, interagissant directement avec la surface et formant une couche autour des RuNPs. De plus, même si l'hydrogénation partielle de $[RuPMe]^+$ pendant la synthèse de l'hybride ne peut pas être exclue, ces résultats suggèrent que l'aromaticité du complexe est très largement préservée.

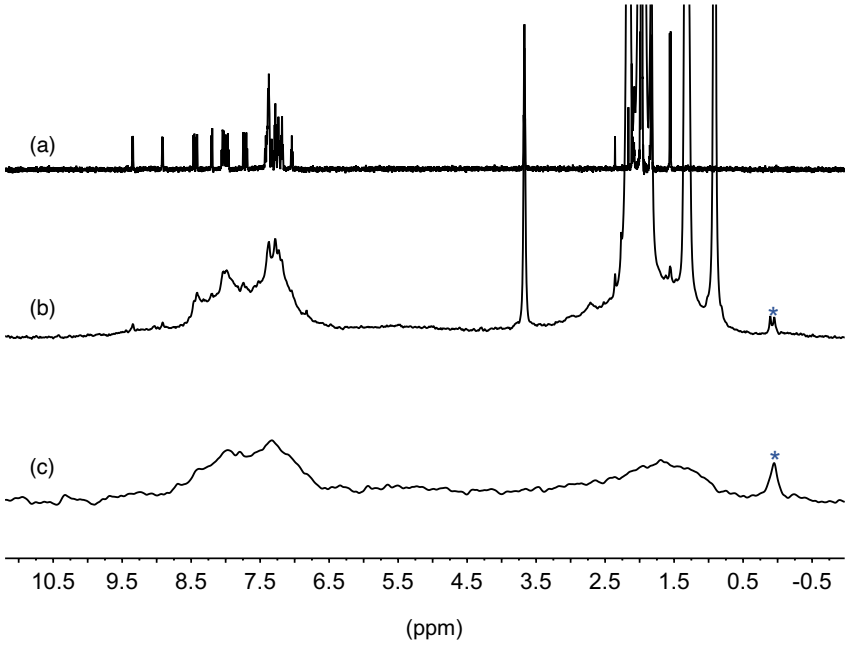

Figure 4. Spectres RMN ^1H de (a) $[RuPMe]^+PF_6^-$, (b) $([RuPMe]_n\text{-}RuNPs)^+(PF_6^-)_n$ purifié et (c) $([RuPMe]_n\text{-}RuNPs)^+(PF_6^-)_n$ dans CD_3CN après application d'un filtre par diffusion. *Graisse.

Sur la crête des signaux larges, on peut aisément apercevoir des pics nets correspondant aux complexes $[RuPMe]^+$. Ces pics sont trop fins pour appartenir à des espèces $[RuPMe]^+$ directement coordonnées à la surface des RuNPs mais sont par ailleurs significativement plus larges que ceux des complexes $[RuPMe]^+$ libres en solution. Ils peuvent donc être raisonnablement attribués à des espèces $[RuPMe]^+$ dans une couche externe du nanomatériau $([RuPMe]_n\text{-}RuNPs)^+(PF_6^-)_n$, nommé $[RuPMe]^+_{exch}$.

Le spectre RMN ^1H avec filtrage en fonction de la vitesse de diffusion (seule le signal des espèces diffusant lentement est conservé) de l'hybride $([RuPMe]_n\text{-}RuNPs)^+(PF_6^-)_n$ est présenté sur la figure 4c. Le premier signal, dans la plage de 6,5 à 9,0 ppm, est attribué aux ligands polypyridyles et phényles du fragment organophosphoré $[RuPMe]^+$. Le deuxième signal, entre 0,5 et 2,5 ppm, pourrait provenir de l'hydrogénation partielle des groupes phényles de $[RuPMe]^+$. En raison des conditions réductrices appliquées pour la synthèse de l'hybride et du

fait que les RuNPs sont de bons catalyseurs d'hydrogénation des arènes, l'hydrogénation des groupes aromatiques lors de la synthèse de RuNPs a déjà été observée dans notre groupe.

Des expériences RMN 2D DOSY ont été menées afin d'obtenir des informations sur la mobilité des différentes espèces $[RuPMe]^+$ présentes en solution. Les données correspondantes sont présentées sur la figure 5. Le tracé RMN de diffusion conduit à deux coefficients de diffusion, à savoir D_1 = 4,0 ($\pm$0,2) · 10^{-10} m^2/s et D_2 = 10,0 ($\pm$0,3) · 10-10 10^{-10} m^2/s, avec un rapport de population de 60/40 ($\pm$5). La valeur la plus faible, D_1, correspond à des espèces peu mobiles et peut donc être attribuée au nanomatériau hybride $([RuPMe]_n\text{-}RuNPs)^+(PF_6^-)_n$ dans lequel les complexes $[RuPMe]^+$ sont directement coordonnés à la surface des RuNPs, formant ainsi une couche de stabilisation interne. La deuxième valeur, D_2, est supérieure à D_1 mais inférieure à celle obtenue pour le $[RuPMe]^+PF_6^-$ libre dans les mêmes conditions ($D_{[RuPMe]PF6}$ = 1,3 · 10^{-9} m^2/s). Cette deuxième valeur, D_2, peut donc être attribuée aux espèces $[RuPMe]^+_{exch}$, présentant une mobilité plus élevée que l'hybride mais pas autant que le complexe libre. Étant donné le caractère ionique des complexes mononucléaires organophosphorés polypyridyles $[RuPMe]^+$, on peut raisonnablement proposer que les complexes organophosphorés $[RuPMe]^+_{exch}$, situés dans une couche extérieure sont en interaction électrostatique avec le nanomatériau hybride $([RuPMe]_n\text{-}RuNPs)^+(PF_6^-)_n$. De telles interactions électrostatiques impliquent un échange des espèces $[RuPMe]^+_{exch}$ entre la couche externe et le solvant.

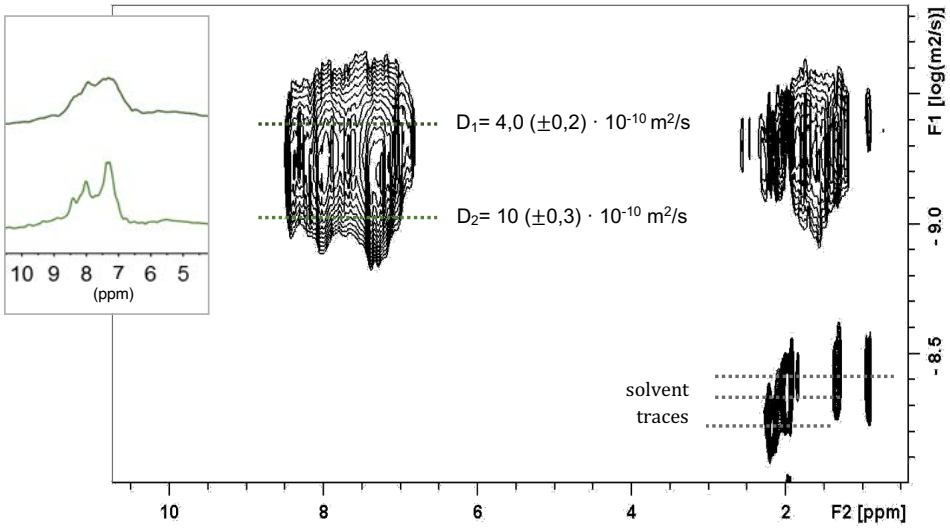

Figure 5. Diagramme RMN DOSY 2D de $([RuPMe]_n\text{-}RuNPs)^+(PF_6^-)_n$ dans CD_3CN, avec les projections RMN ^1H des espèces dans la couche intérieure (D_1) et la couche extérieure (D_2).

L'équation de Stockes-Einstein permet de corréler le coefficient de diffusion d'une entité avec son rayon hydrodynamique, pour un solvant et une température donnés. En appliquant cette équation, pour le coefficient de diffusion D_1, attribué au matériau hybride $([RuPMe]_n\text{-}RuNPs)^+(PF_6^-)_n$ où les complexes $[RuPMe]^+$ sont fortement coordonnés à la surface des RuNPs, un diamètre hydrodynamique de 3,0 nm, a pu être estimé.

Par RMN ^{31}P liquide, un septuplet bien résolu centré à -144,6 ppm a été détecté, attribuable à l'anion PF_6^-. Les caractéristiques de son signal indiquent que cet anion PF_6^- est totalement solvaté par l'acétonitrile et éloigné de l'influence des RuNPs; et que qu'il a donc préserve sa dynamique moléculaire. De plus, un signal net et de faible intensité à 27,3 ppm, peut être attribué à des complexes $[RuPMe]^+$ en périphérie du matériau hybride $([RuPMe]_n\text{-}RuNPs)^+(PF_6^-)_n$, également identifiés par RMN ^1H. Aucun signal attribuable au ligand phosphine PMe du complexe $[RuPMe]^+$ en interaction directe avec la surface RuNPs n'a été observé. Sachant qu'il est bien établi que des fragments d'organophosphorés situés à proximité d'une surface métallique ne sont pas observés par expériences de RMN du ^{31}P liquide, ce résultat confirme la proximité du ligand phosphoré de la surface métallique.

Des expériences RMN à l'état solide ont été réalisées sur des échantillons de $([RuPMe]_n\text{-}RuNPs)^+(PF_6^-)_n$ et $[RuPMe]^+PF_6^-$ adsorbés sur de la poudre de SiO_2. La RMN ^{31}P MAS de $([RuPMe]_n\text{-}RuNPs)^+(PF_6^-)_n$ (Fig. 6b) conduit à des caractéristiques comparables à celles du complexe $[RuPMe]^+PF_6^-$ libre (Fig. 6a) mais avec toutefois des signaux plus larges dus au milieu hétérogène dans lequel l'environnement de l'atome de phosphore est soumis. Comme on le voit sur la figure 6c, la séquence Carr-Purcell-Meiboom-Gill (CPMG) a été appliquée afin d'améliorer le rapport signal/bruit. Cela a permis de mieux détecter un signal PF_6^- intense à environ -144 ppm ainsi qu'un autre signal d'intensité inférieure à 26 ppm. En raison de son déplacement chimique et de sa netteté, le pic à 26 ppm peut être attribué aux espèces $[RuPMe]^+_{exch}$ situées dans la couche externe. En dessous de ce pic, un signal beaucoup plus large centré à 33 ppm est également identifié. Il est attribué au ligand organophosphoré PPh_2Me de complexes $[RuPMe]^+$ directement attachés aux RuNPs, la largeur de ce signal étant due au fait que ces entités $[RuPMe]^+$ sont plus affectées par l'hétérogénéité de la surface des NPs, comme précédemment observé dans le cas de la RMN liquide.

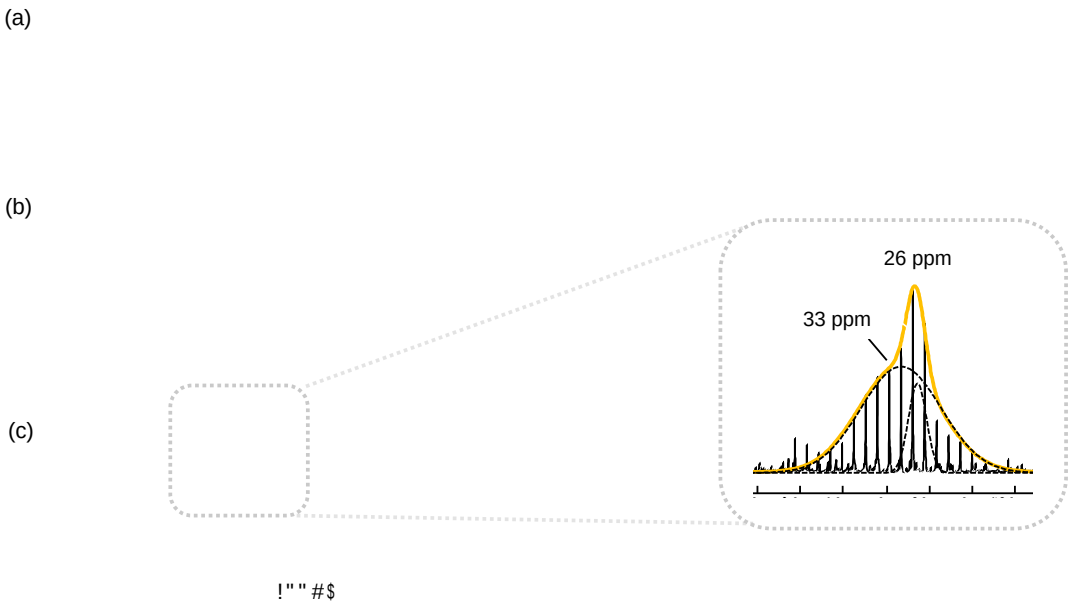

Figure 6. RMN ^{31}P MAS à l'état solide de (a) $[RuPMe]^+PF_6^-$ libre dans SiO_2, (b) $([RuPMe]_n\text{-}RuNPs)^+(PF_6^-)_n$ dans SiO_2 et (c) ^{31}P CPMG MAS NMR de $([RuPMe]_n\text{-}RuNPs)^+(PF_6^-)_n$ dans SiO_2.

Le spectre RMN à l'état solide ^{13}C MAS de l'hybride affiche des signaux aromatiques dans la plage 110-160 ppm de manière similaire à ce qui est observé pour le complexe libre $[RuPMe]^+PF_6^-$. Des carbones aliphatiques centrés à environ 28 ppm sont également visibles, ce qui pourrait correspondre à des fragments PPh_2Me partiellement hydrogénés. Cette hypothèse est corroborée par des études antérieures dans le groupe où l'hydrogénation des groupements aromatiques de ligands phosphines utilisées pour stabiliser des RuNPs a été détectée par RMN.

La quantification des hydrures présents à la surface des RuNPs a été réalisée en analysant l'hydrogénation du 2-norbornène en présence d'une solution colloïdale de nanomatériau hybride fraichement synthétisé sans addition de source d'hydrogène supplémentaire. Cette étude a révélé une valeur d'environ 1,6 hydrure par atome de surface de ruthénium. Cette valeur est la plus élevée enregistrée à ce jour par rapport à celles observées pour d'autres systèmes de RuNPs stabilisées avec des ligands classiques rapportés dans l'équipe. Cela démontre que les RuNPs dans le nanomatériau hybride sont capables d'accueillir une grande quantité d'atomes d'hydrogène de surface, ce qui peut être intéressant pour des applications impliquant des réactions d'hydrogénation.

L'accessibilité de la surface métallique de ruthénium dans le nanomatériau hybride $([RuPMe]_n\text{-}RuNPs)^+(PF_6^-)_n$ a été sondée par adsorption de ^{13}CO. L'analyse RMN ^{13}C MAS à l'état solide de l'échantillon hybride a révélé qu'il existe encore des sites de surface libres et accessibles pour l'adsorption de molécules comme le CO.

Avec les données expérimentales en main, des calculs en utilisant la théorie fonctionnelle de la densité (DFT) ont été effectués par le Dr I. del Rosal et le Pr. R. Poteau (Laboratoire de Physique et Chimie des Nano-objets (LPCNO), Toulouse). Un des objectifs de ces calculs DFT consistait à mieux comprendre la nature des modes de coordination des unités $[RuPMe]^+$ à la surface des nanoparticules de ruthénium. Le rôle du contre anion PF_6^- a également été étudié et complété par des expériences de RMN.

Un modèle de cluster Ru_{55}, qui correspond à une RuNP d'environ 1 nm, a été choisi pour effectuer les calculs DFT. Le cluster Ru_{55} est un modèle optimisé qui représente les sites de surface caractéristiques de petites RuNPs hcp. Les calculs périodiques de DFT ont été effectués à l'aide du package de simulation *ab initio* de Vienne (VASP) (DFT polarisé en spin et potentiel de corrélation d'échange approximé par l'approche de gradient généralisé proposée par Perdew, Burke et Ernzerhof (PBE)).

Des calculs DFT ont ensuite été effectués sur le modèle Ru_{55} avec un rapport d'hydrure/Ru_{surf} préétabli de 0,8 ($Ru_{55}H_{35}$). Les simulations ont montré une coordination du complexe $[RuPMe]^+$ à la surface de la RuNP qui intervient *via* l'atome de chlore du complexe organophosphoré et qui agit comme un ligand pontant. Ce mode d'interaction est observé pour certains complexes dimériques du ruthénium. L'énergie d'adsorption du complexe $[RuPMe]^+$ sur la surface de la NP avec le ligand chlorure ponté est d'environ -33,8 kcal/mol (figure 7b). Dans le conformère le plus favorable (figure 7a), une interaction chélatante de type π-aromatique supplémentaire entre l'un des ligands bipyridine du complexe $[RuPMe]^+$ et un atome de surface Ru adjacent stabilise la structure d'environ 10 kcal/mol supplémentaire et conduit à une énergie d'adsorption totale de -41,4 kcal/mol. La valeur d'énergie d'adsorption de -33,9 kcal/mol obtenue pour $[RuPMe]^+$ interagissant simultanément avec le RuNP par le chlore et la densité d'électrons π de l'un des cycles phényle (Fig. 7c) est très similaire à celle calculée pour le complexe coordonné par le chlore seul (-33,8 kcal/mol).

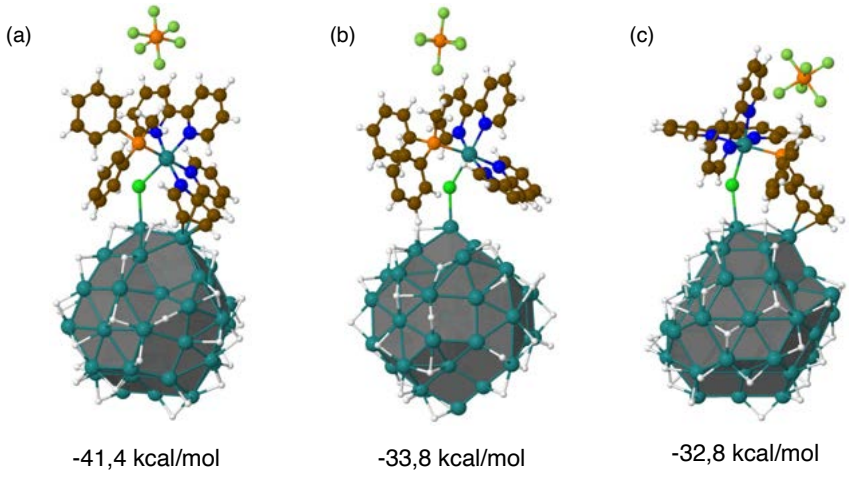

Figure 7. Modes de coordination stables du complexe $[RuPMe]^+$ à la surface d'un cluster de Ru_{55} et énergies d'adsorption associées.

D'un point de vue structurel, la coordination de $[RuPMe]^+$ à la surface de la RuNP n'induit que de légères modifications géométriques sur le complexe comme observé par l'allongement de la liaison Ru–Cl (de 0,05 Å) et pour les liaisons C–N et C–C du ligand bipyridine interagissant avec la surface (respectivement de 0,07 et 0,04 Å).

La rupture de la liaison Ru–Cl induite par la surface de la RuNP suivie de la formation d'une liaison Ru–Ru et de μ-Cl coiffant un bord du RuNP est légèrement défavorisé avec une valeur endothermique de ΔE = 1,1 kcal/mol. Cependant, cette différence d'énergie quelque peu faible pourrait être remise en question. C'est pourquoi d'autres indices énergétiques ont été obtenus à partir d'un cluster de modèles $Ru_{13}H_{17}$. Il semble que dans les deux modes de coordination considérés (l'un très similaire à celui représenté sur la figure 7a, tandis que le second pourrait se produire sur des sommets pointus), le complexe $[RuPMe]^+$ non dissocié est thermodynamiquement plus stable que son homologue dissocié par environ 10 kcal/mol. Cela confirme que le $[RuPMe]^+$ adsorbé conserve son intégrité structurelle et son identité.

Du point de vue théorique, pour la configuration la plus stable $([RuPMe]_n\text{-}RuNPs)^+(PF_6^-)_n$, la différence entre l'anion PF_6^- en interaction électrostatique avec l'hybride (considération initiale) ou bien greffé sur la surface du ruthénium est d'environ +7 kcal/mol (voir Fig.8). Ce résultat est en bon accord avec les données RMN ^{31}P indiquant que le PF_6^- est solvaté et loin de l'influence de la surface des RuNPs.

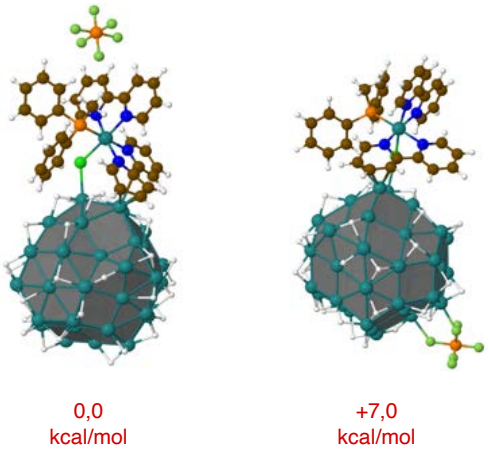

Figure 8. Différences d'énergie d'adsorption de $[RuPMe]^+$ sur Ru_{55} avec PF_6^- en interaction électrostatique avec l'hybride (à gauche) ou adsorbé sur la surface (à droite).

En résumé, la combinaison d'expériences RMN à l'état solide et liquide avec des calculs DFT a permis de déterminer la disposition structurelle des espèces $[RuPMe]^+$ à la surface des RuNPs. Les résultats obtenus sont cohérents avec l'existence de deux populations différentes d'espèces $[RuPMe]^+$ au sein de nanomatériau hybride formé, comme représenté sur le schéma 2:

(i) une population importante complexes organophosphorés de ruthénium $[RuPMe]^+$ qui est coordonné de manière covalente avec la surface de la NP par l'intermédiaire de l'atome de chlore, qui agit comme un ligand pontant. Une interaction chélatante de de type π avec un ligand bipyridine vient compléter l'interaction entre le complexe $[RuPMe]^+$ et la RuNP pour former la couche interne.

(ii) une fraction mineure de complexes organophosphorés de ruthénium $[RuPMe]^+$, en interaction électrostatique avec l'hybride $([RuPMe]_n\text{-RuNPs})^+(PF_6^-)_n$, forme la couche externe. En raison de son caractère ionique, le complexe $[RuPMe]^+$ dans la couche externe est très vraisemblablement en interaction électrostatique avec ses homologues de la couche interne.

Les calculs DFT suggèrent que 5 molécules $[RuPMe]^+$ couvrent la surface des RuNPs. Il est à noter que les calculs DFT sont effectués en conditions sous vide et que le solvant utilisé dans les conditions expérimentales peut également avoir une influence importante. Considérant qu'une RuNP de taille moyenne 1,4 nm contient globalement 106 atomes de Ru, les données expérimentales enregistrées sur la population du nanomatériau hybride ont donné un nombre de 6 complexes $[RuPMe]^+$ par RuNP. Cette valeur a été estimée en tenant compte des résultats obtenus par ICP, qui indiquent que 60% de la quantité de complexe $[RuPMe]^+PF_6^-$ utilisé pour la synthèse intègrent l'hybride $([RuPMe]_n\text{-RuNPs})^+(PF_6^-)_n$. Étant donné que les expériences de

RMN 2D DOSY ont mis en évidence un rapport de population de 60/40 (±5) de molécules $[RuPMe]^+$ directement coordonnées et $[RuPMe]^+_{exch}$, 4 molécules $[RuPMe]^+$ sont susceptibles de se coordonner à la surface des RuNPs. Par conséquent, nous pouvons considérer qu'une moyenne de 4 à 5 complexes $[RuPMe]^+$ sont greffés à la surface des RuNPs.

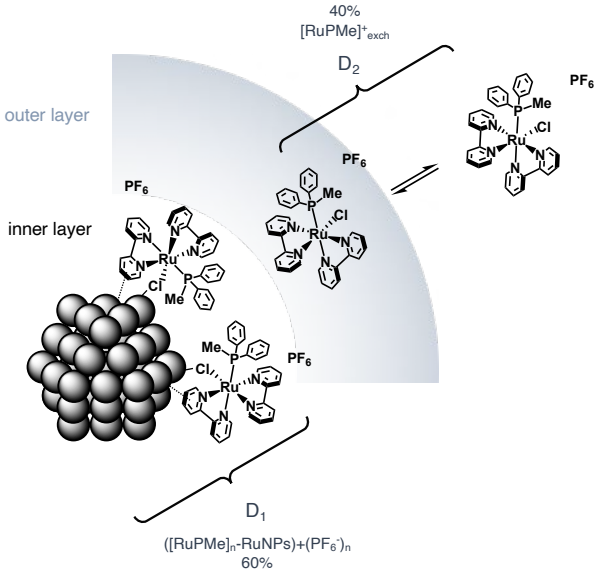

Schéma 2. Représentation schématique de la disposition des espèces $[RuPMe]^+$ autour des noyaux métalliques dans le nanomatériau hybride obtenu sur la base des données de RMN.

Ayant pu obtenir une image précise de la structure du nouveau nanomatériau hybride synthétisé (schéma 2), l'étape suivante a consisté à étudier ses propriétés. Ainsi, une analyse sans précédent des caractéristiques électrochimiques de ce nanomatériau a été menée, en utilisant le complexe $[RuPMe]^+PF_6^-$ comme référence. De plus, des résultats préliminaires sur la réaction photocatalytique d'évolution de l'hydrogène (HER) et sur la transformation du CO_2 en acide formique ont été obtenus et, pour la seconde réaction, comparés à celles obtenues avec des RuNPs stabilisées par des ligands simples.

L'analyse électrochimique de l'hybride $([RuPMe]_n\text{-}RuNPs)^+(PF_6^-)_n$ et de RuNPs stabilisés par des ligands classiques tels que la triphénylphosphine, la tricyclohexylphosphine et la bipyridine (PPh_3, PCy_3 et bpy) a mis en évidence des caractères redox très différents. Les systèmes PPh_3-RuNPs, PCy_3-RuNPs et bpy-RuNPs présentent une vague redox très ample et très large, attribuable à un processus semblable à la corrosion, observé pour les métaux massifs par exemple. Le nanomatériau hybride $([RuPMe]_n\text{-}RuNPs)^+(PF_6^-)_n$ présente plusieurs pics redox

distincts qui sont peuvent être attribués à des processus de transfert d'électrons successifs (voir figure 9).

Outre un premier pic (0,88 V vs SCE) attribué à l'oxydation des espèces $[RuPMe]^+$ (soit $[RuPMe]^+_{exch}$ ou les deux $[RuPMe]^+_{exch}$ et $[RuPMe]^+$ directement coordonnées), il n'est pas simple d'identifier et d'attribuer les autres vagues d'oxydation. Ces oxydations sont continues et se produisent jusqu'à des potentiels oxydants élevés, de l'ordre de 3 V (vs SCE), montrant que le matériau hybride $([RuPMe]_n\text{-}RuNPs)^+(PF_6^-)_n$ se comporte comme un réservoir d'électrons.

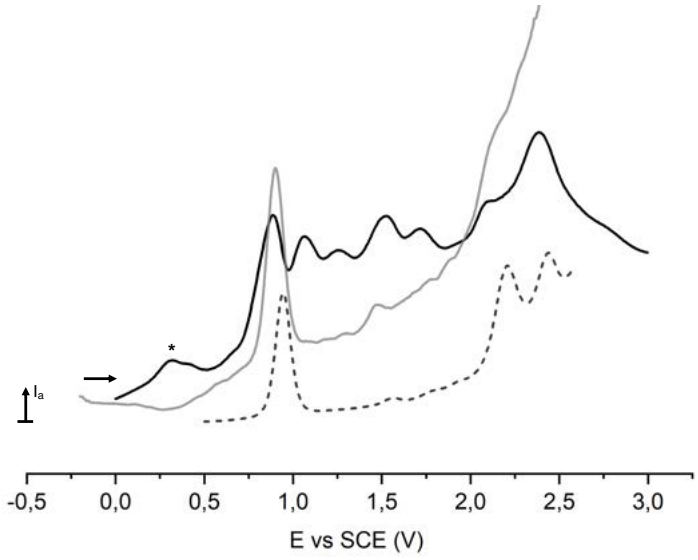

Figure 9. Voltammogramme à vague carrée de l'oxydation de $([RuPMe]_n\text{-}RuNPs)^+(PF_6^-)_n$ (noir), $[RuPMe]^+PF_6^-$ (gris) déposés sur une électrode GC et $[RuPMe]^+PF_6^-$ en solution (pointillés).

En réduction, le voltamogramme du nanomatériau hybride $([RuPMe]_n\text{-}RuNPs)^+(PF_6^-)_n$ affiche deux signaux larges centrés à environ -1,55 et -1,80 V (vs SCE), chacun composé de deux pics. Les intensités relatives des deux pics composant ces signaux larges, similairement à celles observées pour le complexe $[RuPMe]^+PF_6^-$, suggèrent la réduction de deux espèces différentes de Ru(II)-polypyridyl: (i) à -1, 54 et -1,77 V (vs SCE) et (ii) à -1,61 et -1,87 V (vs SCE), marqués comme • et ♦ dans la figure 10, respectivement. Ces deux processus de réduction rapprochés pourraient être la signature des complexes $[RuPMe]^+$ dans la couche intérieure et la couche extérieure de l'hybride.

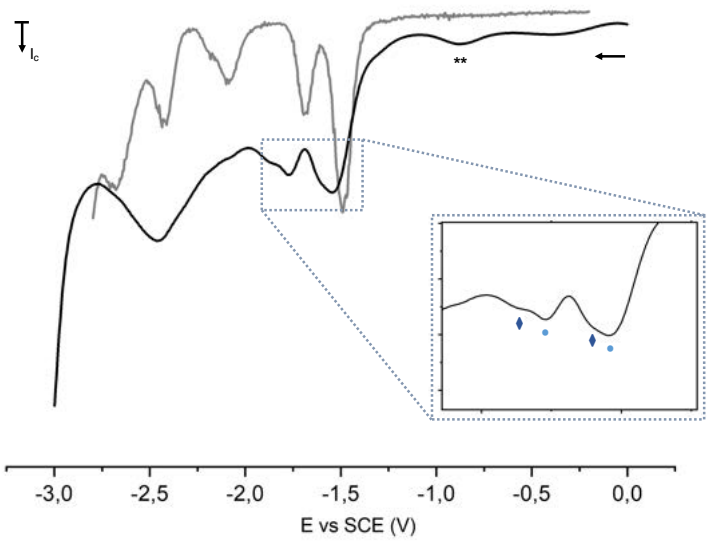

Figure 10. Voltammogrammes à vague carrée de la réduction de $([RuPMe]_n\text{-}RuNPs)^+(PF_6^-)_n$ (noir) et $[RuPMe]^+PF_6^-$ (gris) déposés sur une électrode GC.

Par l'analyse de la voltampérométrie à vague carrée de $([RuPMe]_n\text{-}RuNPs)^+(PF_6^-)_n$, les caractéristiques électrochimiques du complexe $[RuPMe]^+PF_6^-$ semblent préservées dans le $([RuPMe]_n\text{-}RuNPs)^+(PF_6^-)_n$ hybride. De plus, le comportement redox observé semble être cohérent avec la structure du nanohybride dans lesquels on observe par RMN une couche interne et externe $[RuPMe]^+$.

Le nanomatériau hybride $([RuPMe]_n\text{-}RuNPs)^+(PF_6^-)_n$ présente un écart électrochimique notable d'environ 2,4 V (première oxydation à 0,88 V vs SCE et première réduction à -1,55 V vs SCE), typique d'un comportement d'une espèce de type complexe/molécule. De plus, l'hybride $([RuPMe]_n\text{-}RuNPs)^+(PF_6^-)_n$ peut être oxydé successivement sous une forme analogue aux clusters qui se comportent comme des condensateurs quantiques. Ce modèle apparait plus clair lorsque l'on regarde la voltampérométrie à vague carrée obtenue pour $([RuPMe]_n\text{-}RuNPs)^+(PF_6^-)_n$ en solution à une concentration élevée (15 mg / 5 mL), comme présenté dans la figure 11. Ce comportement spécifique n'a pas été expérimentalement observé pour d'autres RuNPs de taille similaire ni pour le complexe organophosphoré $[RuPMe]^+PF_6^-$ seul, ce qui est très en faveur du caractère hybride du nanomatériau $([RuPMe]_n\text{-}RuNPs)^+(PF_6^-)_n$.

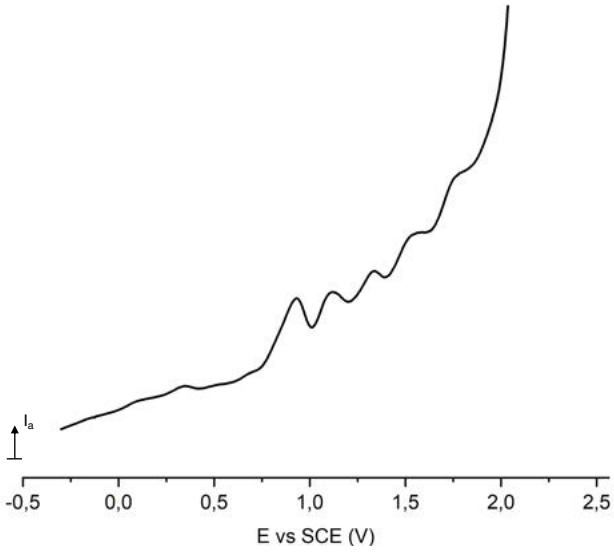

Figure 11. Voltammogramme à vague carrée de $([RuPMe]_n\text{-}RuNPs)^+(PF_6^-)_n$ en solution.

Pour aider à la compréhension des résultats obtenus expérimentalement, les propriétés électroniques de l'hybride $([RuPMe]_n\text{-}RuNPs)^+(PF_6^-)_n$ ont été étudiées par calculs DFT en collaboration avec les Dr I. del Rosal et Pr. R. Poteau (Laboratoire de Physique et Chimie des Nano-objets (LPCNO), Toulouse). L'approche utilisée, la densité d'états (DOS), est définie comme le nombre des niveaux ou états dans un intervalle d'énergie donné. Les courbes DOS décrivent la distribution de la densité électronique et l'occupation des différents états.

Le DOS projeté (pDOS), qui correspond à la décomposition du DOS en contributions des différentes orbitales moléculaires, a été réalisé pour le complexe $[RuPMe]^+PF_6^-$ libre et pour une structure hybride composée d'une molécule de $[RuPMe]^+$ directement coordonnée à la surface d'un cluster $Ru_{55}H_{35}$, $([RuPMe]^+\text{-}Ru_{55}H_{35})PF_6^-$, dans la conformation la plus stable (figure 12).

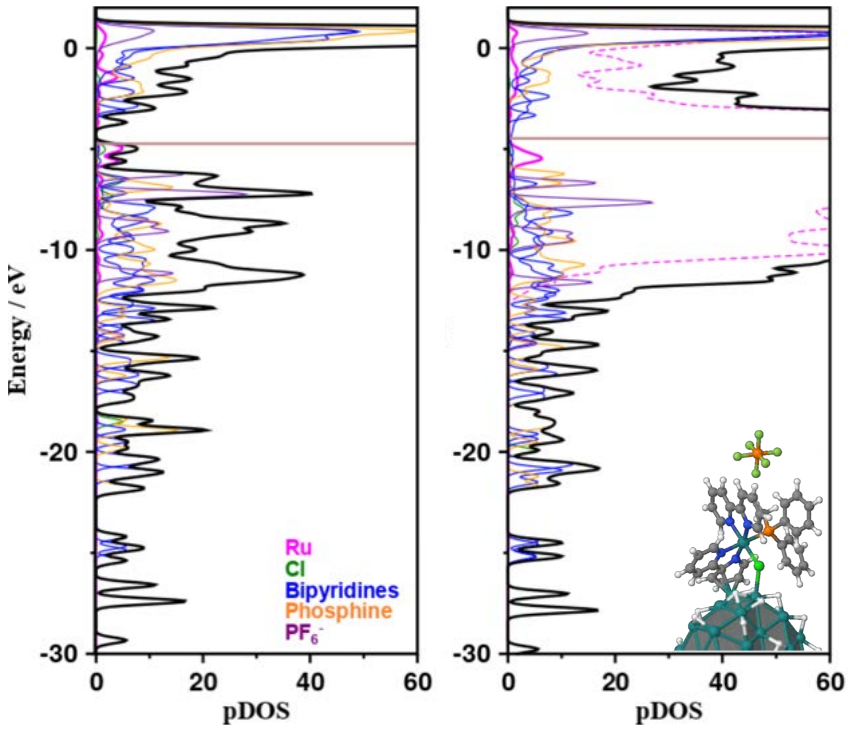

Figure 12. pDOS et profils pour $[RuPMe]^{+}PF_6^{-}$ (gauche) et $[RuPMe]^{+}$-$Ru_{55}H_{35}$ (droite). Ligne horizontale brune: énergie de Fermi. Ligne noire: DOS total.

Le pDOS de $([RuPMe]^{+}$-$Ru_{55}H_{35})PF_6^{-}$ dénote une très forte contribution des orbitales d du noyau métallique Ru (ligne magenta en pointillés). Par ailleurs, la signature électronique du complexe $[RuPMe]^{+}$ est reconnue, peu affectée par sa coordination avec le cluster Ru_{55}. Fait intéressant, la densité électronique du centre de Ru(II) est proche du niveau de Fermi et légèrement stabilisée par sa coordination avec le noyau Ru. Des études antérieures sur le pDOS de clusters Ru_{55} stabilisés par des ligands organiques comme le CO et les éthanoates, à savoir $Ru_{55}(CO)_{66}$ et $Ru_{55}H_{33}(CH_3OO)_{16}$, ont montré que les états occupés les plus élevés reposent essentiellement sur des atomes de métal Ru. Dans ces cas, les contributions des ligands stabilisateurs CH_3OO^{-} et CO au DOS sont de l'ordre de 3 à 6 eV plus bas que le niveau de Fermi, respectivement. Par les profils obtenus pour $Ru_{55}(CO)_{66}$ et $Ru_{55}H_{33}(CH3OO)_{16}$, il semble donc raisonnable d'envisager une corrosion du noyau métallique Ru lors de l'oxydation. En revanche, dans $([RuPMe]^{+}$-$Ru_{55}H_{35})PF_6^{-}$, les états développés sur le Ru(II) des complexes de $[RuPMe]^{+}$ sont juste en dessous de l'énergie de Fermi de l'hybride (<1 eV). Dans ce cas, il est difficile de prédire dans quels états, orbitales d du métal Ru (surface RuNP) ou Ru(II) centre métallique, l'oxydation se produira.

Outre l'étude du comportement électrochimique des RuNPs stabilisées par des ligands classiques (bpy, PPh_3 et PCy_3), la caractérisation électrochimique préliminaire de RuNPs stabilisés par le bis(diphénylphosphino)ferrocène (dppf) a été menée. Le système dppf-RuNPs contient des centres actifs redox greffés à la surface des RuNPs comme c'est le cas pour notre nanomatériau hybride $([RuPMe]_n\text{-}RuNPs)^+(PF_6^-)_n$. On peut remarquer que le nouvel hybride incorporant le dppf ne manifeste pas le processus de corrosion observé pour les RuNP stabilisés avec des ligands phosphines, et ce, même si le fragment de ferrocène est coordonné via le ligand diphénylphosphine sur la nanoparticule. Le comportement observé est similaire à celui du $([RuPMe]_n\text{-}RuNPs)^+(PF_6^-)_n$ hybride. La caractérisation fine des dppf-RuNPs mérite d'être poursuivie, car une meilleure compréhension de la structure de ce nanomatériau est nécessaire pour parvenir à une conclusion plus détaillée.

Ces résultats d'électrochimie ont permis de mettre en évidence que les réponses redox obtenues pour les systèmes étudiés dépendaient fortement de la nature du stabilisant. Un tel niveau d'information pourrait s'avérer au regard d'applications en catalyse ou dans d'autres domaines d'intérêt, comme dans les applications de transfert d'électrons ou les nanocondensateurs, par exemple. Ces travaux pionniers au sein de l'équipe méritent d'être poursuivis de manière exhaustive en étendant la portée de la nature des stabilisants et/ou des nanoparticules métalliques.

Les propriétés catalytiques des nanomatériaux hybrides $([RuPMe]_n\text{-}RuNPs)^+(PF_6^-)_n$ concernant deux réactions importantes en catalyse, la réduction photocatalytique des protons pour la production d'hydrogène et la transformation du CO_2 en acide formique, ont été étudiées.

Les résultats préliminaires obtenus sur la production photocatalytique de H_2 en milieu aqueux en utilisant l'hybride $([RuPMe]_n\text{-}RuNPs)^+(PF_6^-)_n$ comme photocatalyseur ont montré des valeurs de TON et TOF bien inférieures aux meilleurs systèmes catalytiques rapportés dans la littérature. La faible activité photocatalytique observée avec l'hybride $([RuPMe]_n\text{-}RuNPs)^+(PF_6^-)_n$ pourrait provenir d'un transfert d'électrons inefficace entre les entités $[RuPMe]^+PF_6^-$ et les RuNPs ou d'une mauvaise photoactivation du nanomatériau hybride. Ces études ont été réalisées dans le groupe du Dr Xavier Sala, SelOxCat, à l'Université autonome de Barcelone avec lequel notre équipe à une collaboration de longue date.

En ce qui concerne l'hydrogénation du CO_2, nous avons rapporté les tout premiers résultats que nous avons obtenus dans la transformation du CO_2 en HCOOH en utilisant des diverses RuNPs comme catalyseurs, dans des conditions de réaction douces. Ces résultats ont été obtenus lors

d'un séjour de 4 semaines à l'Université Nationale de Singapour, dans le groupe du Pr. Ning Yan, financé par une bourse de mobilité reçue de l'Université Fédérale Toulouse Midi-Pyrénées. Si les résultats présentés sont assez médiocres en termes de valeurs de TON et TOF, il est à noter que seuls quelques exemples de catalyseurs hétérogènes et nanométriques à base de Ru sont rapportés jusqu'à présent dans la littérature pour cette réaction.

En comparant un ensemble de RuNPs stabilisés par différents ligands (PP, PPh_3, PCy_3, bpy), des résultats intéressants sur l'effet du ligand stabilisant ont été observés. Il est apparu que les phosphines PPh_3 et PCy_3 ont un effet positif par rapport à un la phénylpyridine (PP), effet qui s'est avéré plus prononcé avec PCy_3, probablement en raison du caractère σ–donneur plus élevé de cette phosphine. L'activité observée pour les RuNPs stabilisées par la bipyridine s'est également révélée intéressante. Cependant, une étude approfondie serait nécessaire afin d'avoir des données plus précises et de mieux comprendre l'effet du ligand sur l'activité catalytique des RuNPs testées. Pour ces RuNPs stabilisés par des ligands classiques, le dépôt des RuNPs sur TiO_2 comme support fournit en général, des performances catalytiques plus élevées. Une dispersion plus élevée des RuNPs après dépôt à la surface de TiO_2 et une augmentation de la stabilité dans les conditions de réaction appliquées, en limitant l'agrégation des nanoparticules et la perte de sites de surface actifs, pourraient expliquer l'effet positif lors de la mise en oeuvre de RuNPs supportés par TiO_2. Des performances catalytiques plus élevées ont été observées à des temps de réaction plus courts, peut-être en raison d'une certaine désactivation des nanocatalyseurs étudiés dans les conditions de réaction appliquées et/ou d'une certaine réversibilité de la réaction. Ce point, c'est-à-dire la régénération du CO_2 à partir du HCOOH produit, méritera d'être étudié en profondeur. De façon remarquable, les meilleurs résultats catalytiques ont été obtenus avec le nanomatériau hybride non supporté $([RuPMe]_n\text{-}RuNPs)^+(PF_6^-)_n$ à 40 °C. Avec une performance toutefois inférieure, ce nanocatalyseur est resté actif lorsque les réactions ont été effectuées à température ambiante, et surtout il a présenté une activité plus élevée que les autres RuNPs à 40 °C.

Pour conclure, les études préliminaires de catalyse réalisées montrent que les performances de l'hybride $([RuPMe]_n\text{-}RuNPs)^+(PF_6^-)_n$ vers la transformation catalytique de HCO_3^- en $HCOO^-$ sous pression de H_2 sont supérieures à celles observées avec des RuNPs stabilisés par des ligands classiques, tout au moins dans les conditions appliquées. Si un effet de solubilité ne peut pas être écarté, cette différence peut provenir de propriétés synergiques induites par la coordination du complexe $[RuPMe]^+$ à la surface des RuNPs. Les résultats obtenus nous encouragent à poursuivre cette ligne de recherche. La modification de différents paramètres de

réaction comme la température, la pression, le pH, la nature du stabilisant, du solvant, du support solide ou de la source de CO_2, afin d'obtenir des informations précises sur le rôle qu'ils jouent dans l'activité des nanocatalyseurs Ru figure parmi les objectifs principaux.

Pour conclure, nos travaux préliminaires ont permis la synthèse de nanomatériaux hybrides innovants : (i) des nanoparticules à base de Ru stabilisées par des complexes Ru(II)-polypyridyl incorporant d'autres fragments phosphorés et (ii) des nanoparticules métalliques de Co et Pt, synthétisées en utilisant des complexes organophosphorés Ru(II)-polypyridyle comme stabilisants.

Nous avons montré que les complexes organophosphorés Ru(II)-polypyridyle $[(bpy)_2Ru(PPh_2H)Cl]PF_6$ et $[(bpy)_2Ru(Ph_2PO)MeCN]PF_6$ (voir figure 13) sont capables de stabiliser des petites RuNPs par la même procédure de synthèse directe que celle développée pour l'hybride $([RuPMe]_n\text{-}RuNPs)^+(PF_6^-)_n$. Si la caractérisation fine des systèmes hybrides obtenus doit être complétée en utilisant d'autres techniques analytiques et des méthodes théoriques, les résultats préliminaires de RMN ont déjà mis en évidence que les différentes propriétés chimiques des complexes stabilisants peuvent conduire à différents modes de coordination à la surface du ruthénium.

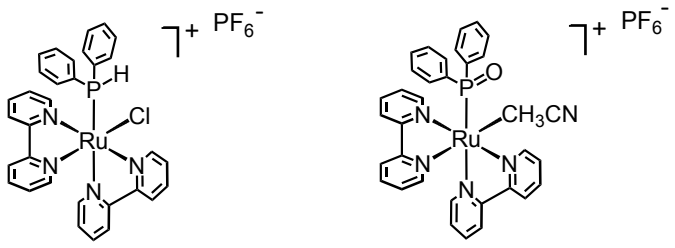

$[RuPH]^+PF_6^-$ $[RuPO]^+PF_6^-$

Figure 13. Complexes de Ru(II)-polypiridyle organophophorés, $[(bpy)_2Ru(PPh_2H)Cl]PF_6$ et $[(bpy)_2Ru(Ph_2PO)MeCN]PF^6$, $[RuPH]^+PF_6^-$ et $[RuPO]^+PF_6^-$ respectivement, utilisé pour la stabilisation des RuNPs.

Le complexe de Ru(II)-polypiridyle organophophorés $[RuPMe]^+PF_6^-$ n'a pas permis la formation de PtNPs contrôlées dans les conditions de réaction appliquées. La variation des paramètres de réaction sera donc une perspective pour d'autres études concernant le nanomatériau $([RuPMe]_n\text{-}PtNPs)^+(PF_6^-)_n$. Concernant les nanomatériaux hybrides à base de Co, nos efforts ont été consacrés à la caractérisation des petites CoNPs stabilisées par le complexe $[RuPH]^+PF_6^-$, $([RuPH]_n\text{-}CoNPs)^+(PF_6^-)_n$.

Même s'ils sont très préliminaires, ces résultats sont suffisamment encourageants pour la poursuite d'études sur la formation de nouveaux nanomatériaux hybrides associant des complexes polypyridyliques phosphorés à des nanoparticules métalliques. Par exemple, les CoNPs obtenues pourraient s'avérer intéressantes d'un point de vue propriétés magnétiques en raison de leur structure cristalline epsilon-Co particulière. De plus, étant très sensibles à l'air, leur oxydation contrôlée (en espèces Co_3O_4 ou $Co(OH)_2$, par exemple) pourrait conduire à des nanomatériaux d'intérêt en tant que nanocatalyseurs dans la réaction de dégagement d'oxygène.

En rendant compte de résultats nouveaux et intéressants quant à la synthèse de nanomatériaux hybrides innovants par une approche de chimie moléculaire, ces travaux de thèse ont permis d'ouvrir de nouvelles perspectives de recherche. Ce travail devrait contribuer fortement au domaine des TMC-MNPs hybrides, en raison de la polyvalence de la stratégie de synthèse qui a été développée pour atteindre les nanohybrides $([RuPMe]_n\text{-}RuNPs)^+(PF_6^-)_n$. Ces travaux ouvrent ainsi de nouvelles voies pour le développement d'une grande variété de nanomatériaux hybrides TMC-MNPs potentiellement d'intérêt pour de futures applications dans des domaines tels que l'électronique, l'électro(photo)catalyse ou le stockage d'énergie.